Contents

List of Symbols

a	constant in emperical formular for U_R
a_1	parameter in Bergeron process
a_2	parameter in Bergeron process
A'	constant in Bigg freezing
A"	coefficient in the diffusion equation for an ice particle
b	constant in empirical formular for U_R
B'	constant in raindrop freezing equation
B"	coefficient in the diffusion equation for ice particle
c	constant in emperical formular for U_S
C_D	drag coefficients for hailstone
C_i	specific heat of ice
c_p	specific heat at constant air pressure
c_w	specific heat of water
c_v	specific heat at constant air volume
d	constant in empirical formula for U_S
D_0	dispersion of cloud droplet distribution
D_G	diameter of hailstone
D_R	diameter of a raindrop
D_S	diameter of a snow crystal
E_{IW}	collection efficiency of cloud ice for cloud water
E_{GI}	collection efficiency of hail for cloud ice
E_{GR}	collection efficiency of hail for rain
E_{GS}	collection efficiency of hail for snow

E_{GW}	collection efficiency of hail for cloud water
E_{RI}	collection efficiency of rain for cloud ice
E_{SI}	collection efficiency of snow for cloud ice
E_{SR}	collection efficiency of snow for rain
E_{SW}	collection efficiency of snow for cloud water
f	Coriolis parameter
g	acceration of gravity
K_a	thermal conductivity of air
K_h	heat eddy coefficient
K_m	momentum eddy coefficient
L_v	latent heat of vaporisation
L_f	latent heat of fusion
L_s	latent heat of sublimation
m_{I50}	mass of a 50 μm size ice crystal
m_{I450}	mass of a 40 μm size ice crystal
M_i	mass of one cloud ice crystal
N_{0G}	intercept parameters of hailstone size distribution
N_{0S}	intercept parameters of snowflake size distribution
N_{0R}	intercept parameters of raindrop size distribution
N_I	number concentration of cloud droplets
N_{I50}	number concentration of hypothetical 50 μm size ice crystal
N_n	number of active natural ice nuclei
P_{IMLT}	production rate for melting of cloud ice to form cloud water
P_{IDW}	production rate for depositional growth of cloud ice at expense of cloud water

P_{IHOM}	production rate for homogeneous freezing of cloud water to form cloud ice
P_{IACR}	production rate for accretion of rain by cloud ice
P_{RACI}	production rate for accretion of cloud ice by rain
P_{RAUT}	production rate for autoconversion of cloud water to form rain
P_{RACW}	production rate for accretion of cloud water by rain
P_{REVP}	production rate for rain evaporation
P_{RACS}	production rate for accretion of snow by rain
P_{SACW}	production rate of accretion of cloud water by snow
P_{SACR}	production rate of accretion of rain by snow
P_{SACI}	production rate of accretion of cloud ice by snow
P_{SAUT}	production rate for autoconversion of cloud ice to form snow
P_{SFW}	production rate for Bergeron process-transfer of cloud water to form snow
P_{SFI}	production rate for Bergeron process embryos (cloud ice) used to calculate transfer rate of cloud ice to snow
P_{SDEP}	production rate for depositional growth of snow
P_{SSUB}	production rate for sublimation of snow
P_{SMLT}	production rate for snow melting to form rain
P_{GAUT}	production rate for autoconversion of snow to form graupel
P_{GFR}	probabilistic freezing of rain to form graupel
P_{GACW}	production rate for accretion of cloud water by graupel
P_{GACI}	production rate for accretion of cloud ice by graupel
P_{GACR}	production rate for accretion of rain by graupel
P_{GACS}	production rate for accretion of snow by graupel

P_{GSUB}	production rate for graupel sublimation
P_{GMLT}	production rate for graupel melting to form rain, $T \geq T_0$
P_{GWET}	wet growth of graupel; may involve P_{GACS} and P_{GACI} and must include P_{GACW} or P_{GACR}, or both (The amount of P_{GACW} which is not able to freeze is shed to rain)
P_{GDRY}	dry growth of graupel; involves P_{GACS}, P_{GACI}, P_{GACW} and P_{GACR}
p	pressure
p_{surf}	surface pressure
p_T	constant pressure at top model
p_s	$\equiv p_{surf} - p_T$
pi	precipitation ice
q_i	mixing ratio of cloud ice
q_c	mixing ratio of cloud water
q_g	mixing ratio of hail/graupel
q_r	mixing ratio of rain
q_s	mixing ratio of snow
q_v	mixing ratio of water vapour
q_{vs}	saturation mixing ratio of water vapour with respect to water
q_{si}	saturation mixing ratio for water vapour with respect to ice
R	gas constant
R_{I50}	radius of hypothetical ice crystal
R_v	specific gas constant for water vapour
S	saturation ratio
S_i	saturation ratio over ice
s	$\equiv (p/p_s)\,(g/RT)$

t	time
τ	tilda
T	temperature
T'	temperature perturbation
T_0	temperature of isothermal atmosphere
T_{ref}	reference state temperature
$T_{ref-ave}$	mean reference state temperature
u	wind speed in x direction
U_G	mass-weighted mean terminal velocity of graupel/hailstones
U_R	mass-weighted mean terminal velocity of raindrops
U_S	mass-weighted mean terminal velocity of snowflakes
U_{DG}	terminal velocity for hail of diameter D_G
U_{DR}	terminal velocity for rain of diameter D_R
U_{DS}	terminal velocity for snow of diameter D_S
V	vector notation of velocity
v	wind speed in y direction
w	wind speed in z direction
z	geometric height
$\triangle x$	constant grid increment along x axis
$\triangle y$	constant grid increment along y axis
$\triangle t$	constant time-step
$\triangle \sigma$	constant grid increment along σ axis
α	specific volume
α_1	autoconversion rate coefficient for P_{SAUT}

α_2	autoconversion rate coefficient for P_{GAUT}
γ	c_p/c_v
θ	potential temperature
θ'	potential temperature perturbation
θ_0	reference state potential temperature
κ	$\equiv R/c_p$ ratio of gas constant to specific heat at constant pressure
λ	latitude
λ_R	slope parameter in rain size distribution
λ_S	slope parameter in snow size distribution
λ_G	slope parameter in hail size distribution
π	hydrostatic pressure
ρ	density
ρ_0	constant basic density
ρ_G	density of hail/graupel
ρ_{ref}	reference state density
ρ_S	density of snow
ρ_W	density of water
σ	pressure-scaled vertical coordinate
$\dot{\sigma}$	$\equiv D\sigma/Dt$ vertical velocity in σ coordinates
ϕ	geopotential height
ϕ'	geopotential perturbation
χ	$\equiv \left[(p/RT)\left(\partial\phi/\partial p\right)\right]^{-1}$
ω	$\equiv Dp/Dt$, vertical velocity is isobaric coordinates
Ω	ω/p

List of Figures

List of Tables

Chapter 1

Introduction

1.1 Background of the research

1.1.1 Introduction

Weather and climate extremes impact significantly on the human society and environment worldwide. There are numerous types of extreme weather events and these include hailstorms, windstorms, tropical cyclones, floods and tornadoes. The nature and severity of extreme weather events vary considerably in time and space, and the degree of severity of damages is different for each event. Windstorm events generally damage roofs, while flooding primarily causes damage to basements that are impacted by water following extreme precipitation (Grollmann and Simon, 2002). The most violent extremes (e.g. hurricanes and tornadoes) cause catastrophic economic losses, but fewer deaths in countries where the early warning system works relatively well. Temperature extremes cause negligible property damage and yet cause a lot of fatalities (e.g Preston, 2005).

South Africa is situated in the subtropics and as a result is affected by the circulation systems prevailing in the tropics, subtropics and the mid-latitudes (Tyson and Preston-Whyte, 2000). South Africa experiences a variety of different weather and climate extremes including drought, floods, and severe heat caused by these circulation systems. Tropical cyclones from the Indian Ocean occasionally make landfall over northeastern South Africa and Mozambique (e.g.

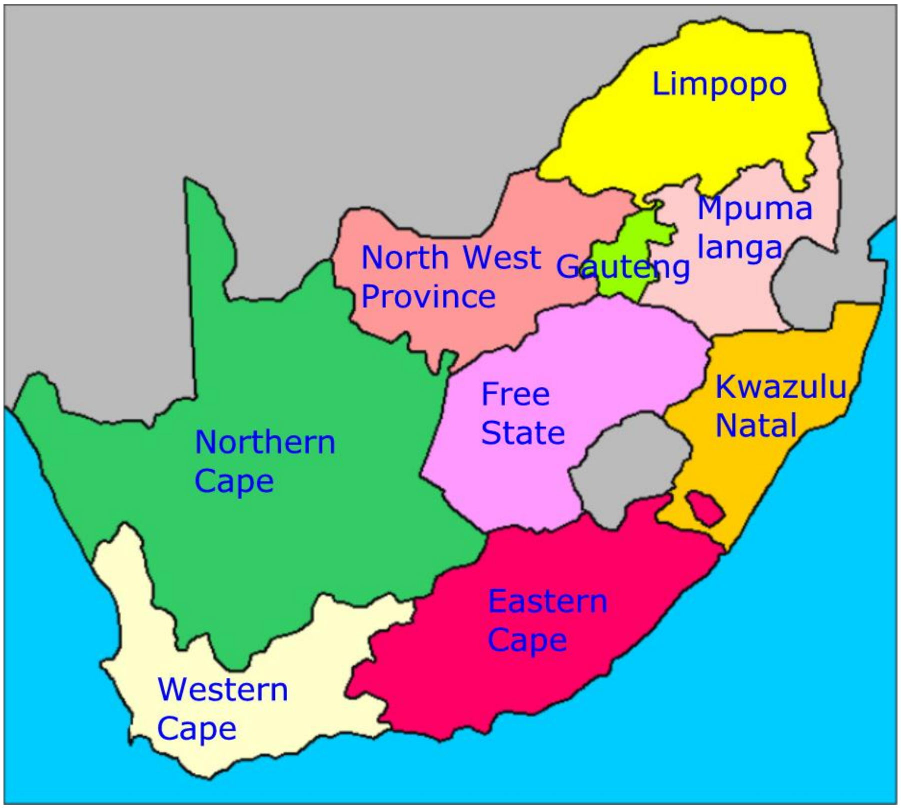

Figure 1.1.1: A map of South African provinces. From www.southafrica.to/provinces.php

Malherbe et al., 2012). For example, in February 2000 tropical cyclone Eline caused damage of more than 300 million ZAR in South Africa alone (Reason and Keibel, 2004; Du Plessis, 2002). The eastern part of South Africa is a summer rainfall region and most of this rainfall is of convective origin. The highest percentage of hail (de Coning et al., 2000) and tornadoes (de Coning and Adam, 2000) occur over this region (Tyson and Preston-Whyte, 2000).

In the summer season of 2011/2012 a number of weather extremes were experienced in South Africa. Two tornadoes formed over the central and north eastern part of South Africa on 2 October 2011 leaving 150 people injured and one person dead (Daniel, 2011). Tropical storm Dando made landfall over the eastern parts of Southern Africa in January 2012. It caused floods in Mpumalanga and Limpopo provinces (Figure 1.1.1) where over 200 people had to be rescued

(Mathes, 2011). A thunderstorm accompanied by strong winds in KwaZulu-Natal caused heavy flooding, damage to homes and left one person dead on 31 December 2011 (Sapa, 2012). Mesoscale Convective Systems are important rain producing systems over South Africa and they can also be associated with severe weather phenomena such as flooding, hail, lightning and strong winds (Tyson and Preston-Whyte, 2000). Weather forecasts which can provide skilful warnings of immenent extreme events are therefore essential since they have the ability to save lives and property. Regional-downscaling studies indicate that eastern South Africa may be expected to receive more extreme rainfall events in the future climate during austral summer (Engelbrecht, 2010). Forecasting is also important for water resource management.

1.1.2 A short history of numerical atmospheric modelling

In 1904, Vilhelm Bjerknes recognised that forecasting is a mathematical physics initial-value problem and that the basic equations that needed to be solved were already known in general form (see Haltiner and Williams, 1980). The first attempt to forecast weather by solving primitive equations using a numerical analysis approach was made by Lewis Fry Richardson. His forecast, which he produced by hand, was flawed because the predicted pressure changes were an order of magnitude larger than those observed (Harper et al., 2007; Holton, 2004). After Richardson's failure Numerical Weather Prediction (NWP) was not tried again until the 1940s (see Holton, 2004). During World War II computers were developed, observational networks expanded and the number of meteorologists increased (Holton, 2004). These, together with a deeper understanding of the atmospheric equations made forecasting weather using a numerical process a possibility in the 1950s (Harper et al., 2007). The governing equations that need to be solved are the momentum (equation 1.1.1), continuity (equation 1.1.2) and the thermodynamic (equation 1.1.3) equations.

$$\frac{DV}{Dt} = -\frac{1}{\rho}\nabla p - fk \times V - gk + F \tag{1.1.1}$$

$$\frac{D\rho}{Dt} = -\rho\nabla . V \tag{1.1.2}$$

$$c_p\frac{DT}{Dt} - \alpha\frac{Dp}{Dt} = 0 \tag{1.1.3}$$

The first term of equation 1.1.1 on the right hand side is the pressure gradient force, the second term is the coriolis effect, the third term is the gravitational force whilst the last term represents friction. u, v and w are the zonal, meridional and vertical components of the total wind V. The density ρ, pressure p and temperature T are related by the perfect gas law $p = \rho RT$. R is the gas constant and $\kappa = R/c_p$ where c_p is the specific heat at constant pressure. Equation (1.1.2) describes the conservation of mass in the atmosphere, while equation (1.1.3) is the thermodynamic equation. The total derivative is defined as $\frac{D}{Dt} \equiv \frac{\partial}{\partial t} + u\frac{\partial}{\partial x} + v\frac{\partial}{\partial y} + w\frac{\partial}{\partial z}$ (Holton, 1992).

The unapproximated equations are called fully-elastic or fully compressible since they describe the full range of wave motions that can occur in the atmosphere - Richardson made use of these (Holton, 1992). Fully compressible Navier-Stokes equations allow gravity and meteorologically significant modes, as well as acoustic modes which propagate at phase speeds about of 300 m/s in both horizontal and vertical directions. These acoustic modes contain very little energy and are unimportant for weather and climate processes. When acoustic waves are not filtered out, the time increment is restricted to a fraction of what can be used without these waves. There are generally two ways to deal with the sound waves. The computational efficiency of nonhydrostatic models can be increased through eliminating the sound waves by modifying the governing equations or computing the terms governing acoustic waves either implicitly or by using time-split techniques (Xu et al., 1991).

The filtering of sound waves from the governing equation set may be achieved by introducing approximations to the fully-elastic equations (Holton, 2004). JG Charney showed in 1948, using a scale-analysis, that the dynamical equations can be simplified by introducing the geostrophic and hydrostatic approximations. These approximations result from noting that, at the synoptic-scale in the mid-latitudes, an approximate balance exists in the horizontal between the pressure gradient force and the Coriolis effect, and between the pressure gradient force and gravitation, in the vertical. These approximations have the effect of filtering sound and gravity oscillations from the governing equations (e.g. Haltiner and Williams, 1980). The hydrostatic approximation filters the vertically propagating sound waves while the geostrophic approximation filters the horizontal sound waves, also called Lamb waves. The hydrostatic equation is thought to hold for horizontal scales greater than approximately 10 km (Davies et al., 2003).

The first real-time barotropic forecasts was made in 1954 by the Joint Numerical Weather Prediction Unit (JNWPU) for 36 hour 400- , 700- and 900- hPa prognoses (Harper et al., 2007). Since then NWP models have evolved quickly. By the 1960s, most models were based on the more complete set of hydrostatic primitive equations (Harper et al., 2007). Because of computational constraints, climate models are still typically integrated at resolutions in the order of 100 km or lower, which is well within the hydrostatic limit (Satoh et al., 2005).

Over the years data sources increased with the development of remote sensing, and high speed communication links made it possible for observational information to be delivered fast to operational forecasting centers. Powerful computers with more memory and faster processing capabilities were also developed (Harper et al., 2007; Holton, 2004). These developments have made it possible for operational NWP and meso-scale models to run at much higher resolutions, where the hydrostatic approximation is no longer valid. Consequently, there is a global trend to develop nonhydrostatic models (e.g. Chen and Sun, 2002; Satoh et al., 2005; Davies et al., 2005; Engelbrecht et al., 2007; Abiodun et al, 2008a). It can be noted that nonhydrostatic models were developed in the 1960s already however their use for NWP purposes was hindered by computational limitations.

Nonhydrostatic equation sets include the fully-elastic equations, and all approximated sets in which the acceleration term is retained in the vertical momentum equation. The acceleration term in the vertical momentum equation is of fundamental importance to describe small and micro-scale circulations, such as updrafts and downdrafts in individual thunderstorms (Stensrud, 2007). In the fully compressible widely used Weather Research and Forecasting (WRF) model, the sound waves are dealt with through the use of a time-split intergration using second and third order Runge-Kutta scheme with smaller time steps for acoustic and gravity-wave modes (Skamarock et al., 2008). The incompressible Bousinesq approximations is commonly used in modelling shallow convections in the atmosphere. Since the anelastic approximations elimates the prognostic nature of the continuity equations one must then solve an elliptic equation derived from momentum equation and continuity equations (Xu et al., 1991).

1.1.3 Vertical coordinates

The use of geometric height (z) as the vertical coordinate in models has certain computational disadvantages in mountaneous regions, because the lower boundary of the atmosphere is not a coordinate surface (Phillips, 1957). Other variables can be used as vertical coordinates, the basic requirement for such a variable is that it varies monotonically with height. A variable that is independent of height over a shallow layer in the atmosphere can also be used (Randall, 2004). Pressure (p) and potential temperature (θ) have been applied successfully in atmospheric modelling as vertical coordinates. Potential temperature coordinates are also called isentropic coordinates. Isentropic coordinates give high resolution during large stable conditions, and poor resolution during near-neutral lapse rates.

The use of pressure as the vertical coordinate in atmospheric dynamics was proposed by Eliassen (1949) and soon became the preferred choice in most studies of large-scale motion, because of the unique advantages it offered. The first advantage is that atmospheric measurements are taken at constant pressure levels during balloon soundings. Interpolation of the observed variables at constant pressure levels to model levels in the vertical is therefore convenient and accurate if the model uses pressure-based coordinates (Phillips, 1957). Another advantage is that the atmospheric equations in pressure coordinates have a simpler form than in most other coordinate systems. In pressure-based coordinates, density is also eliminated from the prognostic equations, which is advantageous since density is not generally part of atmospheric measurements (Miller and White, 1984; Xie and Thorpe, 1991).

The use of p and θ as vertical coordinates does not eliminate the problem of the lower boundary not being a constant surface of the vertical coordinate. The sigma (σ)-coordinate was introduced by Phillips (1957), and has the advantage that it follows the topography. A σ-coordinate system can be obtained by replacing the vertical coordinate p in the x, y, p system by the independent variable $\sigma = \frac{p-p_T}{p_{surface}-p_T}$(Phillips, 1957). $p_{surface}$ is the pressure at the surface while p_T is the pressure at the model top. The pressure-based coordinate system can either be based on the hydrostatic pressure field, or the full pressure field (e.g Miller and White, 1984).

1.1.4 Nonhydrostatic models in p and σ-coordinates

Miller (1974) developed the first nonhydrostatic model that uses the full pressure as the vertical coordinate. The approximations he introduced filtered out the vertical sound waves, while the Lamb waves remained. The Lamb waves can be filtered by applying the appropriate boundary conditions (i.e. $\omega = 0$ at $P = P_0$ where P_0 is a constant at the lower boundary). Miller and Pearce (1974) used the model to study cumulonimbus clouds and the model became known as the Miller-Pearce (MP) model. The MP model relies on the use of a reference thermodynamic profile, and assumes that the departures from this profile only result from processes occuring at the convective scale.

The work of Miller (1974) was extended by Miller and White (1984), who derived the MP model from the basis of a power series expansion. They also formulated the corresponding σ-coordinate equations based on the full pressure field. In the σ-coordinate equations, Lamb waves are maintained whilst the vertically propagating sound waves are filtered out, making the equations quasi-elastic. Xie and Thorpe (1991) developed a nonhydrostatic mesoscale model that made use of the nonhydrostatic σ-coordinate equations derived by Miller and White (1984). Room et al. (2001) filtered the Lamb waves from the σ-coordinate MP-model, by specifying a vertical domain for the model that is fixed in pressure coordinates, and deducing appropriate vertical boundary conditions for the nonhydrostatic geopotential height equation. Room et al. (2001)'s model became known as the NHAD (Nonhydrostatic Adjusted Dynamics) model.

Both the MP and NHAD models are restrictive in the sense that they are formulated in terms of a reference state that is in hydrostatic equilibrium, and is a function of pressure alone. These models can only be applied for mesoscale systems, and more specifically to regions where the horizontal temperature gradient on constant pressure levels is weak (White, 1989). White (1989) realised that a modification to the MP model to represent large temperature variations on pressure surfaces was desirable. He replaced the reference state temperature with the true temperature. The equation set developed by White (1989) appears to be suitable for application at larger scales and in regions such as frontal zones, where the horizontal temperature gradient on pressure surface is steep (White et al., 1989).

1.1.5 Development of a nonhydrostatic σ-coordinate model (NSM) in South Africa

Engelbrecht et al. (2007) extended the work of White (1989) by deriving the σ-coordinate set equivalent to the p-coordinate equations of White (1989). Here σ is defined using the full pressure(p) field as $(p - p_T) / (p_{surf} - p_T)$ where p_T is the constant pressure at the top of the domain and p_{surf} is the surface pressure. p_s is defined as $p_{surf} - p_T$. The extension was achieved by a direct transformation of the p-coordinate equations to σ-coordinates. The resulting equations are filtered of sound waves propagating in the vertical, however, Lamb waves still remain (Engelbrecht et al., 2007). The equations form the core of the numerical model used in the thesis, and may be stated as

$$\frac{Du}{Dt} - fv + \frac{\partial \phi}{\partial x} - \sigma \frac{\partial \phi}{\partial \sigma} \frac{\partial \ln p_s}{\partial x} = 0, \tag{1.1.4}$$

$$\frac{Dv}{Dt} + fu + \frac{\partial \phi}{\partial y} - \sigma \frac{\partial \phi}{\partial \sigma} \frac{\partial \ln p_s}{\partial y} = 0, \tag{1.1.5}$$

$$\frac{R}{g} \frac{D}{Dt} \left(\frac{\omega T}{p} \right) + g + \frac{p}{p_s} \frac{g}{RT} \frac{\partial \phi}{\partial \sigma} = 0, \tag{1.1.6}$$

$$\frac{\partial u}{\partial x} + \frac{\partial v}{\partial y} + \frac{\partial \dot{\sigma}}{\partial \sigma} + \frac{D \ln p_s}{Dt} = 0, \tag{1.1.7}$$

$$\frac{DT}{Dt} - \kappa \frac{\omega T}{p} = 0, \tag{1.1.8}$$

$$\frac{\partial^2 \phi}{\partial x^2} + \frac{\partial^2 \phi}{\partial y^2} + \frac{\partial}{\partial \sigma} \left(s^2 \frac{\partial \phi}{\partial \sigma} \right) - 2\sigma \left(\frac{\partial \ln p_s}{\partial x} \frac{\partial^2 \phi}{\partial x \partial \sigma} + \frac{\partial \ln p_s}{\partial y} \frac{\partial^2 \phi}{\partial y \partial \sigma} \right)$$

$$+ \left[\left(\frac{\partial \ln p_s}{\partial x} \right)^2 + \left(\frac{\partial \ln p_s}{\partial y} \right)^2 \right] \left[\frac{\partial}{\partial \sigma} \left(\sigma^2 \frac{\partial \phi}{\partial \sigma} \right) \right] - \frac{\sigma}{p_s} \left(\frac{\partial^2 p_s}{\partial x^2} + \frac{\partial^2 p_s}{\partial y^2} \right) \frac{\partial \phi}{\partial \sigma} =$$

$$2 \left\{ \left(\frac{\partial u}{\partial x} + \frac{\partial v}{\partial y} \right) \frac{\partial}{\partial \sigma} \left(\Omega \frac{p}{p_s} \right) - \frac{1}{p_s} \left[\frac{\partial}{\partial x} (\Omega p) \frac{\partial u}{\partial \sigma} + \frac{\partial}{\partial y} (\Omega p) \frac{\partial v}{\partial \sigma} \right] \right\}$$

$$+2 \left\{ \frac{\partial u}{\partial x} \frac{\partial v}{\partial y} - \frac{\partial v}{\partial x} \frac{\partial u}{\partial y} + \sigma \left[\frac{\partial \ln p_s}{\partial x} \left(\frac{\partial u}{\partial y} \frac{\partial v}{\partial \sigma} - \frac{\partial v}{\partial y} \frac{\partial u}{\partial \sigma} \right) + \frac{\partial \ln p_s}{\partial y} \left(\frac{\partial v}{\partial x} \frac{\partial u}{\partial \sigma} - \frac{\partial u}{\partial x} \frac{\partial v}{\partial \sigma} \right) \right] \right\}$$

$$+f\left[\frac{\partial v}{\partial x}-\frac{\partial u}{\partial y}+\sigma\left(\frac{\partial u}{\partial \sigma}\frac{\partial \ln p_s}{\partial y}-\frac{\partial v}{\partial \sigma}\frac{\partial \ln p_s}{\partial x}\right)\right]-u\frac{df}{dy}-\frac{\partial}{\partial \sigma}\left(sg-\frac{p}{p_s}\Omega^2\frac{1}{\Upsilon}\right). \tag{1.1.9}$$

The model used in this study, developed by Engelbrecht et al. (2007), is called the Nonhydrostatic σ-coordinate Model (NSM). The NSM solves equations (1.1.4) to (1.1.9), where the total derivative is given by $\frac{D}{Dt} \equiv \frac{\partial}{\partial t}+u\frac{\partial}{\partial x}+v\frac{\partial}{\partial y}+\dot{\sigma}\frac{\partial}{\partial \sigma}$, $\omega = \frac{Dp}{Dt}$,$\dot{\sigma} = \frac{D\sigma}{Dt}$ and $\Omega = \frac{\omega}{p} = \frac{p_s}{\sigma p_s + p_T}\left(\sigma\frac{D \ln p_s}{Dt}+\dot{\sigma}\right)$. Equations 1.1.4, 1.1.5 and 1.1.6 are the momentum equations in the zonal, meridional and vertical directions, respectively. Equation 1.1.7 is the continuity equation, while equation 1.1.8 is the thermodynamic equation. A consequence of filtering the sound waves is that a computationally expensive elliptic equation has to be solved to obtain the geopotential height. Engelbrecht (2006) and Engelbrecht et al. (2007) developed a split semi-Lagrangian numerical method to solve the equations stated above. The resulting numerical model based on this dynamic core did not include physical processes, such as cloud formation and radiation cooling or heating.

1.2 Motivation of the research

1.2.1 Convective processes over South Africa

The tropical and subtropical parts of the world receive the bulk of their precipitation in the form of convective rainfall (Tyson and Preston-Whyte, 2002). Over South Africa, about 80% of rainfall over the summer rainfall region is in the form of convective rain. Most extreme rainfall events and floods over South Africa are the result of convective rain, either in the form of isolated thunderstorms (that cause flash floods) or thunderstorms embedded within cloud bands (Preston-Whyte and Tyson, 1988).

Individual thunderstorms occur in the absence of wind shear (Weisman and Klemp, 1982), are usually 5-10 km in horizontal extent, and are short-lived (less than 60 minutes) (Houze, 1993). Over the Highveld of South Africa (Figure 1.1.1), the lifecycle of a single-cell is usually 18-30 minutes (Tyson and Preston-Whyte, 2004). A number of cells may develop within an individual cumulonimbus cloud mass, alternatively, separate independently formed cells merge to form a multi-cell storm. Multi-cell storms are common over the South African Highveld, where upto 30 cells may form in the life of a storm (Tyson and Preston-Whyte, 2002). Multi-cell storms are sometimes organised in line storms, and contribute substantially to rainfall of the South African interior. They typically occur over several tens of kilometres, and during their north-easterly movement they sweep over large tracts of the country. Maximum development of the storms takes place in the late afternoon and early evening (Weisman and Klemp, 1982).

Supercell storms do occur from time to time over the eastern parts of South Africa (Tyson and Preston-Whyte, 2000). They are notorious for producing damaging hail and tornadoes. De Coning et al. (2000) investigated a hail storm that occured over the Free State (Figure 1.1.1) on 29 December 1997. The storm was accompanied by hailstones of 10 to 25 mm and caused damage to crops amounting to about 15 million ZAR. After analysing the atmospheric parameters associated with the storm, they concluded that the storm must have been a supercell. Pyle (2006) analysed severe, localised, short duration convective storm events for the period 1897 to 2005 in the Eastern Cape (Figure 1.1.1). From a number of sources and interviews, he identified 179 storms which were accompanied by damaging winds (including tornadoes), hail, lightning or flash flooding. More storms were reported in urban areas, which he thought was a consequence of nonreporting of events in sparsely populated rural areas. The majority of the storms occured during the months of November to April, between, 14:00 and 19:00.

There is evidence that tornadoes occur more frequently in South Africa than previously thought. De Coning and Adam (2000) studied 3 case studies of tornadoes, of which one occured in Harrismith on 15 November 1998 at 1500, and another in Mount Ayliff on the 18th of January 1999 at 16:30. The third one occurred in Umtata on 15 December 1998 at 14:30, and it shattered windows and doors of a pharmacy while former president of South Africa, Nelson Mandela was in the pharmacy. He and his guards escaped unharmed. These tornadoes resulted in a lot of damage. It was reported that damage from the Harismith tornado was estimated at 3 million to 4 million ZAR. The Mount Ayliff tornado resulted in 21 deaths and 350 injuries, and the area was declared a natural disaster area by the South African government.

Nontornadic thunderstorms can also produce damaging winds, hail, and flash floods. Damage caused by strong downdrafts from a nontornadic thunderstorm can erroneously be reported as evidence of a tornado (Pyle, 2006). Downdrafts are formed in thunderstorms by precipitation drag as well as microphysics processes that cool the air, such as evaporation of rainwater and melting of snow (Houze, 1993). Liu and Orville (1969) showed that downdrafts occur in both precipitating and nonprecipitating clouds, but are stronger in the former. Downdrafts can help generate new thunderstorm cells and they can also cut old cells off their supply of buoyant air. Damaging winds often occur at the boundary of downdrafts and are often referred to as gustfronts. The downdraft can become locally very intense over a short period of time in which case they are referred to as downbursts (Houze, 1993). There is a need for the dynamics and microphysics of intense convective storms occurring over South Africa to be studied in more detail. Such studies may contribute to the more skillful forecasting of the associated severe weather events.

A variety of synoptic situations may be conducive to convective storm formation over South Africa. The tropical-temperate trough (TTT), which is associated with northwest-southeast aligned cloud bands, is a major synoptic rainfall-producing weather systems over southern Africa (Hart et al., 2010; de Coning et al., 1998; Harrison, 1984). TTTs are formed when weather systems originating in the tropical easterlies migrate south and interact with systems from the mid-latitude westerlies during austral summer. The TTTs can also be associated with heavy rainfall leading to floods in certain parts of the country (Washington and Preston, 2006). The Vaal Dam, one of the largest dams in South Africa, overflowed in February 1996 as a result of the rains associated with a TTT (de Coning et al., 1998). Hart et al. (2010) studied other TTTs that were associated with heavy rainfall that occured on 31 December 1997 to 2 January 1998; 5-7 January 1998 and 15-17 December 2007. It is the cumulonimbus cloud embedded within TTS that are responsible for the bulk of the rainfall and heavy falls of rain, associated with these systems.

In fact, cumulus convection is the dominant rainfall-producing process over most parts of southern Africa. Except for the organised convection taking place within TTTs, heat thunderstorms are common over the interior regions of South Africa in summer. These storms are caused by the diurnal heating cycle of the near-surface air, sometimes in interaction with mesoscale and local effects (e.g. over the eastern escarpment areas of South Africa). Indeed, the convective rainfall process over much of South Africa shows a clear diurnal variability because of the strong influence of diurnal heating. In general, over land areas rain falls most frequently during the afternoon and early evening (Tyson and Preston-Whyte, 2000).

During spring and autumn cut-off lows also bring thunderstorms to the southern parts of the subcontinent (e.g. Singleton and Reason, 2007). These storms can often be severe, and occur in association with dry and moist air masses mixing at the synoptic-scale. Cumulus convection schemes applied over the southern African region therefore need to be versatile enough, to deal with a wide range of synoptic-scale and meso-scale conditions. The current treatment of convective rainfall within regional climate models applied over southern Africa are known to be problematic (e.g. Tadross et al., 2005), and the dynamics and microphysics of storms over the region have not been studied to date through the explicit simulation of moist convection.

1.2.2 Development of a Cloud Resolving Model

Clouds are treated differently by models depending on the models' horizontal resolution. For models running at resolutions lower than about 4 km, the clouds-environment relationship has to be represented statistically because clouds cannot to be captured explicitly since clouds are smaller than the grid resolution (Stensrud, 2007; Jakob, 2010). This option is called cumulus parameterisation which is a way of representing the relationship of clouds and the environment statistically without explicitly simulating the clouds (Weisman et al., 1997). It is thought that this parameterisation of convection is one of the greatest sources of uncertainty in NWP and climate modelling (Randall et al., 2003a; Engelbrecht et al., 2007).

For resolutions higher than 4 km, Cloud Resolving Models (CRMs) should be used. A CRM or a Cumulus Ensemble Model (CEM) is a model that can resolve structures of individual clouds, is integrated over a spatial domain large enough to contain many clouds and for a time long enough to include many cloud life cycles (Randall et al., 1996). Over the past four decades, CRMs have shown much success in replicating the observed structure and evolution of convection, using microphysics parameterisation with cumulus parameterisation neglected. CRMs can also be used to study the atmosphere where observations are lacking, and the findings be used to improve conventional parameterisation schemes (Emanuel, 1994; Grabowski et al., 2006). The hydrostatic atmospheric models, that use cumulus parameterisation schemes, are likely to be applied for decades to come in the computationally expensive study field of climate simulation (and for NWP over large domains) (Randall et al., 2003a; Jakob, 2010).

Engelbrecht (2006) and Engelbrecht et al. (2007) developed a dynamical kernel of a nonydrostatic σ-cordinate model, which was shown to simulate benchmark warm and cold dry bubbles successfully. The model uses a vertical σ-coordinate that uses the full pressure, while most σ-coordinate models use the hydrostatic pressure. The equation set is also not based on a reference profile, and does not assume that changes occur only due to convective processes and may therefore be applied globally. In order for the NSM to be able to simulate clouds, and in particular convective storms, microphysics parameterisation schemes need to be added to the model. Radiation and turbulence should also be considered in cloud studies, because they strongly interact with each other and the microphysics.

1.2.2.1 Microphysics

Microphysics processes play a crucial role in the formation, growth, shrinkage, breakup, and fallout of cloud and precipitation particles. Condensation is a microphysics process that converts water vapour to cloud water, while increasing the atmospheric temperature through the release of latent heat. The simplest cloud model is one with only cloud water and water vapour, and should include a microphysics process that allows water vapour to condense when saturation is reached and cloud water to evaporate during subsaturation. In a warm, nonprecipitating cloud, where it is assumed that cloud droplet sizes have the same size, evaporation and condensation are the only processes that need to be considered (Houze, 1993).

However, clouds in the atmosphere can be far more complicated, and typically contain liquid and ice particles with different sizes, of which some may precipitate. Water in its three phases has to be represented in simulations of such clouds, together with processes that change phases, and those that change the sizes of the hydrometeors. A number of CRMs employ Bulk Microphysics Parameterisations (BMPs), which use a specified functional form for the particle size distributions and predict the particle mixing ratio (Rutledge and Hobbs, 1983; Grabowski, 1998; Stensrud, 2007). Most models predict the mixing ratios of water vapour, cloud water, cloud ice, snow, rain and graupel/hail (e.g. Lin et al., 1983, Chen and Sun, 2002; Khairoutdinov and Randall, 2003; Hong and Lim, 2006). In a BMP scheme the various cloud microphysical processes responsible for transfering the water substance from one species to another are parameterised. It may be noted that Kessler (1969) was the first to develop a BMP, for the special case of parameterising the microphysical processes needed to simulate precipitating warm clouds.

CRMs can also employ multi-moment bulk schemes by predicting more than one moment of the particle size distribution (Milbrandt and Yau, 2006a; Morrison and Milbrandt, 2011). A double moment scheme predicts both the particle mixing ratio and the concentration, while a single-moment schemes predicts only the particle mixing ratio. The benefit of multi-moment schemes is that they should be applicable across a wider range of environments. Multi-moment schemes are starting to be applied in numerical models (e.g. Milbrandt et al., 2010, Stensrud, 2007), however their increased cost due to the prediction of a multiple-moment deters from their use in real-time NWP (Thompson et al., 2008).

1.2.2.2 Turbulence

Turbulence plays a crucial role in cloud formation and development, and therefore cannot be neglected in cloud models. In clouds, turbulence leads to the entrainment of the surrounding environmental air, which modifies the cloud dynamics and microphysics. Turbulence can be caused by microphysical processes such as melting and evaporation, which cool the air, and condensation and freezing, which warm the air. Turbulence can also be due to radiative cooling and warming. Radiative heating at the base of the cloud and the cooling at the top of the cloud cause turbulent mixing at the base and top of thick clouds, respectively (Houze, 1993). Smaller scale turbulence can influence cloud droplet collisions which can have an effect on the droplet distribution and the onset of rainfall (Franklin et al., 2005).

Turbulence causes mixing across the gradients of momentum, energy, and moisture, vertically and horizontally. In a model, the degree of mixing due to turbulence can be quantified with a turbulent flux term which arises from Reynolds averaging. In the case of vertical mixing of horizontal momentum, the term is a function of the kinematic vertical turbulent momentum flux, $\overline{w'u'}$ and $\overline{w'v'}$. In the case of vertical mixing of energy, it is a function of the kinematic vertical turbulent sensible-heat flux, $\overline{w'\theta'}$. In the case of vertical mixing of moisture, it is a function of the kinematic vertical moisture flux, $\overline{w'q'}$ (Jacobson, 2005).

The flux terms mentioned above appear in the mean basic equations of motion when Reynolds averaging is applied. To solve the mean equations, closure assumptions must be made to approximate the unknown fluxes in terms of the known mean state variables. The traditional approach is to assume that turbulent eddies act in a manner that the flux of a given field is proportional to the local gradient of the mean (Holton, 2004; Smagorinsky et al., 1965). This closure scheme is often referred to as K-theory and it is a local first order closure scheme. Constant coefficients can be used in the local diffusion scheme, however these are not realistic because turbulence is dependent on height, shear and buoyancy. Louis (1979) introduced a scheme with coefficients that depend on the gradient Richardson number, to make the diffusion scheme more realistic.

Local diffusion schemes are criticized because they are said to fail in the unstable boundary layer, because the influence of large eddy transports is not accounted for (Stensrud, 2007). Holtslag and Boville (1993) compared a local and nonlocal diffusion schemes and found the total mixing of specific humidity to be underestimated in a local scheme resulting in too moist atmospheric levels near the surface. They found the temperature profile in the lower atmosphere to be simulated reasonable well with both diffusion schemes. The model simulation with the nonlocal diffusion scheme was found to affect a much deeper layer than the simulation with the local diffusion scheme.

1.2.3 Model development in South Africa

Atmospheric model development activities in South Africa were abondoned during the mid-1980s due to policy changes in institutions that were undertaking this kind of work. South African atmospheric scientists are currently using a number of international atmospheric models to make short, seasonal and multi-decadal predictions (Reason et al., 2006). The South African Weather Service (SAWS) uses the United Kingdom Meteorological Office (UKMO) Unified model for short range forecasting. Using output from the Unified Model and the available remote sensing data, SAWS also issues nowcasts of convection. De Coning et al. (2011) and De Coning (2011) developed a Combined Instability Index, which calculates the probability of convection based on satellite derived instability indices, output from the Unified Model, as well as orographic lift. This index is calculated early in the morning, when the sky is cloud free, and is available for use by the operational forecasters. Satellite-based precipitation and rainfall fields from the Unified Model are used to generate accumulations of the hydro-estimator for the South African Flash Flood Guidance System (De Coning and Poolman (2011). SAWS purchased and installed a VAISALA Lightning Network (LDN) in 2005, which is being used to detect lightning throughout South Africa (Gill, 2008).

The Council for Scientific and Industrial Research (CSIR) currently uses the Conformal-Cubic Atmospheric Model (CCAM) to make short-range to multi-decadal predictions (Landman et al., 2010; Engelbrecht et al., 2011). Model development activities in South Africa were renewed by Engelbrecht (2006) and Engelbrecht et al. (2007) in 2002, through the development of the NSM at the University of Pretoria (UP), as part of a project funded by the Water Research Commision (WRC) (Engelbrecht, 2006, Reason et al., 2006). The development of the NSM is continued through the research described in this thesis. The CSIR has additionally embarked on the development of a fully coupled climate model, in collaboration with international partners (Engelbrecht et al., 2012). While these model development intiatiatives are expected to make a contribution in the field of atmospheric science, it is also a major human capital development activity in South Africa where model development skills are lacking critically compared to developed countries. Model development also started recently at the University of Cape Town to further improve the Community Atmospheric Model (CAM) EULAG (Abiodun et al., 2008a and b).

In his essay on a university perspective on Global Climate Modeling, Randall (1996) suggested that model development should continue at universities, to train new model developers at a rate matched to the community's demand for developers. He argues that it is not optimal for a student to learn climate modelling simply by running a community model developed by scientists the student has never met. Students aspiring to be model developers can learn best working with scientists who are contributing actively to model development. Increasing the number of modellers will speed the generation of new ideas. Following his arguments, it can be argued that model development should take place in Africa as well, to allow African scientists to contribute to the science of model development.

1.3 Objectives of the research

Given the state of model development in South Africa, the great importance of thunderstorm activity and convective rainfall in South Africa, and model development initiatives worldwide, the thesis has four main objectives:

To introduce microphysics schemes to the Nonhydrostatic σ-coordinate Model (NSM)

Mixing ratios of water vapour, cloud water, rain water, cloud ice, snow, and graupel are introduced to the NSM, and advected using the semi-Lagrangian scheme of the model. The water classes are allowed to change and evolve into other forms, and the related temperature changes due to latent heat release or absorption are modelled, using BMP schemes obtained from the National Centre for Atmospheric Research Weather Weather Research and Forecasting (NCAR WRF) model (Skamarock et al., 2008). The first scheme is single-moment, was developed by Chen and Sun (2002), and is known as the PURDUE-LIN scheme. The PURDUE-LIN scheme is based on conventional microphysics schemes of Rutledge and Hobbs (1983) and Lin et al. (1983) and it predicts six prognostic equations of mixing ratios of water vapour, cloud water, rain water, cloud ice, snow and graupel. The second scheme was developed by Lin and Colle (2011) and is known as the SBU-YLIN scheme - it was developed using the PURDUE-LIN scheme as a starting point. SBU-YLIN calculates five prognostic equations with snow and graupel sharing a species and processes. The SBU-YLIN scheme uses general formulations that consider the influence of riming intensity and temperature on the prediction of precipitating ice.

To introduce the thermal and mechanical generation of turbulence

Turbulence is a physical process in the atmosphere and it interacts actively with the microphysics and radiation processes. Engelbrecht et al. (2007) introduced a local diffusion scheme that employs constant coefficients. In this study the same local diffusion scheme is used, however, the constant coeffiecients are replaced with those based on the gradient Richardson number, which takes into account the thermal and mechanical generation of turbulence (Louis, 1979). The latter is thought to lead to more realistic simulations within the presence of clouds.

To study the effect of horizontal resolution, microphysics and shear on a thunderstorm

The eastern part of South Africa frequently experiences the occurrence of isolated thunderstorms during the austral summer season. These thunderstorms are usually triggered by surface heating, and are controlled to a lesser extent by the large scale circulation. In this study, a thunderstorm simulation that is triggered by a warm pertubartion, to represent surface heating is performed. The effect of the microphysics schemes on the simulated hydrometeors and dynamics of the thunderstorms is studied by comparing simulations made with the two microphysics schemes introduced in the model. The simulations are made with different horizontal resolutions and with and without shear in two-dimensions.

To study the suppressed, transition and deep convection periods using observed fields of TOGA COARE

Most thunderstorms over South Africa occur in well-organised cloud bands, that are caused by a linkage of tropical and temperate systems. To test if the NSM is able to respond well to the large scale forcing, simulations are made using the large scale forcing obtained from the Tropical Oceans Global Atmosphere Coupled Ocean-Atmosphere Response Experiment (TOGA COARE) experiment which took place in November 1992 to February 1993 over the Western Pacific ocean. Three separate periods dominated by suppressed convection which include the end of a previous period of deep convection and start of subsequent period of convection are simulated. The case study was investigated by the Precipitating Cloud Systems Working Group (PCSWG) of the Global Energy and Water Cycle Experiment (GEWEX) Cloud System Study (GCSS). The simulations are made in two-dimensions.

Chapter 2

Convection in atmospheric models

2.1 Introduction

Clouds typically have length scales of a few kilometres and hence cannot be captured explicitly by atmospheric models using low resolutions. It is essential to represent cumulus convection within atmospheric models, due to the cumulative effect of a large number of individual clouds on the larger scale circulation, through the transfer of heat, moisture and momentum (Cotton and Anthes, 1989). The objective of cumulus parameterisation is to simulate the changes in the large scale variables (i.e. temperature and humidity) due to cumulus convection (Roberts, 2003b) and to simulate the associated occurrence of convective rainfall. A number of cumulus convection schemes (e.g. Kuo, 1974; Arakawa and Schubert, 1974; Grell, 1993; Betts and Miller, 1986; Bougeault, 1985) are available in models and have been useful for Numerical Weather Prediction (NWP) and climate prediction purposes. A long standing problem in models that employ cumulus parameterisations is the daytime convective development, with precipitation peaking several hours too early in the models compared to the observations (Guichard et al., 2004; Grabowski et al, 2006).

2.2 Cloud Resolving Models

Clouds are thought to be captured explicitly when a horizontal resolution of 4 km or higher is used. For such resolutions Cloud Resolving Models (CRMs) that use microphysics parameterisations without cumulus parameterisations are used. The horizontal resolution at which moist convection can be fully resolved is a matter of some controversy. Bryan et al. (2003) showed using scale analysis that grid spacing of order 0.1 mm may be required to simulate all scales of a geophysical turbulent flow. Such a resolution is beyond the capabilities of computers available today, or in the foreseeable future even for NWP purposes and some form of parameterisation is still needed.

Some studies argue that with the use of microphysics, turbulence and radiation parameterisations resolutions as high as 100 m are required (e.g. Engelbrecht et al., 2007; Satoh et al., 2005) for the explicit simulation of clouds. Other studies indicate that resolutions as coarse as 4 km may be sufficient to reproduce the mesoscale convective circulations and net momentum and heat transports of midlatitude type convective systems (Weisman et al., 1997). Roberts (2003b) found that switching off the convection scheme was the best choice for simulating the large storms that could be resolved on the model grid, but was a poor choice for representing the smaller-scale scattered convection that could only be partly resolved. These findings suggest that a hybrid system that uses a cumulus parameterisation scheme for processes that cannot be captured explicitly and leaves the model to capture resolvable processes is desirable (Stensrud, 2007).

Over the past few decades CRMs have shown much success in replicating the observed structure and evolution of convection. CRMs can be used to study aspects of the atmosphere that are not readily observed with current observation tools. Some studies with CRMs have established a strong basis of understanding of the physical processes important to the evolution of convective systems. These insights may be used to help determine how convection should be represented in coarse-grid models (Weissbluth and Cotton, 1993; Randall et al., 1996; Petch et al., 2002). CRMs have been found not to predict rainfall before noon indicating that they don't have a problem with a quick rainfall onset as found when using conventional convection schemes (Guichard et al., 2004; Grabowski et al., 2006). It should be noted that conventional parameterisations will still be needed for very long simulations, for example the projection of future climate change, due to computational constraints (Randall et al., 2003a).

2.2.1 Cloud Resolving Models in Large Scale Models

Grabowski and Smolarkiewics (1999) introduced a formal approach to couple small-scale processes associated with atmospheric moist convection with the large-scale dynamics in models, which they termed Cloud-Resolving Convection parameterisation (CRCP). The approach involves applying a two-dimensional CRM in each column of a three-dimensional large scale model. The CRMs from neighbouring columns interact only through the large scale dynamics. Grabowski (2001) applied the approach to the idealized problem of a convective-radiative equilibrium of a two-dimensional nonrotating atmosphere in the presence of SST gradients. Comparison between CRCP and CRM simulations showed that the large-scale features, such as the mean temperature and moisture profiles and the large-scale flow are reasonably well represented in CRCP.

Khairoutdinov and Randall (2001) made the first simulations with a CRM attached to a GCM using realistic surface boundary conditions and interactive radiation. A CRM was embedded in each grid column of a GCM, replacing the moist convection and large-scale condensation parameterisations. The CRM produced the horizontally averaged fields as its output, which were then used by the GCM to compute tendencies due to subgrid processes. They found results which were comparable in quality to those of a control run that resembles conventional parameterisation.

Randall et al. (2003a) proposed CRCP (which became known as super-parameterisation) as a strategy that will improve the treatment of clouds in climate models. The computational cost of a GCM applying super-parameterisation is between 10^2 to 10^3 more expensive than the same GCM with conventional parameterisations. Running a global CRM is about 10^6 times more expensive than a GCM using conventional parameterisations. They proposed that the parameterisation development proceeds on two parallel paths: the conventional approach and the superparameterisation approach. Conventional parameterisation can be improved more rapidly by taking advantage of what is learnt by using superparameterisation (Randall et al., 2003a). In his review of cumulus parameterisation, Arakawa (2004) shared the opinion that superparameterisation is a promising new approach that can develop into a multi-scale modelling framework.

Superparameterisation was used by Khairoutdinov et al. (2008) in the Colorado State University Multiscale Modelling Framework General Circulation Model to produce Atmospheric Model Intercomparison Project (AMIP) style simulation over 19 years. The GCM was run with a horizontal resolution of 2.8^0 while the CRM used 4 km resolution. The focus of the study was on the simulated interannual and seasonal variability. Although the model produced biases, the annual mean climatology was well simulated. The geographical pattern of the seasonal cycle of precipitation was well reproduced although the seasonal variance was overestimated. The model reproduced the spatial structure and magnitude of major anomalies associated with the El Niño Southern Oscillation.

GCM parameterisations can be tested using a Single-Column Model (SCM) which is a grid column of a climate model, considered in isolation from the rest of the model. Observations are used to specify what is going on in neighbouring columns and results obtained for one observation time are used to predict new values of the prognostic variables, which are then provided as input for the next observation time. The advantage of testing cumulus parameterisations with this approach is that the testing can be performed without complication from the rest of the global climate model (Randall et al., 1996).

CRMs can also be used to test GCM parameterisations and be driven with the same observations as those needed to drive an SCM. The domain of a CRM can be considered to represent a single grid column of a GCM in a similar manner to an SCM. The difference is that a CRM simulates clouds explicitly using microphysics parameterisations while an SCM parameterises convection. SCMs and CRMs can be used together to test GCM parameterisations, and results from the CRM can also be compared with those produced by the SCM to diagnose problems with the SCM. The parameterisation tested on the SCM can be transferred directly to a three dimensional GCM (Randall et al., 1996). With various studies the Global Energy and Water Cycle Experiment (GEWEX) Cloud System Study (GCSS) confirmed that CRM results are superior over those of SCMs. In various cases the simulated water vapour, temperature and cloud fraction profiles simulated by CRMs were found to be in reasonable agreement with observations, while the SCM results were much worse in most cases (Randall et al., 2003b). CRMs use microphysics parameterisation schemes for the explicit simulation of clouds. The next section discusses these microphysics parameterisations.

2.3 Microphysics Parameterisations

CRMs employ microphysical parameterisations which are grouped into bin and bulk approaches (Rutledge and Hobbs, 1983; Stensrud, 2007). A bin approach divides the particle distribution into 20 or more finite sizes and categories. This division of particle distribution into numerous bins requires much larger memory and computational capabilities, and poor knowledge of ice phase physics hampers the accurate representation of evolving ice particle concentrations (Straka and Mansell, 2005; Milbrandt et al., 2008). Bin methods are being used increasingly in research models, but not in operational models as yet (Stensrud, 2007; Morrison and Milbrandt, 2011). Unresolved issues relating to application of bin schemes to CRMs with relatively low spatial resolution also hamper the use of bin schemes in CRM and superparameterised GCMs (Morrison and Grabowski, 2007).

Bulk Microphysics Parameterisation (BMP) schemes specify a functional form for the particle distribution and usually predict one or more characteristics of a particle category, such as the mixing ratio and concentration (Straka and Mansell, 2005; Rutledge and Hobbs, 1983; Lin et al., 1983; Stensrud, 2007). Two-moment schemes predict the mixing ratio and number concentration of at least one species (Morrison and Milbrandt, 2011). Due to their computational advantage over bin schemes, BMP schemes have been widely incorporated into CRMs, mesoscale research and operational models, and climate models (Milbrandt et al., 2008; Liu and Moncrief, 2007).

2.3.1 The Single Moment Scheme

In most BMP schemes, the particle size distribution (PSD) is usually approximated by an exponential distribution written as $N_x\left(D\right) = N_{0x} exp\left(-\lambda_x D\right)$. Here $N_x\left(D\right)$ is the number density as a function of particle diameter D, N_{0x} is the intercept parameter and λ_x is the slope parameter. The subscript x is a placeholder for a given species. The equation has two free parameters, which are not independent in most applications. Typically, one of the parameters (usually N_{0x}) is fixed or diagnosed as a single-value function of the other, and the mixing ratio is predicted. This quantity can then be used, along with the fixed (or diagnosed) parameter, to determine the value of the remaining free parameter, thereby closing the system. Such BMPs are known as single moment schemes, because only one moment of the Drop Size Distribution (DSD) is predicted (Dawson II et al., 2010).

$$\frac{Dq_x}{Dt} = S_{x,}, x = 1, 2, ...n \tag{2.3.1}$$

Equation 2.3.1 governs the mass of water in an air parcel and is called the water continuity equation. The basic idea of BMP models is to assume as few categories of water as possible in order to minimize the number of water continuity equations and calculations (Houze, 1993).q_x is the mixing ratio of one class of the water substance. Water substance can take on a wide variety of forms in a cloud. In the majority of BMPs, these are water vapour, cloud water, rain water, cloud ice, snow and graupel or hail, which are represented as follows:

q_v ≡mass of water vapor/mass of dry air,

q_c ≡mass of cloud liquid water/mass of dry air,

q_r ≡mass of rainwater/mass of dry air,

q_i ≡mass of cloud ice/mass of dry air,

q_s ≡mass of snow/mass of dry air, and

q_g ≡mass of graupel/mass of dry air.

S_x on the right hand side represents the microphysics processes that can be sources and sinks for different water species at the same time. For example condensation is a sink for evaporation and at the same time a source for cloud water. Melting is a sink for cloud ice and a source for cloud water (Houze, 1993).

2.3.1.1 Warm clouds

The simplest type of cloud is a warm (i.e. no ice), nonprecipitating cloud. The minimum number of categories that describe it is two (Equations 2.3.2 and 2.3.3) where PCOND represents condensation of vapor when PCOND>0 and evaporation when PCOND<0 (Houze, 1993). This simple model was used by Bryan and Fritsh (2002) to simulate a benchmark moist bubble simulation.

$$\frac{Dq_v}{Dt} = -PCOND \tag{2.3.2}$$

$$\frac{Dq_c}{Dt} = PCOND \tag{2.3.3}$$

More classes can be added to the model. When rainwater is added, three water continuity equations have to be solved (Equations 2.3.4 to 2.3.6). The number of processes increase on the right hand side as a consequences of adding one more class, equation 2.3.4 replaces equation 2.3.2, while equation 2.3.3 is replaced by equation 2.3.5. A new water continuity equation is added (equation 2.3.6) to the model to predict the changes in the new class that has been added to the model.

$$\frac{Dq_v}{Dt} = -PCOND + PREVP \tag{2.3.4}$$

$$\frac{Dq_c}{Dt} = PCOND - PRAUT - PRACW \tag{2.3.5}$$

$$\frac{Dq_r}{Dt} = PRAUT + PRACW - PREVP - RFALL \tag{2.3.6}$$

PREVP is the evaporation of rainwater, PRAUT is autoconversion, which is the rate at which cloud water content decreases as particles grow to precipitation size by coalescence. PRACW is the collection of cloud water by rain water, which is the rate at which the rain water mixing ratio increases as a result of the large falling drops intercepting and collecting small cloud droplets lying in their paths. RFALL is the sedimentation of the raindrops in the air parcel; it is the net convergence of the vertical flux of rainwater relative to the air (Houze, 1993). Note that the signs before each microphysics process are not based on any particular parameterisation scheme, but are to show whether a process is a sink or a source. A negative sign shows that a process is a sink and a positive sign shows that a process is a source for the water class represented in each water continuity equation.

Whilst most of the bulk microphysical schemes in use today include both water and ice processes, initial schemes only included warm phase microphysics (e.g. Kessler, 1969; Miller and Pearce, 1974; Liu and Orville, 1969). Kessler (1969) was the first to simplify the cloud microphysics calculations by reducing them to a series of parameterised relationships. The Kessler (1969) microphysics was still available in the WRF release as recent as August 2011. Miller and

Pearce (1974) used a warm precipitating cloud bulk model to test the first nonhydrostatic model that used the full pressure field as a vertical coordinate.

Using a simplified model, Kessler (1969) studied the change in precipitation quantity when fall speed of precipitation is greater than the speed of the updrafts. He found that when descent was slow, more precipitation developed during its longer time passage through any defined layer. He also found that the magnitude of precipitation tends to increase with an increasing updraft (Kessler,1969). Wilhemson and Klemp (1978) used a 3-D model that used Kessler (1969) microphysics parameterisations to investigate the splitting of a storm in a one-directional initial wind profile. Their study suggested that strong shear at and just above cloud base is important for the splitting process to be successful. They also found that without precipitation, an induced downdraft and associated low-level outflow splitting do not occur. Later work however showed that it is the vertical pressure gradient associated with eddies on the updraft flanks that is responsible for the splitting, not the precipitation induced downdraft (Houze, 1993).

Liu and Orville (1969) studied the effects of precipitation on a small cumulus cloud by making simulations first without precipitation and then with precipitation. They found the development of the cloud in the model, either with or without precipitation effects, to be similar during the cloud's early stages. The clouds with rainfall dissipated slightly sooner, and the maximum cloud water was less because of the transfer of cloud water to rain. The downdrafts existed for both precipitating and nonprecipitating cases, which they took as indicating that rain is not a prerequisite for downdrafts. The downdrafts in the precipitating case were found to be stronger than in the nonprecipitating one.

2.3.1.2 Cold clouds

The BMPs can be extended to include cold clouds by adding the categories of cloud ice, snow, graupel or hail. A number of BMPs have been developed, and some of the schemes are being used by CRMs and GCM superparameterisations (e.g. Khairoutdinov and Randall, 2003; Chen and Sun, 2002; Hong and Lin, 2006; Tao and Simpson, 1993). These models can be used to study the effect of different microphysics processes to the clouds water substance and dynamics (e.g. Li et al., 2002).

Gao et al. (2006) examined the effects of ice microphysics on rainfall and thermodynamic processes in the tropical deep convective regime, based on hourly zonal-mean data from a pair of two-dimensional (2-D) cloud-resolving simulations: one simulation with ice clouds and the other simulation without ice. The simulation without ice microphysics produced more cloud water than the simulation with ice microphysics. The simulation excluding ice microphysics produced a smaller surface rain rate than the simulation including ice microphysics. The analysis of cloud microphysical budgets revealed that exclusion of vapour deposition processes caused small surface rain rate in the simulation excluding ice microphysics.

Ogura and Takahashi (1971) used simplified microphysics parameterisations in a model that included ice to estimate the importance of various microphysical processes in the life cycle of a thunderstorm. When all the processes were included, a downdraft started developing first at the lower part of the cloud before spreading to a higher altitude. A strong downdraft appeared at the melting zone, and the model simulated two rainfall maxima. When they excluded evaporation of rainwater, the strong downdraft near melting level did not appear and the maximum downdraft was reduced. Excluding evaporation of cloud water shortened the time to reach the maximum updraft by 5 minutes, and decreased the value of the downdraft near the surface. When melting of ice crystals was excluded, the downdraft at the melting level disappeared, the strength of the downdraft was much weaker and the second rainfall peak disappeared.

A number of microphysics schemes used in current models are based on the microphysics schemes presented by Lin et al. (1983) and Rutledge and Hobbs (1983 and 1984) (Figure 2.3.1). The two schemes are similar except that some processes that are included in the Rutledge and Hobbs (1984) model are not included in the Lin et al. (1983) model. The opposite is also true. Lin et al. (1983) also use the square root factor involving air density in most of their definitions that consider fallspeeds to account for increasing fallspeeds with increasing altitude. Rutledge and Hobbs (1983) used pressure instead of air density to allow for the change in fallspeed with air pressure. Rutledge and Hobbs (1984) and Lin et al. (1983) assumed that rainwater, snow and graupel follow an exponential distribution, and that cloud water and ice are monodispersed and have a negligible fallspeed.

Hong and Lim (2006) compared simulations using their microphysics scheme with 6 classes of water substance and its predecessor of 5 classes. They found

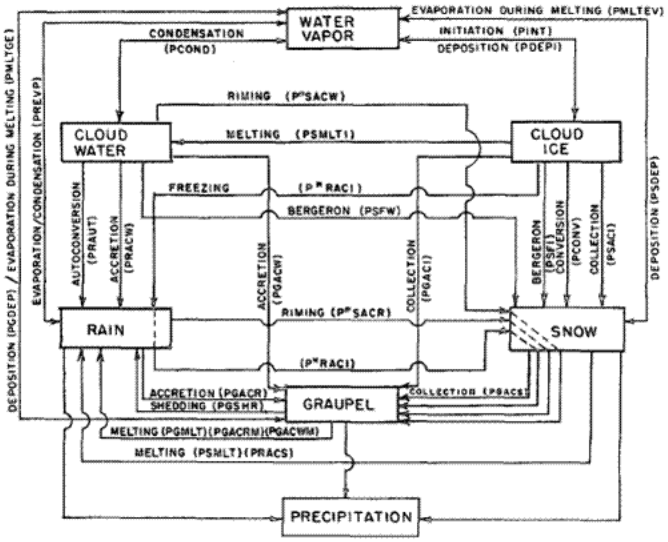

Figure 2.3.1: A schematic depiction of the cloud and precipitation processes, and the water species in the Rutledge and Hobbs (1984) scheme. From Rutledge and Hobbs, 1984.

that the number of predictive hydrometeors has a negligible impact on the simulated precipitation in low resolution simulations. In high resolution simulations, they found distinct differences in the amount of precipitation, and its temporal evolution, with respect to the complexity in the microphysics. The amount of rainfall increased and its peak intensity became stronger with more hydrometeors.

Khairoutdinov and Randall (2003) developed a model that used a BMP with six classes of the water substance (water vapour, cloud water, rainwater, cloud ice with nonneglibile terminal velocity, snow and graupel). They tested the sensitivity of the simulations to different microphysics configurations. The hydrometeors were found to be strongly affected by the changes to the microphysics scheme. The effects on the simulated mean temperature and moisture bias were found to be small, which they attributed to the low frequency of continental low convective clouds and strong large-scale advective tendencies. All the simulations looked reasonable so that none of the microphysics configuration could be chosen as the preferred one, since detailed observations of the mean cloud statistics were not available.

Van den Heever and Cotton (2004) performed a study to determine the impact changes in the hail size distribution may have on simulated deep convective storms, using the Regional Atmospheric Modeling System (RAMS). The mean hail diameters of 3 mm, 5 mm, 7 mm and 1 cm were used, and the spectrum of simulated supercell storm characteristics that developed was investigated. The smaller hail cases generated stronger low-level downdrafts throughout most of the simulation, and less hail reached the surface than in the large hail cases. The smaller hailstones melted more quickly, and therefore produced rain more rapidly, and hence greater rates of evaporative cooling were achieved than in the larger hail runs. The strength and depth of the cold pool increased as the mean hail diameter was decreased. The downdraft in the large hail case did not occlude the updraft and as a result the left moving storm in this case lasted longer than in the smaller hail cases.

Van Weverberg et al. (2011) followed a systematic setup to investigate the influence of a modified size distribution of rain, snow and hail, within a bulk one-moment microphysics scheme, on microphysical and thermodynamical aspects of deep, moist convection. Weighting the largest precipitating ice species of the microphysics scheme to small graupel resulted in an increase of surface precipitation. The precipitation formation process slowed down, resulting in lower precipitation efficiency. The impact of sized distribution assumptions of snow was found to be small, but more realistic size distribution assumptions of rain led to the strongest effect on surface precipitation. Cold pools shrunk because of weaker rain evaporation at the cold pool boundaries, leading to a decreased surface rain area.

Gilmore et al. (2004) varied constants of N_{0x} and ρ_x of the precipitating classes one at a time while other microphysics parameters were kept constant. For a particular q_x, if N_{0x} or ρ_x are decreased, the distribution becomes more heavily weighted towards larger sized parameters. Tests were conducted for a single thermodynamic profile and three idealized wind shear profiles. It was found that the larger the hail, the smaller the time-averaged horizontally summed q_h mass and time averaged maximum temperature perturbation at higher altitudes. They found that the minimum temperature was lower and more pronounced near the melting level for smaller graupel cases and the cooling started at a higher altitude. They concluded that they do not advocate the use of single moment schemes in cloud scale precipitation forecasting. While these studies show a great dependence on cloud simulations on particle distribution size, one moment bulk microphysics schemes are still relevant because multi-moment schemes are computationally expensive (Van Weverberg et al., 2011). The next section highlights work done with multi-moment schemes and comparisons with single-moment schemes.

2.3.2 Multimoment schemes

The Rutledge and Hobbs (1983) and Lin et al. (1983) microphysics schemes were expanded through the 1990s to take models to a greater understanding of liquid and ice physics (Straka and Mansell, 2005). By adopting a more general gamma distribution function $N(D) = N_0 D^{\alpha} e^{-\lambda D}$ and by predicting more than one moment of the size distribution, it is possible to develop multimoment (MM) schemes that allow α, N_0 and λ to vary independently (Dawson II et al., 2010). The benefit of using MM schemes over single-moment schemes is that MM schemes should be applicable across a wider range of environments. MM schemes require less tuning of parameters that are related to particle number concentrations (Stensrud, 2007). The MM schemes are beginning to be available in numerical models, however their increased cost due to the prediction of multi-moments limits their use in real-time numerical weather prediction (Thompson et al., 2008). Key processes that are strongly affected by using the two-moment approach include melting, evaporation, collection and particle size sorting. The evaporation of rain plays an important role in determining the cold pool strength, which in turn affects the storm dynamics associated with intense continental convection (Morrison and Milbrandt, 2011).

Liu and Moncrieff (2007) evaluated the sensitivity of explicit simulations of rainfall simulations to four BMPs with different orders of complexity. The four schemes were as follows 1) simple ice (cloud water=cloud ice and rain=snow at freezing temperatures), 2) two categories of ice (allows the prediction of cloud water, rain, ice and snow at the same time), 3) three categories ice allows the prediction of cloud ice, snow and graupel and 4) allows the prediction of cloud ice, snow and graupel and also predicts number concentration of ice). The three mixed phase schemes shared the same discrepancies such as underpredicting rainfall in parts and extending the rainfall too far. They found the mixed phase schemes are superior over the simple ice scheme in terms total rainfall distributions. They concluded that for operational forecasting the sensitivity to cloud microphysics in convection-resolving ensembles might not introduce sufficient spread among the ensemble.

Milbrandt and Yau (2006a) tested a triple-moment scheme in a high-resolution three dimensional model, and studied the effects of predicting three independent moments of the size distribution. They used a mesoscale model initialised with synoptic data and nested a 1 km resolution domain to simulate a real case of a supercell storm. The simulated supercell exhibited many of the same characteristics as the observed storm, such as the propagation speed and direction, storm structure and surface precipitation. The effects of the three-moment approach in improving the simulation of hydrometeor size distribution were explored by examining the simulated hail sizes and hail size spectra. The model successfully captured the period of moderately intense hail. The simulated size distribution of the simulated hail was in reasonable agreement with observations.

In a similar study by Milbrandt et al. (2008), comparisons of the simulation were made with observations from radar, raingauges and in situ aircraft measurements of cloud microphysical properties and vertical air motion. The model simulated too much snow mass and too little cloud mass. The simulated reflectivity structure and values compared favourably to radar observations during various precipitation stages of the event. The vertical motion field in simulations corresponded reasonably well to the observations, indicating that biases in the simulations can be attributed in part to the microphysics scheme. The overall spatial distribution of the hydrometeor field was simulated realistically including the mean-mass particle diameter for each category and the observed trend of larger snow sizes to be located at the lower altitudes.

Milbrandt and Yau (2006b) and Milbrandt et al. (2010) investigated the abilities of one- and two-moment schemes to reproduce simulations made with a three-moment scheme. The double and triple-moment simulations were similar - both had a realistic precipitation field, though generally overpredicted in quantity. Both simulations also overpredicted the snow mass and exhibited an overprediction of cloud water aloft. Switching from the triple- to single- moment configuration resulted in a simulation with a precipitation pattern shifted upwind and with a larger positive bias, but with hydrometeor mass fields that corresponded more closely to the observations. Milbrandt et al. (2010) also made simulation with a different single-moment scheme and found that changing the particular single-moment shceme used had a greater impact than changing the number of moments predicted in the same scheme. The added degree of freedom in a two-moment scheme over one-moment scheme seemed to play an important role in the simulations. In fact, the view was expressed that no amount of tuning in a one-moment can produce simulations that were close to a two-moment or three-moment simulations, for a case of deep convection. Dawson II et al. (2010) also found that the third-moment scheme performed better than a single-moment scheme.

Morrison and Milbrandt (2011) conducted simulations of an idealized supercell using the WRF model, with two two-moment bulk microphysics schemes. Despite general similarities in these schemes, the simulations were found to produce distinct differences in storm structure, precipitation and cold pool strength. One scheme produced much higher surface precipitation rates and a stronger cold pool, especially in the early stages of storm development. Different approaches in treating graupel and hail were found to be responsible for many of the key differences between simulations.

Morrison and Grabowski (2007) compared a one-moment and two-moment warm-rain bulk microphysics schemes with a detailed bin-resolving microphysics scheme. Their objective was to characterize uncertainties and validate the bulk approach for modelling shallow cumulus and stratocumulus in the context of different aerosol regimes. There was almost no change in fractional cloud cover across the domain for the various simulations (or change in the cloud lifetime in the time-varying cumulus case). The most important difference between bulk and detailed microphysics simulations was a premature onset of significant surface precipitation (by several minutes) in all bulk schemes. One-moment scheme results were highly sensitive to the specification of the rain size distribution intercept parameter.

Wu and Petty (2010) used the National Centre for Atmospheric Reseearch Weather Weather Research and Forecasting (NCAR WRF) version 3 to simulate four polar lows while comparing five microphysics schemes. They nested a 5 km resolution domain within a bigger 25 km resolution domain, and applied no cumulus parameterization scheme for the 5 km run. The five microphysics schemes that they compared are the PURDUE-LIN (Chen and Sun, 2002), the WSM6 (Hong and Lim, 2006), the Goddard Community Ensemble models (Tao and Simpsom, 1993), the New Thompson scheme (Thompson et al, 2008) and the Morrison et al. (2009) double moment scheme. All the schemes include classes of water substances, water vapour, cloud water, rain, cloud ice, snow, and graupel. The simulations using the different microphysics schemes were broadly similar. They found that different schemes do not influence the propagation of the low system significantly, but that the simulated cloud top temperature is affected significantly. Overall, they found that the PURDUE-LIN and New Thompson schemes performed poorly in simulating cloud fields, while the cloud fields in the other three schemes seem fairly realistic (Wu and Petty, 2010).

According to most of the studies highlighted above, the large variability in the intercept using the two-moment scheme, combined with the large sensitivity of the one-moment scheme to the intercept N_0, suggests the need to predict both the mixing ratio and the intercept - and hence allow the intercept and the mean raindrop size to vary as free parameters in a physically consistent way. According to Morrison and Grabowski (2007) this may be important for microphysics schemes that are intended for use across a wide range of cloud type and conditions, as in regional and global climate simulations using CRMs. The drawback with the multimoment schemes is increased computational costs associated with the added prognostic variable.

2.3.3 2-D vs 3-D tests

Xu et al. (2000) compared seven CRMs for the simulation of midlatitude continental summer convection. The simulations were made for domain sizes approximately 500 km in the horizontal and 20 km in the vertical for 2-D simulations, and approximately 250 km x 250 km x 20 km for three-dimensional (3-D) simulations. The horizontal grid size used in these simulations was 2 km and the vertical resolution varied from model to model in the range 100$m$to 1 km, with stretched coordinates applied in the vertical in some of the models. Two of the models were used to perform 3-D simulations. They found 2-D models to produce similar statistical properties of cumulus convection to the 3-D versions, and therefore recommended the application of 2-D models for testing microphysical schemes (because they are computationally economical). They also found the inter-model differences of temperatures with observations were smaller for CRMs compared to among SCMs. The performance of CRMs was found to be inferior for simulating midlatitude continental convection, relative to that of tropical ocean convection.

Grabowski et al. (1998) performed 2-D and 3-D dimensional simulations of cloud systems for the period of 1-7 September 1974 in Phase III of the Global Atmospheric Research Programme (GARP) Atlantic Tropical Experiment (GATE). Comparisons were presented between three experiments driven by the same large-scale conditions: 1) a fully three-dimensional experiment, 2) a two-dimensional experiment and 3) a high resolution version of the two-dimensional experiment. When averaged over a few hours, surface sensible and latent heat fluxes and surface precipitation evolved very similarly in all three experiments and when evaluated against observations. When compared with the fully three-dimensional results, the two-dimensional simulations produced a much higher temporal variability of domain averaged quantities. Khairoutdinov and Randall (2003) found the vertical profiles of various hydrometeors to be similar in 2-D and 3-D simulations, except for snow which was falling slower in the 3-D model because of stronger updrafts. They found the 2-D CRM to agree well with the 3-D CRM results on the evolution of mean fields and scalar fluxes, but differ quite considerably in velocity and scalar variances. In this study the testing of the microphysics schemes is only done in 2-D.

2.4 Turbulence

Turbulence is a natural response to instabilities in a flow - it acts to reduce the instability (Stull, 2006). Clouds are often turbulent, because of cloud-top radiative cooling and cloud-base radiative warming, as well as latent heat release and absorption. The rate of entrainment is partly determined by turbulent processes (Randall et al., 2003a). Turbulent motions have spatial and temporal variations at scales smaller than those resolved by models and the meteorological observation network. Even if observations would have been taken at very short temporal and spatial separations, a turbulent flow will always have scales that are unresolvable - because there would be eddies with frequencies greater than the observation frequency and spatial scales smaller than the scale separation of the observations (Bryan et al., 2003; Holton, 2004).

Bryan and Morrison (2012) made squall line simulations with horizontal resolutions of 4 km, 1 km and 0.25 km resolution, and found that the high resolution simulations rained less because of increased condensation and evaporation rate of cloud water as a result of increased mixing. Bryan et al. (2003) found that simulations made with 1 km grid spacing do not produce equivalent squall-line structure and evolution to higher-resolution simulations of order 100 m. With grid spacing of order 1 km, overturning occurs in a relatively laminar manner. Using grid spacing of order 100 m, the simulated fields are turbulent, with resolved entrainment and overturning within clouds. Bryan et al. (2003) concluded that the use of better turbulence schemes can improve the simulations.

To account for turbulent motions on a conserved variable A, the variable can be divided it into a mean $\overline{A}$ and perturbation A' components, in short $A = \overline{A} + A'$. Similarly, any other variable w can be written as $w = \overline{w} + w'$. By definition the time means of the pertubations vanish (Holton, 1992), as shown by Reynolds averaging giving $\overline{w}\,\overline{A'} = \overline{w'\overline{A}} = 0$. This implies that the average of the product of two variables will be the product of the average of the means plus the product of two variables of the average of the deviations.

$$\overline{wA} = (\overline{w} + w')\left(\overline{A} + A'\right) = \overline{w}\,\overline{A} + \overline{w'A'} \tag{2.4.1}$$

Using geometric height as the vertical coordinate and using the Bousinesq approximation, it can be shown that

$$\begin{aligned} \frac{Du}{Dt} &= \frac{\partial u}{\partial t} + u\frac{\partial u}{\partial x} + v\frac{\partial u}{\partial y} + w\frac{\partial u}{\partial z} + u\left(\frac{\partial u}{\partial x} + \frac{\partial v}{\partial y} + \frac{\partial w}{\partial z}\right) \\ &= \frac{\partial u}{\partial t} + \frac{\partial u^2}{\partial x} + \frac{\partial\,(uv)}{\partial y} + \frac{\partial\,(uw)}{\partial z}. \end{aligned} \tag{2.4.2}$$

Separating each dependent variable into mean and fluctuating parts and then averaging yields

$$\overline{\frac{Du}{Dt}} = \frac{\partial \overline{u}}{\partial t} + \frac{\partial}{\partial x}\left(\overline{u}\,\overline{u} + \overline{u'u'}\right) + \frac{\partial}{\partial y}\left(\overline{u}\,\overline{v} + \overline{u'v'}\right) + \frac{\partial}{\partial z}\left(\overline{u}\,\overline{w} + \overline{u'w'}\right). \tag{2.4.3}$$

Noting that the above equation satisfies the continuity equation gives

$$\overline{\frac{Du}{Dt}} = \frac{\overline{D}\,\overline{u}}{Dt} + \frac{\partial}{\partial x}\left(\overline{u'u'}\right) + \frac{\partial}{\partial y}\left(\overline{u'v'}\right) + \frac{\partial}{\partial z}\left(\overline{u'w'}\right), \tag{2.4.4}$$

where

$$\frac{\overline{D}}{Dt} = \frac{\partial}{\partial t} + \overline{u}\frac{\partial}{\partial x} + \overline{v}\frac{\partial}{\partial y} + \overline{w}\frac{\partial}{\partial z} \tag{2.4.5}$$

is the rate of change of the mean motion.

The mean equations thus have the form

$$\frac{\bar{D}\bar{u}}{Dt}=-\frac{1}{\rho_0}\frac{\partial\bar{p}}{\partial x}+f\bar{v}-\left[\frac{\partial\overline{u'u'}}{\partial x}+\frac{\partial\overline{u'v'}}{\partial y}+\frac{\partial\overline{u'w'}}{\partial z}\right], \tag{2.4.6}$$

$$\frac{\bar{D}\bar{v}}{Dt}=-\frac{1}{\rho_0}\frac{\partial\bar{p}}{\partial y}-f\bar{u}-\left[\frac{\partial\overline{u'v'}}{\partial x}+\frac{\partial\overline{v'v'}}{\partial y}+\frac{\partial\overline{v'w'}}{\partial z}\right], \tag{2.4.7}$$

$$\frac{\bar{D}\bar{w}}{Dt}=-\frac{1}{\rho_0}\frac{\partial\bar{p}}{\partial z}+g-\left[\frac{\partial\overline{u'w'}}{\partial x}+\frac{\partial\overline{v'w'}}{\partial y}+\frac{\partial\overline{w'w'}}{\partial z}\right], \tag{2.4.8}$$

$$\frac{\bar{D}\bar{\theta}}{Dt}=-\frac{S_h}{c_p\Pi}-\left[\frac{\partial\overline{u'\theta'}}{\partial x}+\frac{\partial\overline{v'\theta'}}{\partial y}+\frac{\partial\overline{w'\theta'}}{\partial z}\right], \tag{2.4.9}$$

$$\frac{\partial\bar{u}}{\partial x}+\frac{\partial\bar{v}}{\partial y}+\frac{\partial\bar{w}}{\partial z}=0, \tag{2.4.10}$$

$$\frac{D\overline{q_x}}{Dt}=\overline{S_x}-\left[\frac{\partial\overline{u'q_x'}}{\partial x}+\frac{\partial\overline{v'q_x'}}{\partial y}+\frac{\partial\overline{w'q_x'}}{\partial z}\right],\quad x=v,c,i. \tag{2.4.11}$$

The model captures the average variables explicitly and the covariance terms (turbulence fluxes) have to be parameterised (Stull, 2006). In a cloud resolving model, the covariance terms represent turbulence which influences the entrainment of clouds, occuring at much smaller scales than a cloud model can simulate explicitly. To solve the mean equations, closure assumptions must be made to approximate the unkown fluxes in terms of the known mean state variables (Holton, 2004).

Turbulence closure assumptions are categorized both by their statistical order and by the amount of non-localness that is included (e.g. Smagorinsky et al., 1965; Troen and Mahrt, 1986). The traditional approach is to assume that the flux is linearly proportional to, or directed down, the local gradient (Holton, 2004; Stull, 2006). This is a first order local closure assumption. In this case the turbulent flux terms can be written as $\overline{u'w'}=-K_m\left(\frac{\partial\bar{u}}{\partial z}\right)$, $\overline{v'w'}=-K_m\left(\frac{\partial\bar{v}}{\partial z}\right)$, and the potential temperature flux can be written as $\overline{\theta'w'}=-K_h\left(\frac{\partial\bar{\theta}}{\partial z}\right)$ where $K_m\left(m^2s^{-1}\right)$is the eddy viscosity coefficient and $K_h$is the eddy diffusivity of heat. This closure scheme is often referred to as K theory.

The flux terms in the basic equations above can then be written as

$$\frac{\partial\overline{u'u'}}{\partial x}+\frac{\partial\overline{u'v'}}{\partial y}+\frac{\partial\overline{u'w'}}{\partial z}=\frac{\partial}{\partial x}\left(-K_m\frac{\partial\overline{u}}{\partial x}\right)+\frac{\partial}{\partial y}\left(-K_m\frac{\partial\overline{u}}{\partial y}\right)+\frac{\partial}{\partial z}\left(-K_m\frac{\partial\overline{u}}{\partial z}\right), \tag{2.4.12}$$

$$\frac{\partial\overline{u'v'}}{\partial x}+\frac{\partial\overline{v'v'}}{\partial y}+\frac{\partial\overline{v'w'}}{\partial z}=\frac{\partial}{\partial x}\left(-K_m\frac{\partial\overline{v}}{\partial x}\right)+\frac{\partial}{\partial y}\left(-K_m\frac{\partial\overline{v}}{\partial y}\right)+\frac{\partial}{\partial z}\left(-K_m\frac{\partial\overline{v}}{\partial z}\right), \tag{2.4.13}$$

$$\frac{\partial\overline{u'w'}}{\partial x}+\frac{\partial\overline{v'w'}}{\partial y}+\frac{\partial\overline{w'w'}}{\partial z}=\frac{\partial}{\partial x}\left(-K_m\frac{\partial\overline{w}}{\partial x}\right)+\frac{\partial}{\partial y}\left(-K_m\frac{\partial\overline{w}}{\partial y}\right)+\frac{\partial}{\partial z}\left(-K_m\frac{\partial\overline{w}}{\partial z}\right), \tag{2.4.14}$$

$$\frac{\partial\overline{u'\theta'}}{\partial x}+\frac{\partial\overline{v'\theta'}}{\partial y}+\frac{\partial\overline{\dot{w}'\theta'}}{\partial z}=\frac{\partial}{\partial x}\left(-K_h\frac{\partial\overline{\theta}}{\partial x}\right)+\frac{\partial}{\partial y}\left(-K_h\frac{\partial\overline{\theta}}{\partial y}\right)+\frac{\partial}{\partial z}\left(-K_h\frac{\partial\overline{\theta}}{\partial z}\right) \tag{2.4.15}$$

$$\frac{\partial\overline{u'q'_x}}{\partial x}+\frac{\partial\overline{v'q'_x}}{\partial y}+\frac{\partial\overline{w'q'_x}}{\partial z}=\frac{\partial}{\partial x}\left(-K_h\frac{\partial\overline{q_x}}{\partial x}\right)+\frac{\partial}{\partial y}\left(-K_h\frac{\partial\overline{q_x}}{\partial y}\right)+\frac{\partial}{\partial z}\left(-K_h\frac{\partial\overline{q_x}}{\partial z}\right), \tag{2.4.16}$$

where K_m and K_h are different coefficients for the mixing of momentum and mass, respectively.

Engelbrecht et al. (2007) implemented a scheme that uses constant values of K_m and K_h for the whole domain in the NSM. The values K_m and K_h can be prescribed to increase with the intensity of the turbulence. Turbulence varies with height above ground, mean wind shear, and surface heating by the sun (Stull, 2006).

2.4.1 K-Theory - Richardson based

Turbulence can be generated mechanically, thermally and inertially. Mechanical turbulence can form when there is shear in the mean wind. Thermal or convective turbulence consists of plumes or thermals of warm air that rises and cold air that sinks due to buoyancy forces. Inertial turbulence forms when the shear is generated by large eddies. For turbulence to exist there must be continual generation of turbulence from shear or buoyancy. The existence of shear depends on the relative strengths of mechanical generation (M) by wind shear versus buoyant consumption by static stability (B) (Stull, 2006).

$$Ri = \frac{-B}{M} = \frac{\left(g/\overline{\theta_v}\right) \frac{\partial \theta_v}{\partial z}}{\left[\left(\frac{\partial \overline{u}}{\partial z}\right)^2 + \left(\frac{\partial \overline{v}}{\partial z}\right)^2\right]}. \tag{2.4.17}$$

The ratio of the terms B and M in the equation above defines the dimensionless Richardson number, Ri, which can be approximated by the vertical gradients of wind and potential temperature (Stull, 2006). Louis (1979) presented a scheme for the representation of vertical eddy fluxes of heat, momentum and water vapour in a forecast model based on the gradient Richardson number (equation 2.4.18 and 2.4.19).

$$K_h = l^2 |\frac{\partial \overline{u}}{\partial z}| F\left(Ri\right) \tag{2.4.18}$$

$$K_m = l^2 |\frac{\partial \overline{u}}{\partial z}| F\left(Ri\right) \tag{2.4.19}$$

where l is the mixing length and is usually approximated by $l = kz$ where $k =$ 0.41 is the von Karman constant and z is height above ground level (Stull, 2006). Holtslag and Boville (1993) defined l as $l = \frac{kz\lambda}{\lambda + kz}$ where λ is the asymptotic length scale. The definitions of λ and $F(Ri)$ are empirical and have been defined differently by different authors. In this study, l and λ are defined as in Holtslag and Boville (1993) because they chose the values so that they are applicable for both the free atmosphere and the boundary layer. The asymptotic length scale is defined as $\lambda = 30 + 270exp\left(1 - z/1000\right)$ so that $\lambda = 300m$ for z$\leq$1000 m, and $\lambda = 30m$ in the free atmosphere. For unstable conditions (i.e. $Ri < 0$) the function used is

$$F\left(Ri\right) = \left(1 - 18Ri\right)^{\frac{1}{2}} \tag{2.4.20}$$

while for stable conditions ($Ri > 0$) the function

$$F(Ri) = \frac{1}{1 + 10Ri(1 + 8Ri)} \tag{2.4.21}$$

is used.

The limiting factor of the K-theory is that it depends only on the local values of the model variables. During the day time, mass and momentum transport is mostly accomplished by the largest eddies, and these eddies are more representative of the properties of the entire boundary layer than the local conditions at one vertical level. When surface heating is strong, K-theory can produce very deep superadiabatic layers near the surface that are unrealistc. In addition, not all turbulent transport is downgradient (Stensrud, 2007). Under unstable conditions, thermals cause intense mixing and homogenization which can act to eliminate the vertical gradient of mean potential temperature in the middle of the boundary layer, yet there are strong positive heat fluxes caused by the rising thermal (Stull, 2006).

Holtslag and Boville (1993) compared a local and nonlocal diffusion schemes. They found that the nonlocal scheme transported moisture away from the surface, depositing the moisture at higher levels. The local scheme transported the moisture slower and saturated the lower levels unrealistically, and lead to clouds too low in the atmosphere. For locations in which deep convection is important, the outputs of the runs with the two vertical diffusion schemes were found to be very similar. For their model NCAR Community Climate Model Version 2, they decided the best diffusion scheme to use was the nonlocal one.

2.5 Summary

In this Chapter, CRMs were discussed in detail. CRMs can be used to study aspects of the atmosphere that cannot be observed using current observational tools. They can also be used as superparameterisations in GCMs and to test conventional schemes. The CRMs use microphysical parameterisations which are grouped into bin and bulk approaches. Bin schemes are available in research models, but are currently not used in operational CRMs and GCM superparameterisations, because they are computationally expensive. Bulk schemes specify an exponential function for particle distribution and predict one or more characteristics of a particle category. Single-moment schemes fix one parameter, usually the intercept parameter and predict the mixing ratio.

A number of studies have shown that the microphysics and dynamics of thunderstorms are sensitive to the particle distribution in single-moment schemes. Multi-moment scheme are therefore advocated because they allow the prediction of mixing ratio and the number concentration to be made independently. Because of computational costs associated with multi-moment schemes, single-moment schemes are still relevant today and they have been shown to be capable of providing realistic simulations of thunderstorms attributes. The local diffusion schemes were also discussed and it is noted that they tend to cause limited mixing compared to nonlocal schemes.

One study found that high resolution simulations rain more because of increased condensation and evaporation rate of cloud water as a result of increased mixing. Another study found that a 1 km grid spacing simulation does not produce squall-line structures and evolution similar to that of very high resolution simulations of the order of 100 m. It is thought that the use of improved turbulence schemes can improve simulations make with horizontal resolutions of about 1 km.

In the next chapter, changes to the basic equations of the NSM are discussed. The two microphysics schemes that are added to the NSM as well as the improvements made to the diffusion scheme are discussed in detail. The numerical techniques used in the model which are similar to those used by Engelbrecht et al. (2007) are discussed briefly.

Chapter 3

Introduction of the microphysics schemes to the nonhydrostatic σ-coordinate model

3.1 Introduction

Engelbrecht et al. (2007) developed the dynamical core for the Nonhydrostatic σ-coordinate Model (NSM). This core is related to the nonhydrostatic equation set developed by White (1989), which employs the full pressure field as the vertical coordinate. Unlike the equation sets of Miller (1974), Miller and Pearce (1974) and Miller and White (1984), which all rely on the use of a reference state (and which assume that changes from the reference state occur only because of convective processes), the equation set of White (1989) avoids the use of such a reference state. Potentially, White's 1989 equations may be applied globally, since they are not restricted to areas with relatively homogeneous temperature reference profiles. That is, the extended equations of White (1989) may be applied in regions of steep temperature gradients along a pressure surface such as cold fronts. The NSM relies on the use of the σ-coordinate equivalent set of White's 1989 pressure coordinate equations. The σ-coordinate in the NSM uses the full pressure field and is defined as $\sigma = \frac{P-P_T}{P_{surf}-P_T} = \frac{P-P_T}{P_s}$. p_{surf} is the surface pressure, p_T is pressure at the top of the model domain, and p is the full pressure. The σ-coordinate equation set equivalent to the pressure-based equations of White (1989) is given by:

$$\frac{Du}{Dt} - fv + \frac{\partial \phi}{\partial x} - \sigma \frac{\partial \phi}{\partial \sigma} \frac{\partial \ln p_s}{\partial x} = 0 \tag{3.1.1}$$

$$\frac{Dv}{Dt} + fu + \frac{\partial \phi}{\partial y} - \sigma \frac{\partial \phi}{\partial \sigma} \frac{\partial \ln p_s}{\partial y} = 0 \tag{3.1.2}$$

$$\frac{R}{g} \frac{D}{Dt} \left(\frac{\omega T}{p} \right) + g + \frac{p}{p_s} \frac{g}{RT} \frac{\partial \phi}{\partial \sigma} = 0 \tag{3.1.3}$$

$$\frac{\partial u}{\partial x} + \frac{\partial v}{\partial y} + \frac{\partial \dot{\sigma}}{\partial \sigma} + \frac{D \ln p_s}{Dt} = 0 \tag{3.1.4}$$

$$\frac{DT}{Dt} - \kappa \frac{\omega T}{p} = 0 \tag{3.1.5}$$

$$\begin{aligned}
&\frac{\partial^2 \phi}{\partial x^2} + \frac{\partial^2 \phi}{\partial y^2} + \frac{\partial}{\partial \sigma} \left(s^2 \frac{\partial \phi}{\partial \sigma} \right) - 2\sigma \left(\frac{\partial \ln p_s}{\partial x} \frac{\partial^2 \phi}{\partial x \partial \sigma} + \frac{\partial \ln p_s}{\partial y} \frac{\partial^2 \phi}{\partial y \partial \sigma} \right) \\
&+ \left[\left(\frac{\partial \ln p_s}{\partial x} \right)^2 + \left(\frac{\partial \ln p_s}{\partial y} \right)^2 \right] \left[\frac{\partial}{\partial \sigma} \left(\sigma^2 \frac{\partial \phi}{\partial \sigma} \right) \right] - \frac{\sigma}{p_s} \left(\frac{\partial^2 p_s}{\partial x^2} + \frac{\partial^2 p_s}{\partial y^2} \right) \frac{\partial \phi}{\partial \sigma} = \\
&2 \left\{ \left(\frac{\partial u}{\partial x} + \frac{\partial v}{\partial y} \right) \frac{\partial}{\partial \sigma} \left(\Omega \frac{p}{p_s} \right) - \frac{1}{p_s} \left[\frac{\partial}{\partial x} (\Omega p) \frac{\partial u}{\partial \sigma} + \frac{\partial}{\partial y} (\Omega p) \frac{\partial v}{\partial \sigma} \right] + \frac{\partial u}{\partial x} \frac{\partial v}{\partial y} - \frac{\partial v}{\partial x} \frac{\partial u}{\partial y} \right\} \\
&+2\sigma \left[\frac{\partial \ln p_s}{\partial x} \left(\frac{\partial u}{\partial y} \frac{\partial v}{\partial \sigma} - \frac{\partial v}{\partial y} \frac{\partial u}{\partial \sigma} \right) + \frac{\partial \ln p_s}{\partial y} \left(\frac{\partial v}{\partial x} \frac{\partial u}{\partial \sigma} - \frac{\partial u}{\partial x} \frac{\partial v}{\partial \sigma} \right) \right] \\
&+f \left[\frac{\partial v}{\partial x} - \frac{\partial u}{\partial y} + \sigma \left(\frac{\partial u}{\partial \sigma} \frac{\partial \ln p_s}{\partial y} - \frac{\partial v}{\partial \sigma} \frac{\partial \ln p_s}{\partial x} \right) \right] - u \frac{df}{dy} - \frac{\partial}{\partial \sigma} \left(sg - \frac{p}{p_s} \Omega^2 \frac{1}{\Upsilon} \right)
\end{aligned} \tag{3.1.6}$$

Engelbrecht (2006) and Engelbrecht et al. (2007) derived equations 3.1.1 to 3.1.6 and solved the set using a time-split semi-Langragian approach, formulated on an unstaggered grid. The total derivative in σ-coordinates is defined as $\frac{D}{Dt} = \frac{\partial}{\partial t} + u\frac{\partial}{\partial x} + v\frac{\partial}{\partial y} + \dot{\sigma}\frac{\partial}{\partial \sigma}$. Equations 3.1.1, 3.1.2 and 3.1.3 are the momentum equations in the zonal, meridional and vertical directions, respectively. Equation 3.1.4 is the continuity equation, whilst equation 3.1.5 is the thermodynamic energy equation. A consequence of the approximations made in deriving the nonhydrostatic equations in coordinates bases on the full pressure field, following the methodology of Miller and White (1984), is that sound waves propagating in the vertical are filtered (Miller and White, 1984). This provides a computational advantage over solving the fully elastic equations. However, another consequence of the approximations made in order to arrive at the Miller and White (1984) equation system, is the absence of a prognostic equation for the geopotential equation. The numerical solution of the pressure or σ-coordinate equations for this equation system therefore requires the use of an elliptic equation (equation 3.1.6).

Engelbrecht et al. (2007)'s model does not include physics processes such as radiation and microphysics processes. The aim of this study is to introduce a microphysics scheme for the explicit simulation of clouds to the set of nonhydrostatic equations, and to subsequently apply the model to study the physics and dynamics of moist convection. Microphysics processes introduce thermal instabilities, through the release and absorption of latent heat. Turbulence is therefore an important process in clouds that interacts actively with the microphysics and radiation. The existing diffusion scheme within the NSM is also improved in this study, to make it more physically-based. In the next section, the microphysics schemes introduced to the original NSM are discussed. A discussion of the new diffusion scheme follows, and then the numerical techniques used in the model are also discussed briefly.

3.2 Basic Equations with moisture and radiation

Within Bulk Microphysics Parameterisation (BMP) scheme, microphysics processes function to change a particular water species from one phase to another, and also change the temperature through the release and absorption of latent heat. The change in temperature due to microphysics processes is represented by the first term on the right hand side of thermodynamic equation (3.2.1), while radiation heating and cooling are represented by the last term on the right hand side. Note that Equation (3.2.1) replaces Equation (3.1.5) in an equation system that describes moist processes, and note that the right hand side of Equation (3.1.5) above is zero. This implies that the equation is for a dry, adiabatic atmosphere.

$$\frac{DT}{Dt} - \frac{R_d T\omega}{c_p p} = S_h + radhr \tag{3.2.1}$$

$$\begin{aligned}
&\frac{\partial^2\phi}{\partial x^2} + \frac{\partial^2\phi}{\partial y} + \frac{\partial}{\partial\sigma}\left[s^2\frac{\partial\phi}{\partial\sigma}\right] - 2\sigma\left[\frac{\partial\ln p_s}{\partial x}\left(\frac{\partial^2\phi}{\partial x\partial\sigma}\right) + \frac{\partial\ln p_s}{\partial y}\left(\frac{\partial^2\phi}{\partial y\partial\sigma}\right)\right]\\
&+\frac{\partial}{\partial\sigma}\left(\sigma^2\frac{\partial\phi}{\partial\sigma}\right)\left[\left(\frac{\partial\ln p_s}{\partial x}\right)^2 + \left(\frac{\partial\ln p_s}{\partial y}\right)^2\right] - \frac{\sigma}{p_s}\frac{\partial\phi}{\partial\sigma}\left[\left(\frac{\partial^2 p_s}{\partial x^2}\right) + \left(\frac{\partial^2 p}{\partial y^2}\right)\right] =\\
&2\left(\frac{\partial u}{\partial x} + \frac{\partial v}{\partial y}\right)\frac{\partial}{\partial\sigma}\left(\frac{\Omega p}{p_s}\right) - \frac{2}{p_s}\left[\frac{\partial u}{\partial\sigma}\frac{\partial}{\partial x}(p\Omega) + \frac{\partial v}{\partial\sigma}\frac{\partial}{\partial y}(p\Omega)\right] + 2\left(\frac{\partial u}{\partial x}\frac{\partial v}{\partial y} - \frac{\partial v}{\partial x}\frac{\partial u}{\partial y}\right)\\
&+2\sigma\left[\frac{\partial\ln p_s}{\partial x}\left(\frac{\partial u}{\partial y}\frac{\partial v}{\partial\sigma} - \frac{\partial v}{\partial y}\frac{\partial u}{\partial\sigma}\right) + \frac{\partial\ln p_s}{\partial y}\left(\frac{\partial v}{\partial x}\frac{\partial u}{\partial\sigma} - \frac{\partial u}{\partial x}\frac{\partial v}{\partial\sigma}\right)\right]\\
&+\sigma f\left[\frac{\partial\ln p_s}{\partial y}\frac{\partial u}{\partial\sigma} - \frac{\partial\ln p_s}{\partial x}\frac{\partial v}{\partial\sigma}\right] + f\left(\frac{\partial v}{\partial x} - \frac{\partial u}{\partial y}\right) - u\frac{\partial f}{\partial y}\\
&-\frac{\partial}{\partial\sigma}\left(sg - \frac{p}{p_s}\Omega^2\frac{1}{\gamma}\right) - \frac{\partial}{\partial\sigma}\left(\frac{S_h p\Omega}{p_s T}\right) - \frac{\partial}{\partial\sigma}\left(\frac{p\Omega radhr}{p_s T}\right)
\end{aligned} \tag{3.2.2}$$

$$\frac{Dq_v}{Dt} = S_v \tag{3.2.3}$$

$$\frac{Dq_c}{Dt} = S_c \tag{3.2.4}$$

$$\frac{Dq_r}{Dt} = S_r \tag{3.2.5}$$

$$\frac{Dq_i}{Dt} = S_i \tag{3.2.6}$$

$$\frac{Dq_s}{Dt} = S_s \tag{3.2.7}$$

$$\frac{Dq_g}{Dt} = S_g \tag{3.2.8}$$

Two extra terms appear in the modified elliptic equation (Equation 3.2.2), as a result of the microphysics and radiation processes. The full derivation of the new elliptic equation is provided in Appendix A. The momentum equations take on a similar form as for dry air. The assumption is made that the gas constant of dry air may be used in the momentum equations for a moist atmosphere. Indeed, it is conventional to assume that the effects of moisture on the gas constant are negligible, since the gas constant for mixed air in the atmosphere is typically very similar to that of dry air. Note that although the form of the momentum equation stays the same, the equations contain the geopotential height as a dependant variable - this variable in turn depends on the microphysics and radiation processes as can be seen from the elliptic equation.

When moisture is introduced to the atmospheric equations, water continuity equations have to be solved for all the water species in the model. The BMP schemes introduced to the NSM use five or six water species. Equation (3.2.3) to (3.2.8) are the water continuity equations for water vapour, cloud water, rain water, cloud ice, snow and graupel or hail, in the order that they are written. The water continuity equations predict the change in the mixing ratios of the water species due to advection as well as the microphysics processes. The right hand side of each equation represents the microphysical processes that act as sources and sinks for that particular water substance. For example, melting of snow is a sink for snow but a source for rainwater, while collection of cloud water by snow is a source for snow and a sink for cloud water. The microphysics schemes chosen in this study were obtained from the National Centre for Atmorpheric Research (NCAR) Weather Research and Forecasting (WRF) model (Skamarock et al., 2005) and are based on the Lin et al. (1983) and Rutledge and Hobbs (1983;1984) schemes.

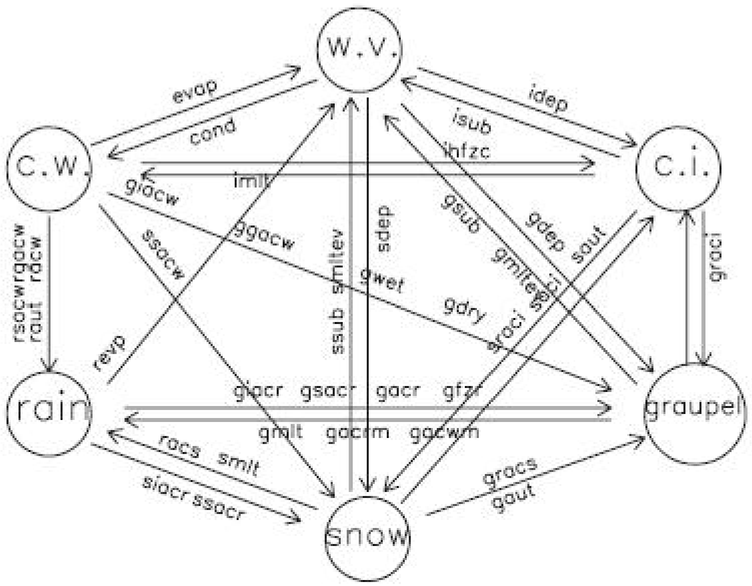

Figure 3.3.1: A schematic depicting the water species and microphysics processes in the PURDUE-LIN scheme. (From Lin and Colle, 2011)

3.3 The microphysics parameterisations

3.3.1 The PURDUE-LIN microphysics schemes

Chen and Sun (2002) developed a BMP that is based on the schemes of Lin et al. (1983) and Rutledge and Hobbs (1983). The scheme was developed at the Purdue University and is known as the PURDUE-LIN scheme. It includes six classes of the water substance, namely water vapour, cloud water, cloud ice, rain, snow and graupel (Figure 3.3.1). They also applied the saturation adjustment of Tao et al. (1989).

If a layer is supersaturated and cloud water or cloud ice exists, the amount of water vapour condensed to cloud water or deposited to cloud ice depends upon the ratio of cloud ice and cloud water. The same principle is applied to unsaturated conditions. If supersaturation occurs in a layer without cloud ice and cloud water, the ratio of water vapour conversion to cloud water and cloud ice is a function of temperature. No liquid water exists when the temperature is lower than -$40^0 C$. Liquid and solid phases can coexist when the temperature is between 0 ^0C and -40^0C; graupel or snow can exist without ice crystals when the temperature is above 0 ^0C (Chen and Sun, 2002). The relevant microphysics processes are described in Appendix B.

The size distribution of rain, snow and graupel are given respectively by

$$N_R\left(D_r\right) = N_{0R}\exp(-\lambda_R D_R) \tag{3.3.1}$$

$$N_S\left(D_s\right) = N_{0S}\exp(-\lambda_S D_S) \tag{3.3.2}$$

$$N_G\left(D_G\right) = N_{0G}\exp(-\lambda_G D_G) \tag{3.3.3}$$

where N_{0R}, N_{0S} and N_{0G} are the intercept parameters of rain, snow and hail/graupel size distributions, respectively. D_R, $D_S$and D_G are diameters of the rain, snow and hail particles, respectively. The slope parameters of the rain, snow and hail size distribution (λ_R, λ_S, and λ_G) are as follows:

$$\lambda_R = \left(\frac{\pi\rho_w N_{0R}}{\rho q_r}\right)^{0.25} \tag{3.3.4}$$

$$\lambda_S = \left(\frac{\pi\rho_S N_{0S}}{\rho q_S}\right)^{0.25} \tag{3.3.5}$$

$$\lambda_G = \left(\frac{\pi\rho_G N_{0G}}{\rho q_G}\right)^{0.25} \tag{3.3.6}$$

The terminal velocities for a precipitating particle of diameter D_R, $D_S$and D_G are given by

$$U_{DR} = aD_R^b\left(\frac{\rho_0}{\rho}\right)^{1/2} \tag{3.3.7}$$

$$U_{DS} = cD_S^d\left(\frac{\rho_0}{\rho}\right)^{1/2} \tag{3.3.8}$$

$$U_{DG} = \left(\frac{4g\rho_G}{3C_D\rho}\right)^{1/2} D_G^{1/2} \tag{3.3.9}$$

where $b = 0.8$, $a = 2115 * 0.01^{1-b}$, $d = 0.25$, $c = 152.93 * 0.01^{(1-d)}$, $\rho_0 = 1.29$kg m^{-3} and a drag coefficient, $C_D = 0.6$

The mass-weighted mean terminal velocities is

$$U_R = \frac{a\Gamma\left(4+b\right)}{6\lambda_R^b}\left(\frac{\rho_0}{\rho}\right)^{1/2} \tag{3.3.10}$$

$$U_S = \frac{c\Gamma\left(4+b\right)}{6\lambda_S^b}\left(\frac{\rho_0}{\rho}\right)^{1/2} \tag{3.3.11}$$

$$U_G = \frac{\Gamma\left(4+b\right)}{6\lambda_G^{0.5}}\left(\frac{4g\rho_G}{3C_D\rho}\right)^{1/2} \tag{3.3.12}$$

If the precipitation content at a point is distributed over particles of different size and fallspeeds, U_R or U_S or U_G are averages (Kessler, 1969). All precipitating fields are assumed to fall at their mass-weighted fall speed. Cloud water and cloud ice are assumed to be monodispersed and nonfalling. The scheme can be used both with five water classes (i.e. excluding graupel) and with six species. Temperature is passed to the scheme which is then used as input for the calculation of microphysics processes and it also gets updated as a result of latent heating or cooling.

3.3.2 The SBU-YLIN scheme

A new BMP scheme was recently developed at the Stony Brook University (SBU) using the PURDUE-LIN scheme as a starting point (Lin and Colle, 2011). The developers of the scheme called it SBU-YLIN. The SBU-YLIN scheme includes five prognostic mixing ratios; water vapour, cloud ice, precipitating ice, cloud water and rain. Dry ice, rimed ice, and graupel are included in the precipitating ice category. Snow and graupel share the same category and hence the same processes too. The new scheme reduces the number of microphysical processes from ~40 to less than 20 (Lin and Colle, 2011), which makes the scheme cheaper to run. Figure 3.3.2 shows the water species and microphysics processes available in the SBU-YLIN scheme.

The SBU-YLIN scheme uses a generalized gamma distribution to describe size distribution of cloud water droplets:

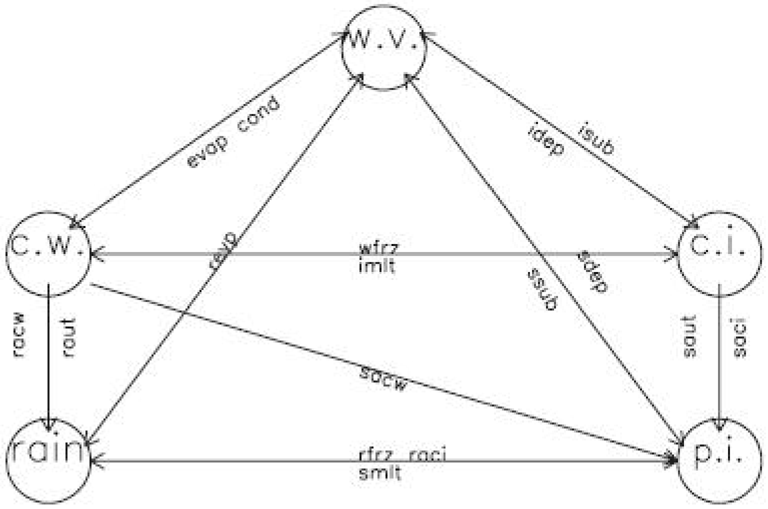

Figure 3.3.2: A schematic depicting the water species and microphysics processes in the SBU-YLIN scheme. (From Lin and Colle 2011)

$$N_c = N_{0c} D^{\mu} e^{-\lambda D} \tag{3.3.13}$$

where N_{0C} is the intercept, μ is the shape parameter, and λ is the slope. The number concentration of cloud droplets generally depends on the ambient aerosol distribution and properties. 100 cm^{-3} is used currently for maritime and 250 cm^{-3} is used for continental air mass. The autoconversion parameterisations are based on the definition of Liu and Daum (2004), which suggests a strong dependence of the autoconversion rate liquid water content, droplet concentration, and relative dispersion of cloud droplets. The autoconversion parameterisation is described in Appendix C. Rain and its related parameterizations are similar to that of the PURDUE-LIN scheme.

Cloud ice is assumed to be monodispersed, similar to the PURDUE-LIN scheme, however it is allowed to fall. A maximum size of 100 microns is applied for cloud ice to snow conversion. The scheme uses a more flexible and general approach that considers both temperature and riming impact on ice particle properties. The scheme has a diagnosed riming intensity parameter, so that a continuous spectrum from pristine ice to heavily rimed snow and graupel can be represented. Dry snow, rimed snow and graupel are included in the precipitation ice category through the introduction of varying riming intensity parameters. Power laws are used to describe the mass-diameter, area-diameter and fall velocity-diameter relationships for ice particles.

3.4 Turbulence

Turbulence was discussed in detail in the previous chapter, for the case where geometric height is used as the vertical coordinate. In this chapter the introduction of turbulence and a more sophisticated diffusion scheme to the NSM, which uses a σ-coordinate in the vertical, is discussed. Any conserved variable A, can be divided into a time mean $\overline{A}$ and perturbation A' components, in short $A = \overline{A} + A'$. Similarly, any other variable w can be written as $w = \overline{w} + w'$. By definition the time means of the pertubations vanish (Holton, 1992), which gives $\overline{w}\overline{A'} = \overline{w'}\overline{A} = 0$. This implies that the average of the product of two variables will be the product of the average of the means, plus the product of the average of the deviations of the two variables:

$$\overline{wA} = \left(\overline{w} + w'\right)\left(\overline{A} + A'\right) = \overline{w}\,\overline{A} + \overline{w'A'} \tag{3.4.1}$$

In σ-coordinates and using the continuity equation it can be shown that

$$\begin{aligned} \frac{Du}{Dt} &= \frac{\partial u}{\partial t} + u\frac{\partial u}{\partial x} + v\frac{\partial u}{\partial y} + \dot{\sigma}\frac{\partial u}{\partial \sigma} + u\left(\frac{\partial u}{\partial x} + \frac{\partial v}{\partial y} + \frac{\partial \dot{\sigma}}{\partial \sigma} + \frac{Dlnp_s}{Dt}\right) \\ &= \frac{\partial u}{\partial t} + \frac{\partial u^2}{\partial x} + \frac{\partial uv}{\partial y} + \frac{\partial u\dot{\sigma}}{\partial \sigma} + u\frac{Dlnp_s}{Dt}. \end{aligned} \tag{3.4.2}$$

Separating each dependent variable into the mean and fluctuating parts and then averaging yields

$$\overline{\frac{Du}{Dt}} = \frac{\partial \overline{u}}{\partial t} + \frac{\partial}{\partial x}\left(\overline{u}\,\overline{u} + \overline{u'u'}\right) + \frac{\partial}{\partial y}\left(\overline{u}\,\overline{v} + \overline{u'v'}\right) + \frac{\partial}{\partial \sigma}\left(\overline{u}\,\overline{\dot{\sigma}} + \overline{u'\dot{\sigma}'}\right) + u\overline{\frac{Dlnp_s}{Dt}}, \tag{3.4.3}$$

$$\overline{\frac{Du}{Dt}} = \frac{\partial \overline{u}}{\partial t} + \frac{\partial}{\partial x}\overline{uu} + \frac{\partial}{\partial y}\left(\overline{uv}\right) + \frac{\partial}{\partial \sigma}\left(\overline{u\dot{\sigma}}\right) + u\overline{\frac{Dlnp_s}{Dt}}$$

$$+\frac{\partial}{\partial x}\left(\overline{u'u'}\right) + \frac{\partial}{\partial y}\left(\overline{u'v'}\right) + \frac{\partial}{\partial \sigma}\left(\overline{u'\dot{\sigma}'}\right), \qquad (3.4.4)$$

$$\overline{\frac{Du}{Dt}} = \frac{\partial \overline{u}}{\partial t} + \overline{u}\frac{\partial \overline{u}}{\partial x} + \overline{v}\frac{\partial \overline{u}}{\partial y} + \overline{\dot{\sigma}}\frac{\partial \overline{u}}{\partial \sigma} + \overline{u}\left(\frac{\partial \overline{u}}{\partial x} + \frac{\partial \overline{v}}{\partial y} + \frac{\partial \overline{\dot{\sigma}}}{\partial \sigma} + \overline{\frac{Dlnp_s}{Dt}}\right)$$

$$+\frac{\partial}{\partial x}\left(\overline{u'u'}\right) + \frac{\partial}{\partial y}\left(\overline{u'v'}\right) + \frac{\partial}{\partial \sigma}\left(\overline{u'\dot{\sigma}'}\right). \qquad (3.4.5)$$

Noting that the equation above satisfies the continuity equation gives

$$\overline{\frac{Du}{Dt}} = \frac{\overline{D}\overline{u}}{Dt} + \frac{\partial}{\partial x}\left(\overline{u'u'}\right) + \frac{\partial}{\partial y}\left(\overline{u'v'}\right) + \frac{\partial}{\partial \sigma}\left(\overline{u'\dot{\sigma}'}\right), \qquad (3.4.6)$$

where

$$\frac{\overline{D}}{Dt} = \frac{\partial}{\partial t} + \overline{u}\frac{\partial}{\partial x} + \overline{v}\frac{\partial}{\partial y} + \overline{\dot{\sigma}}\frac{\partial}{\partial \sigma} \qquad (3.4.7)$$

is the rate of change of the mean motion.

3.4.1 The basic equations

3.4.1.1 Momentum equations

The mean horizontal momentum equations take the form

$$\frac{\bar{D}\bar{u}}{Dt} - f\overline{v} + \frac{\partial \overline{\phi}}{\partial x} - \overline{\sigma}\frac{\partial \overline{\phi}}{\partial \sigma}\frac{\partial \ln p_s}{\partial x} + \left[\frac{\partial \overline{u'u'}}{\partial x} + \frac{\partial \overline{u'v'}}{\partial y} + \frac{\partial \overline{u'\dot{\sigma}'}}{\partial \sigma}\right] = 0, \qquad (3.4.8)$$

$$\frac{\bar{D}\bar{v}}{Dt} + f\overline{u} + \frac{\partial \overline{\phi}}{\partial y} - \overline{\sigma}\frac{\partial \overline{\phi}}{\partial \sigma}\frac{\partial \ln p_s}{\partial y} + \left[\frac{\partial \overline{u'v'}}{\partial x} + \frac{\partial \overline{v'v'}}{\partial y} + \frac{\partial \overline{v'\dot{\sigma}'}}{\partial \sigma}\right] = 0. \qquad (3.4.9)$$

The vertical momentum equation as used in the NSM is written as

$$\frac{1}{g}\frac{D}{Dt}\left(\frac{R_d\omega T}{p}\right)+g+\frac{p}{p_s}\frac{g}{R_dT}\frac{\partial\phi}{\partial\sigma}=0. \tag{3.4.10}$$

Using the definition of vertical velocity $w=-\frac{\omega RT}{gp}$ it becomes

$$\frac{Dw}{Dt}-g-\frac{p}{p_s}\frac{g}{R_mT}\frac{\partial\phi}{\partial\sigma}=0 \tag{3.4.11}$$

The mean vertical momentum equation can then be written as

$$\frac{\overline{D}\overline{w}}{Dt}-g-\frac{\overline{p}}{p_s}\frac{g}{\overline{R_dT}}\frac{\partial\overline{\phi}}{\partial\sigma}+\left[\frac{\partial\overline{u'w'}}{\partial x}+\frac{\partial\overline{v'w'}}{\partial y}+\frac{\partial\overline{w'\dot{\sigma}'}}{\partial\sigma}\right]=0 \tag{3.4.12}$$

Converted back as used in the NSM, it is given by

$$\frac{1}{g}\frac{D}{Dt}\left(\frac{R_d\omega T}{p}\right)+g+\frac{\overline{p}}{p_s}\frac{g}{R_d\overline{T}}\frac{\partial\overline{\phi}}{\partial\sigma}-\left[\frac{\partial\overline{u'w'}}{\partial x}+\frac{\partial\overline{v'w'}}{\partial y}+\frac{\partial\overline{w'\dot{\sigma}'}}{\partial\sigma}\right]=0 \tag{3.4.13}$$

3.4.1.2 Thermodynamic energy equation

The temperature equation is written as

$$\frac{DT}{Dt}-\frac{R_dT\omega}{c_pp}=S_h+radhr. \tag{3.4.14}$$

Choosing to diffuse potential temperature(θ) rather than temperature, the thermodynamic energy equation may be written in terms of potential temperature

$$\frac{D}{Dt}\left[\theta\left(\frac{p}{\hat{p}}\right)^{R_d/c_p}\right]-\frac{R_d\theta\left(\frac{p}{\hat{p}}\right)^{R_d/c_p}\omega}{c_pp}=S_h+radhr \tag{3.4.15}$$

Using the product rule we get

$$\left(\frac{p}{\hat{p}}\right)^{R_d/c_p}\frac{D\theta}{Dt}+\frac{\theta}{\hat{p}^{R_d/c_p}}\frac{Dp^{R_d/c_p}}{Dt}-\frac{R_d\theta\left(\frac{p}{\hat{p}}\right)^{R_d/c_p}\omega}{c_pp}=S_h+radhr \tag{3.4.16}$$

Dividing by the Exner function ($\Pi = \left(\frac{p}{\hat{p}}\right)^{R_d/c_p}$) and taking the derivative of p^{R_d/c_p} we get

$$\frac{D\theta}{Dt} + \frac{R_d}{c_p}\frac{\theta p^{R_d/c_p - 1}}{p^{R_d/c_p}}\frac{Dp}{Dt} - \frac{R_d\theta\omega}{c_p p} = \frac{S_h}{\Pi} + \frac{radhr}{\Pi}. \tag{3.4.17}$$

Noting that $\frac{Dp}{Dt} = \omega$ we get

$$\frac{D\theta}{Dt} = \frac{S_h}{\Pi} + \frac{radhr}{\Pi} \tag{3.4.18}$$

The temperature equation in terms of θ, assuming that the radiation scheme gives output in the correct units that do not require division by the specifit heat capacity with constant pressure, is

$$\frac{\overline{D\theta}}{Dt} = \frac{\overline{S_h}}{\Pi} - \left[\frac{\partial\overline{u'\theta'}}{\partial x} + \frac{\partial\overline{v'\theta'}}{\partial y} + \frac{\partial\overline{\dot{\sigma}'\theta'}}{\partial\sigma}\right] + \frac{\overline{radhr}}{\Pi}, \tag{3.4.19}$$

Rewriting in terms of temperature gives

$$\frac{D}{Dt}\left[T\left(\frac{\hat{p}}{p}\right)^{R_d/c_p}\right] = \frac{S_h}{\Pi} - \left[\frac{\partial\overline{u'\theta'}}{\partial x} + \frac{\partial\overline{v'\theta'}}{\partial y} + \frac{\partial\overline{\dot{\sigma}'\theta'}}{\partial\sigma}\right] + \frac{radhr}{\Pi}. \tag{3.4.20}$$

For simplicity the bars were left out of the mean terms until the last step. Using the product rule, we get

$$\left(\frac{\hat{p}}{p}\right)^{R_d/c_p}\frac{DT}{Dt} + T\hat{p}^{R_d/c_p}\frac{D}{Dt}\left(\frac{1}{p}\right)^{R_d/c_p} = \frac{S_h}{\Pi} - \left[\frac{\partial\overline{u'\theta'}}{\partial x} + \frac{\partial\overline{v'\theta'}}{\partial y} + \frac{\partial\overline{\dot{\sigma}'\theta'}}{\partial\sigma}\right] + \frac{radhr}{\Pi}. \tag{3.4.21}$$

Dividing by $\left(\frac{\hat{p}}{p}\right)^{R_d/c_p}$ and applying $\frac{D}{Dt}\left(\frac{1}{p}\right)^{R_d/c_p}$,

$$\frac{DT}{Dt} - \frac{p^{R_d/c_p}TR_d}{c_p}\left(\frac{1}{p}\right)^{R_d/c_p - 1}\frac{1}{p^2}\frac{Dp}{Dt} = S_h - \left(\frac{p}{\hat{p}}\right)^{R_d/c_p}\left[\frac{\partial\overline{u'\theta'}}{\partial x} + \frac{\partial\overline{v'\theta'}}{\partial y} + \frac{\partial\overline{\dot{\sigma}'\theta'}}{\partial\sigma}\right] + radhr \tag{3.4.22}$$

Noting that $\frac{Dp}{Dt} = \omega$ we get

$$\frac{\overline{DT}}{Dt} - \frac{\overline{R_d T \varpi}}{c_p \overline{p}} = \overline{S_h} - \left(\frac{p}{\hat{p}}\right)^{R_d/c_p} \left[\frac{\partial \overline{u'\theta'}}{\partial x} + \frac{\partial \overline{v'\theta'}}{\partial y} + \frac{\partial \overline{\dot{\sigma}'\theta'}}{\partial \sigma}\right] + \overline{radhr} \qquad (3.4.23)$$

3.4.1.3 The water continuity equations

The mean water continuity equation is

$$\frac{D\overline{q_x}}{Dt} = \overline{S_x} - \left[\frac{\partial \overline{u'q'_x}}{\partial x} + \frac{\partial \overline{v'q'_x}}{\partial y} + \frac{\partial \overline{\dot{\sigma}'q'_x}}{\partial \sigma}\right] x = v, c, i. \qquad (3.4.24)$$

3.4.1.4 The elliptic equation

Diffusion is also included in the elliptic equation.

$$\frac{\partial^2 \phi}{\partial x^2} + \frac{\partial^2 \phi}{\partial y} + \frac{\partial}{\partial \sigma}\left[s^2 \frac{\partial \phi}{\partial \sigma}\right] - 2\sigma \left[\frac{\partial \ln p_s}{\partial x}\left(\frac{\partial^2 \phi}{\partial x \partial \sigma}\right) + \frac{\partial \ln p_s}{\partial y}\left(\frac{\partial^2 \phi}{\partial y \partial \sigma}\right)\right]$$

$$+\frac{\partial}{\partial \sigma}\left(\sigma^2 \frac{\partial \phi}{\partial \sigma}\right)\left[\left(\frac{\partial \ln p_s}{\partial x}\right)^2 + \left(\frac{\partial \ln p_s}{\partial y}\right)^2\right] - \frac{\sigma}{p_s}\frac{\partial \phi}{\partial \sigma}\left[\left(\frac{\partial^2 p_s}{\partial x^2}\right) + \left(\frac{\partial^2 p}{\partial y^2}\right)\right] =$$

$$2\left(\frac{\partial u}{\partial x} + \frac{\partial v}{\partial y}\right)\frac{\partial}{\partial \sigma}\left(\frac{\Omega p}{p_s}\right) - \frac{2}{p_s}\left[\frac{\partial u}{\partial \sigma}\frac{\partial}{\partial x}(p\Omega) + \frac{\partial v}{\partial \sigma}\frac{\partial}{\partial y}(p\Omega)\right] + 2\left(\frac{\partial u}{\partial x}\frac{\partial v}{\partial y} - \frac{\partial v}{\partial x}\frac{\partial u}{\partial y}\right)$$

$$+2\sigma\left[\frac{\partial \ln p_s}{\partial x}\left(\frac{\partial u}{\partial y}\frac{\partial v}{\partial \sigma} - \frac{\partial v}{\partial y}\frac{\partial u}{\partial \sigma}\right) + \frac{\partial \ln p_s}{\partial y}\left(\frac{\partial v}{\partial x}\frac{\partial u}{\partial \sigma} - \frac{\partial u}{\partial x}\frac{\partial v}{\partial \sigma}\right)\right]$$

$$+\sigma f\left[\frac{\partial \ln p_s}{\partial y}\frac{\partial u}{\partial \sigma} - \frac{\partial \ln p_s}{\partial x}\frac{\partial v}{\partial \sigma}\right] + f\left(\frac{\partial v}{\partial x} - \frac{\partial u}{\partial y}\right) - u\frac{\partial f}{\partial y}$$

$$-\frac{\partial}{\partial \sigma}\left(sg - \frac{p}{p_s}\Omega^2 \frac{1}{\gamma}\right) - \frac{\partial}{\partial \sigma}\left(\frac{S_h p \Omega}{p_s T}\right) - \frac{\partial}{\partial \sigma}\left(\frac{p \Omega radhr}{p_s T}\right)$$

$$+\frac{\partial}{\partial \sigma}\left\{s\left[\frac{\partial \overline{u'w'}}{\partial x} + \frac{\partial \overline{v'w'}}{\partial y} + \frac{\partial \overline{w'\dot{\sigma}'}}{\partial \sigma}\right]\right\} - \frac{\partial}{\partial y}\left[\frac{\partial \overline{u'v'}}{\partial x} + \frac{\partial \overline{v'v'}}{\partial y} + \frac{\partial \overline{v'\dot{\sigma}'}}{\partial \sigma}\right]$$

$$-\frac{\partial}{\partial x}\left[\frac{\partial\overline{u'u'}}{\partial x}+\frac{\partial\overline{v'u'}}{\partial y}+\frac{\partial\overline{u'\dot{\sigma}'}}{\partial\sigma}\right]-\frac{\partial}{\partial\sigma}\left\{\frac{p\Omega}{p_sT}\left(\frac{p}{\hat{p}}\right)^{R_d/c_p}\left[\frac{\partial\overline{u'\theta'}}{\partial x}+\frac{\partial\overline{v'\theta'}}{\partial y}+\frac{\partial\overline{\dot{\sigma}'\theta'}}{\partial\sigma}\right]\right\} \tag{3.4.25}$$

Engelbrecht et al (2007) did not include the diffusion terms in the elliptic equation. Here the terms are added, for the elliptic equation to become fully consistent with the basic equations.

3.4.2 K-theory and conversion from geometic height to the σ-coordinate

3.4.2.1 K-Theory

When using K-theory the flux terms become

$$\frac{\partial\overline{u'u'}}{\partial x}+\frac{\partial\overline{u'v'}}{\partial y}+\frac{\partial\overline{u'\dot{\sigma}'}}{\partial\sigma}=-K_m\left(\frac{\partial^2\overline{u}}{\partial x^2}+\frac{\partial^2\overline{u}}{\partial y^2}\right)-\frac{\partial}{\partial\sigma}\left(K_{m\sigma}\frac{\partial\overline{u}}{\partial\sigma}\right) \tag{3.4.26}$$

$$\frac{\partial\overline{u'v'}}{\partial x}+\frac{\partial\overline{v'v'}}{\partial y}+\frac{\partial\overline{v'\dot{\sigma}'}}{\partial\sigma}=-K_m\left(\frac{\partial^2\overline{v}}{\partial x^2}+\frac{\partial^2\overline{v}}{\partial y^2}\right)-\frac{\partial}{\partial\sigma}\left(K_{m\sigma}\frac{\partial\overline{v}}{\partial\sigma}\right) \tag{3.4.27}$$

$$\frac{\partial\overline{u'w'}}{\partial x}+\frac{\partial\overline{v'w'}}{\partial y}+\frac{\partial\overline{w'\dot{\sigma}'}}{\partial\sigma}=-K_m\left(\frac{\partial^2\overline{w}}{\partial x^2}+\frac{\partial^2\overline{w}}{\partial y^2}\right)-\frac{\partial}{\partial\sigma}\left(K_{m\sigma}\frac{\partial\overline{w}}{\partial\sigma}\right) \tag{3.4.28}$$

$$\frac{\partial\overline{u'\theta'}}{\partial x}+\frac{\partial\overline{v'\theta'}}{\partial y}+\frac{\partial\overline{\dot{\sigma}'\theta'}}{\partial\sigma}=-K_h\left(\frac{\partial^2\overline{\theta}}{\partial x^2}+\frac{\partial^2\overline{\theta}}{\partial y^2}\right)-\frac{\partial}{\partial\sigma}\left(K_{h\sigma}\frac{\partial\overline{\theta}}{\partial\sigma}\right) \tag{3.4.29}$$

$$\frac{\partial\overline{u'q_x'}}{\partial x}+\frac{\partial\overline{v'q_x'}}{\partial y}+\frac{\partial\overline{\dot{\sigma}'q_x'}}{\partial\sigma}=-K_h\left(\frac{\partial^2\overline{q_x}}{\partial x^2}+\frac{\partial^2\overline{q_x}}{\partial y^2}\right)-\frac{\partial}{\partial\sigma}\left(K_{h\sigma}\frac{\partial\overline{q_x}}{\partial\sigma}\right) \tag{3.4.30}$$

For the convective bubble tests to be described later, diffusion is applied both in the horizontal and vertical, to be consistent with the simulations of Engelbrecht (2006) and Engelbrecht et al. (2007). For thunderstorm simulations, diffusion is only calculated in the vertical, with coefficients that depend on the gradient Richardson number as described in Chapter 2.

3.4.2.2 Conversion from height to σ

The constant or gradient Richardson number dependent coefficients are first stated in height coordinates, and then converted to σ-coordinates for use in the NSM. Using potential temperature (θ) as an example and considering only the local change because of turbulence, the conversion is achieved as follows:

$$\frac{\partial\bar{\theta}}{\partial t} = -\frac{1}{\bar{\rho}}\frac{\partial\left(\bar{\rho}\overline{w'\theta'}\right)}{\partial z}, \tag{3.4.31}$$

Noting that $\sigma = \frac{p-p_T}{p_s}$, it follows that

$$\frac{\partial\bar{\theta}}{\partial t} = \frac{g}{p_s}\frac{\partial\left(\bar{\rho}\overline{w'\theta'}\right)}{\partial\sigma}. \tag{3.4.32}$$

Noting that $w = -\frac{\omega RT}{gp} = -\frac{\omega}{g\rho}$, it follows that

$$\overline{\dot{\sigma}'\theta'} = -g\frac{\rho\overline{w'\theta'}}{p_s}, \tag{3.4.33}$$

$$K_{h\sigma}\frac{\partial\bar{\theta}}{\partial\sigma} = -g\frac{\bar{\rho}}{p_s}\left(K_{hz}\frac{\partial\bar{\theta}}{\partial z}\right), \tag{3.4.34}$$

$$K_{h\sigma} = -g\frac{\bar{\rho}}{p_s}\left(K_{hz}\left(\frac{\partial\bar{\theta}}{\partial\sigma}\left[\frac{\partial z}{\partial\sigma}\right]^{-1}\right)\right)\left(\frac{\partial\bar{\theta}}{\partial\sigma}\right)^{-1}, \tag{3.4.35}$$

$$K_{h\sigma} = -g\frac{\bar{\rho}}{p_s}\left(K_{hz}\frac{\partial\bar{\theta}}{\partial z}\right)\frac{\partial\sigma}{\partial\bar{\theta}}, \tag{3.4.36}$$

$$K_{h\sigma} = -g\frac{\bar{\rho}}{p_s}\left(K_{hz}\left(\frac{\partial\bar{\theta}}{\partial\sigma}\left[\frac{1}{g}\frac{\partial\phi}{\partial\sigma}\right]^{-1}\right)\right)\left(\frac{\partial\bar{\theta}}{\partial\sigma}\right)^{-1}, \tag{3.4.37}$$

$$K_{h\sigma} = -g\frac{\overline{\rho}}{p_s}\left(K_{hz}\left(\left[\frac{1}{g}\frac{\partial\phi}{\partial\sigma}\right]^{-1}\right)\right), \tag{3.4.38}$$

$$K_{h\sigma} = -g^2\frac{\overline{\rho}}{p_s}\left(\frac{\partial\phi}{\partial\sigma}\right)^{-1}K_{hz}, \tag{3.4.39}$$

$$K_{h\sigma} = -g^2\frac{\overline{p}}{p_sRT}\left(\frac{\partial\phi}{\partial\sigma}\right)^{-1}K_{hz}. \tag{3.4.40}$$

3.4.3 Surface Fluxes

The surface fluxes of momentum, heat, and water vapour are given by

$$\overline{(w'u')}_0 = -C_M|V_1|u_1, \tag{3.4.41}$$

$$\overline{(w'v')}_0 = -C_M|V_1|v_1, \tag{3.4.42}$$

$$\overline{(w'\theta')}_0 = C_H|V_1|\left(\theta_0 - \theta_1\right), \tag{3.4.43}$$

$$\overline{(w'q')}_0 = D_wC_H|V_1|\left(q_{v0} - q_{v1}\right). \tag{3.4.44}$$

The subscripts 0 and 1 refer to values at the surface and the lowest model level respectively. D_w represents the availability of water at the surface and is given a value of 1 in this study, indicating that the relevant simulations are performed over the ocean. q_{v0} is the saturation value of q_{v1} at potential temperature θ_0 (Holtslag and Boville, 1993; Emanuel, 1993).

The surface layer exchange coefficients are calculated as discussed in Holtslag and Boville (1993) given as

$$C_M = C_Nf_M\left(Ri_0\right), \tag{3.4.45}$$

$$C_H = C_Nf_H\left(Ri_0\right). \tag{3.4.46}$$

The neutral exchange coefficient is

$$C_N = \frac{k^2}{ln\left(\left(z_1 + z_{0M}\right)/z_{0M}\right) ln\left(\left(z_1 + z_{0M}\right)/z_{0M}\right)}, \tag{3.4.47}$$

where z_1 is the height of the lowest model level, and z_{0M} is the roughness length for momentum. The roughness length for momentum, heat and constituents are assumed to be the same and have a value of 10^{-4}m in this study (representing conditions over the ocean).

The surface layer gradient Richardson number is defined as

$$Ri_0 = \frac{gz_1\left(\theta_{v1} - \theta_{v0}\right)}{\theta_1 |V_1|^2}. \tag{3.4.48}$$

Under unstable conditions ($Ri_0 < 0$) the functions are given by

$$f_M\left(Ri_0\right) = 1 - \frac{10Ri_0}{1 + 75C_N\left\{\left[\left(z_1 + z_{0M}\right)/z_{0M}\right]|Ri_0|\right\}^{1/2}} \tag{3.4.49}$$

$$f_H\left(Ri_0\right) = 1 - \frac{15Ri_0}{1 + 75C_N\left\{\left[\left(z_1 + z_{0M}\right)/z_{0M}\right]|Ri_0|\right\}^{1/2}} \tag{3.4.50}$$

Under stable conditions ($Ri_0 \geq 0$) the functions are

$$f_M\left(Ri_0\right) = f_H\left(Ri_0\right) = \frac{1}{1 + 10Ri_0\left(1 + 8Ri_0\right)} \tag{3.4.51}$$

3.5 The numerical technique used in the NSM

Engelbrecht (2006) and Engelbrecht et al. (2007) derived the nonhydrostatic σ-coordinate equation set equivalent to the pressure coordinate equation set of White (1989) as discussed in section 3.1, and continued to develop an adiabatic kernel for a new mesoscale model based on these equations. This dynamical kernel employs a split semi-Langragian approach to solve the quasi-elastic σ-coordinate equations. That is, for numerical solution, the equations are split into an advective and non-advective part. The slow advection process is treated during a semi-Langragian advection step that may employ a large time step (McDonald, 1984; McGregor, 1993). Hereafter the remaining terms, which describe the fast moving waves, are treated explicitly during an adjustment phase that employes a smaller time step. The microphysics parameterisations are solved in the adjustment stage, while the diffusion scheme is applied during the advection step. The numerical scheme is formulated on a nonstaggered grid to avoid the calculation of two sets of departure points in the semi-Lagrangian scheme (Engelbrecht et al., 2007). It is necessary to apply the Shapiro filter on the nonstaggered grid, in order to filter the two-grid interval waves.

Finite-difference methods are numerical methods for approximating the solutions to differential equations, using finite differences to approximate derivatives. Accuracy, stability, simplicity and computational economy are all important considerations in the design of finite difference schemes. The stability of numerical schemes is closely associated with numerical error. A finite difference numerical scheme is stable if the errors made at one time step of the calculation do not cause the errors to increase as the computations continue (Mesinger and Arakawa, 1976; Randall, 2004). To allow the use of a bigger time step in numerical schemes, whilst maintaining stability, a number of methods have been devised.

The splitting method allows for a complex system of equations to be split into a number of simpler subsystems, which are then solved consecutively one at a time (Bates, 1984; Gadd 1978). If the schemes chosen for the solution of subsystems are stable, the combined scheme constructed by the splitting method will also be stable. Different time steps can be used for different subsystems so that a long timestep can be applied for slow processes, and a number of smaller steps used to calculate faster processes. The advantage of a splitting technique is that it enables different numerical methods to be applied to different terms or groups of terms in the governing equations (Gadd, 1978). In atmospheric models the complex system is usually split into the advection, adjustment and turbulence subsystems (Mesinger and Arakawa, 1976). The disadvantage of the method is that calculation of the effects of different physical factors one at a time usually leads to an increase in the truncation error (Gadd, 1978).

Implicit schemes are stable for any choice of the time step, as far as the treatment of fast-moving waves are concerned In a semi-implicit time-differencing scheme, terms giving rise to the high frequency motions are treated implicitly while the remaining terms are treated explicitly. The limitations on the size of the time step is then imposed mainly by the CFL condition for advection in regions of strong wind. Forecasts made for large-scale flow features with explicit differencing and time step of 1 min were found to be almost identical to those made with semi-implicit differencing and time step of 60 min (Mesinger and Arakawa, 1976). A possible disadvantage of semi-implicit schemes is the damping of fast moving waves, for cases where these waves carry an important amount of energy.

Lagrangian advection schemes preserve the probability density function of the advection variable, they are monotone and positive definite and they can employ a very long timestep without triggering computational instability (Staniforth and Cote, 1991). A disadvantage is that a regularly spaced set of particles will evolve to a highly irregular spaced set at later times. Semi-Langragian schemes permit large advection time-steps while using the regular resolution of Eulerian schemes (Staniforth and Cote, 1991). The semi-Langragian approach for solving the advection terms consists of two steps: the calculation of the departure point at each grid point in the model, and secondly, the evaluation of variables at the departure point by means of spatial interpolation (Bates and McDonalds, 1982; Chen and Bates, 1996; Kuo and Williamns, 1990; McGregor, 1993). Robert et al. (1985) found that the time step could be increased by a further factor of 6 with semi-lagrangian semi-implicit scheme over that of an Eulerian semi-implicit scheme. The scheme used in our study was developed by McGregor (1993) and it avoids both interpolation and iteration for determining the departure points of trajectories and has been found to achieve a high degree of accuracy.

3.6 Summary

In this chapter an extended NSM equation set, that includes moisture and radiation was derived. Heating or cooling by microphysics and radiation processes were added to the thermodynamic equation. These processes also require new terms to be introduced to the elliptic equation. Two BMP schemes were obtained from the WRF model and introduced to the NSM. The first scheme is single-moment, was developed by Chen and Sun (2002) and is called the PURDUE-LIN scheme. It is based on conventional schemes of Lin et al. (1983) and Rutledge and Hobbs (1983). The scheme assumes that precipitating particles follow a gamma distribution and predicts the mixing ratios of all the water species. Cloud water and ice are assumed to be monodispersed and to have a negligible terminal speed.

The second scheme, the SBU-YLIN scheme was developed by Lin and Colle (2011) using the PURDUE-LIN scheme as a starting point. In the new scheme, snow and graupel share the same category and the number of microphysics schemes were reduced from 40 to less than 20. The cloud water is assumed to follow a generalised exponential distribution and cloud ice has a fallspeed. The precipitating ice particles are calculated with consideration of the influence of riming intensity and temperature on the projected area, mass, and fall velocity of the particles. The first order closure scheme was discussed in reference to the σ-coordinate used in the NSM. The diffusion scheme was improved to include the mechanical and thermal general of turbulence. Diffusion was also included in the elliptic equation for it to be more consistent with the basic equations used in the model. The numerical techniques used to solve the NSM equation set were also discussed.

Chapter 4

Numerical Experiments: Convective bubbles and an Isolated Thunderstorm

4.1 Introduction

In this study two microphysics schemes have been added to a two-dimensional (2-D) dynamical core of the Nonhydrostatic σ-coordinate Model (NSM) for the explicit simulation of clouds, and the local diffusion scheme has been improved to make the model's treatment of turbulence more realistic. The two microphysics schemes were obtained from the National Center for Atmospheric Research (NCAR) Weather Research and Forecasting (WRF) model (Skamarock et al. 2005). The first scheme (known as PURDUE-LIN) was developed by Chen and Sun (2002) at Purdue University and it is based on conventional schemes of Lin et al. (1983) and Rutledge and Hobbs (1983). The second scheme was developed at the Stony Brook University (SBU-YLIN scheme) using the PURDUE-LIN scheme as a starting point (Lin and Colle, 2011) (see chapter 3 for a more comprehensive description of the two schemes).

Engelbrecht et al. (2007) used a first order local diffusion scheme with constant coefficients. Because turbulence varies with height, bouyancy and shear, a scheme that calculates the diffusion coefficients based on the gradient Richardson number has been introduced (Louis, 1979; Holtslag and Boville, 1993). For a thunderstorm simulation presented in this Chapter, a sponge layer was introduced from 17 km above sea level. The NSM code of Engelbrecht (2006) and Engelbrecht et al. (2007) was written in fortran 77. The code was reorganised into modules and subroutines and written in fortran 90, because a code written in modular form is easier to control and add microphysics modules.

Engelbrecht et al. (2007) showed that the model is stable by simulating dry convective bubbles. In the first part of this chapter the convective bubble simulations by Engelbrecht et al. (2007) are repeated, to show that the reorganising of the code did not introduce errors to the model. The effects of the diffusion scheme, applied with different coefficients, are also discussed.

Simulations with the two microphysics schemes are compared to study the effects of microphysics processes on a thunderstorm simulation. Two sets of simulations are made with the PURDUE-LIN scheme, one with graupel (called PURDUE-LIN1 from now) and the other without graupel (PURDUE-LIN2). A thunderstorm is initiated by introducing a warm perturbation to a reference profile first used by Weisman and Klemp (1982). This experiment is thought to represent the development of isolated thunderstorms that form in the absence of strong synoptic forcing. The effects of shear and resolution on the thunderstorm simulations will also be discussed.

4.2 Warm Dry Bubbles

Turbulence is a physical process in the atmosphere that is very effective in mixing momentum, heat and moisture in the atmosphere. Turbulence works to remove instabilities and it also induces entrainment, which modifies microphysics and dynamical properties of clouds. Instabilities in clouds can exist because of radiative cooling and heating, or latent heat absorption and release, which all cause changes in cloud temperatures.

Engelbrecht et al. (2007) used K-theory with constant diffusion coefficients everywhere in the domain, and for the whole duration on the simulations, in order to represent turbulence in the model. K-Theory is a traditional way of parameterising diffusion, which assumes that the flux of a variable is proportional to the gradient of the mean of the variable. In this study a physically more realistic scheme, which calculates coefficients based on the gradient Richardson number

(Louis, 1979; Holtslag and Boville, 1993), has been introduced. Engelbrecht et al. (2007) did not include diffusion terms in the elliptic equation, but here the elliptic equation is derived to be fully consistent with the basic equations including diffusion terms.

Warm and cold bubble tests are usually performed in the development of non-hydrostatic atmospheric models to investigate the stability, accuracy and efficiency of the numerical integration scheme. A cold bubble is expected to induce a density current and to sink, forming a gust front at the surface, whilst a warm thermal is expected to rise for as long as it maintains its positive buoyancy. Warm bubble simulations are discussed in the following two subsections.

4.2.1 Constant K

Engelbrecht et al. (2007) tested the NSM with the Janjic et al. (2001) warm bubble, which is defined as a potential temperature perturbation of $\theta' = 6.6cos^2\left(\frac{\pi L}{2}\right)$ in an isentropic environment. Here

$$L = \sqrt{\left(\frac{x - x_c}{x_r}\right)^2 + \left(\frac{z - z_c}{z_r}\right)}, \tag{4.2.1}$$

with $x_c = 10.0\ km$, $z_c = 2.75\ km$, and $x_r = z_r = 2.5\ km$.

A similar simulation is performed in this study. The model top is located at 13.5 km above sea level, with a horizontal resolution of 100 m and a streched vertical resolution of about 60 m at the surface and 230 m at the top of the domain. An isentropic atmosphere with a background potential temperature of 300 K is used. Diffusion is applied with constant coefficients along the x-axis of $K_s = 300m^2s^{-1}$and $K_{\theta s} = 50m^2s^{-1}$. Similar magnitudes of explicit diffusion are applied in the vertical, and the coefficients are converted from geometric height to σ coordinates. An advection timestep of 1 s and an adjustment timestep of 0.1 s are used.

The simulation depected in panels a and b are for the same settings of that of Engelbrecht et al. (2007). The simulation resembles one made by Engelbrecht et al. (2007). The warm bubble ascends because it is less dense than its environment (Figure 4.2.1a). Two symmetrical vortices develop on each side of the symmetry axis. Three strong updraft areas are visible at t=900 s, because of the

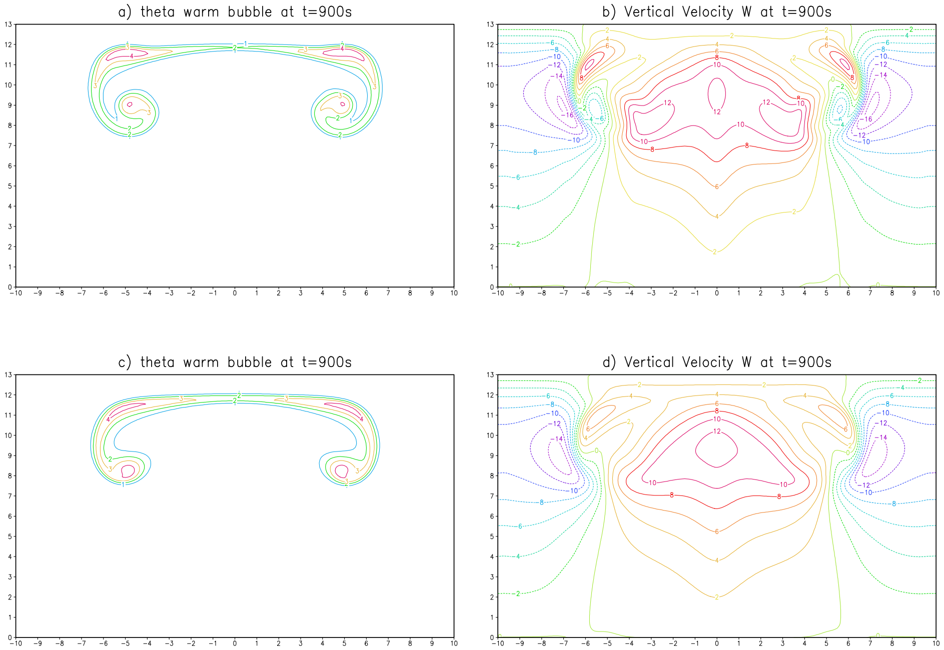

Figure 4.2.1: a) Potential temperature and b) vertical velocity after 900 s of simulation of the Janjic warm bubble, with settings similar to those of Engelbrecht et al. (2007) .c) Potential temperature and d) vertical velocity of the warm bubble simulation after 900 s of simulation, with diffusion in the elliptic equation included. The x-axis is horizontal distance and the y-axis is vertical distance in km.

initial perturbation which was in centre of the domain, and two vortices of high potential temperature on both sides of the bubble (Figure 4.2.1b). The close correspondence of the simulated bubble and that of Engelbrecht et al. (2007) show that the code was reorganised into modules and fortran 90 successfully.

A second simulation [represented by panels a and c] was made with diffusion terms included in the elliptic equation. The bubble (Figure 4.2.1c) is slightly more diffused compared to the case where diffusion terms are not included in the elliptic equation (Figure 4.2.1a). There is one well developed updraft in the centre of the domain (Figure 4.2.1d), with a single maximum, whilst the three maxima were present in the case where no diffusion is applied to the elliptic equation. This result is to be expected, because by applying diffusion to the elliptic equation, more diffusion is applied to the bubble. For all the subsequent simulations presented in this study, the elliptic equation that includes the effects of diffusion is solved.

4.2.2 Richardson based K

Warm bubble simulations were made using vertical diffusion coefficients that vary with height, buoyancy and shear (i.e. based on the gradient Richardson number (Louis, 1979)), with the same constant horizontal diffusion coefficients used in Engelbrecht et al. (2007). This scheme allows the eddy diffusivity to change with height, so that bigger coefficients are found closer to the surface, and increase with increased buoyancy and shear. This scheme is an improvement over the original scheme used in the model, which employed constant values of the coefficients throughout the domain and simulation time.

The simulation was performed with diffusion in the elliptic equation activated. Three updraft cores (Figure 4.2.2c) are visible in the run, which indicate that the simulation is less diffused compared to the case of constant K diffusion coefficients. This is visible also in the potential temperature simulation (Figure 4.2.2a). The values of the coefficients (Figure 4.2.2d) differ across the domain with higher values closer to the surface, in areas of strong shear (Figure 4.2.2b) and of high buoyancy.

All the experiments conducted in this study were performed using double precision. An experiment was performed to illustrate the effects of using single precision to perform the simulations. When using single precision without supplying diffusion, high levels of desymmetry are visible (Figure 4.2.3 c) compared

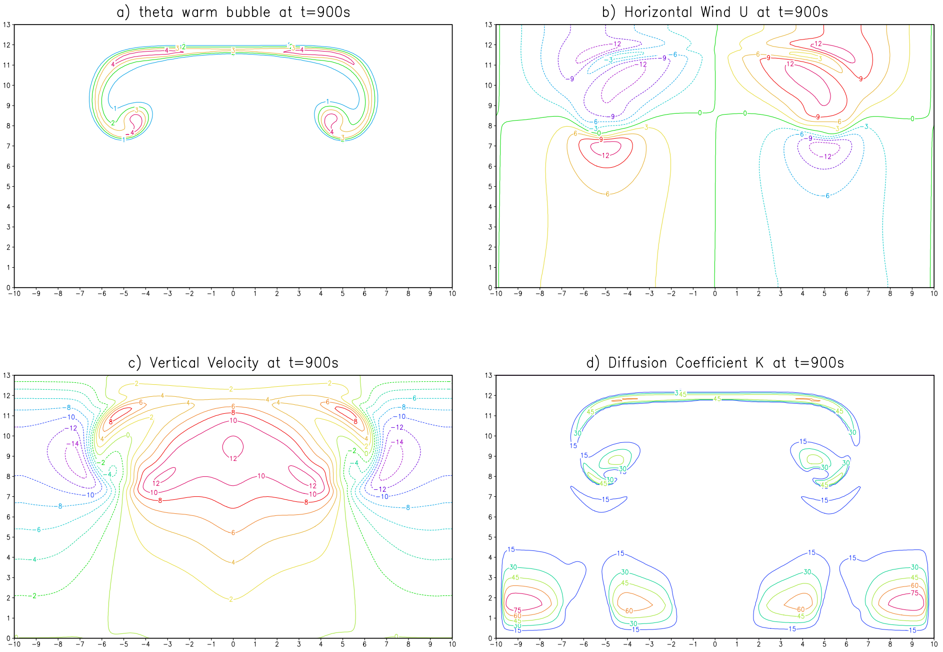

Figure 4.2.2: a) Potential temperature, b) horizontal wind, c) vertical velocity and d) eddy diffusivity coefficient after 900 s of simulation, using the Richardson number based, local first-order diffusion scheme. The x-axis represents horizontal distance, and the y-axis represent vertical distance in km.

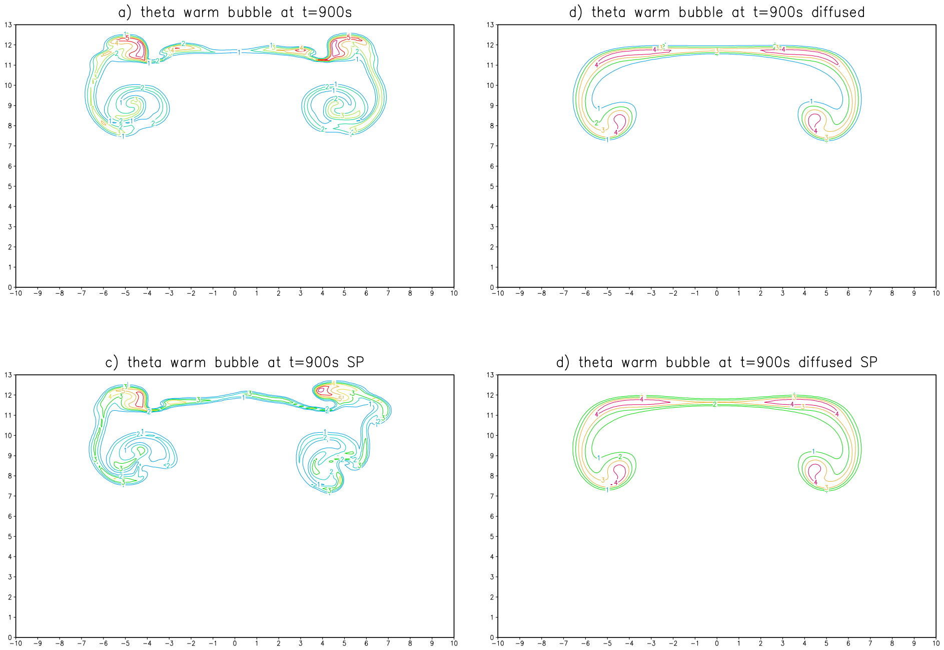

Figure 4.2.3: Potential temperature after 900 s of simulation: a) without diffusion but with double precision. b) with diffusion and with double precision, c) without diffusion and with single precision. d) with diffusion and with single precision. The x-axis represents horizontal distance, and the y-axis represent vertical distance in km.

to the double precision run with no diffusion (Figure 4.2.3 a). The desymmetry is increased when a bigger time step is used (not shown).

When diffusion is applied to the runs with single and double precision, respectively, the simulations look very similar (Figure 4.2.3b and Figure 4.2.3d). This suggests that for operational forecasting or climate simulation the use of double or single precision will not have a huge impact on the simulations, because for real atmospheric simulations, diffusion should always be applied - turbulence is a physical process. Graphical Processing Units (GPUs) are said to function best with single precision (Farber, 2012) It is however preferred that where possible, double precision be applied because it is more accurate. Double precision also has the advantage of saving computer time because, the elliptic equation converges sooner compared to when single precision is used.

For the vertical wind simulations, wave features are visible along the surface boundaries. When a bigger time step is applied, the waves become even more visible. These waves are thought to exist due to the unstaggered grid that is applied in this study. The unstaggered grid is known to have poor gravity wave dispersion characteristics. The waves are filtered using the Shapiro filter, however, the filter does not remove all of these waves. Applying a stronger filter, or using a stricter tollerance factor in the elliptic equation, reduces the waves significantly.

4.3 A Thunderstorm

Thunderstorms over South Africa are usually embedded within cloud bands and are strongly controlled by the large-scale circulation (Tyson and Prestorn-Whyte, 2000). Isolated thunderstorms that are less dependent on mesoscale and synoptic-scale features also form often. In this section a thunderstorm based on the profile of Weisman and Klemp (1982) that represent the latter is discussed. A domain that is 100 km in horizontal extent and that extends to about 25 km above sea level is used. The vertical resolution is stretched so that higher resolution is obtained closer to the surface and lower resolution is used towards the top of the domain with an average resolution of 200 m.

The environmental potential temperature and relative humidity profiles are given by

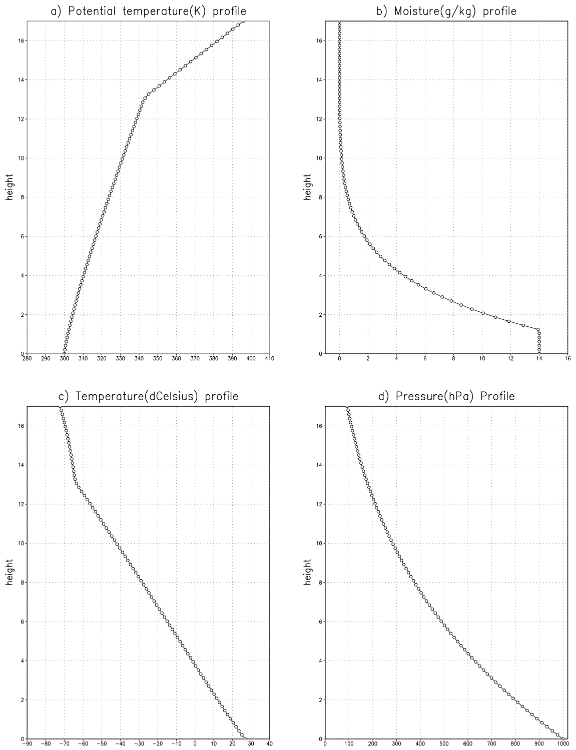

a) Potential temperature(K) profile

b) Moisture(g/kg) profile

c) Temperature(dCelsius) profile

d) Pressure(hPa) Profile

Figure 4.3.1: The a)potential temperature, b) moisture, c) temperature and d) pressure profiles that are equivalent to those of Weiman and Klemp (1982) used in the initial conditions.

$$\overline{\theta}\left(z\right)=\theta_0+\left(\theta_{tr}-\theta_0\right)\left(\frac{z}{z_{tr}}\right)^{5/4},z\leqslant z_{tr} \tag{4.3.1}$$

$$\overline{\theta}\left(z\right)=\theta_{tr}exp\left[\frac{g}{c_pT_{tr}}\left(z-z_{tr}\right)\right],z>z_{tr} \tag{4.3.2}$$

$$H\left(z\right)=1-\frac{3}{4}\left(\frac{z}{z_{tr}}\right)^{5/4},z\leq z_{tr} \tag{4.3.3}$$

$$H\left(z\right)=0.25,z>z_{tr} \tag{4.3.4}$$

where $z_{tr}=12\ km$, $\theta_{tr}=343\ K$, $T_{tr}=213\ K$ and $\theta_0=300\ K$. The mixing ratio of water vapour is kept constant at a maximum value of $q_{v0}=0.014$ near the surface to represent a fairly well mixed boundary layer, also with a close to constant potential temperature (Fig 4.3.1). A thermal perturbation with a 10 km horizontal radius and a 1400 m vertical radius is introduced at the centre of the domain. A temperature excess of 2^0C is specified at the center of the thermal and decreases gradually to 0^0C at its edge which initiates convection. The model was allowed to run for two hours with different microphysics, horizontal resolutions and with and without shear. Diffusion is applied only in the vertical with coefficients that depend on the gradient Richardson number. Surface fluxes are not calculated nor prescribed and therefore the water that leaves the atmosphere is not returned in anyway.

To prevent outward-propagating disturbances from reflecting back into the domain when they encounter the upper boundary, a wave absorbing layer is placed at the edge of the domain. The sponge layer is applied from 17 km above sea-level, because for the sponge to be effective it has to be applied over a thick layer. The sponge layer uses vertical $\alpha\left(z\right)\frac{\partial^2u}{\partial\sigma^2}$ and horizontal diffusion, $\alpha\left(z\right)\frac{\partial^2u}{\partial x^2}$ of the horizontal wind with a vertically varying viscosity $\alpha\left(\sigma\right)$ (Durran, 1999; Janjic et al., 2001). When this layer is not applied in the current thunderstorm simulation, the model becomes unstable because of unrealistic high velocities associated with waves that are reflected at the model top back into the domain.

4.3.1 The effect of the microphysics scheme

Two hour simulations are made with a horizontal resolution of 500 m with 100 km big domain. The PURDUE-LIN scheme is used with graupel included in the simulation (PURDUE-LIN1) and without graupel (PURDUE-LIN2) to study the effects of graupel on thunderstorms. The combined simulations of PURDUE-LIN1 and PURDUE-LIN2 are referred to as PURDUE-LIN simulations in this thesis. The simulations are also made with the SBU-YLIN scheme. In the SBU-YLIN scheme, snow and graupel share a category and will be referred to as precipitating ice in this thesis.

The first updraft peaks associated with the cell triggered by the warm perturbation occur at the same time in all the simulations using the three microphysics schemes (Figure 4.3.2 a, c and e) and Fig 4.3.3 a. The maxima updraft lines for the three runs in the horizontal and vertical are on top of one another in the first 40 minutes of the simulation (Figure 4.3.3a). The first maximum updraft peak is immediately followed by smaller peaks in all three simulations which unlike the first updraft are different. The differences beyond 40 minutes are because of the varying hydrometeor simulations by the three microphysics schemes that affect the cloud dynamics. At about 100 minutes, the two simulations with the PURDUE-LIN scheme simulate a second cell associated with big updrafts which do not extend as high in altitude as those associated with the first cell (Figures 4.3.2 a and b) while the SBU-YLIN scheme (Figure 4.3.2c) simulates a much smaller new cell and a bit later compared to the PURDUE-LIN simulations.

The downdrafts' behaviour is similar to that of the updrafts (Figure 4.3.3 b) which suggests that downdrafts develop in response to the updrafts. The downdraft peaks are smaller compared to the updraft. According to our simulations, the bigger the updraft, the bigger the downdraft. Downdrafts start developing even when there is very little falling hydrometeors. This is in line with the findings of Lin and Orville (1969) that downdrafts form even in nonprecipitating thunderstorms. Observational studies have shown that on each side of the convective updraft is a downdraft that is forced by the downward pressure perturbation force found on either side of buoyant element (Houze, 1993)

Our results suggest that the second cell is triggered by the cold pool that results when downdrafts reach the surface. Figure 4.3.2 b, d and f show the maximum absolute value of the horizontal wind for the three microphysics schemes/settings. The PURDUE-LIN1 simulation produced the strongest hor-

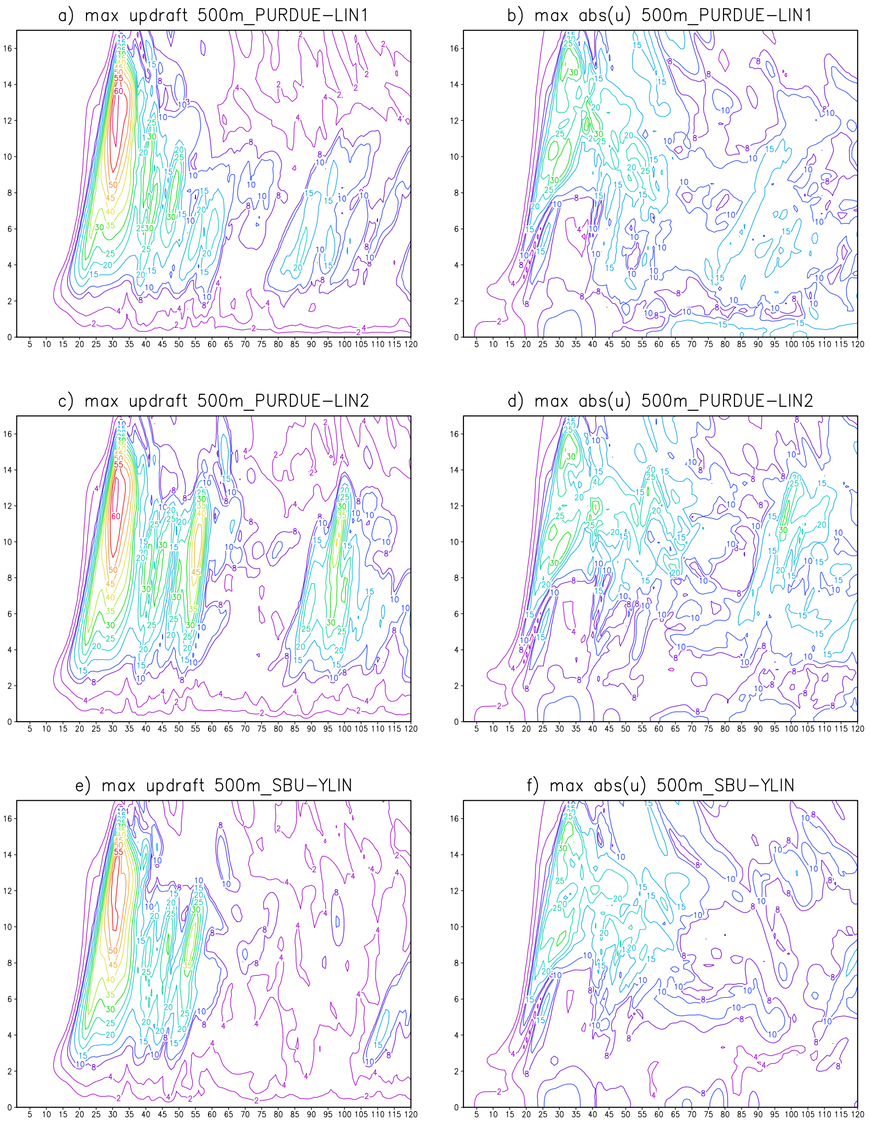

Figure 4.3.2: a) Updraft and b) absolute horizontal wind maxima with the PURDUE-LIN1 scheme, c) updraft and d) absolute horizontal wind maxima with the PURDUE LIN2 scheme e) Updraft and f) absolute horizontal wind maxima with the SBU-YLIN microphysics scheme. The x-axis is time in minutes while the y-axis is height in km. The updrafts and downdrafts are in m/s.

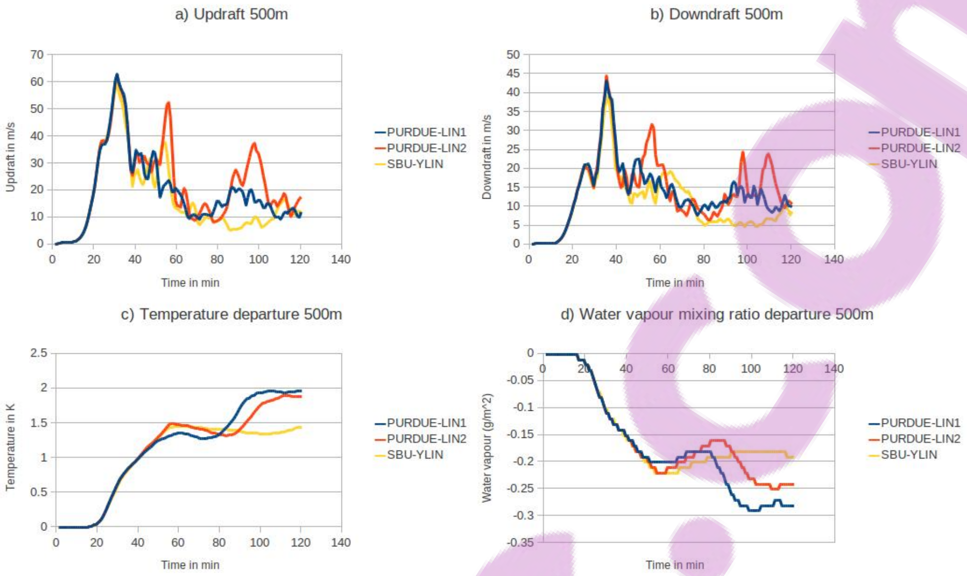

Figure 4.3.3: a) The updraft, b) downdraft, c) Temperature departure and d) water vapour density departure over the two hour simulation. A resolution of 500 m was used.

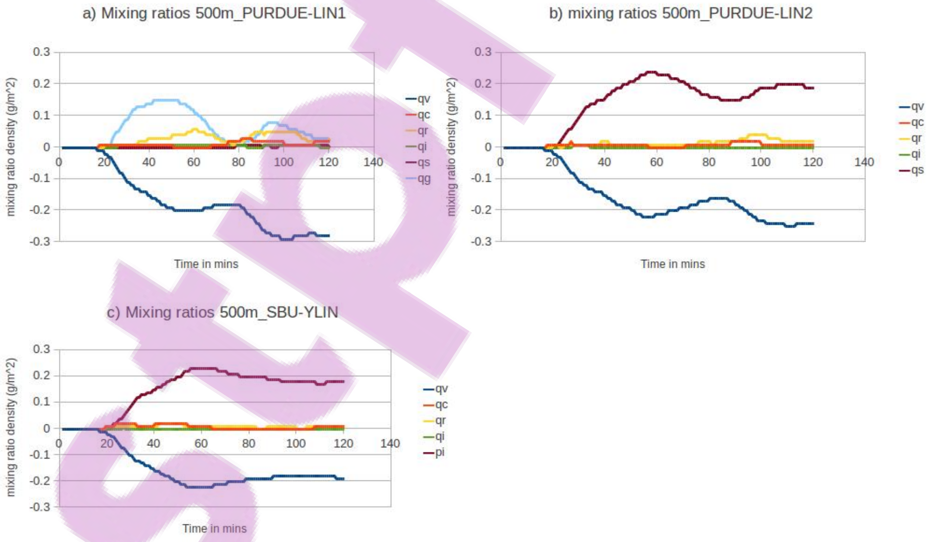

Figure 4.3.4: The change in mixing ratio with the a) PURDUE-LIN b) PURDUE-LIN with no graupel and c) SBU-YLIN microphysics scheme. A resolution of 500 m was used.

izontal wind from about 64 minutes along the surface which is at the time that the downdraft reached the surface and caused a cold pool. The horizontal winds are smaller in the PURDUE-LIN2 simulation, and even smaller in the SBU-YLIN simulation.

The area averaged temperature (Figure 4.3.3 c) starts to increase in all three simulations as soon as water vapour (Figure 4.3.3 d) starts decreasing in the model, to form hydrometeors. This is expected because as the water vapour is converted to form droplets and ice particles, latent heat is released warming up the atmosphere. The simulation with the SBU-YLIN scheme warms up the least, and the least amount of water vapour is converted to hydrometeors. The results seem physical because with less water vapour converted to hydrometeors, less latent heat is released. The PURDUE-LIN1 simulation converted more water vapour and warmed up more than the other two simulations.

At the beginning of the simulation, water vapour was provided and the hydrometeors were set to zero. When the hydrometeors start forming, the amount of water vapour starts to decrease, because it is converted to hydrometeors and this is shown by negative values in Figures 4.3.5a, 4.3.6a and 4.3.7a. In the PURDUE-LIN simulations the first cell is associated with more cloud ice (Figures 4.3.5d and 4.3.6d), while the second cell towards the end of the simulation is associated with more cloud water (Figures 4.3.5 b and 4.3.6 b). This is because the first cell is associated with stronger updrafts and therefore able to transport moisture to the high altitude cold regions were ice forms. The second cell was weaker and shallower and therefore its impacts are felt more in the lower troposphere, where more cloud water forms. The first cell is associated with more cloud ice also in the SBU-YLIN scheme simulations (Figure 4.3.7). The second cell which is very small and is associated with some cloud water.

The simulated cloud water with the SBU-YLIN microphysics scheme (Figure 4.3.7 b) associated with the first cell is more than in the simulations employing the PURDUE-LIN scheme (Figure 4.3.5b and 4.3.6b). This is because the treatment of ice and cloud water is different in the SBU-YLIN scheme. Lin and Colle (2011) showed that the SBU-YLIN scheme reduces the cloud water underprediction by single-moment schemes based on Rutledge and Hobbs (1983) and Lin et al. (1983) BMP schemes. The single-moment scheme also tend to overpredict snow aloft which Lin and Colle (2011) showed is no longer a problem in the SBU-YLIN scheme.

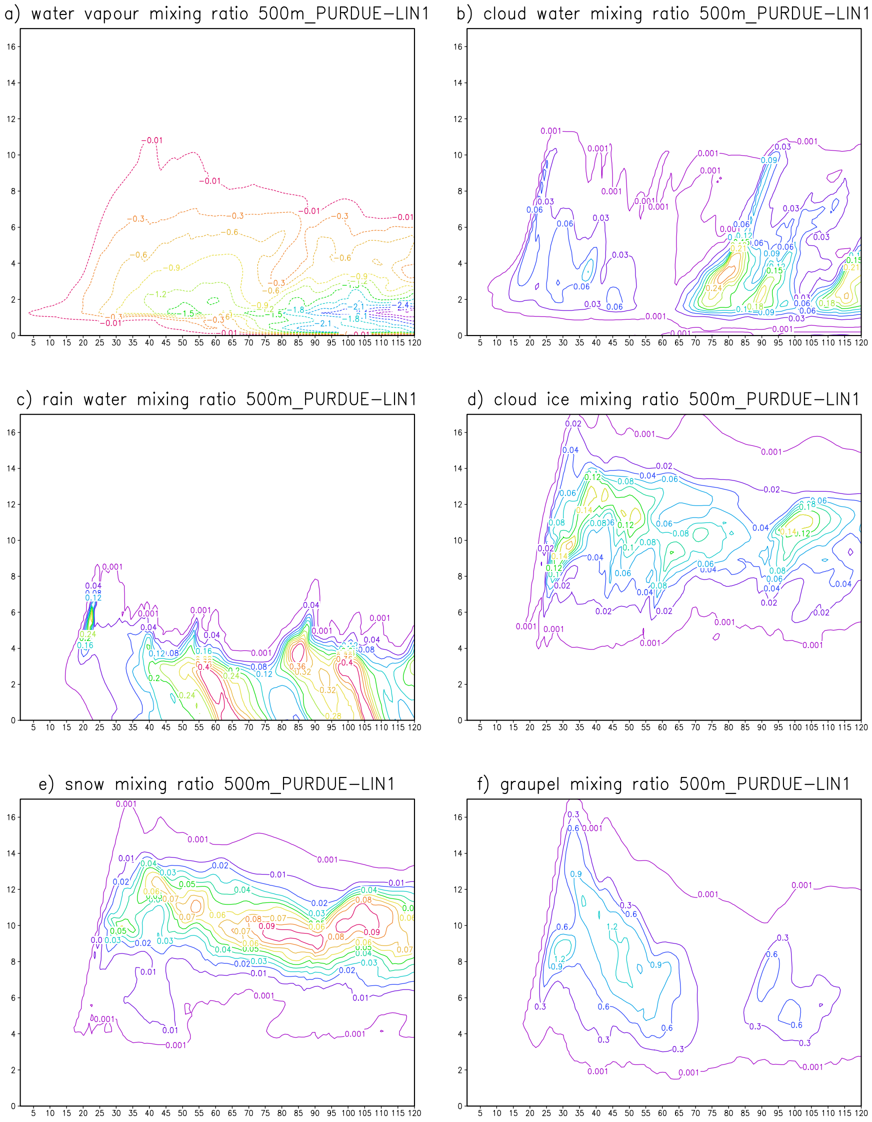

Figure 4.3.5: a) The horizontally domain averaged water vapour mixing ratio, b) the cloud water, c) rain water, d) cloud ice, e) snow, and f) graupel mixing ratios minus the initial conditions over the two hour simulation with the PURDUE-LIN1 scheme. A resolution of 500$m$was used.

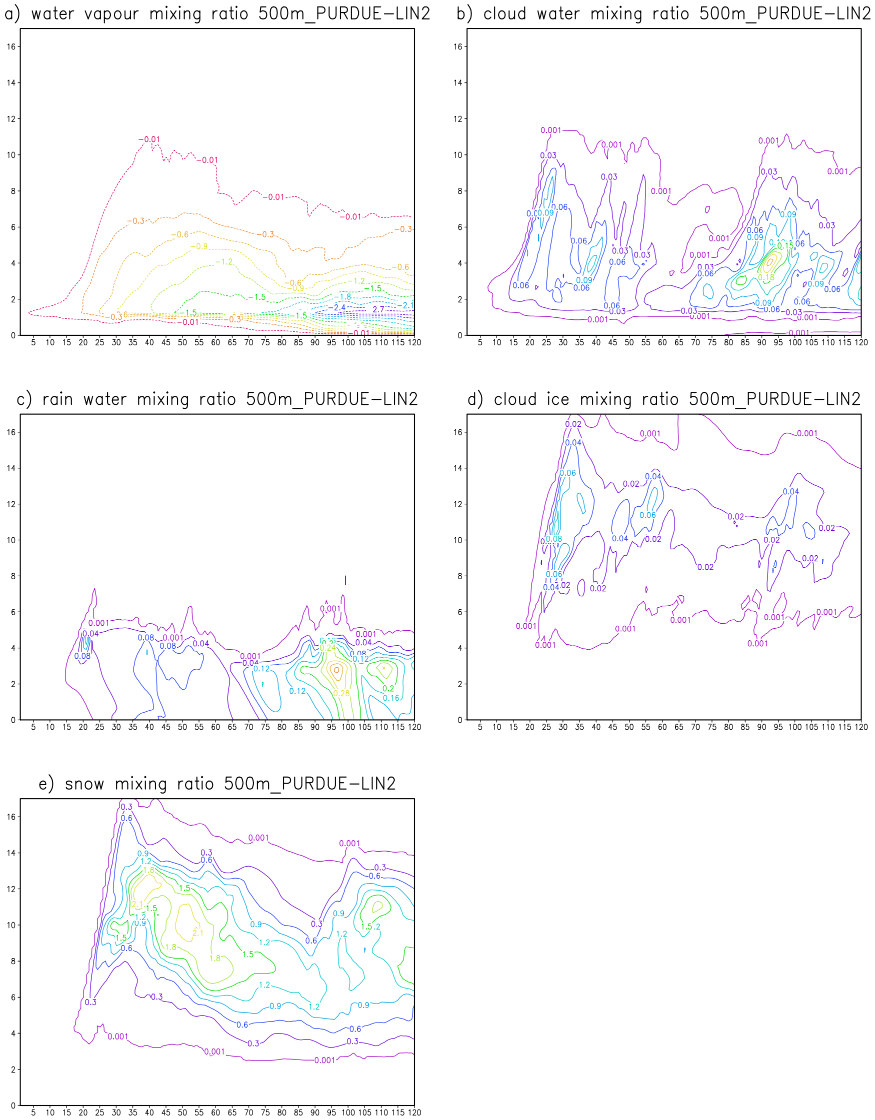

Figure 4.3.6: a) The change in water vapour mixing ratio, b) the cloud water, c) rain water, d) cloud ice, e) snow mixing ratios over the two hour simulation with the PURDUE-LIN2 scheme. A resolution of 500$m$was used.

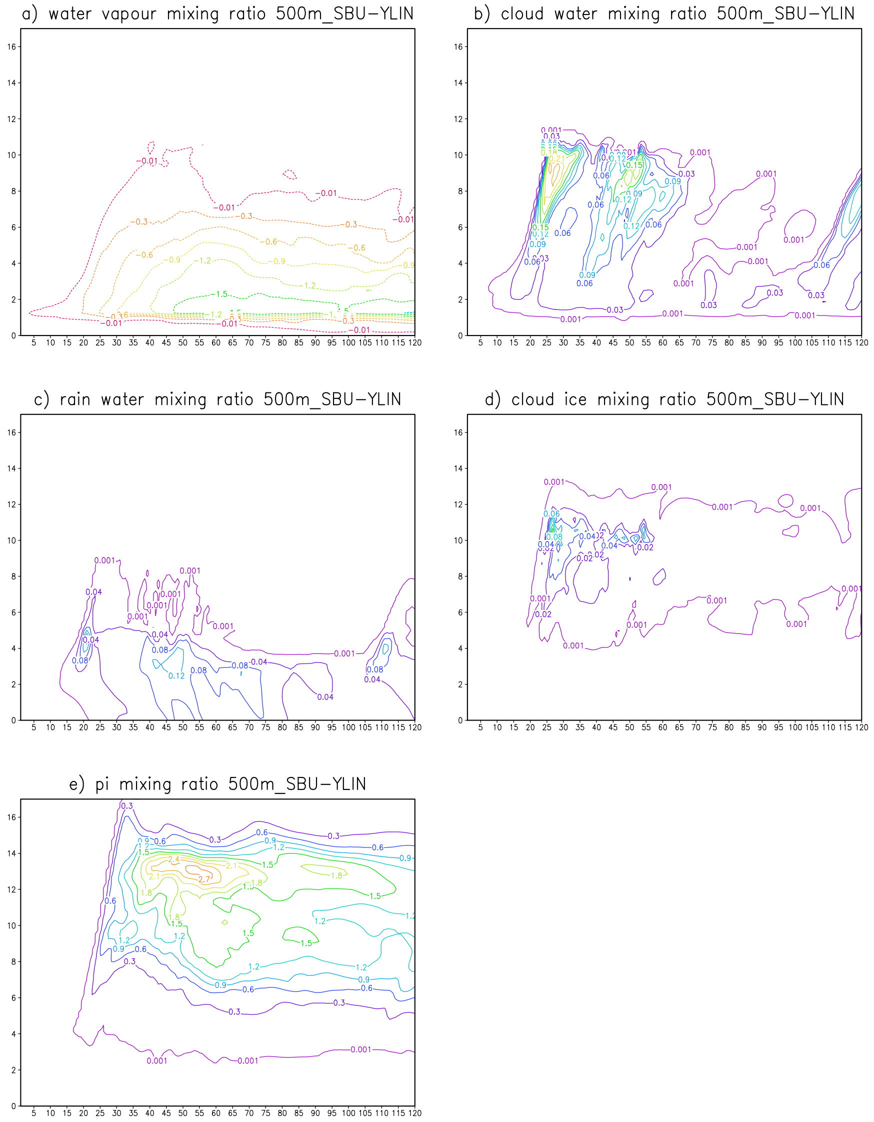

Figure 4.3.7: a) The change in water vapour mixing ratio, b) the cloud water, c) rain water, d) cloud ice, e) precipitating ice mixing ratios over the two hour simulation with SBU-YLIN microphysics scheme. A resolution of 500 m was used.

Rainfall has two maxima, the first one between 60 and 70 minutes, and the second one is after 100 minutes in the PURDUE-LIN1 simulation (Figure 4.3.4a and 4.3.6c). The PURDUE-LIN2 simulation simulates only one maximum which coincide with the second maximum in PURDUE-LIN1 simulation (Figure 4.3.4b and 4.3.7c). This is in agreement with the findings of Hong and Lim (2006) who compared a six class microphysics scheme with a five class one and found that the amount of rainfall increased and its peak intensity became stronger with more hydrometeors. The SBU-YLIN scheme simulates the least amount of rainfall. The amount of rainfall produced by each scheme is proportional to the magnitude of the maximum horizontal wind caused by the cold pool.

Precipitating ice does not reach the surface, it is converted to other hydrometeors and water vapour before it reaches the surface in all three simulations. The dominating hydrometeor is the largest ice in all three simulations, graupel for the PURDUE-LIN1 (Figure 4.3.4a) and snow for the PURDUE-LIN2 simulation (Figure 4.3.4b) and precipitating ice for the SBU-YLIN simulation (Figure 4.3.4c). In the PURDUE-LIN1 simulation, graupel reaches a maximum after about 40 minutes and starts decreasing. As it decreases the rainfall increases, which gives the first rainfall peak. At the same time as graupel is decreasing, the water vapour increases slightly and the temperature decreases slightly. The temperature decrease (Figure 4.3.3c) is because of the latent heat absorption associated with melting and evaporation (Figure 4.3.3d). Graupel reaches a minimum after about 75 minutes of simulation and starts to increase again after 80 minutes because of the development of the second cell at about the same time. A peak is reached just before 100 minutes and then graupel decreases to a minimum at about 2 hours. At the same time that graupel starts increasing rainfall also increases but its peak is smaller compared to that of graupel and a minimum is reached at about the same time.

The PURDUE-LIN2 simulation (Figure 4.3.4b and 4.3.6c) produced less rainfall compared to the PURDUE-LIN1 simulation (Figure 4.8c and 4.7a). The amount of snow produced in this simulation is greater than the amount of graupel produced in the PURDUE-LIN1 simulation. Snow starts decreasing after about 60 minutes but unlike graupel it does not decrease to almost zero. A minimum of 0.15 g/m^2 is reached and the amount of snow starts to increase again because of the development of the second cell. The updrafts in the second cell in this simulation are greater than the updrafts in the PURDUE-LIN1 and the SBU-YLIN simulations. This is likely because graupel is heavier than snow and therefore decreases the size of the updraft in the PURDUE-LIN1 simulation even though it has the strongest cold pool. The updraft in the SBU-YLIN simulation is small because the cold pool that should trigger the second storm is too small.

As snow decreased in the PURDUE-LIN2 simulation , the water vapour increased and temperature decreased slightly which shows that there was cooling due to latent heat absorption. As snow decreased the amount of rainfall increased slightly, the amount did not increase as much as it did in the simulation with graupel. The decrease in snow started later than the decrease in graupel and as a result a minimum was reached later. Graupel falls quicker because it is heavier. The amount of snow starts increasing again after 90 minutes and this associated with the updraft towards the end of the simulation that is triggered by the cold pool.

The differences in rainfall suggests that because graupel is heavier, it falls faster and melts below freezing level to form rainfall. The rain water droplets are big enough to reach the surface before evaporating. Melting reduces the temperature and therefore results in a downdraft that acts to cut the supply of moist air to the storm. The graupel minimum happens at the same time as the minimum in cloud water which confirms that the supply of moist air was limited. Rainfall is usually preceded by a downdraft and a rainfall maximum occurs in the simulation with graupel just before a minimum in other hydrometeors is reached. Lin and Orville (1969) found that precipitating clouds dissipated sooner than nonprecipitating ones, which agrees with our results that the cloud that precipitated the most, dissipated sooner (Figure 4.3.4a and b).

The behaviour of the hydrometeors in the simulation with the SBU-YLIN microphysics scheme was similar to those with PURDUE-LIN2 until about 60 minutes. The behaviour of precipitating ice (which is both snow and graupel) follows more that of snow in the PURDUE-LIN2 run (Fig4.2.4c) in the sense that there is no big decrease in precipitating ice seen in PURDUE-LIN1 runs. The amount of precipitating ice is also similar to the snow in the PURDUE-LIN2 run , both of which are higher than the graupel that formed. The peak in precipitating ice occurs almost at the same time as the peak in snow in the PURDUE-LIN2 run and later than the peak in graupel. With the decrease in precipitating ice, water vapour increases slightly. At the end of the simulation more water vapour was converted to hydrometeors in the PURDUE-LIN simulations because of the second updraft which is very small in the SBU-YLIN simulation.

4.3.2 The effect of resolution on individual thunderstorms

Simulations were made with the PURDUE-LIN scheme with graupel (PURDUE-LIN1), without graupel (PURDUE-LIN2) and also with the SBU-YLIN microphysics scheme with horizontal resolutions of 1 km and 2 km while keeping the vertical resolution unchanged. The domain was kept the same and therefore fewer grid points than those used for the 500 m resolution simulations were used. An advection timestep of 5 s was used with an adjustment timestep of 1 s for 1km resolution simulations while an advection timestep of 10s and an adjustment timestep of 2 s were used for the 2 km resolution simulation.

4.3.2.1 1 km resolution simulations

The maximum updrafts and downdrafts for the three runs with a 1 km resolution (Figure 4.3.9 a and b) are smaller compared to the 500 m resolution ones (Figure 4.3.3 a and b). This is because the high resolution simulations capture the small intense updrafts and downdrafts that the low resolution simulation is not able to capture. The second cell that was seen in the PURDUE-LIN 500 m resolution runs is also found in the 1 km resolution simulations. The second cell in the PURDUE-LIN2 simulation (Figure 4.3.9a and Figure 4.3.8 c) is associated with bigger updrafts than in the PURDUE-LIN1 simulation (Figure 4.3.8a) similar to the 500 m resolution simulations.

The total amount of warming at the end of the simulation (Figure 4.3.9 c) differs from the 500 m resolution simulations (Figure 4.3.3 c). The PURDUE-LIN1 simulation has warmed up the least due to latent heat release and less water vapour has been converted to hydrometeors than in the two other simulations. The PURDUE-LIN2 simulation warmed up the most and more water vapour was converted to hydrometeors.

In the PURDUE-LIN1 simulation there is an increase in graupel from about 20 minutes and a peak is reached after 40 minutes (Figure 4.3.10 a). From there graupel starts to decrease while water vapour and rain water increase. The temperature decreases slightly as a sign of latent heat absorption. Graupel increases slightly again after 80 minutes but unlike in the 500 m resolution simulations, more rainwater forms than graupel. This is because the updrafts

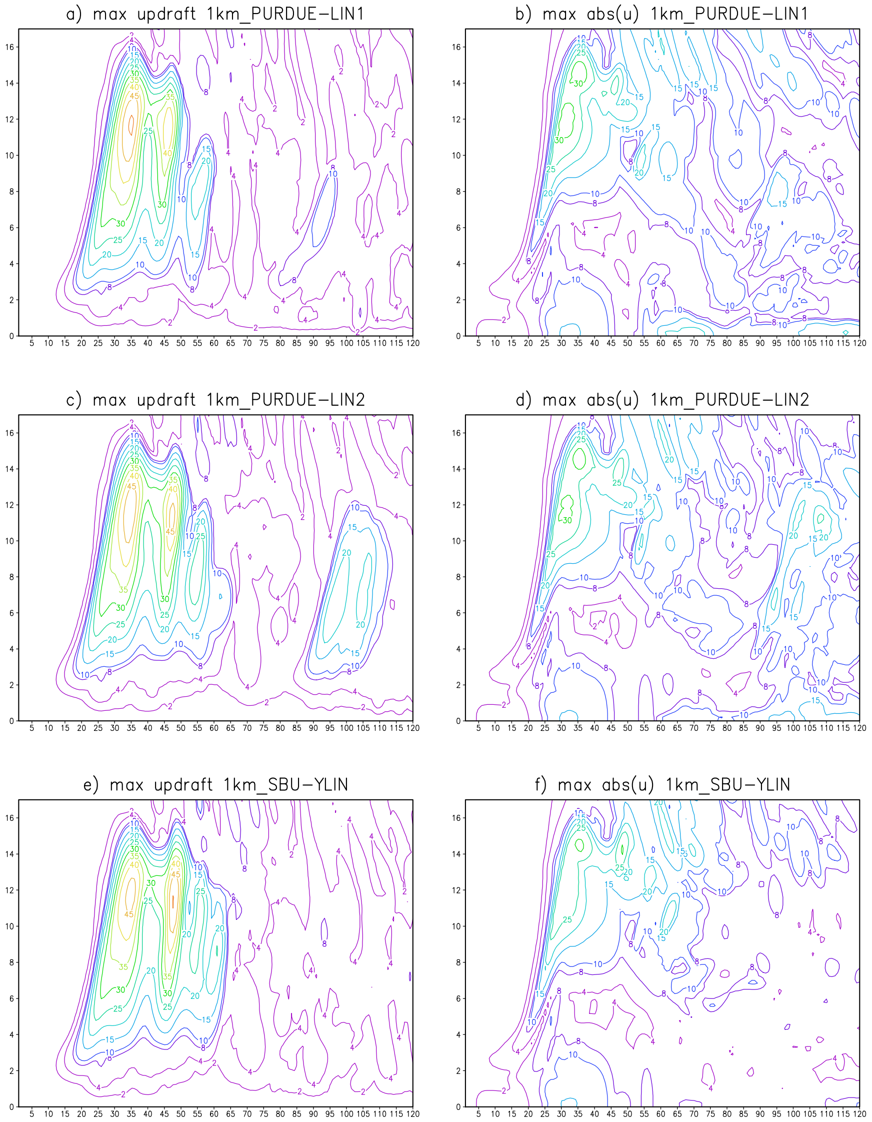

Figure 4.3.8: a) Updraft and b) absolute horizontal wind maxima with the PURDUE-LIN scheme, c) updraft and d) absolute horizontal wind maxima with the PURDUE LIN scheme without graupel. e) Updraft and f) absolute horizontal wind maxima with the SBU-YLIN microphysics scheme. The x-axis is time in minutes while the y-axis is height in km. The updrafts and downdrafts are in m/s. These simulations were made with a horizontal resolution of 1 km.

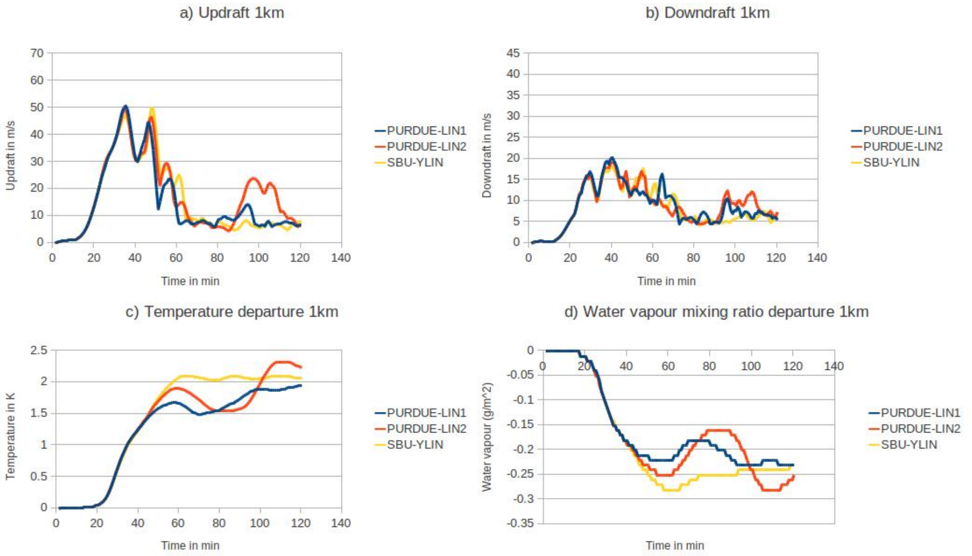

Figure 4.3.9: a) The updraft, b) downdraft, c) Temperature departure and d) water vapour density departure over the two hour simulation with a 1 *km* resolution.

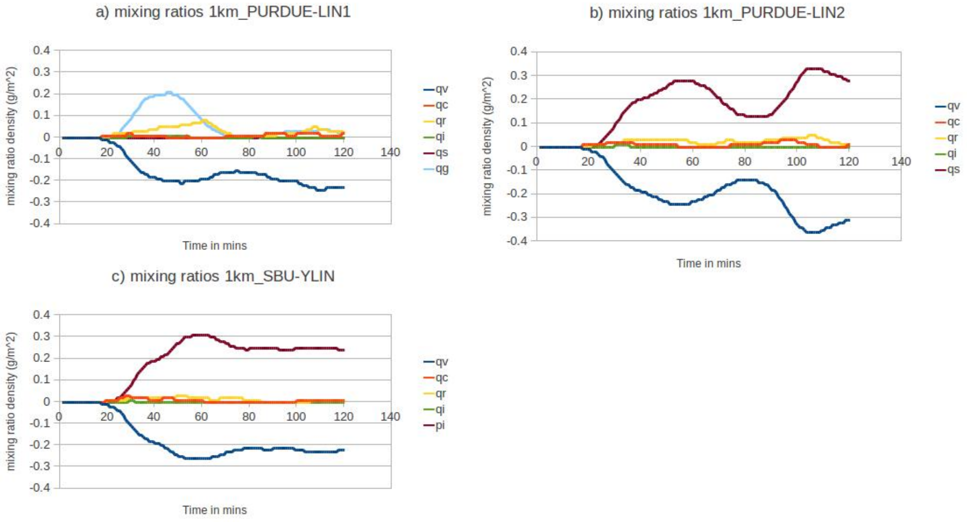

Figure 4.3.10: The change in mixing ratio with the a) PURDUE-LIN b) PURDUE-LIN with no graupel and c) SBU-YLIN microphysics scheme. A resolution of 1 *km* was used.

in the low resolution simulations are weaker compared to the high resolution ones that allows more ice to form. The weaker updrafts only manages to transport moisture to lower levels where saturation is reached that allows for cloud and rain water to form, but not enough ice. This simulation shows that when the temperature is suitable graupel grows faster at the expense of water vapour and other hydrometeors. Because of the weaker updrafts associated with the second cell, less graupel formed and as a result less water vapour was removed from the atmosphere.

In the 1 km resolution simulations with the PURDUE-LIN2 scheme, snow dominates as in the 500 m resolution simulations and reaches a maximum at about 60 minutes (Figure 4.3.10 b). Snow starts to decrease while water vapour increases significantly so that it becomes more than in the simulation with graupel. The temperature decreases (Figure 4.3.9 c) at the same time more than in the simulation with graupel. A possible explanation for this is that snow particles are smaller, they fall slower, melt and evaporate making a smaller contribution to rainfall than the simulation with graupel. Graupel is bigger, when it melts it forms bigger raindrops that reach the surface before evaporating. Snow starts to increase from about 90 minutes and more of it form. This is attributed to a bigger updrafts associated with the second cell compared to in the simulations with the other two microphysics scheme/setting. The water vapour starts to decrease again while snow increases until a peak is reached. Snow decreases again as the water increases until the end of the simulation. Because of the updrafts associated with the second cell, more water vapour in this simulation gets converted to hydrometeors, mostly snow.

In the SBU-YLIN simulation, precipitating ice reaches a maximum at about 60 minutes (Figure 4.3.10 c) similar to the PURDUE-LIN2 simulation. The precipitating ice starts to decrease, however slower than snow in the PURDUE-LIN2 simulation. As it decreases, water vapour increases and the temperature decreases similar to the two other simulations. Precipitating ice stops to decrease after reaching about 0.25 g/m^2 and then stabilises there. There is no second increase in precipitating ice because there is no second cell.

4.3.2.2 2 km resolution simulations

The maximum updrafts and downdrafts in the 2 km resolution (Figure 4.3.12 a and b) are smaller than in the 1 km resolution simulations for the same reasons

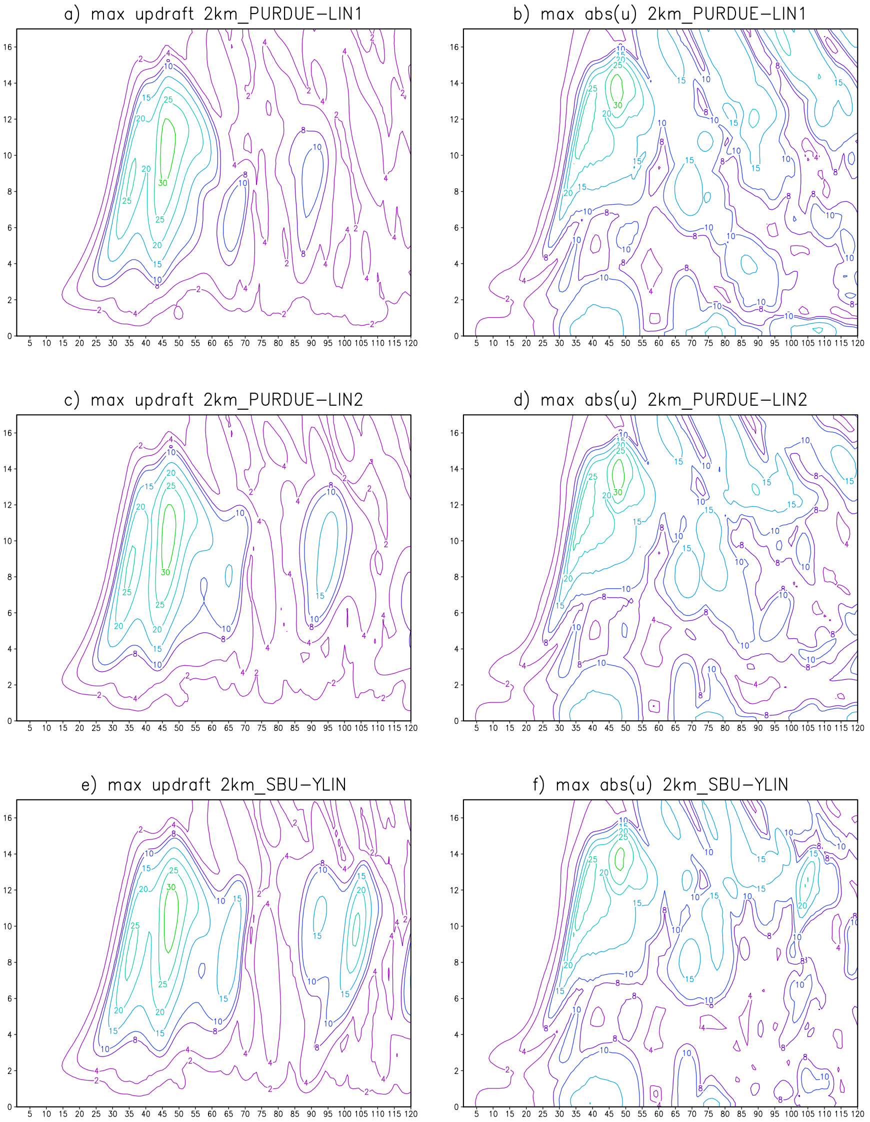

Figure 4.3.11: a) Updraft and b) absolute horizontal wind maxima with the PURDUE-LIN scheme, c) updraft and d) absolute horizontal wind maxima with the PURDUE LIN scheme without graupel. e) Updraft and f) absolute horizontal wind maxima with the SBU-YLIN microphysics scheme. The x-axis is time in minutes while the y-axis is height in km. The updrafts and downdrafts are in m/s. These simulations were made with a horizontal resolution of 2 km.

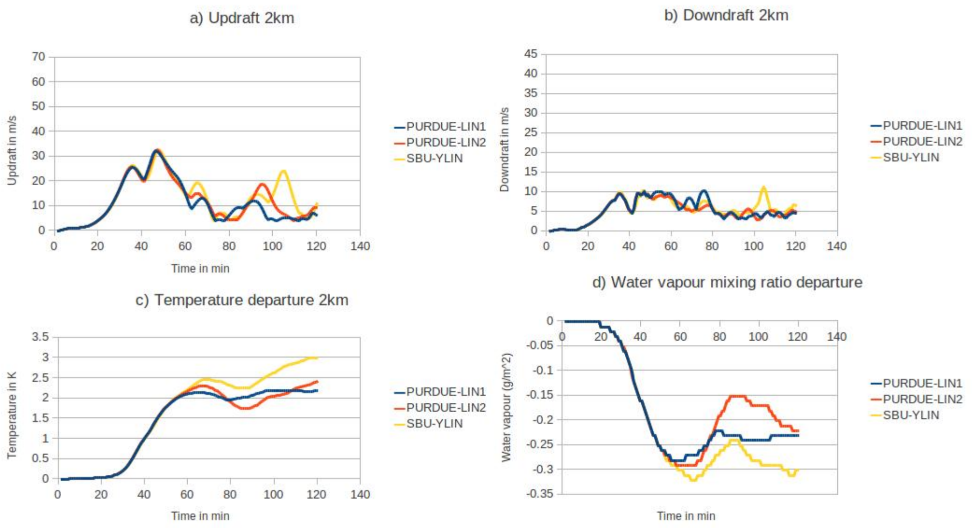

Figure 4.3.12: a) The updraft, b) downdraft, c) Temperature departure and d) water vapour density departure over the two hour simulation with a 2 km resolution.

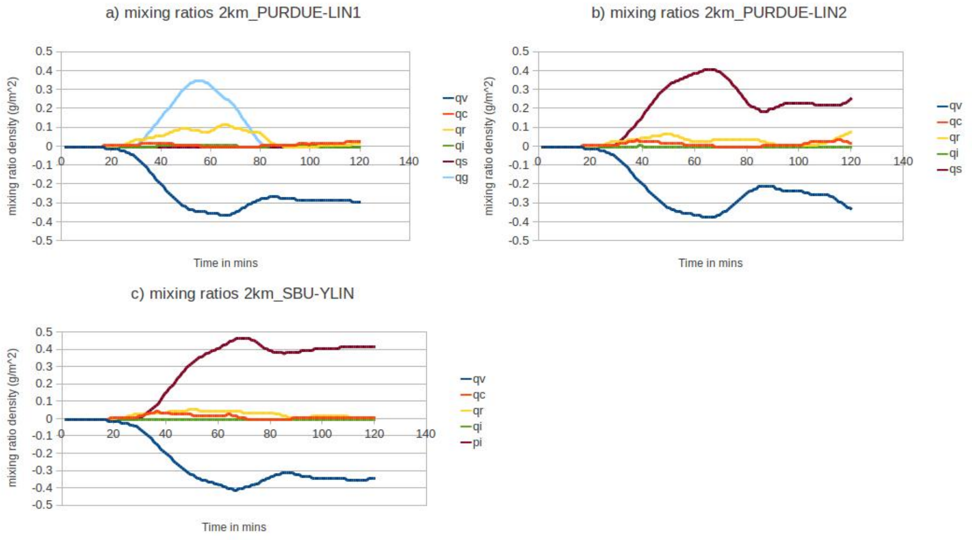

Figure 4.3.13: The change in mixing ratio with the a) PURDUE-LIN b) PURDUE-LIN with no graupel and c) SBU-YLIN microphysics scheme. A resolution of 2 km was used.

that the 1 km updrafts are smaller than 500 m simulation updrafts. A second cell is found in all three simulations (Figure 4.3.11 a, c and e), including the SBU-YLIN simulation that had a small one in the 500 m and none in the 1 km resolution simulations. The updrafts associated with the second cell are bigger in the SBU-YLIN simulation than in the two other simulations. This has the effect that at the end of the simulation, more water vapour is converted to hydrometeors in the SBU-YLIN simulation than in the other two simulations. The SBU-YLIN simulation also warms up more because of latent heating.

Similar to the 500 m and 1 km simulations, graupel dominates the PURDUE-LIN1 simulation (Figure 4.3.13 a). The hydrometeor start increasing slightly later and a maximum is also reached slightly later in lower resolution simulations. A maximum is reached just before 60 minutes and starts decreasing and as expected the rainfall and water vapour increase while temperature decreases. A minimum is reached at about 80 minutes and there is no increase after that. This is because the second updraft is weak and is therefore not able to carry moisture to levels where graupel can form. Towards the end of the simulation where in the 500 m and 1 km simulations there was an increase in graupel and rainfall, there is a slight increase in cloud water and rain water. The rainwater is much less compared to that in the 1 km and 500 m resolution simulations. This is in agreement with Kessler (1969) who found that the magnitude of precipitation tends to increase with an increasing updraft.

In the PURDUE-LIN2 simulation (Figure 4.3.13 b), snow dominated similar to the 500 m and 1 km resolution simulations and reached a maximum soon after 60 minutes. Snow then started to decrease as water vapour increased. Snow decreased to about 0.2 g/m^2 and stabilised there. There is no second increase in snow as seen in the higher resolution simulations. Hong and Lim (2004) found smaller differences in the hydrometeors when using coarser resolution. The results presented here also suggest that the hydrometeor differences are smaller in the 2 km resolution simulations compared to the 500 m and 1 km resolution simulations.

In the simulation with the SBU-YLIN microphysics schemes (Figure 4.3.13c), the precipitating ice maximum is reached at the same time as when the snow maximum of the PURDUE-LIN2 run is reached. A slight decrease in precipitating ice takes place similar to the PURDUE-LIN simulations, however in the SBU-YLIN the decrease is smaller. The precipitating ice stabilises at about 0.4 g/m^2. The updrafts associated with the second cell only cause a slight increase in precipitating ice. All three simulations simulated the cold pool at the surface, it does not look stronger in the SBU-YLIN scheme which simulated the strongest second updraft. A possible explanation for the updraft being bigger than in the PURDUE-LIN simulations is that SBU-YLIN simulates smaller hydrometeors and hence its cold pool triggered updraft is affected less by hydrometeor loading. Weisman and Klemp (1982) found no redevlopment when using a Kessler microphysics scheme which does not include ice. Our results show redevelopment which is because of the cold pool that is possibly stronger than that simulated by Weisman and Klemp (1982) - our simulation include ice.

4.3.3 The effect of shear on thunderstorms

Weisman and Klemp (1982) conducted experiments in which shear is given by

$$U = U_S tanh(z/z_s) \tag{4.3.5}$$

where $z_s = 3km$ is kept constant through all the simulations and U_s is varied from 0 through 45 m/s and they found different storms depending on the amount of shear. The storms were initiated and allowed to evolve through 2 hours. When $U_s = 15$ the storm redeveloped twice. Rotunno et al. (1988) showed that with strong shear along the surface and weaker shear aloft, lines of ordinary cells occur, while strong deep shear a line of nearly steady supercells occur. In this section 2 hour simulations are made using $U_s = 15ms^{-1}$ (Fig 4.3.14) with the PURDUE-LIN and SBU-YLIN BMP schemes. Simulations are made with a 500 m, 1 km and 2 km horizontal resolutions. The vertical resolution is stretched with higher resolution closer to the surface and lower towards the top of the domain with an average resolution of 200 m in all the simulations.

4.3.3.1 500 m resolution simulations with shear

The updraft and downdraft maxima in the simulations made with 500 m resolution simulation with shear (Figure 4.3.16 a) are smaller compared to the simulations without shear (Figure 4.3.3 a). This is because shear encourages mixing/turbulence which promotes entrainment that dilutes the incloud air. In the simulation without shear the updrafts associated with the second cell were much smaller compared to the updraft associated with the first cell. In the

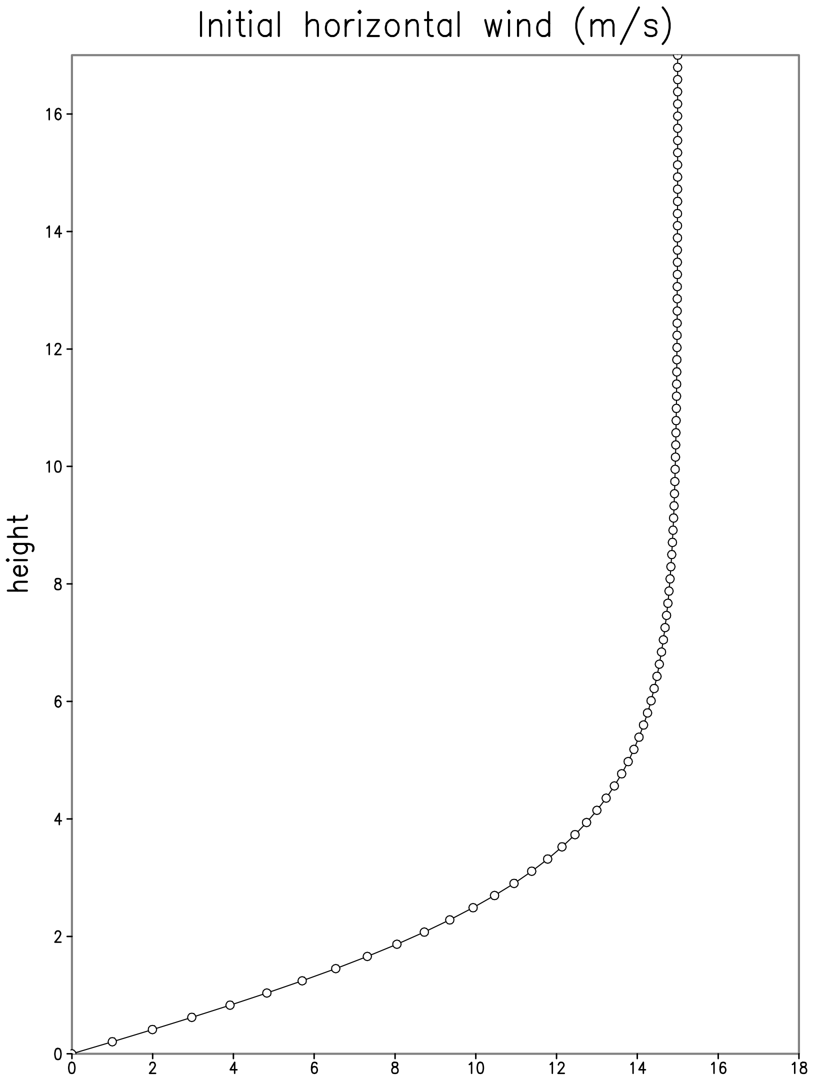

Figure 4.3.14: The horizontal wind with $U_s = 15ms^{-1}$

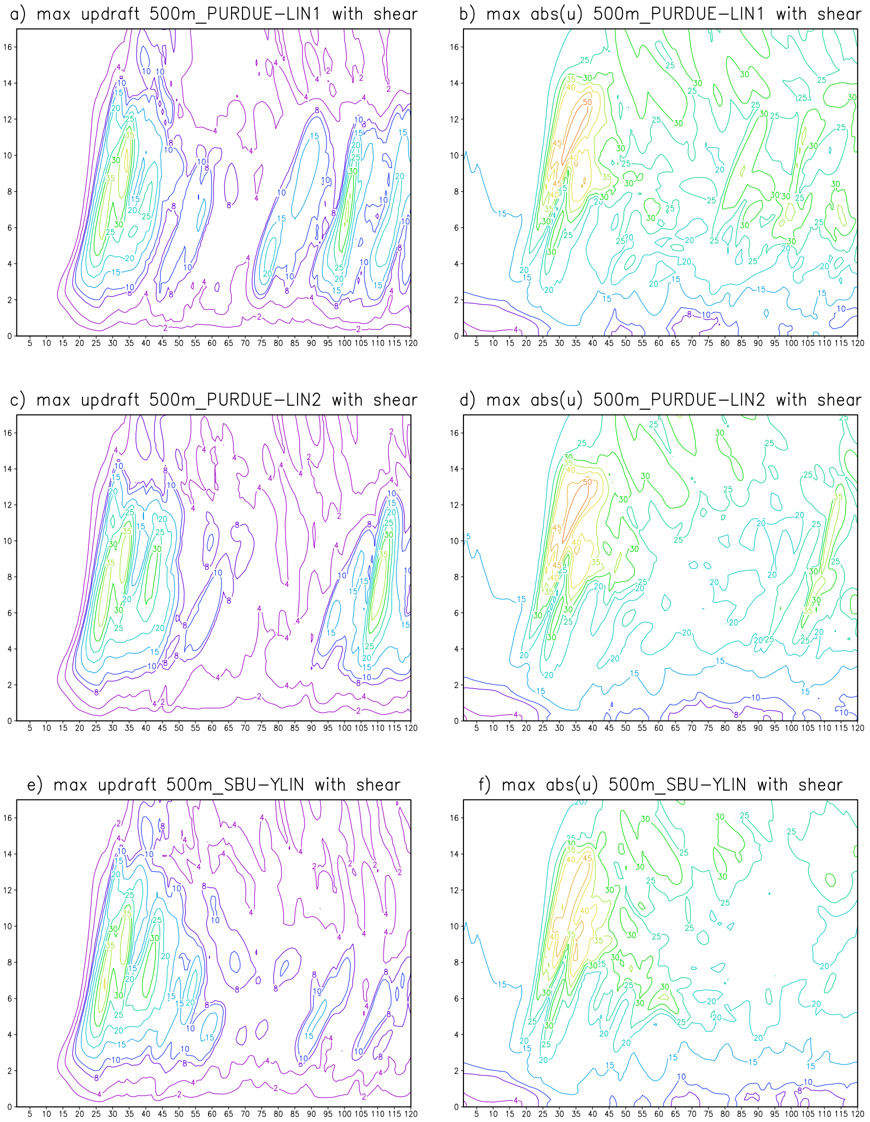
a) max updraft 500m_PURDUE−LIN1 with shear
b) max abs(u) 500m_PURDUE−LIN1 with shear
c) max updraft 500m_PURDUE−LIN2 with shear
d) max abs(u) 500m_PURDUE−LIN2 with shear
e) max updraft 500m_SBU−YLIN with shear
f) max abs(u) 500m_SBU−YLIN with shear

Figure 4.3.15: a) Updraft and b) absolute horizontal wind maxima with the PURDUE-LIN scheme, c) updraft and d) absolute horizontal wind maxima with the PURDUE LIN scheme without graupel. e) Updraft and f) absolute horizontal wind maxima with the SBU-YLIN microphysics scheme. The x-axis is time in minutes while the y-axis is height in km. The updrafts and downdrafts are in m/s. These simulations were made with a horizontal resolution of 500 m.

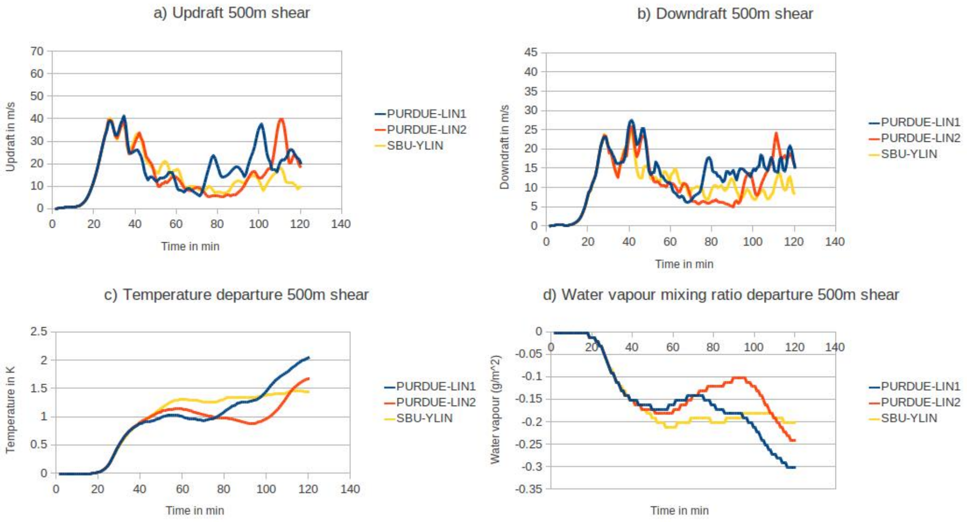

Figure 4.3.16: a) The updraft, b) downdraft, c) Temperature departure and d) water vapour density departure over the two hour simulation with a 500 *m* resolution.

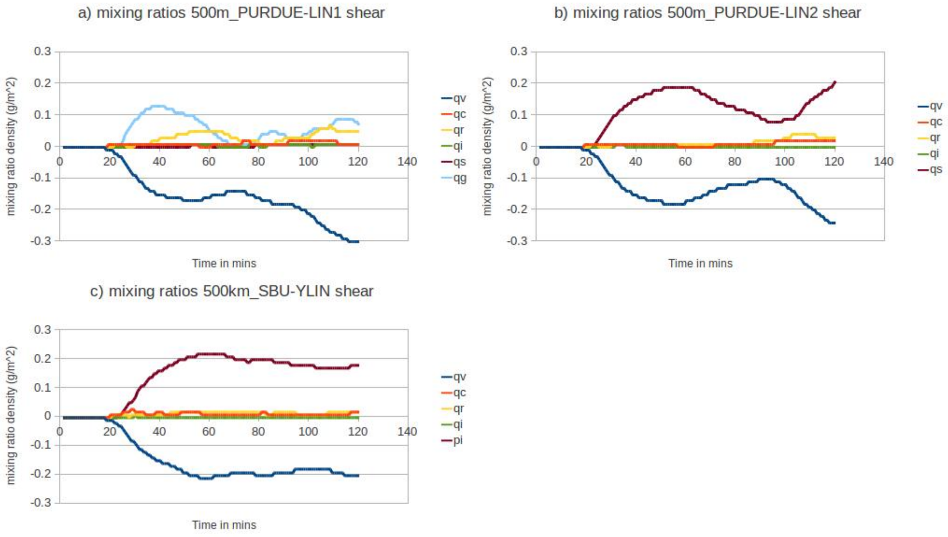

Figure 4.3.17: The change in mixing ratio with the a) PURDUE-LIN b) PURDUE-LIN with no graupel and c) SBU-YLIN microphysics scheme. A resolution of 500 *m* was used.

simulations with shear, updrafts that form later that are associated with cell redevelopments, are almost as big as those associated with the first cell (Figure 4.3.16a and 4.3.15a).

This suggests that the thunderstorm redevelopments in an atmosphere that has shear are stronger compared to the atmosphere with no shear. This supports findings of Weisman and Klemp (1982) that used the Kessler (1969) microphysics with no ice to show that shear is important for redevelopment of thunderstorms. Our simulations show that the microphysics have an important role regarding the redevelopment of storms because in one of the simulations, one with the SBU-YLIN scheme, very little redevelopment was found in the simulation with no shear, while there was a redevelopment in the simulations using the PURDUE-LIN microphysics scheme. In a sheared environment, the environmental vorticity works together with the vorticity in the cold outflow from the cloud to initiate strong convection as shown in Figure 4.3.18.

In the PURDUE-LIN1 simulation, there is a big updraft after about 100 minutes. In the PURDUE-LIN2 simulation, at about 110 minutes an updraft maximum of similar size to the first updraft occurs and it is associated with a big downdraft (Figure 4.19a). This is similar to the simulations without shear that the maximum updrafts that happen after the first hour of simulation in the PURDUE-LIN scheme with graupel occurs earlier than in the PURDUE-LIN2 simulation. This shows that the microphysics have an important role to play in the dynamics of clouds.

Similar to the simulations with no shear, the updrafts that form after an hour are stronger in the simulation with the PURDUE-LIN2 scheme and smaller in the SBU-YLIN simulation. More water is converted to hydrometeors by the end of the simulation in the PURDUE-LIN1 simulation and similar to simulation with no shear, it has warmed up the most. The SBU-YLIN simulation converted the least water vapour to hydrometeors and warmed up the least.

The many redevelopments that occur because of shear working together with the environment are visible in the graupel simulations. There are three graupel maximum as opposed to only two in the simulation with no shear (Figure 4.7 a and 4.20 a). Similar to the no shear simulations, graupel reaches a maximum at about 40 minutes, although slightly sooner in the simulations with shear. It then starts decreasing as rainfall and water vapour increase, while cooling the atmosphere slightly. A second local graupel maximum occurs which is not

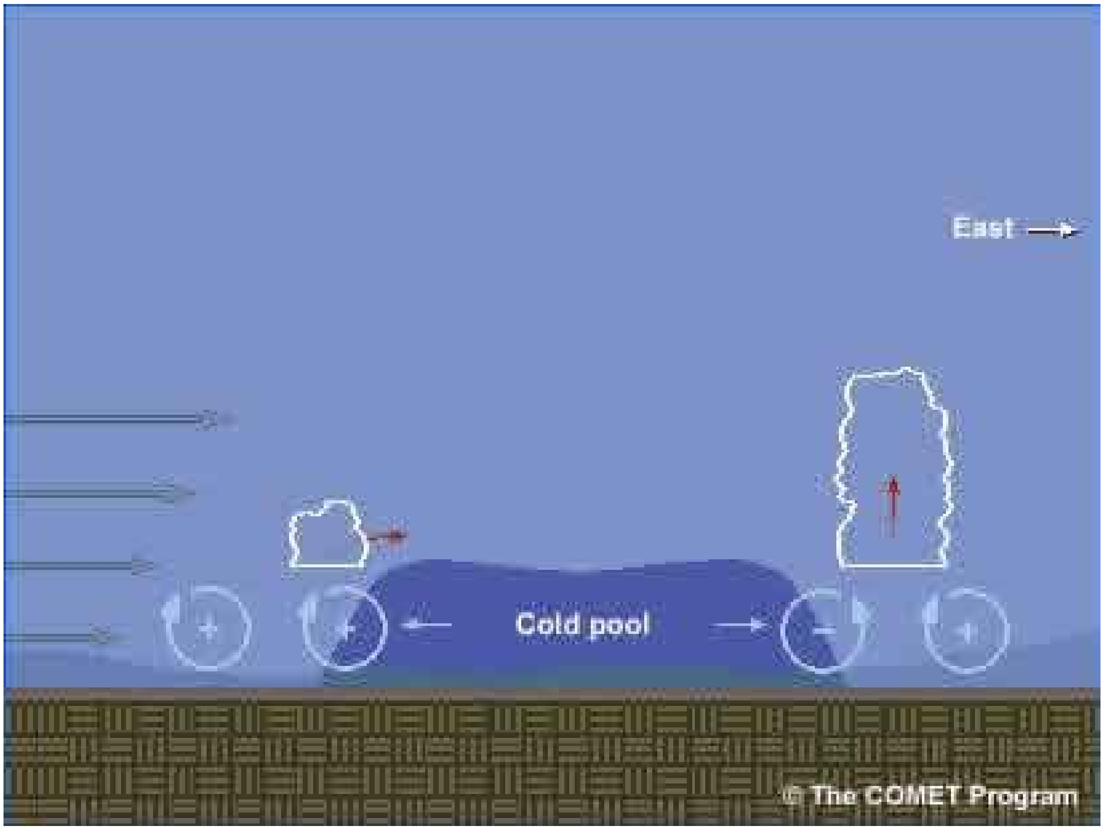

Figure 4.3.18: Vorticity caused by environmental shear and cold pool encourage storm development in the east. From the COMET Program.

accompanied by an increase in rainfall. At about 100 minutes graupel starts to increase again and reaches a maximum just before 2 hours. The amount of rainfall also started to increase at about 100 minutes. The bigger the updraft maximum (Figure 4.3.16a), the higher the amount of graupel that forms (Figure 4.3.17a).

The snow simulation of PURDUE-LIN2 with no shear are very similar to those with shear (Figure 4.3.17 b). Snow reaches a maximum at about 60 minutes and starts to decrease while rainfall and water increase and the temperature decreases. A minimum is reached at about 0.15 g/m^2 and the effect of the second big updraft is seen as the amount of snow start to increase again while water vapour decreases. The SBU-YLIN simulations (Figure 4.3.17 c) are similar to PURDUE-LIN2 simulations. A maximum in precipitating ice is reached at the same time as snow, and then a decrease starts taking place but much slower compared to the PURDUE-LIN2 simulations and there is no big increase in snow towards the end of the simulation. The updraft towards the end of the simulation was captured (Figure 4.3.16a)but it is much smaller to produce significant changes in precipitating ice amounts (Figure 4.3.17c).

4.3.3.2 1 km resolution simulations with shear

Similar to the 500 m resolution simulations, the updraft and downdraft peaks are smaller in the simulations with shear (Figure 4.3.19) because of increased entrainment. Very clear redevelopments are seen in the 1 km resolution simulations with the simulation with PURDUE-LIN1 scheme having another redevelopment at about 60 minutes. The 1 km resolution run with the PURDUE-LIN2 scheme simulated the largest updraft towards the end of the simulation similar to the 500 m resolution simulations. Redevelopments are found in the SBU-YLIN simulation and are smaller similar to the 1 km resolution simulations with no shear. Unlike in the 1 km resolution simulation with no shear (Figure 4.3.20 d), the PURDUE-LIN1 scheme simulation losses the most water vapour to hydrometeors and warms up the most (Figure 4.3.20 d). The SBU-YLIN simulation warms up the least and looses the least water vapour.

Graupel in the PURDUE-LIN1 simulation increases to a maximum after about 40 minutes as a result of the first big updraft (Figure 4.3.21 a). It then starts decreasing as rainfall increases to a maximum at about 60 minutes. A local minimum is reached in graupel and then graupel increases again to a local

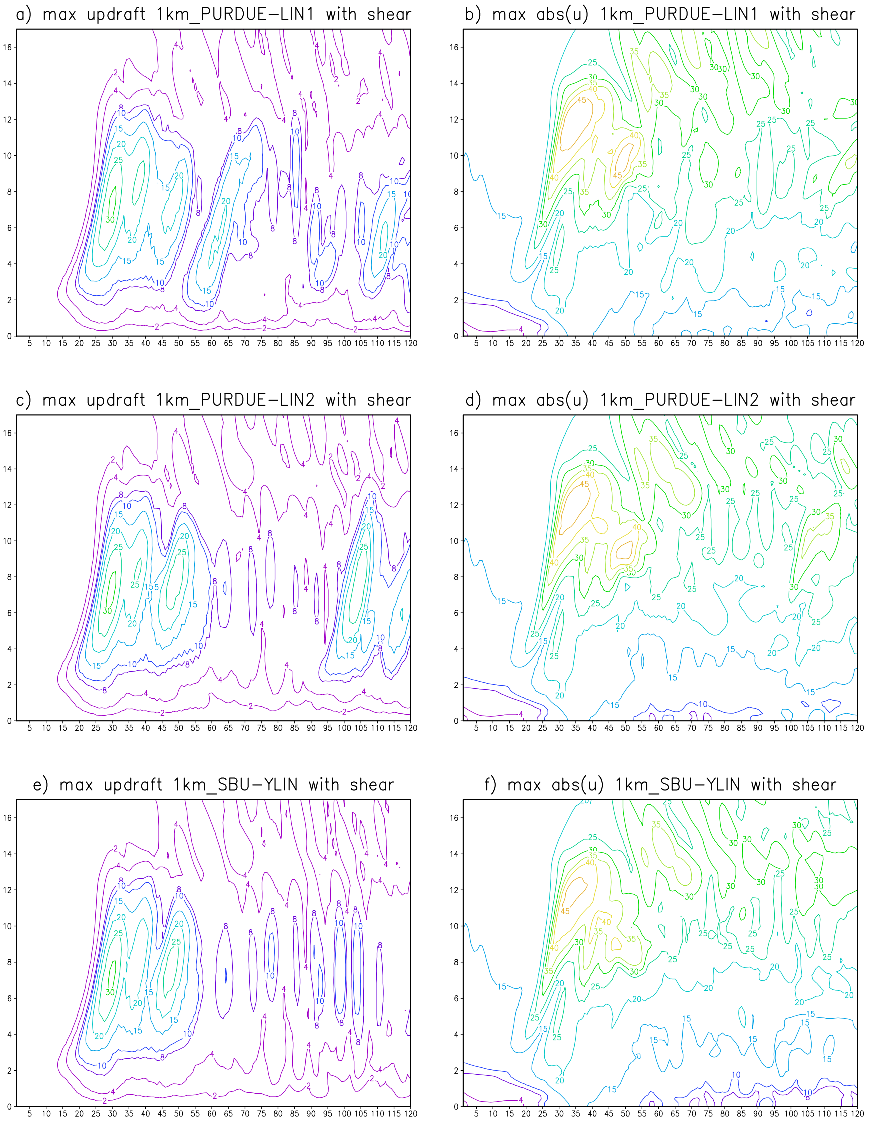

Figure 4.3.19: a) Updraft and b) absolute horizontal wind maxima with the PURDUE-LIN scheme, c) updraft and d) absolute horizontal wind maxima with the PURDUE LIN scheme without graupel. e) Updraft and f) absolute horizontal wind maxima with the SBU-YLIN microphysics scheme. The x-axis is time in minutes while the y-axis is height in km. The updrafts and downdrafts are in m/s. These simulations were made with a horizontal resolution of 1 km.

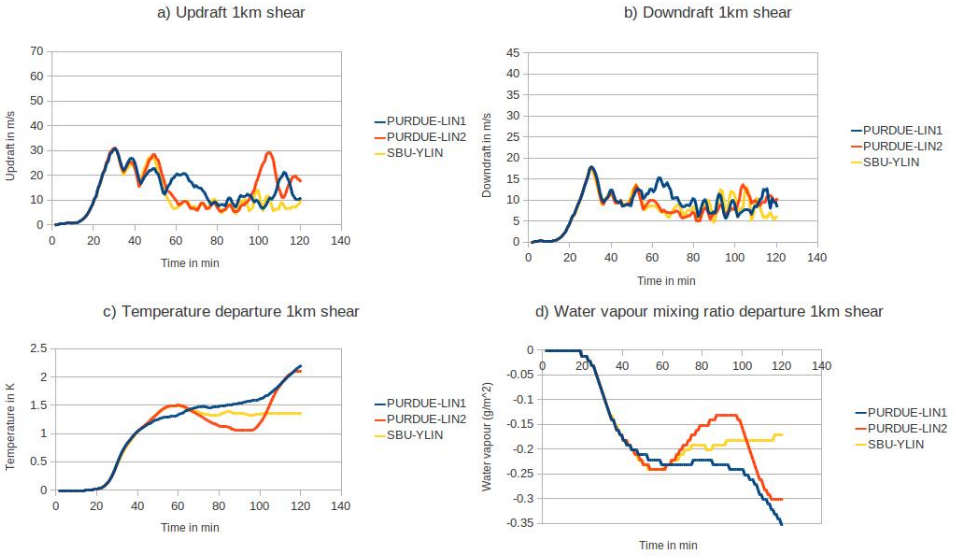

Figure 4.3.20: a) The updraft, b) downdraft, c) Temperature departure and d) water vapour density departure over the two hour simulation with a 1 *km* resolution.

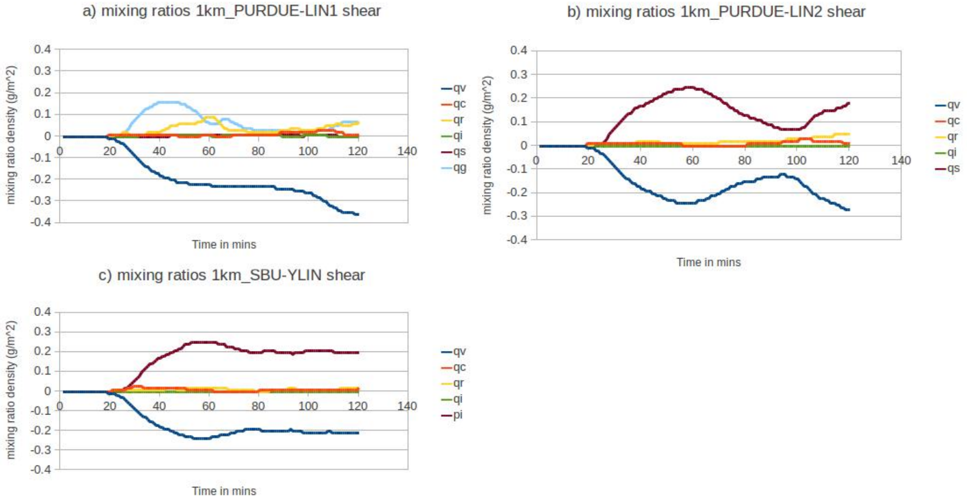

Figure 4.3.21: The change in mixing ratio with the a) PURDUE-LIN b) PURDUE-LIN with no graupel and c) SBU-YLIN microphysics scheme. A resolution of 1 *km* was used.

maximum. While the rainfall maximum seems to have been caused by melting graupel, the updraft at about 60 minutes may have played a role in increasing its amount through a supply of warm moist air. This same updraft is also associated with a local graupel maximum at about the same time. Snow in the PURDUE-LIN2 simulation reaches a maximum at about 60 minutes and starts decreasing until it reaches a minimum at about 100 minutes (Figure 4.3.21 b). At the time that snow was decreasing the updrafts were small. A big updraft occurs at about 100 minutes which revives an increase in snow and a decrease in water vapour. The updraft also causes an increase in rainfall in the model. Precipitating ice in the SBU-YLIN simulation reaches a maximum at the same time as snow and starts decreasing to a local minimum of about 0.2 g/m^2 where it remains constant (Figure 4.3.21 c). The simulated updrafts towards the end of the simulation are small and therefore do not lead to a significant increase in the precipitating ice.

4.3.3.3 2 km resolution simulations with shear

The updraft lines are almost on top of one another until just after 80 minutes (Figure 4.3.23 a). Towards the end of the simulation the PURDUE-LIN2 microphysics simulation produces a big updraft, and the updraft in the SBU-YLIN scheme is the smallest. The PURDUE-LIN1 simulation warms up the most (Figure 4.3.23 c) and looses the most water vapour (Figure 4.3.23 d). The SBU-YLIN scheme warm up the least and looses the least water vapour. The SBU-YLIN simulations are the least variable throughout the two hour simulations and this was observed in the runs discussed in the previous sections. When there is no shear, the SBU-YLIN scheme simulated the biggest updraft towards the end of the simulation when a 2 km resolution was used. That big updraft is not simulated in the realisation with shear.

Graupel in the PURDUE-LIN1 increases to a maximum at about 60 minutes and starts to decrease. As it decreases the rainfall and water vapour increase causing cooling (Figure 4.3.24a). The updrafts towards the end of the simulation are smaller and therefore only manage to increase the amount of rainfall and cloud water slightly and no ice is formed at the end of the simulation. A maximum in snow in the PURDUE-LIN2 is reached at about 60 minutes and then snow starts to decrease while increasing rainfall and cloud water slightly (Figure 4.3.24b). The amount of water vapour that is formed because of the decrease in

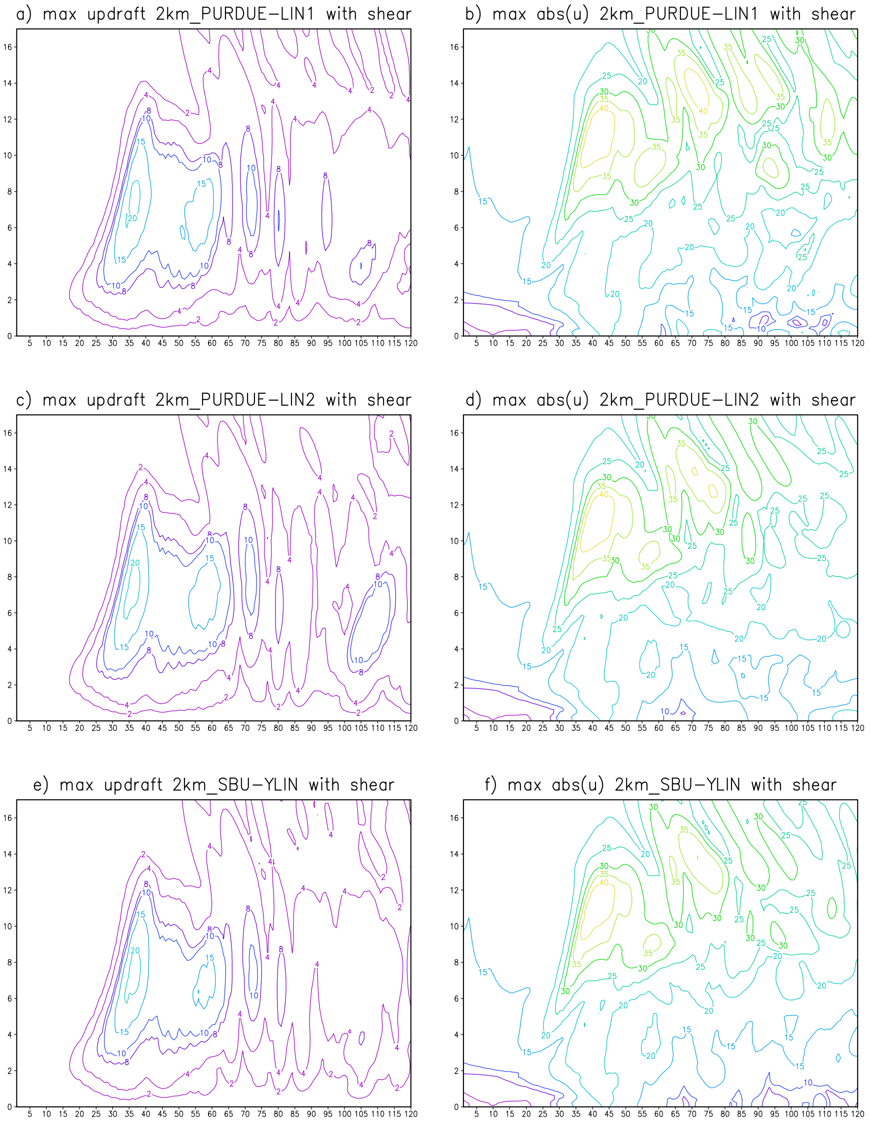

Figure 4.3.22: a) Updraft and b) absolute horizontal wind maxima with the PURDUE-LIN scheme, c) updraft and d) absolute horizontal wind maxima with the PURDUE LIN scheme without graupel. e) Updraft and f) absolute horizontal wind maxima with the SBU-YLIN microphysics scheme. The x-axis is time in minutes while the y-axis is height in km. The updrafts and downdrafts are in m/s. These simulations were made with a horizontal resolution of 2 km.

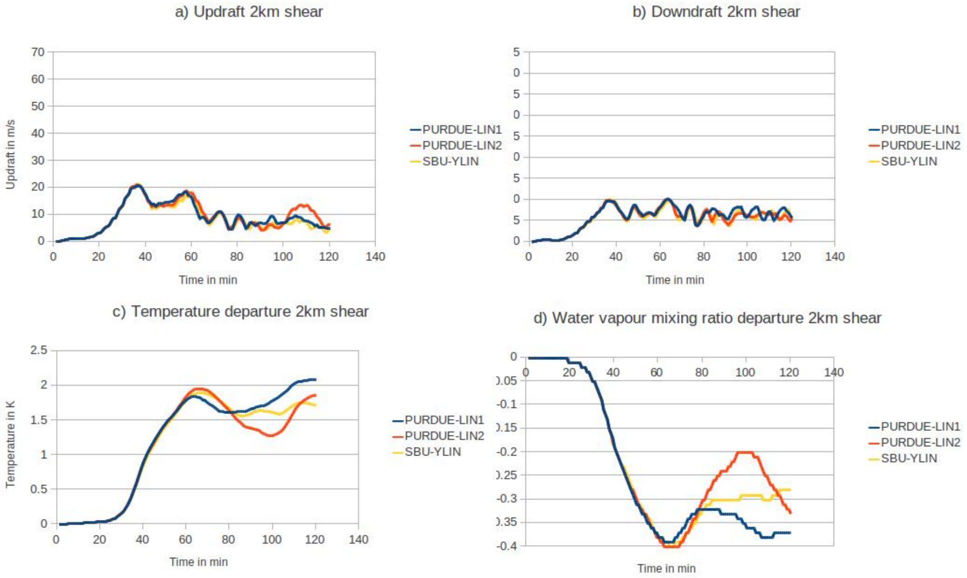

Figure 4.3.23: a) The updraft, b) downdraft, c) Temperature departure and d) water vapour density departure over the two hour simulation with a 2 *km* resolution.

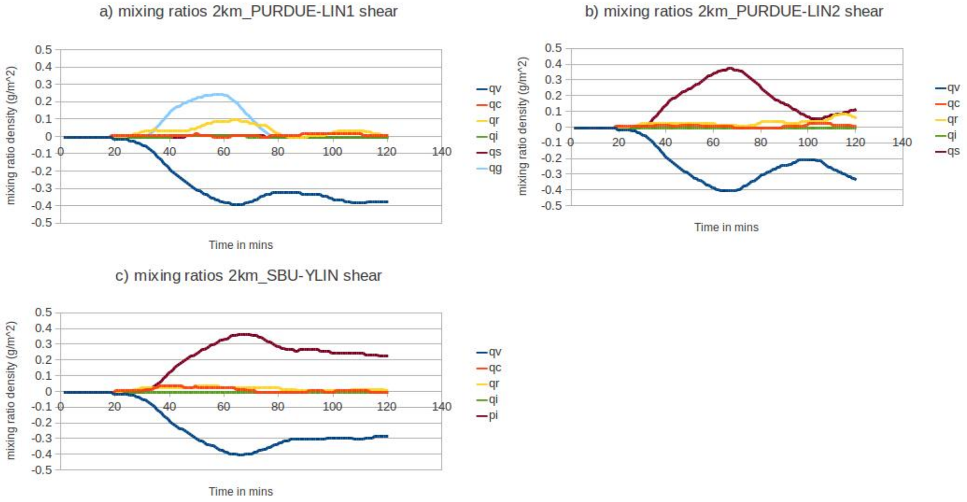

Figure 4.3.24: The change in mixing ratio with the a) PURDUE-LIN b) PURDUE-LIN with no graupel and c) SBU-YLIN microphysics scheme. A resolution of 2 *km* was used.

snow is greater than in the other two simulations. Cooling as a result of latent heat absorption was more in the PURDUE-LIN2 simulation (Figure 4.3.23c). After 100 minutes another updraft develops which increases snow and rainwater (Figure 4.3.24 b). In the SBU-YLIN simulation, the precipitating ice reaches a maximum at the same time as snow and starts to decrease (Figure 4.3.24 c). The decrease is slower compared to snow or graupel in the PURDUE-LIN simulations.

4.4 Discussion

A thunderstorm simulation based on the profile of Weisman and Klemp (1982), and initiated with a warm temperature perturbation was made for a two hour period. The PURDUE-LIN microphysics scheme was used with five (PURDUE-LIN2) and six (PURDUE-LIN1) water classes. At the beginning of the simulation only water vapour was provided to the model and hydrometeors were formed by the microphysics processes in the BMP schemes. For the most part, the six-water class simulation produced more rainfall than the one with five-classes. These findings are in agreement with the findings of Hong and Lim (2006). More water vapour was lost in the simulation that produced the most rainfall, and warming due to latent heating was more in the simulation that lost the most water vapour.

Towards the end of the two hours, a second cell developed developed in both PURDUE-LIN runs, and for the most part it was stronger updrafts in the PURDUE-LIN2 simulation. The second cell was triggered by the cold pool that formed as downdrafts reached the surface. This is shown by Figure 4.4.2 a and c that show the downdraft at different points of the PURDUE-LIN1 simulation. After 45 minutes there are some downdrafts but nothing strong is reaching the surface and as a result the horizontal winds at the surface are also weak. After about 65 minutes, there is a downdraft that has reached the surface and at the same point there are big horizontal winds. After 90 minutes of simulation, the areas of maximum horizontal wind at the surface have moved in the east and west directions (Figure 4.4.2 f) and triggered some storms (Figure 4.4.2 e). The cold pool is stronger in the simulation with graupel (Figure 4.4.1 a), however the updrafts in the second cell are stronger in the simulation without graupel. This is likely because of hydrometeor loading - graupel particles are bigger than snow particles.

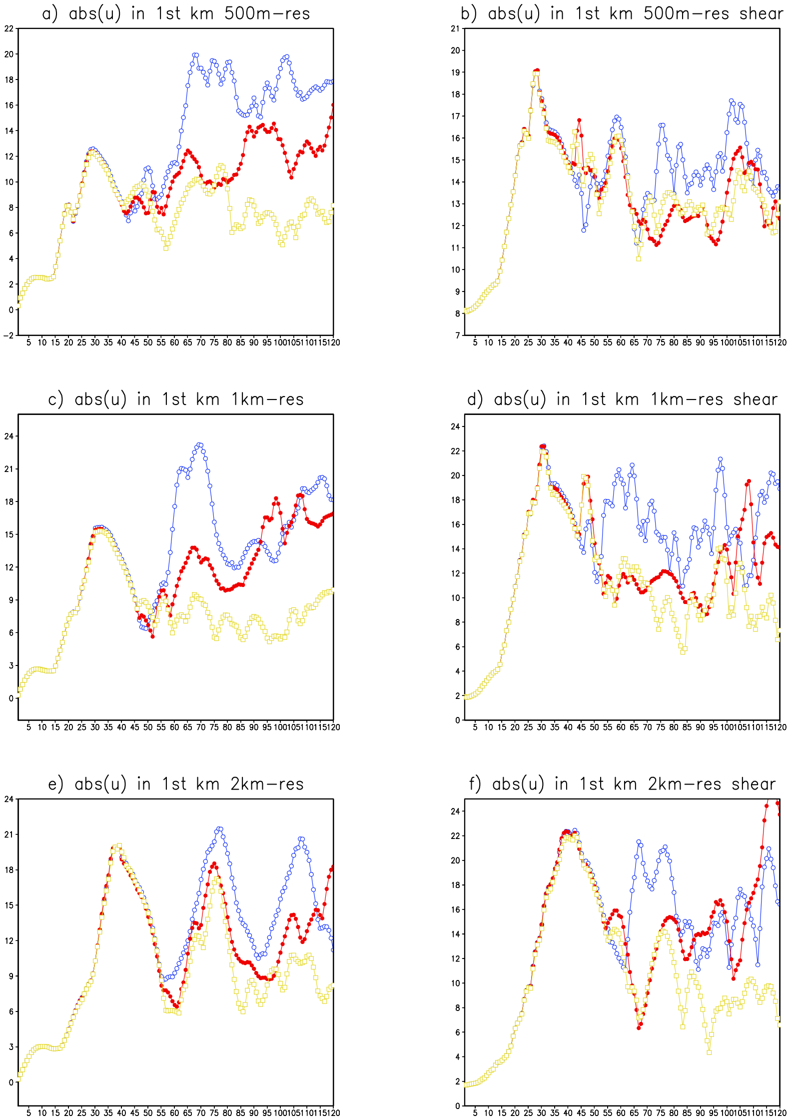

Figure 4.4.1: Maximum absolute horizontal wind with the three different microphysics scheme below 1 *km* in the atmosphere. The blue line represents simulations employing the PURDUE-LIN scheme, the red line shows simulation with PURDUE-LIN scheme with no graupel and the yellow is for the simulation using the SBU-YLIN scheme for a) 500 *m* resolution, b) 500 *m* resolution with shear, c) 1 *km* resolution, d) 1 *km* resolution with shear and e) 2 *km* resolution and f) 2 *km* resolution with shear.

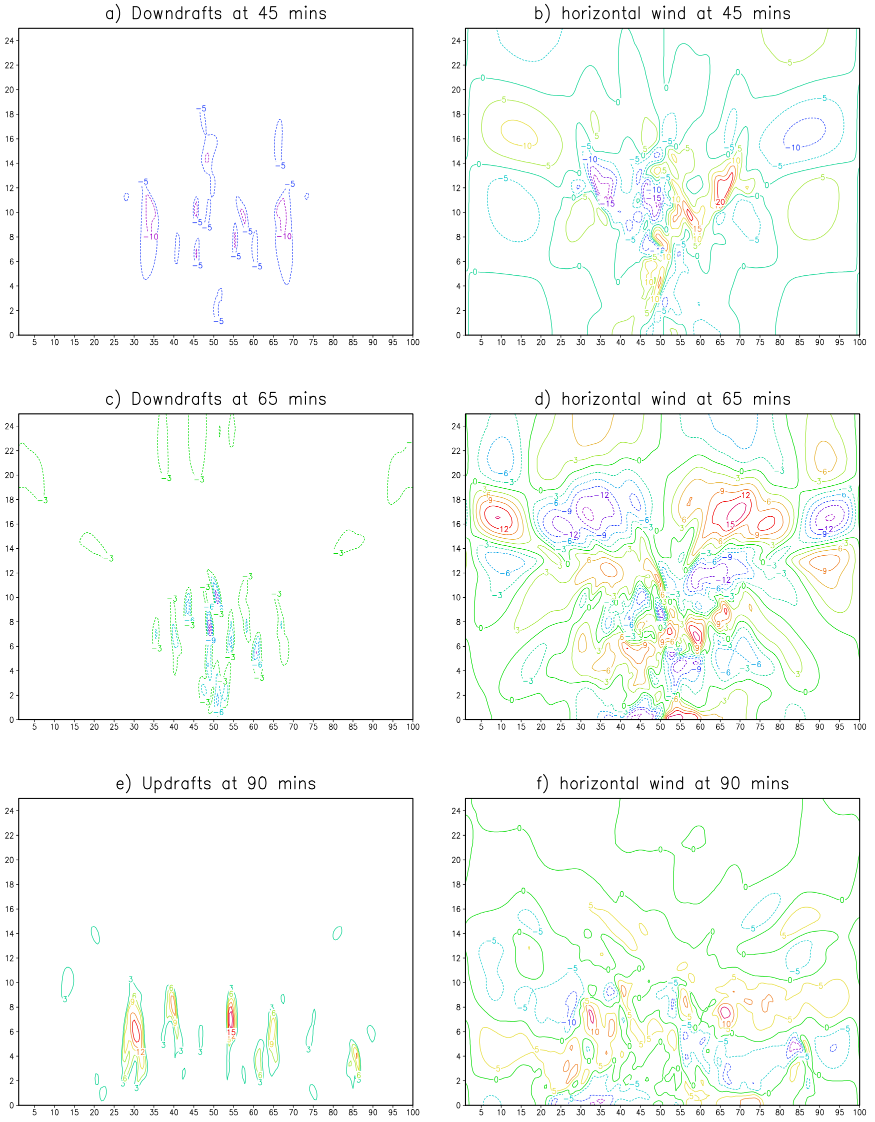

a) Downdrafts at 45 mins

b) horizontal wind at 45 mins

c) Downdrafts at 65 mins

d) horizontal wind at 65 mins

e) Updrafts at 90 mins

f) horizontal wind at 90 mins

Figure 4.4.2: a) Downdraft and b) horizontal wind maxima after 45 minutes of simulation, c) downdraft and d) horizontal wind maxima after 65 minutes of simulation, e) Updraft and horizontal wind maxima after 90 minutes of simulation using the PURDUE-LIN six-class microphysics scheme. The updrafts and horizontal wind are in m/s and a resolution of 500 m was used.

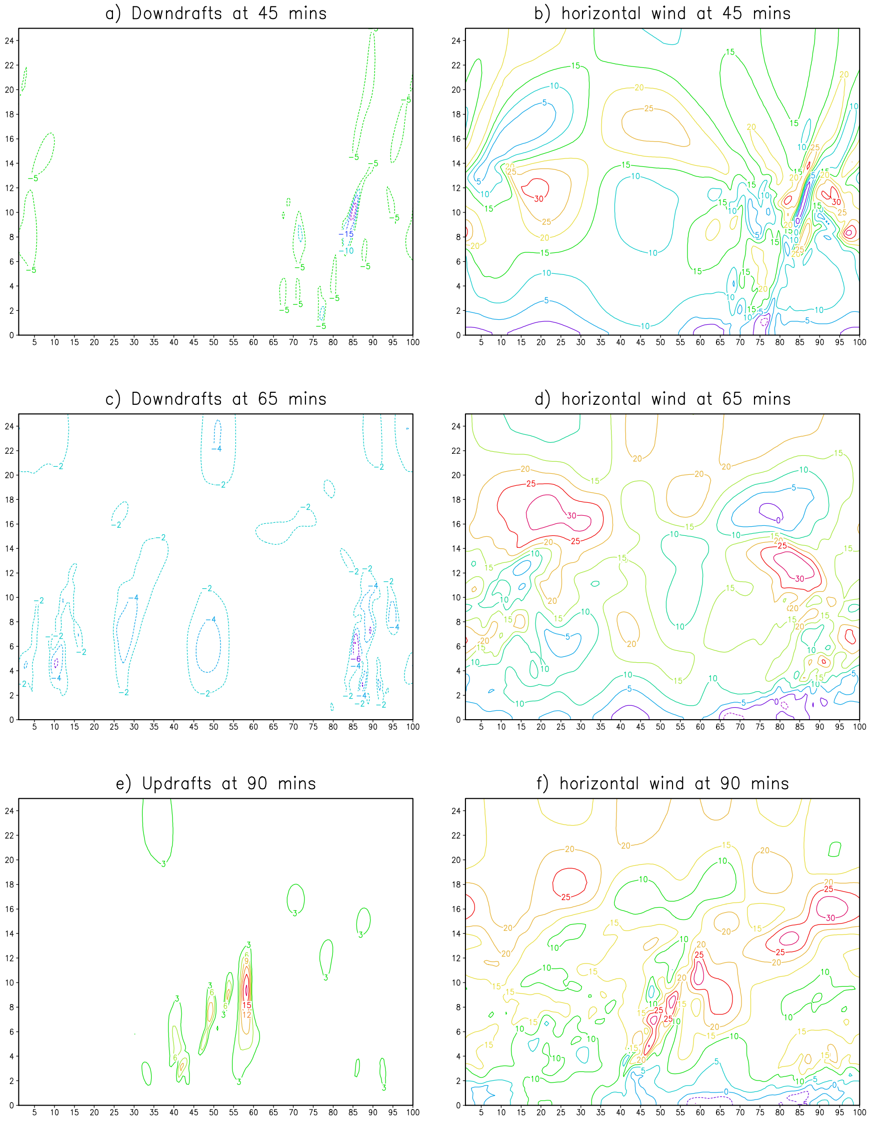

Figure 4.4.3: a) Downdraft and b) horizontal wind maxima after 45 minutes of simulation, c) downdraft and d) horizontal wind maxima after 65 minutes of simulation, e) Updraft and horizontal wind maxima after 90 minutes of simulation using the PURDUE-LIN six-class microphysics scheme. The updrafts and horizontal wind are in m/s and a resolution of 500 m was used.

Another simulation was made with the SBU-YLIN microphysics scheme which was developed using the PURDUE-LIN scheme as a starting point. In this scheme, snow and graupel share a category and processes. Cloud water is assumed to follow a gamma distribution and is double-moment, while cloud water is assumed to be monodispersed in the PURDUE-LIN scheme. Cloud ice is monodispersed in both schemes but is allowed to fall in the SBU-YLIN scheme. The precipitating ice simulated by the NSM with the SBU-YLIN scheme follows more the behaviour of snow in the PURDUE-LIN2 scheme than graupel in the PURDUE-LIN1 scheme. For all three simulations, the largest precipitating ice was the dominating hydrometeor. Graupel dominated in the six-class PURDUE-LIN scheme, snow dominated in the five-class PURDUE-LIN scheme while precipitating ice (snow and graupel) dominated in the SBU-YLIN scheme simulations.

Graupel was found to be the most variable, it reached a maximum faster and as soon as the updraft was reduced it started falling. As it falls it gets converted into rainfall and water vapour while cooling the atmosphere at the same time because of latent heat absorption. Snow and precipitating ice reach a maximum at the same time which is a bit later compared to graupel. When the updrafts get weaker, both snow and precipitating ice start to reduce, however snow reduces faster than precipitating ice. The cell that developed towards the end of the simulation in the PURDUE-LIN simulations is not captured in the SBU-YLIN simulations when horizontal resolutions of 500 m and 1 km are used. Horizontal surface winds are small in this simulation too, which suggests the absence of a trigger for the second storm.

Weisman and Klemp (1982) found that with no shear, there was no redevelopment, however in this study redevelopments were simulated which varied depending on the microphysics scheme used. Weisman and Klemp (1982) used the Kessler scheme which does not have ice, the schemes used in this study all include ice. Our results show that the second redevelopment is because of a stronger downdraft in the simulations with ice which grows at lower relative humidity than liquid water. When ice melts latent heat is absorbed and therefore stronger downdrafts and hence a stronger cold pool are produced than in a simulation with no ice. Although there is no shear in the atmosphere to help with the redevelopment, the cold air is strong enough to act as a trigger for a second smaller storm.

The effect of resolution on thunderstorm simulations was also tested. The lower the resolution the smaller the updraft and downdraft maxima. This was expected because a high resolution simulation captures intense updrafts that a low resolution simulation is not able to capture. The change in updrafts also influenced the hydrometeors. A good example is that of graupel that has two maxima in the 500 m and 1 km resolution simulations, however the maximum is reduced in the 1 km resolution simulations. In the 2 km resolutiom simulations, the second maximum disappears because the updraft towards the end of the simulation is not strong enough to transport moisture to higher altitudes where temperatures are lower that enable the formation of ice. When the updraft is smaller and in the lower atmosphere, more cloud and rain water form. When the updraft is much stronger, more cloud and precipitating ice form.

When a 2 km horizontal resolution is used, the SBU-YLIN simulates a stronger updraft towards the end of the simulation that is triggered by the cold pool. The hydrometeor simulations suggest that SBU-YLIN simulates precipitating particles that are smaller compared to the PURDUE-LIN simulations. When there is increased mixing because bigger updrafts associated with higher resolution, the SBU-YLIN hydrometeors do not manage to produce a coldpool that is strong enough to trigger convection. When the resolution is lower, mixing is reduced because of weaker winds, and as a result, the SBU-YLIN hydrometeors manage to grow to cause a pool of similar size to the PURDUE-LIN simulations that is able to trigger convection. The updrafts in the SBU-YLIN are stronger because of reduced water loading. Bryan and Morrison (2012) showed that with higher resolution, less rainfall is simulated because of increased evaporation as a result of more mixing. The SBU-YLIN scheme seems to behave similar to schemes used by Bryan and Morrison (2012).

The three microphysics schemes were also used to simulate a thunderstorm that forms in an environment with moderate shear. Stronger redevelopments of storms in the simulations with shear were found, similar to the work of Weisman and Klemp (1982). This is because of the vorticity that is caused by the cold outflow from the cloud and the environmental vorticity, that work together to produce stronger storms. Figure 4.4.3 e shows that the simulated storm on the right is stronger compared to the one on the left. The maximum updrafts and downdrafts are however smaller in the simulation with shear because shear encourages mixing that increases entrainment diluting the cloud microphysics and dynamics. There is no significant difference in the water vapour reduction based on the amount of shear applied. With shear SBU-YLIN converts the least amount of water vapour to hydrometeors and warms up the list in all the simulations with 500 m, 1 *km* and 2 *km* resolutions most likely because of increased mixing that is caused by shear.

4.5 Summary and Conclusions

In this chapter simulations with the updated NSM were made and showed that the model is stable by simulating a symmetrical warm bubble. A warm bubble simulation by Engelbrecht et al. (2007) was repeated in this study, to show that after the model was organised into modules and subroutines, it is still able to reproduce the warm bubbles it simulated when it used a fortran 77 code. A modular code is easier to control and it makes adding other components of the model easier. A simulation was also made, with diffusion terms included in the elliptic equation and the NSM simulated a more diffused bubble compared to one that does not include diffusion in the elliptic equation.

Simulations were made with the improved diffusion scheme that calculates the eddy diffusivity based on the gradient Richardson number. The coefficients vary depending on height above the surface, the amount of buoyancy and shear in the atmosphere. The advantange of this scheme is that it is more physical and the value of the coefficients do not have to be assumed based on different factors for different simulations because they are calculated in the model. The bubble simulated with the improved diffusion scheme is slightly less diffused compared to the simulation that uses constant coefficients in the vertical. Two simulations were made with single and double precision and the bubble with single precision was not symmetrical. When diffusion was applied to both single and double precision runs, the bubble looked exactly the same. This shows that single precision still has a role in atmospheric modelling. This is especially relevant for the use of GPUs which are said to function best with single precision. It is however preffered that whenever possible, double precision should be used instead of single precision because it saves computer power since the elliptic solver converges quicker.

An isolated thunderstorm initiated by a warm perturbation was simulated for a period of two hours with a five class and six class PURDUE-LIN microphysics scheme, and the SBU-YLIN BMP scheme with horizontal resolutions of 500 m, 1 *km* and 2 *km*. Simulations with no shear show that by using different microphysics schemes we can get both thunderstorm redevelopment and no redevelopment. PURDUE-LIN simulations generally simulates a cold pool that is able to trigger a new smaller storm. The SBU-YLIN scheme triggers a new storm that has stronger updrafts that PURDUE-LIN simulations when a 2 km resolution is used, but does not when a 500 m and 1 km resolution simulations are used. This result is thought to be a result of increased mixing in higher resolution simulations. When shear is introduced, more storm redevelopment are simulated because of the environmental vorticity that works together with the cold pool to trigger stronger and more storms.

The aim of this chapter was not to determine which of the three microphysics schemes is the best because there are no observations for the simulated thunderstorm. Understanding an individual thunderstorm simulation is important because individual thunderstorms are important weather-producing phenomena in their own right and they are building blocks of larger multicell and mesoscale convective systems. In this chapter we were able to learn how an individual thunderstorm is simulated by the different microphysics schemes introduced to the NSM. In the next chapter, simulated ensembles of thunderstorms using two microphysics schemes that are forced by large scale advective tendencies will be analysed.

Chapter 5

Numerical Experiments: Thunderstorms controlled by large-scale conditions - TOGA-COARE suppressed and active periods

5.1 Introduction

Synoptic and mesoscale motions play a major role in the formation, maintenance and structure of thunderstorms. Tropical Temperate Troughs (TTTs) which form when tropical and midlatitude systems interact are responsible for most of the rainfall in South Africa (Harrison, 1984; Tyson and Preston-Whyte, 2000). Cloud Resolving Models (CRMs) can be used to study the response of thunderstorms to the large-scale circulations. To do this CRMs are driven with large scale observations similar to the procedure that is followed when testing cumulus parameterisation schemes with a Single Column Model (SCM) (Randall et al., 1996). When compared with SCM simulations, CRMs can also be used to test General Circulation Model (GCM) parameterisations. A CRM can also be coupled to a GCM and replace the cloud and conventional cumulus parameterisation schemes (Randall et al., 2003).

To simulate the formation of an ensemble of cumulus clouds under given large scale conditions with a CRM, the large scale advective tendencies are forced to the CRM as if the CRM is situated within a grid box of a large scale numerical model (Xu and Randall, 1996; Grabowski et al., 1996). The observed large-scale advective tendencies of potential temperature, water vapour mixing ratio, and horizontal momentum are used as the main large-scale forcing. Moisture and potential temperature tendencies are applied uniformly on x. The horizontal winds are relaxed towards the observed fields with a time scale (τ) (equation 5.2.2) (Xu and Randall, 1996). This method constraints the domain-averaged horizontal velocities to follow the observed values and thereby provide a simple means in controlling the cloud system dynamics by the large-scale momentum and shear (Johnson et al., 2002).

A CRM controlled with time-dependent large scale forcing over the whole domain was used as early as 1980 to investigate the response of shallow and deep convective clouds to large-scale processes (Soong and Ogura, 1980). Many other studies have been conducted in the past two decades over the tropical (e.g. Wu et al., 1998; Grabowski et al., 1996) and midlatitude regions (e.g. Xu and Randall, 2000; Khairoutdinov and Randall, 2003). CRMs and SCMs have been evaluated using data from field experiments of the Global Atmospheric Research Program's (GARP) Atlantic Tropical Experiment (GATE) (e.g. Xu and Randall, 1996; Grabowski et al., 1996; Grabowski, 1998) conducted in the northern hemisphere summer of 1974 and Tropical Oceans Global Atmosphere Coupled Ocean-Atmosphere Response Experiment (TOGA COARE) in November 1992 to February 1993 over the tropics (e.g. Woolnough et al., 2010).

The simulations were made for a few days or longer with two-dimensional (2-D) and three-dimensional (3-D) models and the objectives of the studies were to investigate the ability of models to simulate the statistical properties of cumulus ensembles with the observed large scale forcing. The detailed spatial structure and temporal evolution of simulated cloud systems were found to have a good correspondence with observations. Although the CRMs were able to successfully simulate the statistical properties of cumulus ensembles, some deficiencies were also found (Xu and Randall, 1996).

Simulations have also been made over the midlatitudes using field data from the

Southern Great Plains site of the Atmospheric Radiation Measurement (ARM) program (e.g. Khairoutdinov and Randall, 2003; Xu and Randall, 2000). The differences between simulated and observed temperature and moisture profiles, especially during convectively inactive portions in the midlatudes of the Intensive Observation Period (IOP) were found to be much larger over the midlatitudes than over the tropics (Xu and Randall, 2000), nevertheless CRMs were still found to be usefull tools to study midlatitude convection.

In this study, forcing data from the TOGA COARE field experiment is used, to simulate three separate periods dominated by suppressed convection which includes the end of a previous period of deep convection and start of subsequent period of convection (Woolnough et al., 2010). The case study was investigated by the Precipitating Cloud Systems Working Group (PCSWG) of the Global Energy and Water Cycle Experiment (GEWEX) Cloud System Study (GCSS). The aim of PCSWG was to support the development of the parameterisation of precipitating convective cloud systems in global climate models and numerical weather prediction models (Petch et al., 2007).

Simulations with the Nonhydrostatic σ-coordinate model (NSM) are made using a domain size of 256 km in horizontal extent, with a 2 km horizontal resolution. The model top is situated at 10 hPa and the model surface is the observed surface pressure which is prescribed at every time step. Two microphysics schemes, the PURDUE-LIN (Chen and Sun, 2000) and the SBU-YLIN (Lin and Colle, 2011) which were discussed in more details in Chapter 3 are used. Simulations with the PURDUE-LIN scheme are made both with and without graupel. Simulations made with graupel are called PURDUE-LIN1 and those without graupel are termed PURDUE-LIN2.

5.2 TOGA COARE

TOGA COARE is an observational and modelling program aimed at understanding the basic processes that maintain the warmest waters of the oceans and the role the warm water play in determining the mean state and variability of climate. The TOGA COARE intensive observing period (IOP) took place from 1 November 1992 to February 1993 in the near equatorial western pacific ocean, part of a region commonly referred to as the warm pool (Webster and Lukas, 1992). The intensive flux array (IFA) is the focus area of many of the observing systems deployed during TOGA COARE, it is a region of about 400 *km* by 250 *km* centred on 2^0S and 155^0E (Petch et al, 2007).

A number of CRM sentivity studies have been conducted using TOGA COARE for forcing and validation. Wu et al. (1998) made simulations for the period 5 December to 12 January using TOGA COARE forcing employing a 2-D CRM with a 3 *km* resolution. Model produced temperature and moisture fields were found to generally agree with those observed except during undisturbed periods that occur after strong convective events.

Gao et al. (2006) used forcing derived from TOGA COARE to simulate thunderstorms with a 2-D cloud-resolving model with ice clouds and the other without ice clouds for the period 18 December 1992 to 9 January 1993. Simulations with ice were found to be more realistic compared to those without ice in the upper troposphere. The simulation excluding ice microphysics was found to produce a smaller surface rain rate than the simulation including ice microphysics. The mass-weighted mean temperature was found to be colder and the amount of precipitable water larger in the simulation excluding ice microphysics because the absence of ice hydrometeors in the simulation produces a smaller cloud heating and consumes a smaller amout of vapour.

Johnson et al. (2002) tested the effect of the horizontal domain size on simulations made for 19-27 December 1992 using TOGA COARE forcing. They concluded that a horizontal domain of at least 512 *km* was needed to simulate the active convective cloud system features which had scales of several hundred kilometers. They found that a small domain size of 128 *km* allowed more cloud water and ice mass to remain in the model domain, leading to a greater and unrealistic layer of cloudiness in the 200 *mb* ice and 600 *mb* cloud water layer regions, while a larger domain was generally drier. They attributed this to a greater latent heating release due to greater net condensation and deposition in the largest domain. Overall, the increased latent heat release with increased grid domain size resulted in 10.5 *mm* more average total rainfall for the bigger domain case compared to the smaller domain.

In this study simulations for a case study investigated by PCCSWG of GCSS for three TOGA COARE suppressed and active convection periods are made. The objective of the case study was to examine the role of the convective process in moistening the atmosphere during the suppressed phase of the Madden-Julian Oscillation (MJO) and assess the impact of moistening on the subsequent evolution of the convection in numerical simulations. Willet et al. (2008) described results from Global Atmospheric Models (GAMs) for the case study which showed that all the GAMs were able to distinguish between suppressed and active regimes. Petch et al. (2007) simulated periods of suppressed and active convection using a CRM, global Numerical Weather Prediction (NWP) model and an SCM version of the NWP model. Woolnough et al. (2010) compared simulations made with CRMs. Each experiment begins with a few days of active convection to spin up the CRMs. This is followed by periods of suppressed convection and then active convection, with a transition between the suppressed and active periods (Table 5.1).

$$\frac{Du}{Dt} + \frac{\partial \phi}{\partial x} - \sigma \frac{\partial \phi}{\partial \sigma}\frac{\partial \ln p_s}{\partial x} - \left(\frac{\partial u}{\partial t}\right)_l = 0 \tag{5.2.1}$$

$$\left(\frac{\partial u}{\partial t}\right)_l = -\frac{< u > - u_{obs}}{\tau} \tag{5.2.2}$$

$$\frac{DT}{Dt} - \frac{R_d T \omega}{c_p p} = S_h + radhr + \left(\frac{\partial T}{\partial t}\right)_l \tag{5.2.3}$$

$$\frac{Dq_v}{Dt} = S_v + \left(\frac{\partial q_v}{\partial t}\right)_l \tag{5.2.4}$$

The large scale advective tendencies of potential temperature and water vapour which are provided six hourly were made by Ciesielski et al. (2003). These tendencies are interpolated linearly to the NSM's vertical grid and every time step and applied directly to the NSM (Equation 5.2.3 and 5.2.4). The domain average NSM's simulated horizontal winds ($< u >$) are relaxed towards the observed horizontal wind (u_{obs}) with a timescale (τ) of 2 hours and applied at every time step (Equation 5.2.1 and 5.2.2). Similar to Woolnough et al (2010) the large scale forcing is applied only upto 150 hPa level. The Sea Surface Temperatures (SSTs) and surface pressure are prescribed at every time step. Surface fluxes are calculated using aero dynamic equations as described in Holtslag and Boville (1993) (discussed in more detail in Chapter 3). The NSM is run without a radiation scheme, however a radiative cooling of $2K/day$ is applied in the troposphere.

The three periods are from 28 November to 10 December (A0), 9 January to 21 January (B0) and a shorter period of 21 January to 29 January(C0). Active

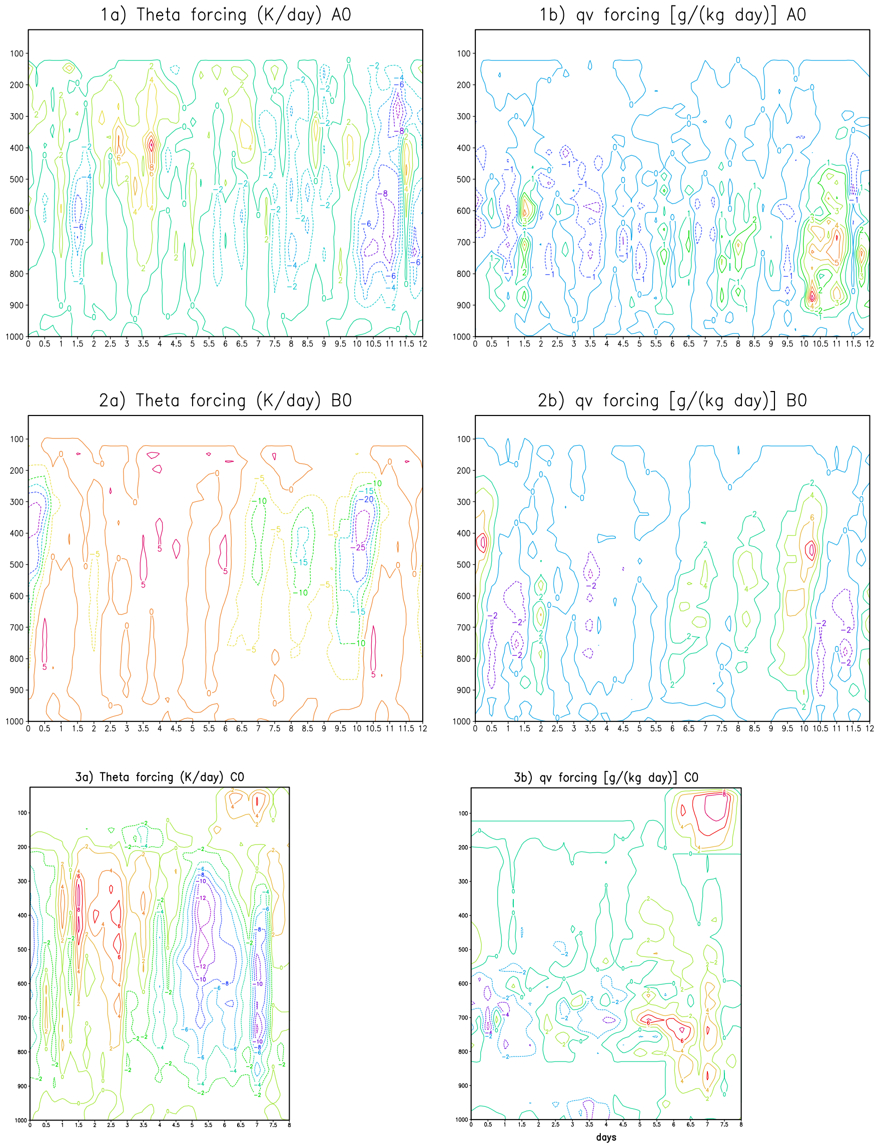

Figure 5.2.1: The large-scale advective tendencies of potential temperature for the 1a) A0, 2a) B0 and 3a) C0 experiments and water vapour mixing ratio for the 1b) A0, 2b)B0 and 3)C0 experiments that are interpolated to the NSM's grid and applied directly at every time step.

Periods	A0 (days)	B0 (days)	C0 (days)
spin up - deep convection	1 to 2 - two	1 to 2- two	1 to 2 - two
suppressed	3 to 5 - three	4 to 6 - three	3 to 4 - two
transition	6 to 10 - five	7 - one	5 - one
deep convection	11 to 12 - two	8 to 11 - four	6 to 8 - three

Table 5.1: The types of events expected during the different days simulated for experiments A0, B0 and C0. Number written in symbols represent the day of the simulation, while the number written in full words represent the total number of days each event was observed.

and suppressed periods are defined by the suppressed and active periods by the nature of the large-scale forcing applied (Woolnough et al., 2010; Figure 5.2.1). The suppressed periods are defined by periods when the large-scale forcing is acting to dry and warm the column. The active periods are defined by periods during which there is substantial cooling and moistening of nearly the entire column by the large-scale forcing.

Each of the experiments (A0, B0 and C0) were run initially for day 1 of the simulation, with updated large scale tendencies. The simulated average temperature and water vapour mixing ratio in x were then replaced with the initial condition temperature and water vapour mixing ratio at every time step. In this way perturbations were generated and used with the initial conditions and the runs were resubmitted and allowed to simulate twelve (A0 and B0) or eight day (C0) periods.

5.3 Comparing Simulations with Observations

5.3.1 Temperature

5.3.1.1 A0 experiment

The simulations were compared with the reanalysed full fields generated by Ciesielski et al. (2003) and therefore correspond fully with the initial conditions and forcing fields used to make the simulation. Figure 5.3.1a shows observed temperatures over the twelve day period, with 6 hourly intervals of the A0 experiment, while Figure 5.3.1b shows how the temperature has changed over the twelve day period with respect to the initial conditions. The troposphere is generally warmer compared to the initial conditions. Almost throughout the simulated period, there is a cooler region at about 900 to 700 hPa level.

The simulated temperature by the three microphysics schemes (Figure 5.3.1. 2a,3a,4a) decreases significantly in the first few hours of the simulation. The heat seems to be transported from the lower parts of the troposphere to the upper parts. This is shown by a much warmer upper troposphere and stratosphere compared to the initial conditions in Figure 5.3.1.2b,3b,4b in the A0 experiment. The model reaches a steady state with lower temperatures in the lower troposphere and higher temperature in the upper troposphere and stratosphere after a few hours of simulation. This is a problem that will be investigated further beyond this study. It should also be noted that the model does not include a radiation scheme, a 2 K/day cooling is applied throughout the troposphere in all the simulations. All the microphysics schemes simulate a much cooler region between 700 and 900 hPa levels which is much thicker compared to the observations. The strong cooling is shorter in the PURDUE-LIN2 simulation ending in day 7 of the simulation. This suggests that the mechanism that leads to a cooler region in the observations is simulated by the NSM, the simulated cooler region is however thicker compared to the observations.

5.3.1.2 B0 experiment

The observed atmosphere is generally cooler in the upper troposphere in the B0 experiment compared to the initial conditions. The first half of the B0 experiment period is generally cooler in the lower troposphere compared to the second half in the observations. Similar to the A0 simulations, the NSM cools rapidly in the first few hours of the simulation and reaches a steady state after about a day (Figure 5.3.2). The steady state is reached when the lower troposphere is much cooler than the initial conditions and observations while the upper troposphere and stratosphere are much warmer compared to the observations and initial conditions. The NSM simulates much cooler conditions during days 6 to 8 with all the microphysics schemes, however this feature is not observed. The three days cover periods of suppressed convection, transition to deep convection and deep convection. Apart from the three days of significant cooling in all the microphysics scheme realisations, SBU-YLIN is generally warmer compared to the PURDUE-LIN simulations between 900 and 600 hPa levels. This shows that PURDUE-LIN scheme simulates processes that cool the atmosphere in that region that the SBU-YLIN scheme is not capturing probably because of different hydrometeors simulated by the different schemes.

5.3.1.3 C0 experiment

The C0 experiment period is generally cooler thoughout the atmosphere in comparison with the initial conditions (Figure 5.3.3). The simulated temperature decreases quickly in the first few hours of simulation as already noted in the A0 and B0 experiments. The troposphere is simulated to be much cooler compared to the observations expecially after a day and half. The simulated cooling is bigger than in the A0 and B0 experiments, similar to observations. This suggests that although the model has a general bias of being cooler in the lower and middle troposphere, and warmer in the upper troposphere and stratosphere, it is still able to capture the general changes in the atmosphere due to the large scale forcing.

5.3.2 Specific Humidity

5.3.2.1 A0 experiment

The deep convection periods of the A0 experiments are characterised by moister conditions in the upper troposphere compared to other days of the simulation period (Figure 5.3.4.1b). The specific humidity is higher everywhere in the lower troposphere upto the 600 hPa level throughout the 12 days period compared to the initial conditions. The moister region corresponds to the cooler region seen in the temperature figures. This suggests that hydrometeors generally melt and evaporate in the layer increasing the amount of water vapour in the atmosphere while cooling the atmosphere at the same time because of latent heat absorption.

The simulated atmosphere becomes much drier than the initial conditions and observations in the first few hours of the simulation, and then it recovers at some point but not to the magnitudes in the initial conditions or observations. The cooler and drier troposphere are in agreement because cooler air carries less water vapour than warmer air. Although much drier than the observations, there is a layer close to the 900 hPa level that is less dry in comparison to layers below and above. This suggests that the NSM is able to capture the mechanism that gives rise to a cooler and moister region near the 900 hPa level.

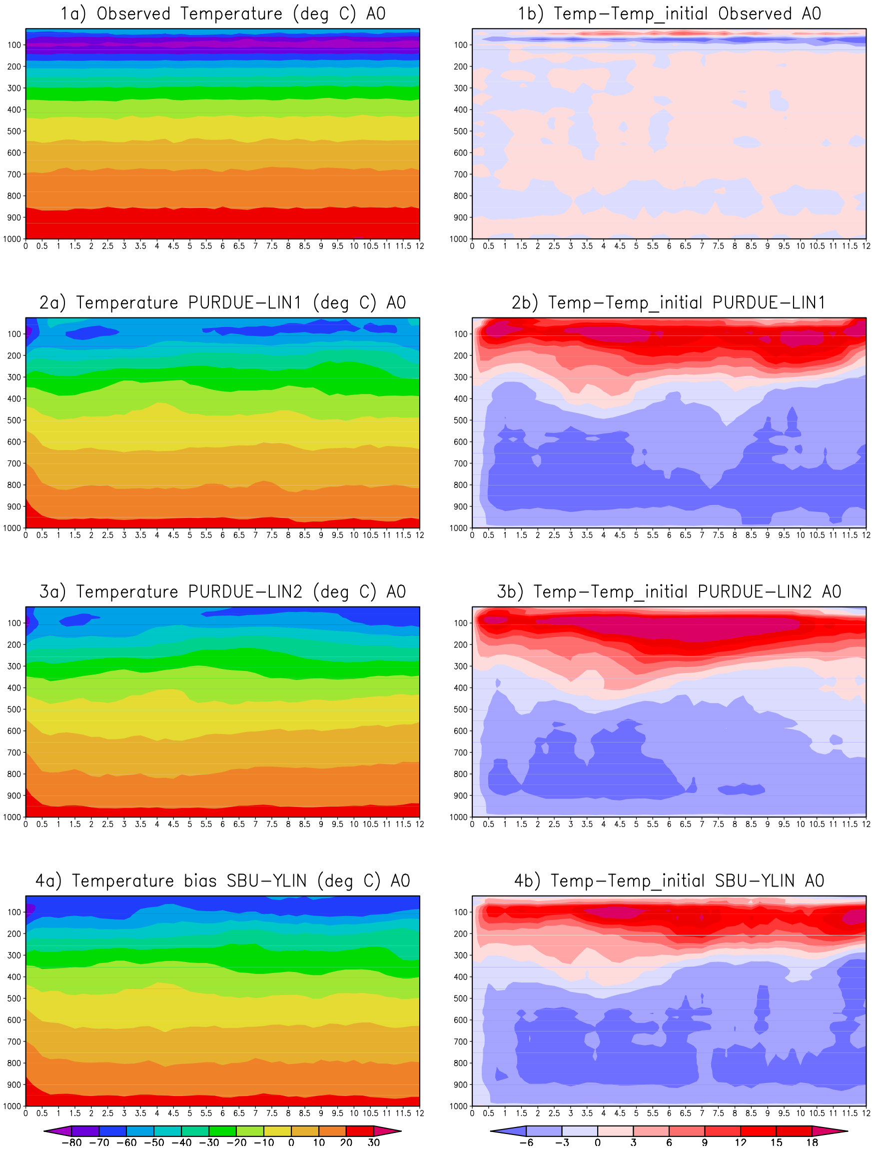

Figure 5.3.1: Observed 1a) temperature b) change in temperature from the initial conditions, simulated temperature and change from the initial conditions by the 2a) and 2b) PURDUE-LIN1 scheme, the 3a) and 3b) the PURDUE-LIN2 and the 4a and 4b) the SBU-YLIN schemes respectively over the A0 twelve day period. The x-axis shows time in days and y-axis shows height in hPa.

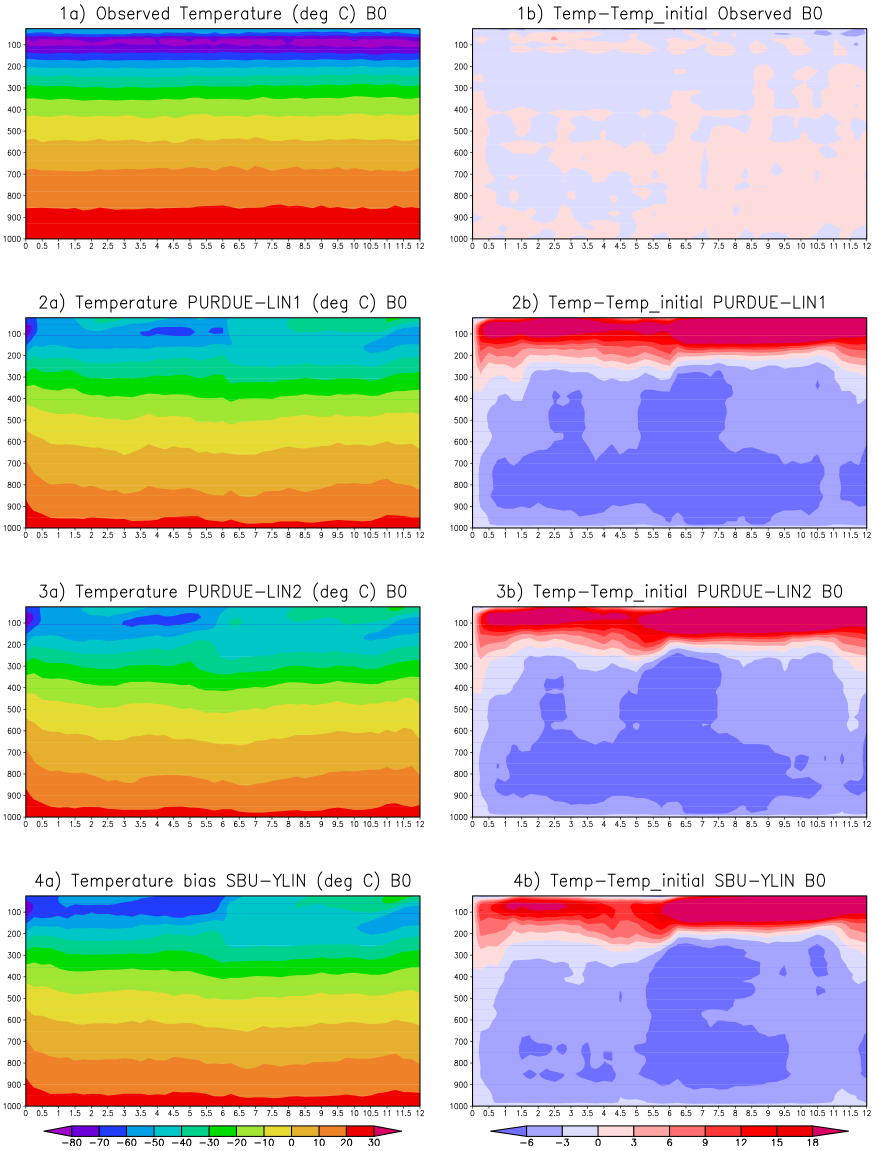

1a) Observed Temperature (deg C) B0

1b) Temp−Temp_initial Observed B0

2a) Temperature PURDUE−LIN1 (deg C) B0

2b) Temp−Temp_initial PURDUE−LIN1

3a) Temperature PURDUE−LIN2 (deg C) B0

3b) Temp−Temp_initial PURDUE−LIN2 B0

4a) Temperature bias SBU−YLIN (deg C) B0

4b) Temp−Temp_initial SBU−YLIN B0

Figure 5.3.2: Observed 1a) temperature b) change in temperature from the initial conditions, simulated temperature and change from the initial conditions by the 2a) and 2b) PURDUE-LIN1 scheme, the 3a) and 3b) the PURDUE-LIN2 and the 4a and 4b) the SBU-YLIN schemes respectively over the B0 twelve day period. The x-axis shows time in days and y-axis shows height in hPa.

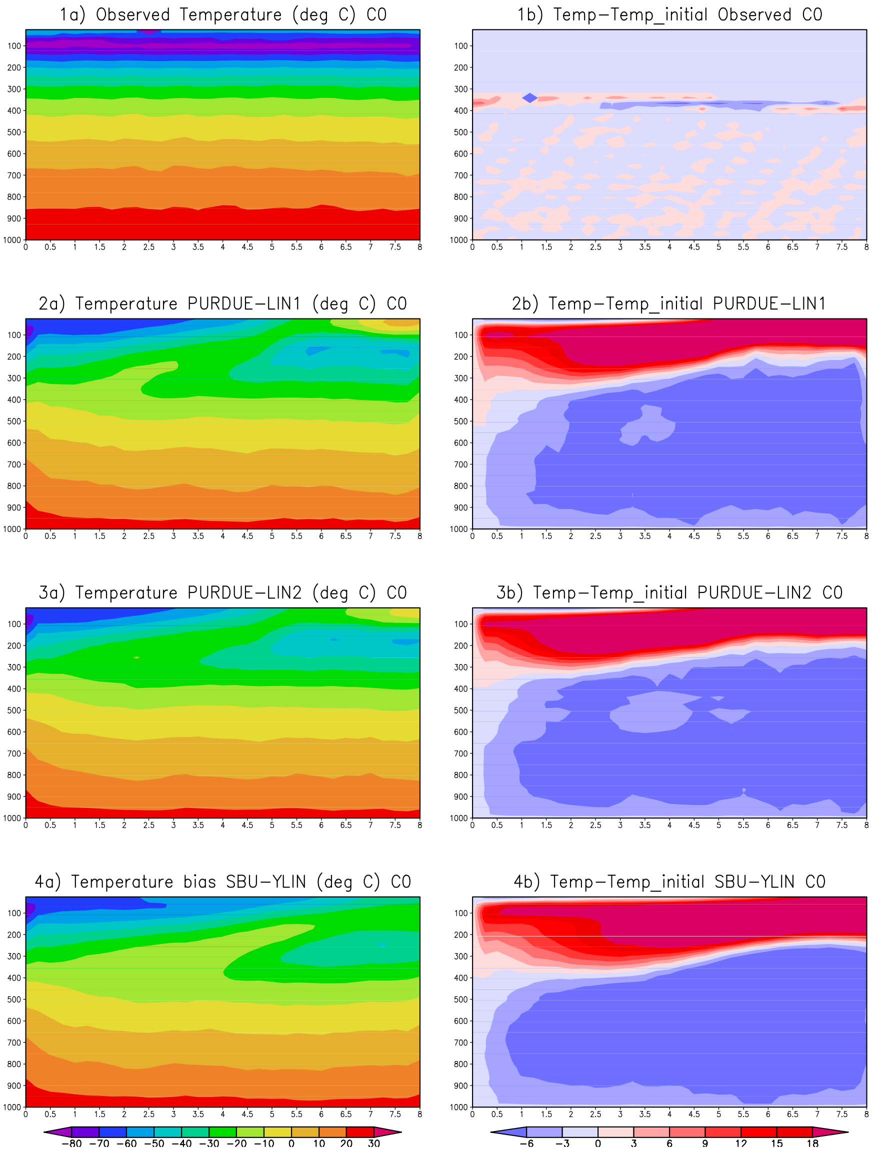

Figure 5.3.3: Observed 1a) temperature b) change in temperature from the initial conditions, simulated temperature and change from the initial conditions by the 2a) and 2b) PURDUE-LIN1 scheme, the 3a) and 3b) the PURDUE-LIN2 and the 4a and 4b) the SBU-YLIN schemes respectively over the C0 eight day period.The x-axis shows time in days and y-axis shows height in hPa.

The PURDUE-LIN2 simulation is less drier in the last 2 days of simulations which are expected to be associated with deep convection. The temperature was also simulated to be warmer compared to the PURDUE-LIN1 and SBU-YLIN microphysics scheme simulations.

5.3.2.2 B0 experiment

The B0 experiment period is much moister in day eight to twelve throughout the troposphere compared to the initial conditions (Figure 5.3.5). This is in agreement with findings of Lucas and Zipster (2000) who studied the TOGA COARE observations and found that during rainy periods, the midtroposphere was rather moist with relative humidities on the order of 70%, while during periods without widespread precipitation, the opposite was seen with relative humidities of ~40% in the midtroposphere. The transition to deep convection was observed in day 6 while days 7 to 11 were deep convection days. Days three to five were associated with suppressed conditions and were simulated by the three microphysics schemes to be drier. Days 7 to 11 were simulated to be less drier compared to the suppressed periods before and after them. Day 12 is much drier in all three simulations, but it was observed to be wetter compared to the initial conditions.

5.3.2.3 C0 experiment

The observed specific humidity was lower throughout the simulated period in the lower troposphere in the C0 experiment period in comparison to the initial conditions (Figure 5.3.6). The model simulated much drier conditions in the lower troposphere, compared to the observations. The simulated specific humidity values are smaller compared to in the other two experiments, similar to differences seen in observations.

5.3.3 Horizontal Winds

5.3.3.1 A0 experiment

The winds were observed to be westerly in a bigger part of the stratosphere during the deep convection period of the spin-up in the A0 experiment (Figure

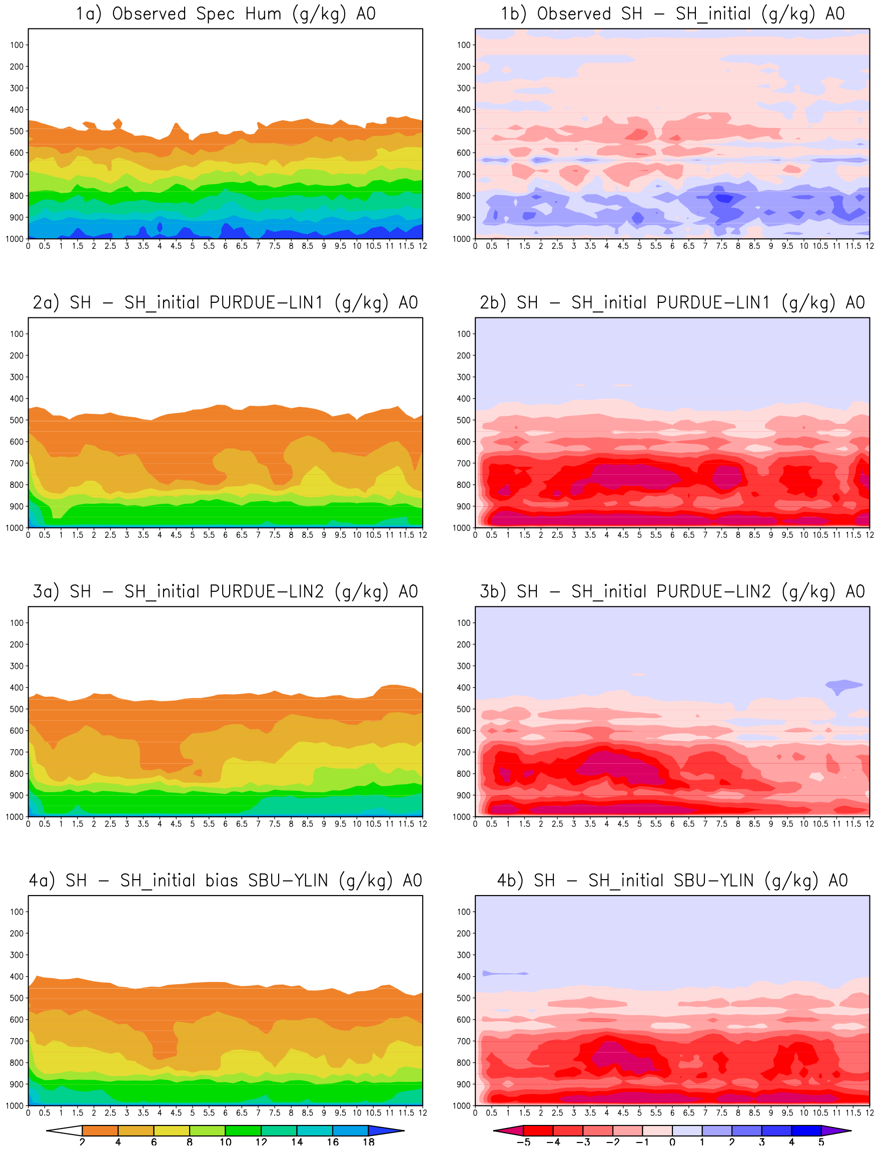

Figure 5.3.4: Observed 1a) Specific Humidity b) change in Specific Humidity from the initial conditions, simulated Specific Humidity and change from the initial conditions by the 2a) and 2b) PURDUE-LIN1 scheme, the 3a) and 3b) the PURDUE-LIN2 and the 4a and 4b) the SBU-YLIN schemes respectively over the A0 twelve day period. The x-axis shows time in days and y-axis shows height in hPa.

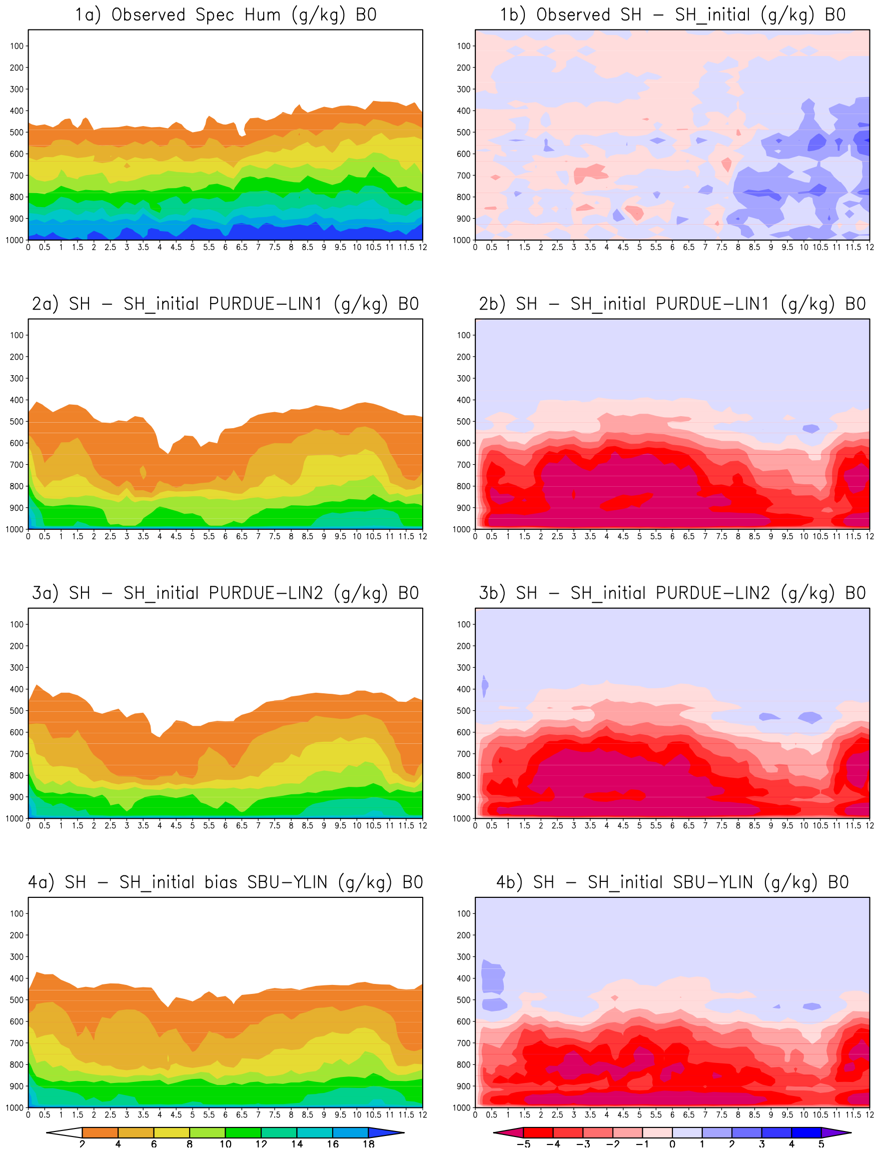

Figure 5.3.5: Observed 1a) Specific Humidity b) change in Specific Humidity from the initial conditions, simulated Specific Humidity and change from the initial conditions by the 2a) and 2b) PURDUE-LIN1 scheme, the 3a) and 3b) the PURDUE-LIN2 and the 4a and 4b) the SBU-YLIN schemes respectively over the B0 twelve day period. The x-axis shows time in days and y-axis shows height in hPa.

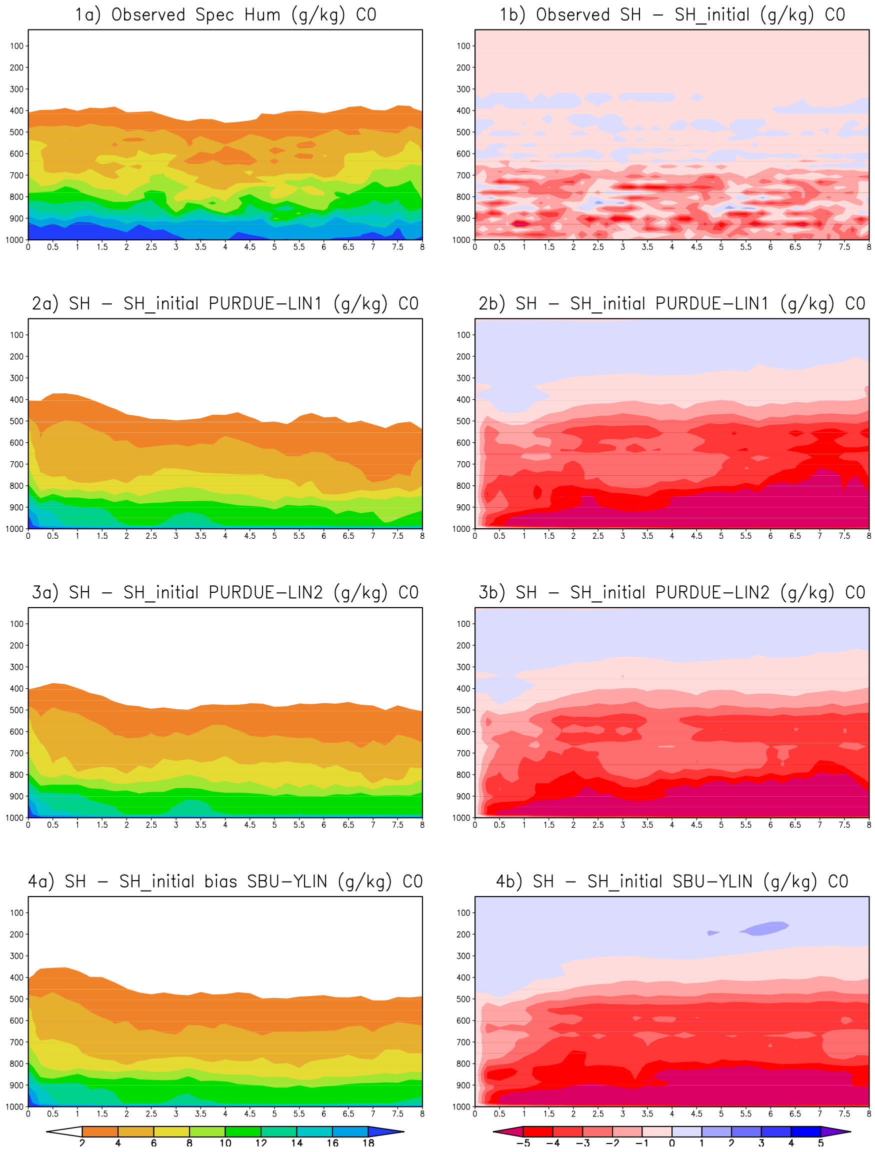

Figure 5.3.6: Observed 1a) Specific Humidity b) change in Specific Humidity from the initial conditions, simulated Specific Humidity and change from the initial conditions by the 2a) and 2b) PURDUE-LIN1 scheme, the 3a) and 3b) the PURDUE-LIN2 and the 4a and 4b) the SBU-YLIN schemes respectively over the C0 twelve day period. The x-axis shows time in days and y-axis shows height in hPa.

5.3.7). The transition period is initially associated with easterly winds and later the winds become westerly. The simulated winds were relaxed towards the observed winds at every time step. The simulated winds look very similar to the observed winds in troposphere. The differences are much bigger at the top of the domain where the relaxation is not applied.

5.3.3.2 B0 experiment

The observed wind is easterly during the deep convection in the spin up period in the mid trosphere in the B0 experiment (Figure 5.3.8). It then becomes westerly in the lower troposphere upto about 300 hPa level. During the four day deep convection period, the winds were found to be westerly along the lower troposphere and easterly in the upper troposphere. The direction in the upper troposphere extends to the stratosphere because of a lack of large scale forcing at the top of the model.

5.3.3.3 C0 experiment

During the deep convection of the spin-up period, the suppressed period and the transition period to convection the winds were observed to be westerlerly in the lower troposphere and generally easterly in the upper troposphere (Figure 5.3.9). The winds were opposite to those in the first period during the three day deep convection period. They were easterly in the lower troposphere and westerly in the upper troposphere. All the microphysics processes simulated similar directions as found in the observations.

5.4 Microphysics Effects

5.4.1 The spin-up period

Two twelve day (A0 and B0) and an eight day (C0) were made for three different periods that fall within the four months during which intensive observations were made in the warm pool for the TOGA COARE field experiment. Two microphysics schemes were used, PURDUE-LIN which is used with graupel (PURDUE-LIN1) and without graupel (PURDUE-LIN2), and the SBU-YLIN scheme. The twelve and eight day simulated periods are characterised by four

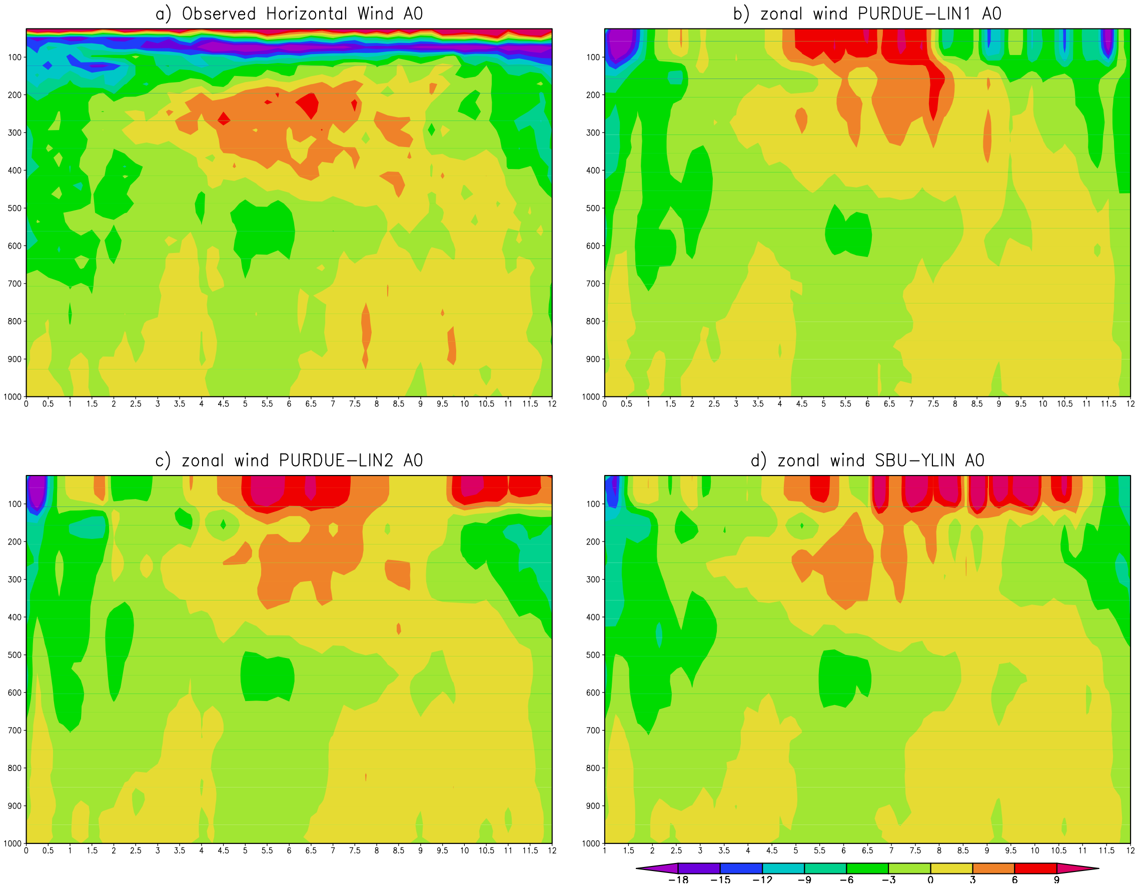

Figure 5.3.7: a) Observed average horizontal wind and simulated average horizontal wind as simulated by the NSM using the b) PURDUE-LIN1, c) PURDUE-LIN2 and d) SBU-YLIN scheme over the A0 twelve day period. The x-axis shows time in days and y-axis shows height in hPa.

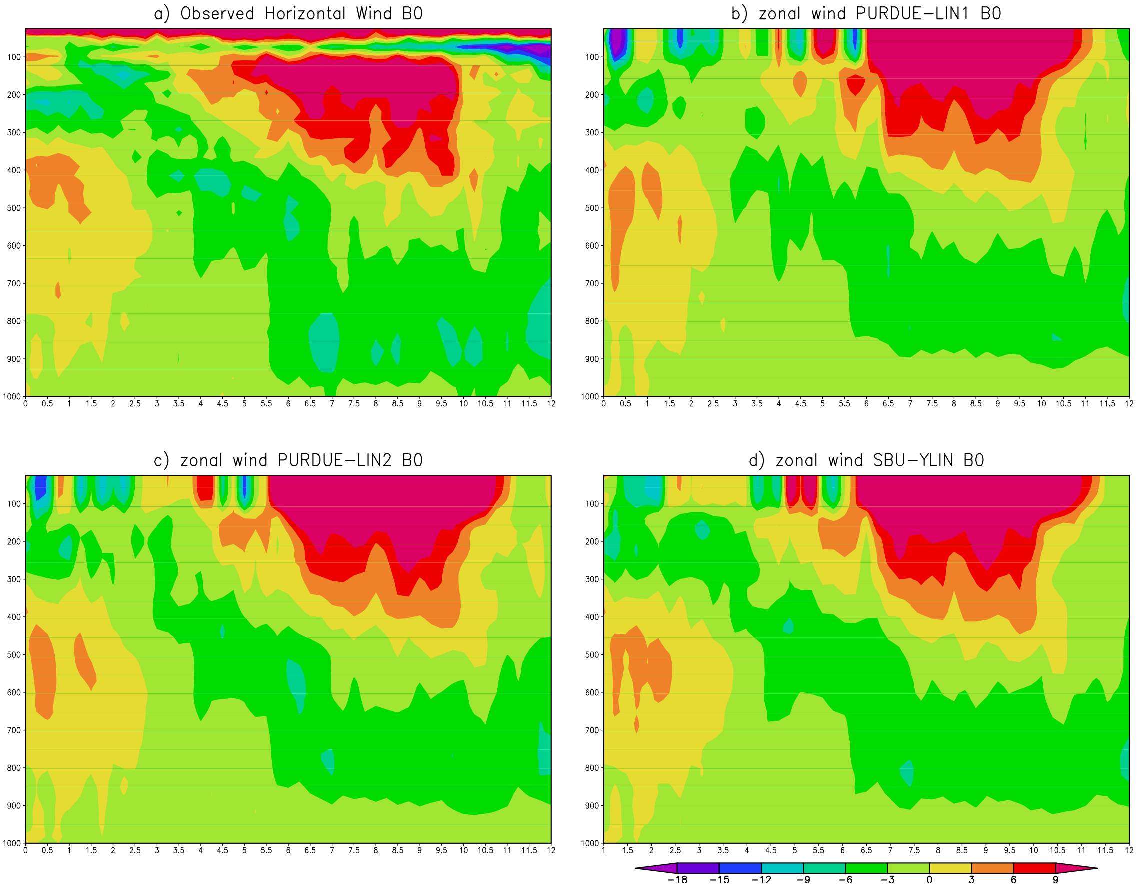

Figure 5.3.8: a) Observed average horizontal wind and simulated average horizontal wind as simulated by the NSM using the b) PURDUE-LIN1, c) PURDUE-LIN2 and d) SBU-YLIN scheme over the B0 twelve day period. The x-axis shows time in days and y-axis shows height in hPa.

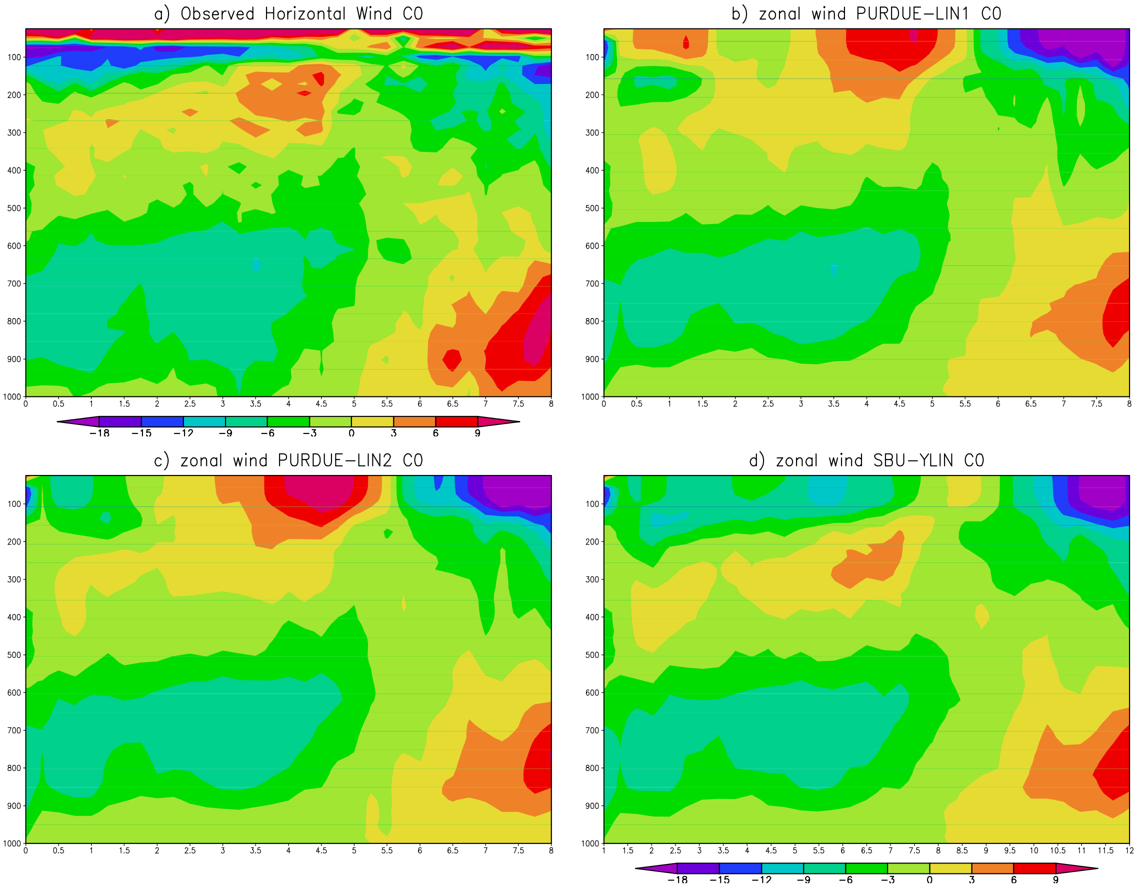

Figure 5.3.9: a) Observed average horizontal wind and simulated average horizontal wind as simulated by the NSM using the b) PURDUE-LIN1, c) PURDUE-LIN2 and d) SBU-YLIN scheme over the C0 twelve day period. The x-axis shows time in days and y-axis shows height in hPa.

different events (Table 5.1). For all three simulations, the first two days are associated with deep convection which is used to spin-up the models.

5.4.1.1 A0 experiment

Large scale cooling and moistening were applied in the first two days of the simulation for the three experiments. These conditions are favourable for convection to form. In the A0 experiment, convection formed before the end of the first two hours of simulation using all the three microphysics schemes (Figure 5.4.1). As soon as the hydrometeors started forming, the simulated maximum updrafts started looking different. In all three simulations with different microphysics schemes, the updrafts are stronger in the first day of simulation than in the second day of simulation. In the second day the updrafts are stronger in the PURDIE-LIN1 simulation and weaker in the SBU-YLIN simulations.

The differences in the simulated updrafts are likely to be because of the strength of the cold pools simulated using the different microphysics schemes. In the previous chapter it was shown that PURDUE-LIN1 generally simulates a stronger cold pool, which in turn triggers others storms. The simulations suggest that the PURDUE-LIN scheme simulates a stronger cold pool that is able to trigger stronger storms compared to other SBU-YLIN schemes. Simulated temperature differences (Figure 5.4.10) show that in the first two days of the simulation, the PURDUE-LIN2 and SBU-YLIN scheme are generally warmer closer to the surface than the PURDUE-LIN1 simulation which confirms the presence of a stronger cold pool. The SBU-YLIN scheme is the warmest along the surface.

The higher temperatures in the SBU-YLIN scheme compared to the PURDUE-LIN schemes extend into the middle and higher troposphere from about 12 hours until 24 hours in the PURDUE-LIN2 simulation and 26 hours in the PURDUE-LIN1 simulation. The higher temperatures suggest the presence of more ice in the SBU-YLIN scheme simulations which was associated with more latent heat release in its formation. The values of the total mixing ratio of ice (Figure 5.4.4) confirm that more ice was simulated by the SBU-YLIN scheme.

The PURDUE-LIN1 scheme acts quicker to remove cloud water and ice from the atmosphere because of the presence of graupel. This is confirmed by the amount of simulated ice by this scheme which is the least (Figure 5.4.4). The precipitating ice particles simulated by the SBU-YLIN scheme seem to be smaller in size compared to snow and graupel simulated by the PURDUE-LIN schemes. The

SBU-YLIN hydrometeors fall slower and hence produce weaker downdrafts and cold pools. PURDUE-LIN1 simulates the least amount of liquid water, while PURDUE-LIN2 simulates the highest amount of liquid water. This is because graupel and rain water remove cloud water from the atmosphere faster than will be possible in the PURDUE-LIN2 and SBU-YLIN schemes. The simulated liquid water is generally deeper in the SBU-YLIN scheme simulations.

5.4.1.2 B0 experiment

All the microphysics schemes simulate deep storms in the first 14 hours of the simulation. SBU-YLIN simulates the weakest updrafts in this period. Between 18 and 36 hours, SBU-YLIN simulates the strongest storms (Figure 5.4.2). The surface temperature are colder (Figure 5.4.11) in the PURDUE-LIN1 and PURDUE-LIN2 simulation which suggests that the cold pool may have a smaller role to play in the formation of the higher vertical speeds in the SBU-YLIN scheme between 18 and 36 hours. The storm looks like it is more triggered by the large scale tendencies that the cold pool. This suggests that the SBU-YLIN responds better to the large scale forcing. This is most likely because the SBU-YLIN scheme does not dry the atmosphere as quickly as the PURDUE-LIN schemes. Figure 5.3.4 4b shows that between 12 hours and about 36 hours, SBU-YLIN was moister than the PURDUE-LIN schemes.

The simulated total ice shows that total ice changes faster in the PURDUE-LIN schemes simulation with gaps of no ice before the end of day1 in the PURDUE-LIN schemes (Figure 5.4.5). Although the amount of ice reduced in the SBU-YLIN scheme simulation, there was still more ice left in the atmosphere than in the PURDUE-LIN schemes. Beyond 36 hours stronger vertical updrafts were simulated by the PURDUE-LIN schemes. The surface temperatures are much cooler in the PURDUE-LIN schemes compared to the SBU-YLIN scheme which suggests that the large scale forcing may have worked together with the cold pool to produce stronger storms in the PURDUE-LIN scheme simulations.

5.4.1.3 C0 experiment

The C0 experiment was made for eight days, and the first two days of the simulation are also used to spin up the model. The large scale cooling is applied directly at the beginning of the simulation which triggers convection in all three

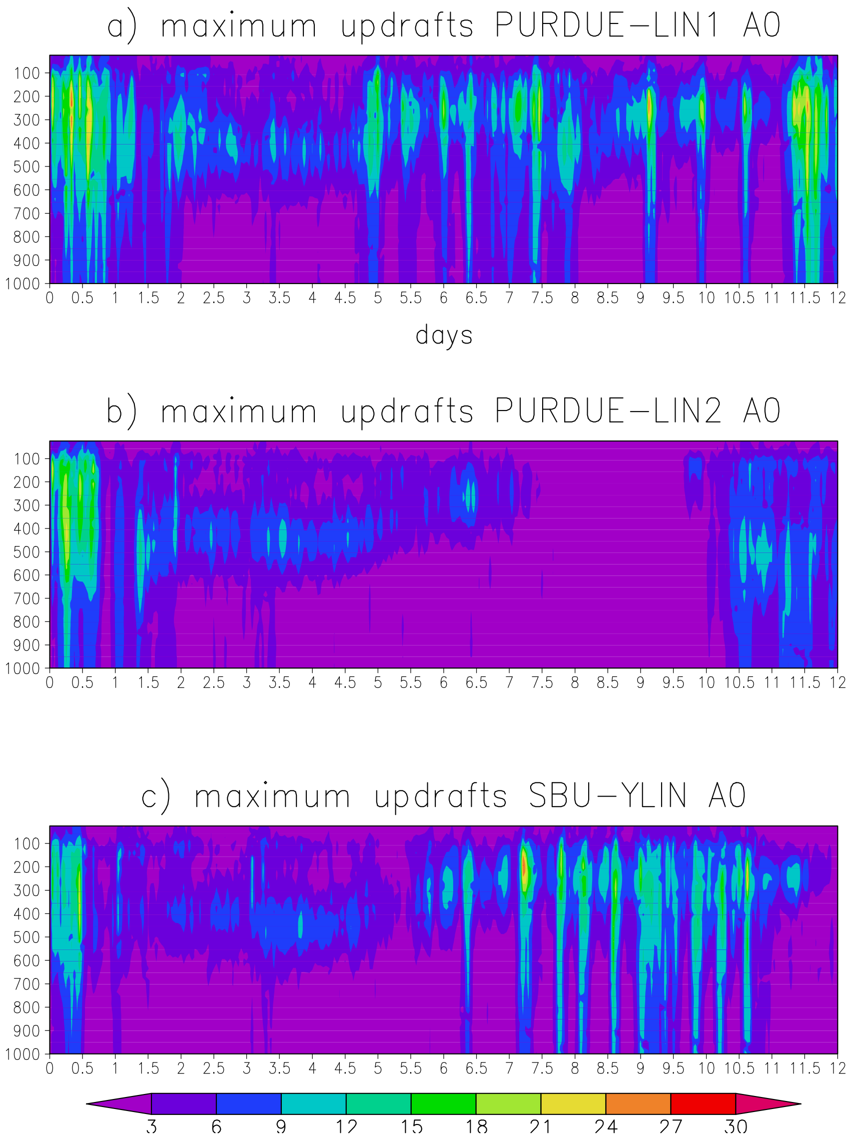

Figure 5.4.1: The simulated maximum updrafts using the a) PURDUE-LIN1, b) PURDUE-LIN2 and c) SBU-YLIN microphysics schemes in the twelve days of simulation for the A0 experiment. The x-axis shows time in days and y-axis shows height in hPa.

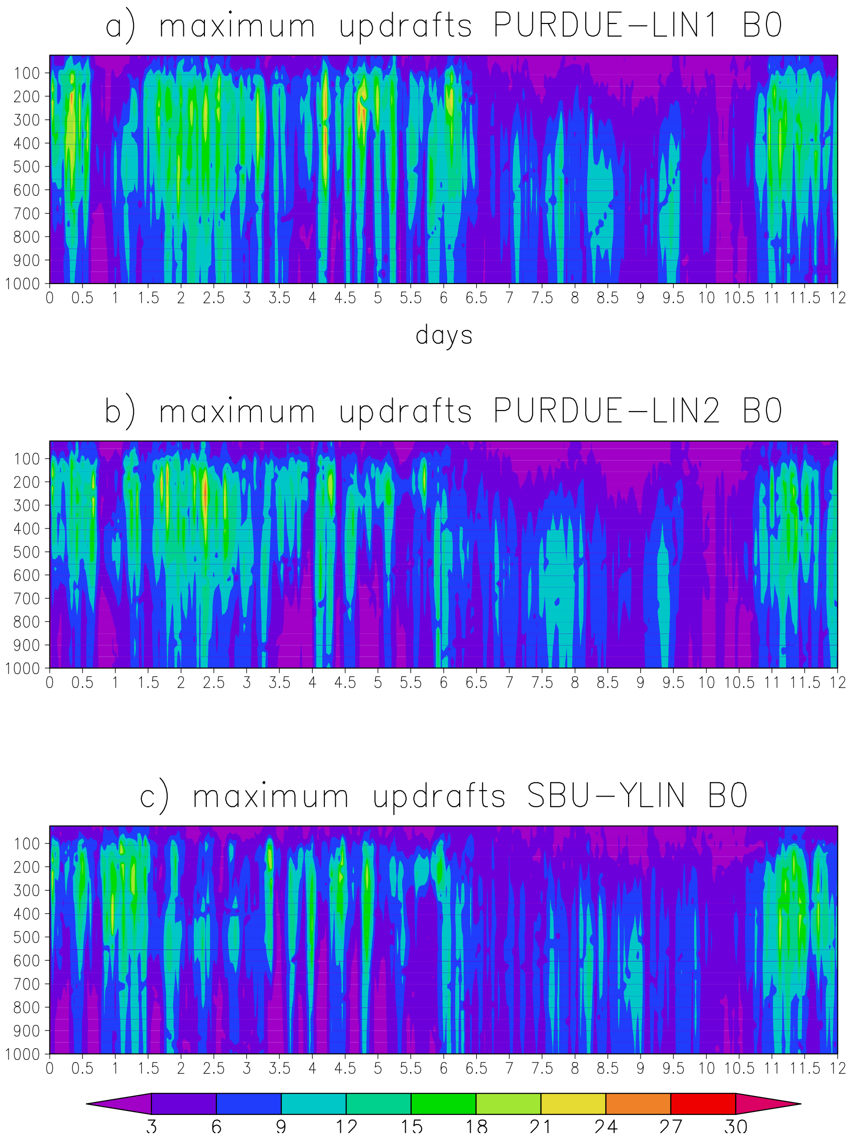

Figure 5.4.2: The simulated maximum updrafts using the a) PURDUE-LIN1, b) PURDUE-LIN2 and c) SBU-YLIN microphysics schemes in the twelve days of simulation for the B0 experiment. The x-axis shows time in days and y-axis shows height in hPa.

simulations with different microphysics schemes. The layer of maximum updrafts becomes thinner from about six hours of simulation and occurs in the upper troposphere. Beyond six hours SBU-YLIN simulates the least amount of maximum updrafts (Figure 5.4.3). SBU-YLIN simulates the highest amount of total ice, followed by PURDUE-LIN2 and PURDUE-LIN1 simulates the least amount of ice and changes much quicker than the other two schemes (Figure 5.4.6). SBU-YLIN simulates the deepest cloud water which again suggests that PURDUE-LIN1 acts to remove cloud water and cloud ice faster than SBU-YLIN and PURDUE-LIN2. PURDUE-LIN2 simulates the most cloud water at certain times (Figure 5.4.9).

5.4.2 The suppressed period

5.4.2.1 A0 experiment

The suppressed conditions in the A0 experiment last for three days. The simulated maximum updrafts are much smaller compared to those in the spin-up period discussed in the previous section (Figure 5.4.1). Some ice particles are simulated, but they are much smaller compared to the other periods. SBU-YLIN simulates two layers of ice particles (Figure 5.4.4). The simulated liquid water is the least in the PURDUE-LIN1 simulation, while SBU-YLIN simulates the thickest layer of liquid water similar to the previous section (Figure 5.4.7). Woolnough et al. (2010) found the suppressed period to be dominated by shallow convection with some updrafts penetrating above the melting level in the A0 experiment.

5.4.2.2 B0 experiment

The suppressed period in the B0 experiment also lasted for a period of three days. The convective activity is stronger than in the A0 experiment with more ice and liquid water simulated here (Figure 5.4.5). Some updrafts in this experiments were also found to penetrate beyond the melting level by Woolnough et al. (2010). This period forms part of the period where the large scale forcing was suspected to have errors (Woolnough et al., 2010). Temperatures in the SBU-YLIN scheme are generally higher than the PURDUE-LIN temperatures in the troposphere. This suggests that the cooler and drier biases that are found in the simulations are stronger in the PURDUE-LIN simulations.

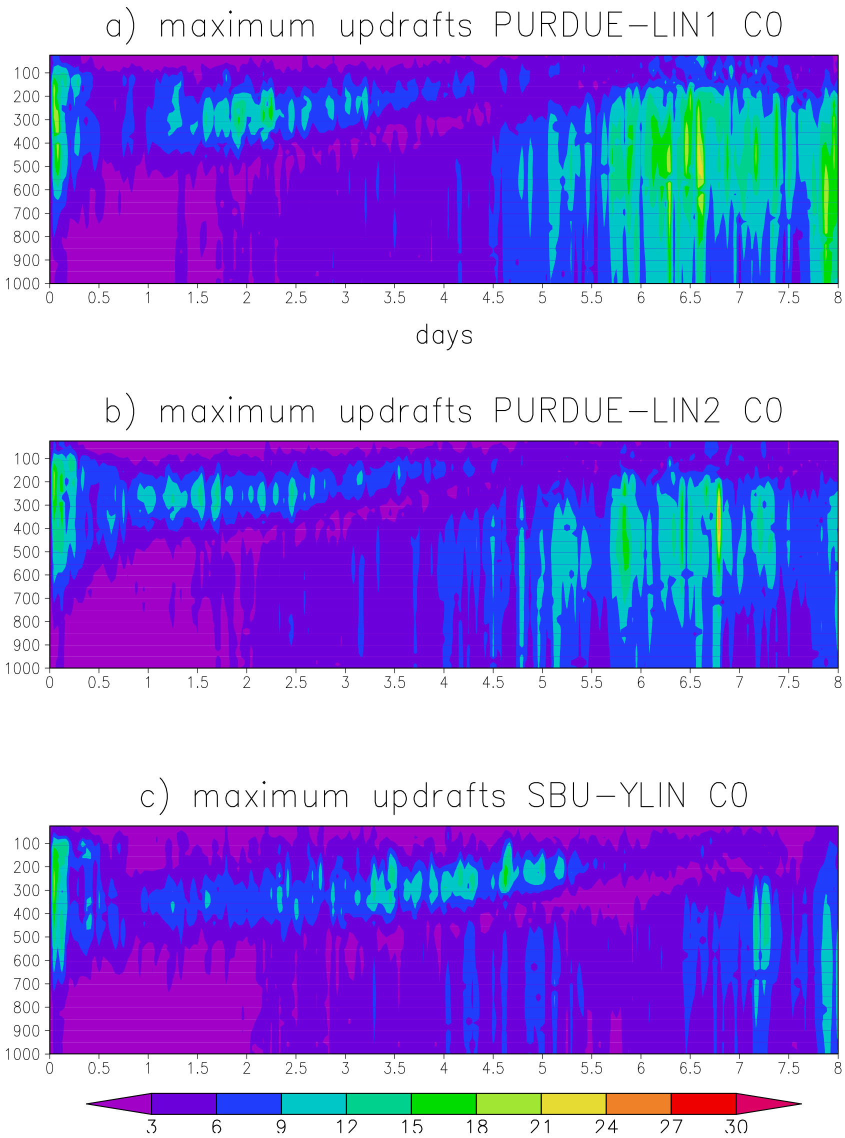

Figure 5.4.3: The simulated maximum updrafts using the a) PURDUE-LIN1, b) PURDUE-LIN2 and c) SBU-YLIN microphysics schemes in the eight days of simulation for the C0 experiment. The x-axis shows time in days and y-axis shows height in hPa.

5.4.2.3 C0 experiment

The highest updrafts occur at about 200 to 400 hPa levels. SBU-YLIN simulates two cloud levels, one a bit lower compared to the maximum updrafts (Figure 5.4.6). The PURDUE-LIN scheme simulates only one cloud layer with PURDUE-LIN1 simulating the least amount of ice. PURDUE-LIN2 simulates the highest amount of cloud water, while SBU-YLIN simulates the deepest amount of cloud water. Woolnough et al (2010) found the weakest updrafts in the C0 experiment that did not penetrate beyond the melting layer. The updraft simulations made by the NSM in this experiment are more similar to those made in experiment A0. B0 simulates much higher values of the updrafts than the two other experiments.

5.4.3 The transition period

5.4.3.1 A0 experiment

Experiment A0 has the longest transition period of the three experiments which is five days. The simulated maximum updrafts are stronger compared to the suppression period in the PURDUE-LIN1 and SBU-YLIN simulations (Figure 5.4.1). No recovery is simulated in the PURDUE-LIN2 simulations. This is despite the fact that large scale cooling and moistening are applied from the large-scale advective tendencies. This simulation illustrates the need for graupel in simulations. The temperature differences show that the PURDUE-LIN2 is generally much warmer compared to the PURDUE-LIN1 and SBU-YLIN. More ice is simulated by the SBU-YLIN scheme. Although the maximum updrafts are smaller in the simulation with PURDUE-LIN2 the simulated ice and liquid water are comparable with simulations made with the two other microphysics schemes (Figure 5.4.1).

5.4.3.2 B0 experiment

The transition period lasted for only one day in this experiment. Bigger updrafts are simulated in the first eight hours in this period by all the microphysics schemes. Similar to all other simulations the SBU-YLIN scheme is generally warmer than the PURDUE-LIN scheme in the lower and mid troposphere. The

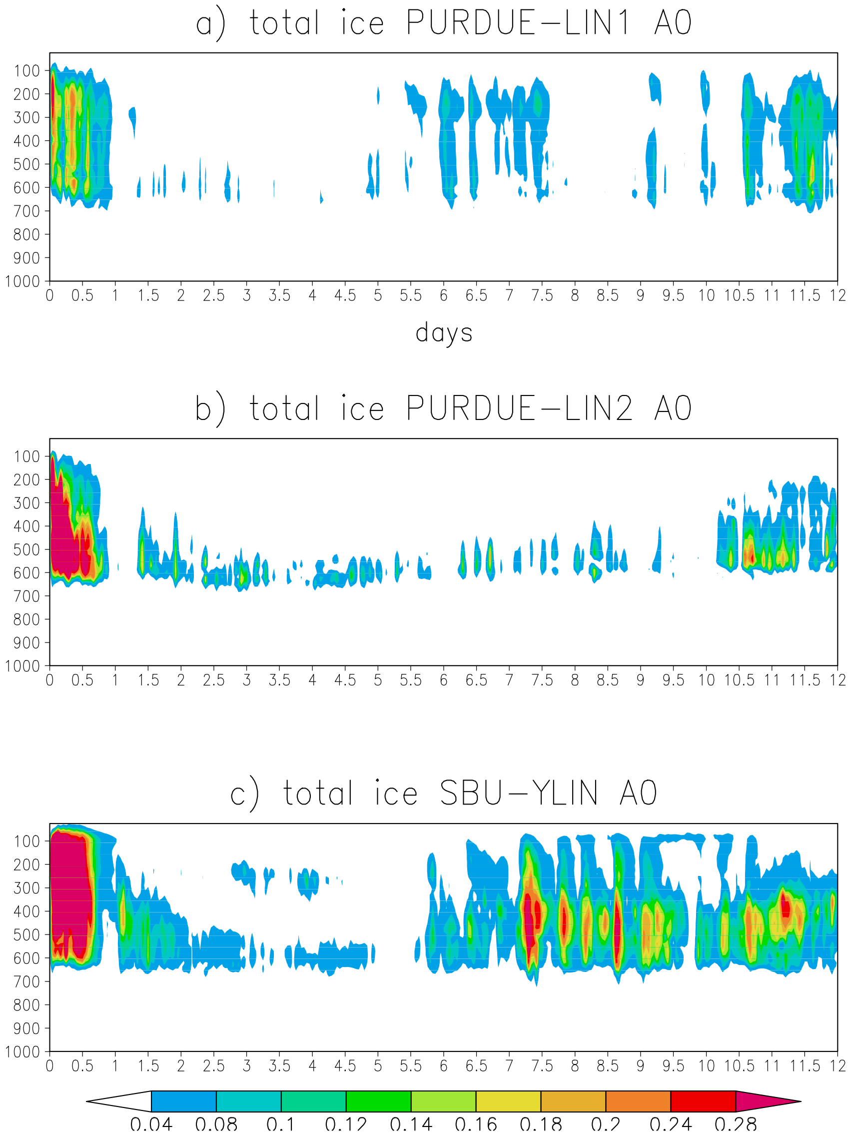

Figure 5.4.4: The simulated total ice using the a) PURDUE-LIN1, b) PURDUE-LIN2 and c) SBU-YLIN microphysics schemes in the twelve days of simulation for the A0 experiment. The x-axis shows time in days and y-axis shows height in hPa.

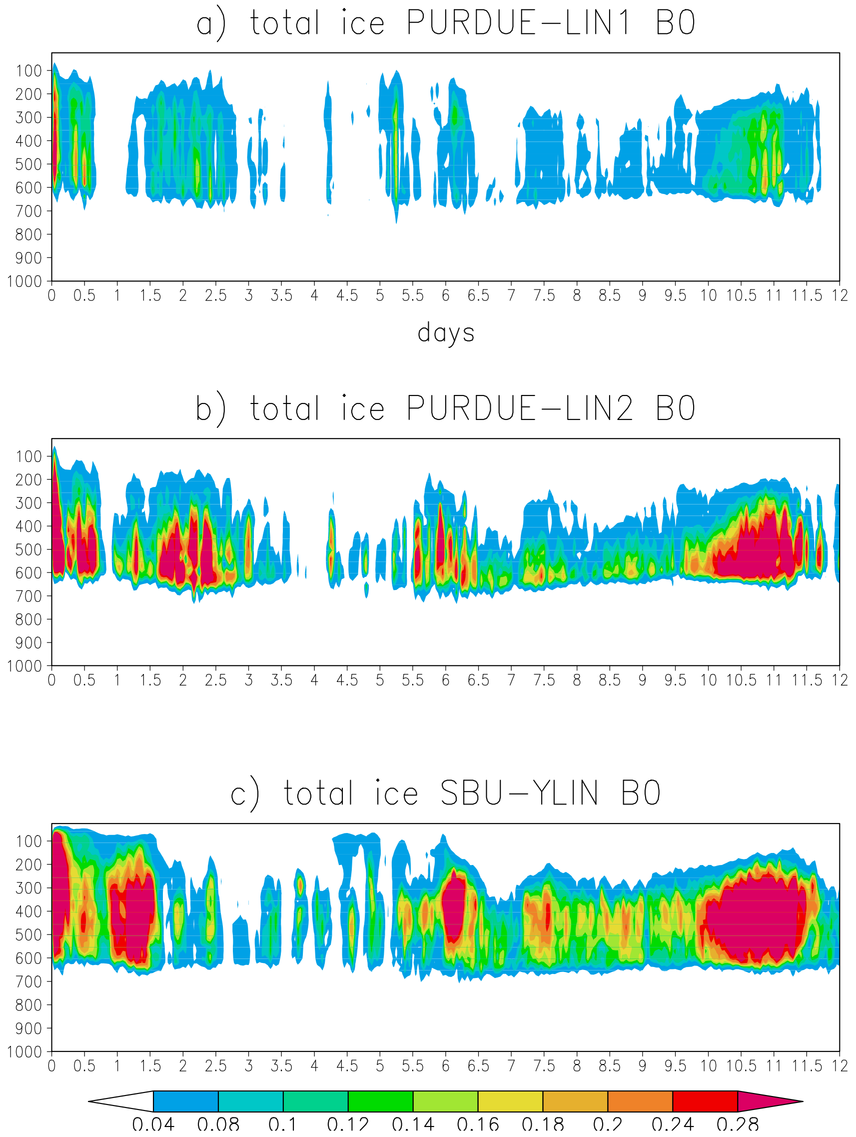

Figure 5.4.5: The simulated total ice using the a) PURDUE-LIN1, b) PURDUE-LIN2 and c) SBU-YLIN microphysics schemes in the twelve days of simulation for the B0 experiment. The x-axis shows time in days and y-axis shows height in hPa.

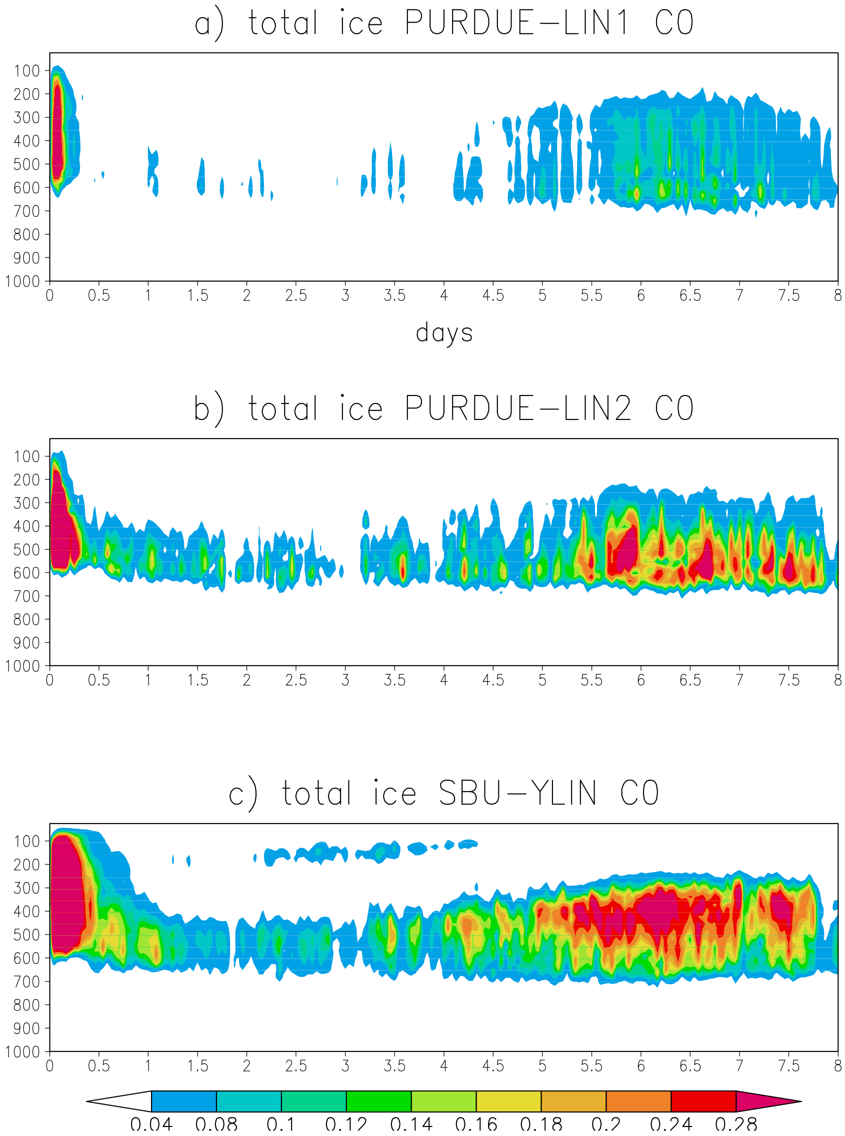

Figure 5.4.6: The simulated total ice using the a) PURDUE-LIN1, b) PURDUE-LIN2 and c) SBU-YLIN microphysics schemes in the eight days of simulation for the C0 experiment. The x-axis shows time in days and y-axis shows height in hPa.

SBU-YLIN scheme simulates the most ice. The simulated liquid water is deeper in the SBU-YLIN scheme simulations.

5.4.3.3 C0 experiment

The transition period lasted for only one day in this experiment as well. The maximum updrafts in the trasition period are much bigger than those in the suppressed period. The PURDUE-LIN schemes are generally colder compared to the SBU-YLIN scheme. PURDUE-LIN1 simulates the highest values of the updrafts. The PURDUE-LIN2 is generally warmer than the PURDUE-LIN1 simulations along the surface. That suggests the stronger updrafts in the PURDUE-LIN1 simulations may be a result of the strong cold pool working together with the large scale forcing that is favourable for deep convection to form. Woolnough et al. (2010) found a steady increase in precipitation in the simulations and observations during the transition between the suppressed period and the active period. There is a general recovery in the amount of simulated specific humidity in all the simulations during the transition period.

5.4.4 The active period

5.4.4.1 A0 experiment

SBU-YLIN simulates the highest updrafts during the first day, while PURDUE-LIN1 simulates the highest values during the second day of the active period. PURDUE-LIN2 simulates the smallest values of maximum updrafts and it is also found to be warmer than simulations with two other microphysics schemes. The PURDUE-LIN1 simulation is colder along the surface compared to SBU-YLIN until about hour 31. The stronger storms that PURDUE-LIN1 simulates occur at about 31 hours, SBU-YLIN does not simulate these storms.

5.4.4.2 B0 experiment

The SBU-YLIN scheme generally simulates regions of high values of the maximum updrafts a bit later than the PURDUE-LIN1 scheme. As shown in all other simulations, the SBU-YLIN scheme is generally warmer than the PURDUE-LIN simulations especially along the surface. PURDUE-LIN2 is generally warmer

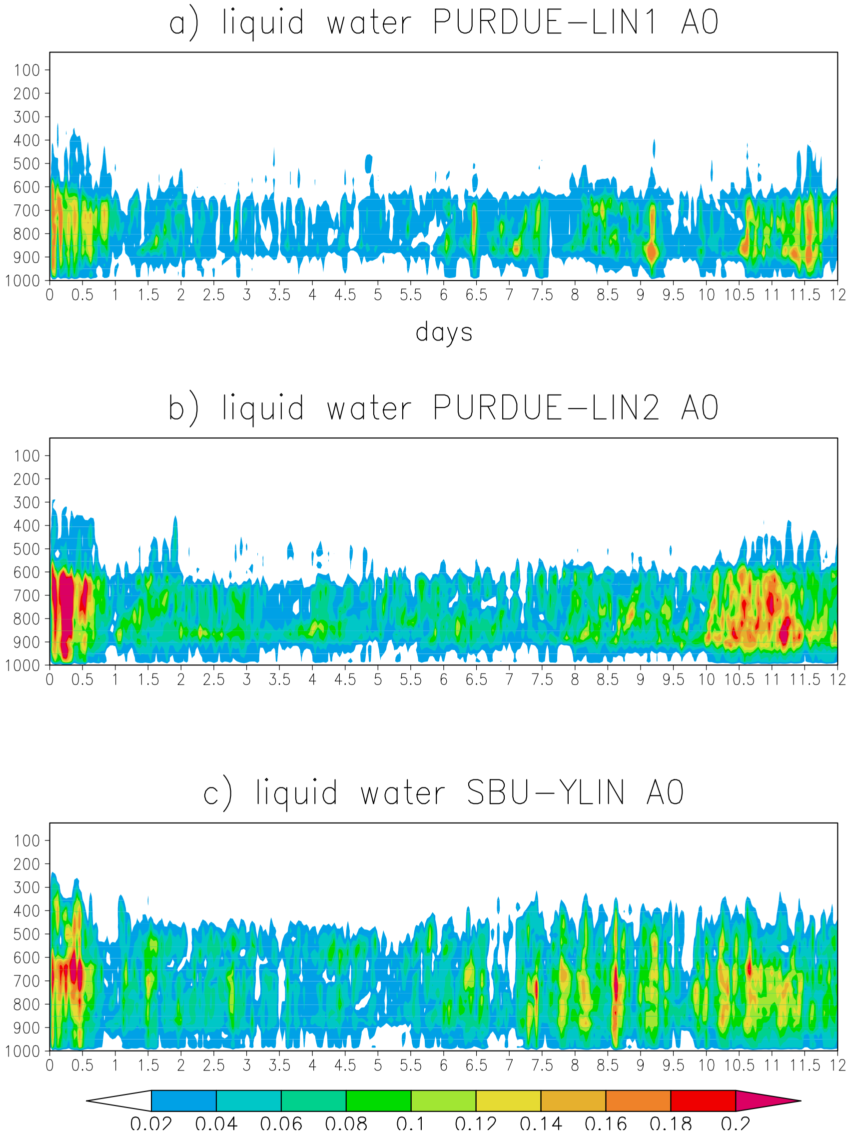

Figure 5.4.7: The simulated total liquid water using the a) PURDUE-LIN1, b) PURDUE-LIN2 and c) SBU-YLIN microphysics schemes in the twelve days of simulation for the A0 experiment. The x-axis shows time in days and y-axis shows height in hPa.

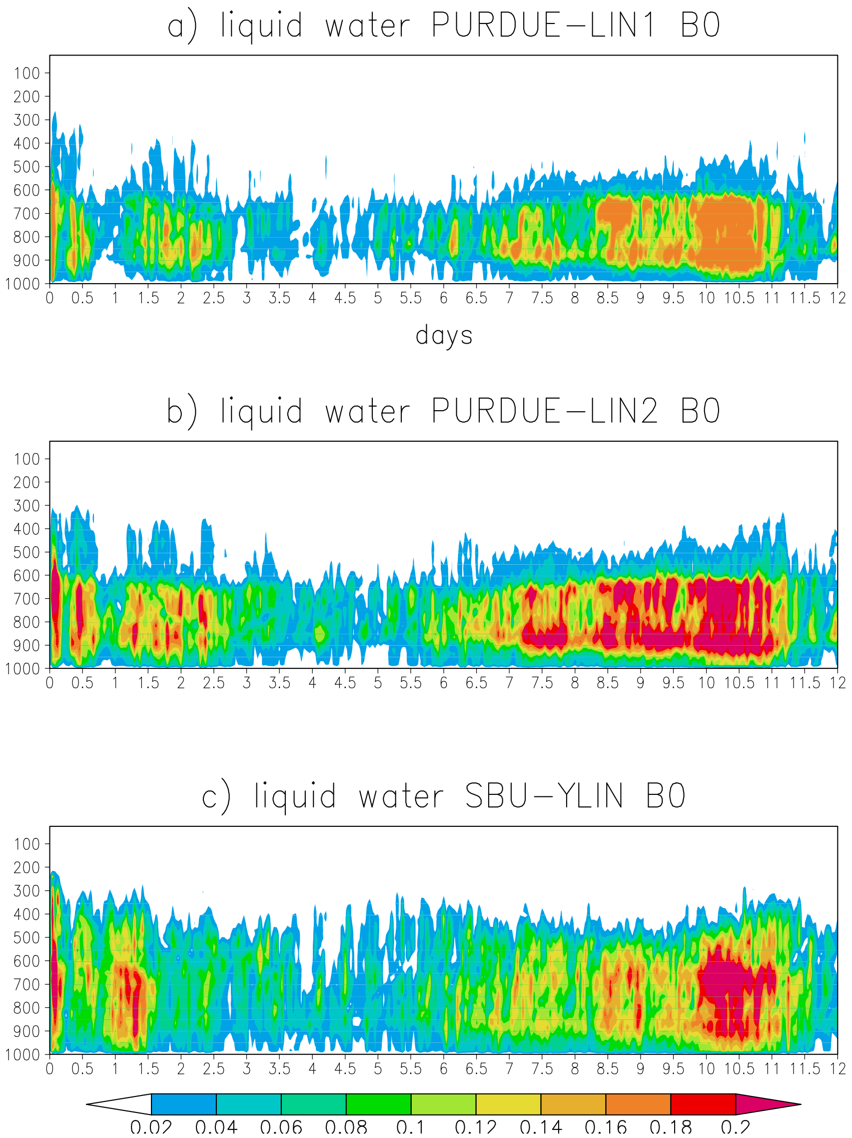

Figure 5.4.8: The simulated total liquid water using the a) PURDUE-LIN1, b) PURDUE-LIN2 and c) SBU-YLIN microphysics schemes in the twelve days of simulation for the B0 experiment. The x-axis shows time in days and y-axis shows height in hPa.

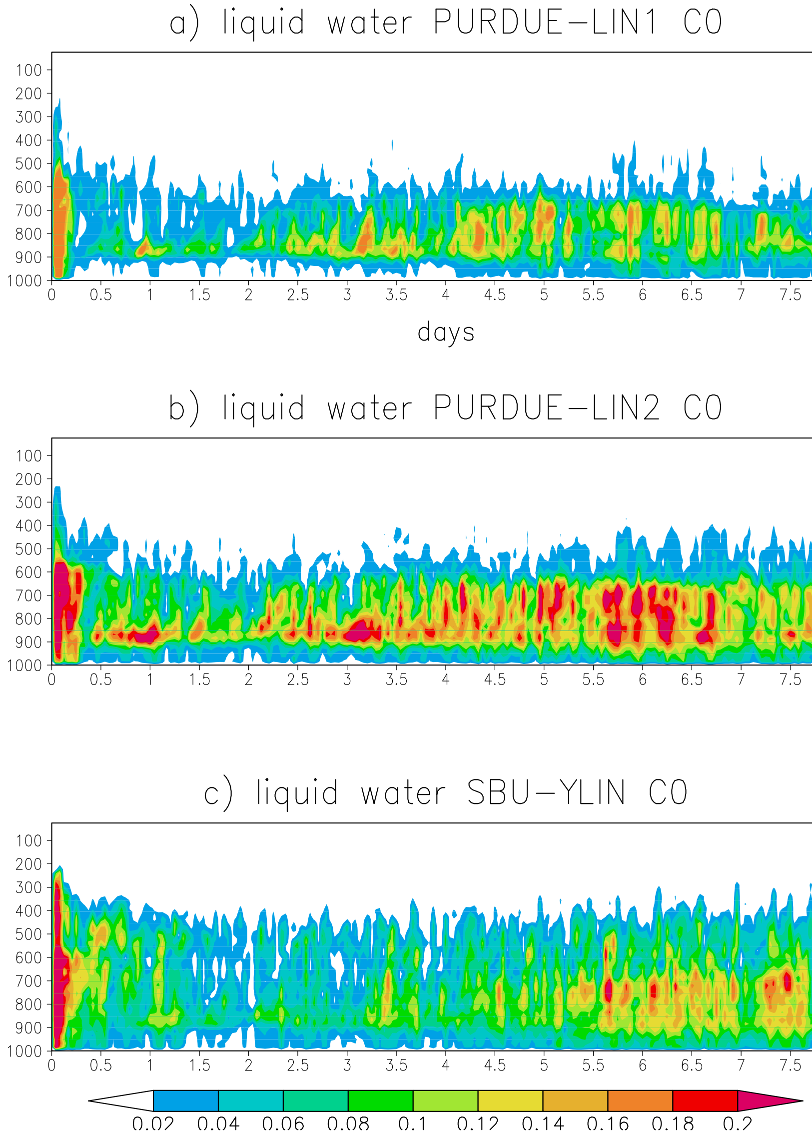

Figure 5.4.9: The simulated total liquid water using the a) PURDUE-LIN1, b) PURDUE-LIN2 and c) SBU-YLIN microphysics schemes in the eight days of simulation for the C0 experiment. The x-axis shows time in days and y-axis shows height in hPa.

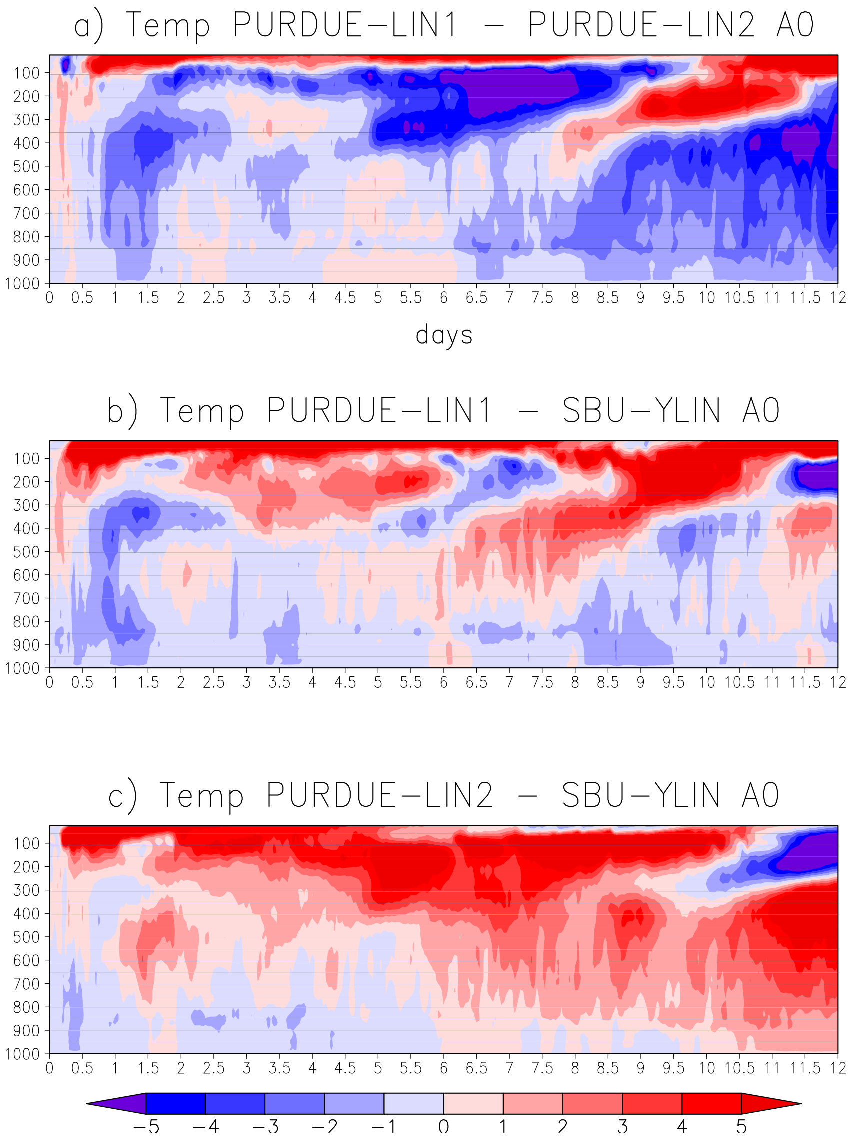

Figure 5.4.10: The simulated temperature difference between a) PURDUE-LIN1 and PURDUE-LIN2, b) PURDUE-LIN1 and SBU-YLIN and c) PURDUE-LIN2 and SBU-YLIN in the A0 experiment. The x-axis shows time in days and y-axis shows height in hPa.

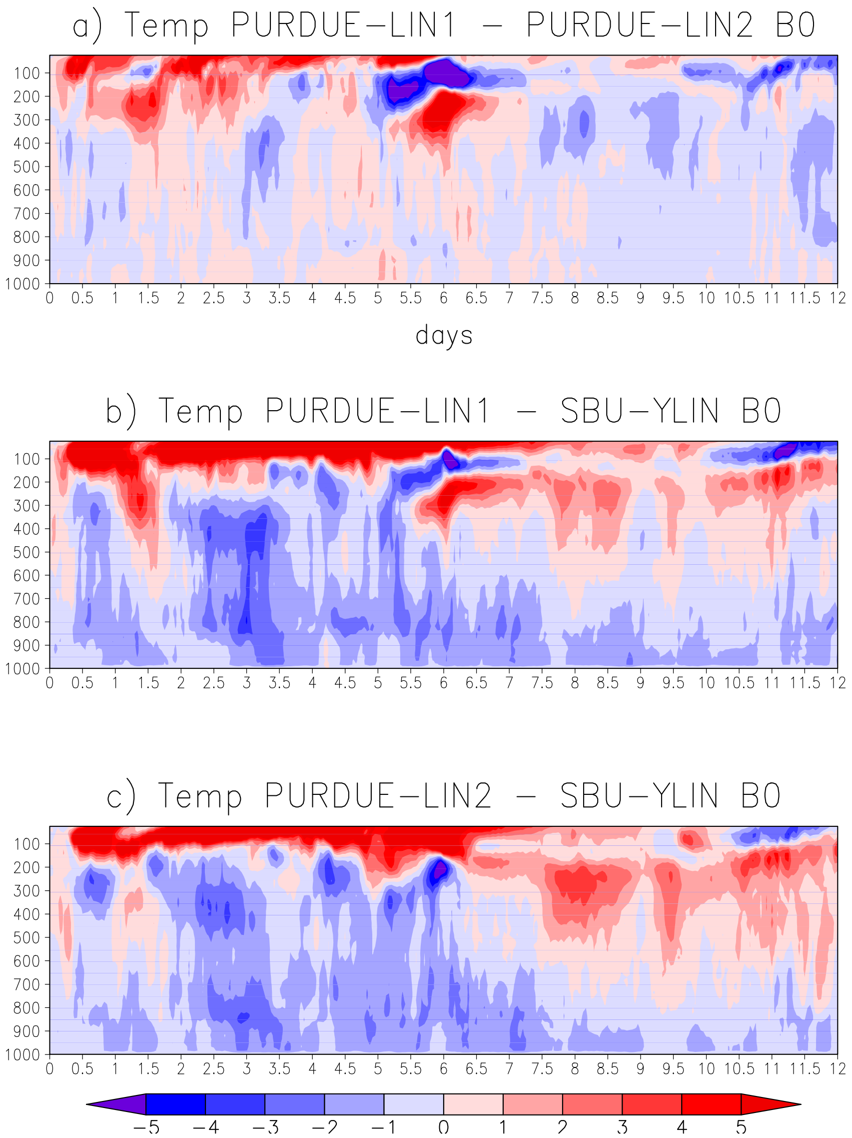

a) Temp PURDUE−LIN1 − PURDUE−LIN2 B0

b) Temp PURDUE−LIN1 − SBU−YLIN B0

c) Temp PURDUE−LIN2 − SBU−YLIN B0

Figure 5.4.11: The simulated temperature difference between a) PURDUE-LIN1 and PURDUE-LIN2, b) PURDUE-LIN1 and SBU-YLIN and c) PURDUE-LIN2 and SBU-YLIN in the B0 experiment. The x-axis shows time in days and y-axis shows height in hPa.

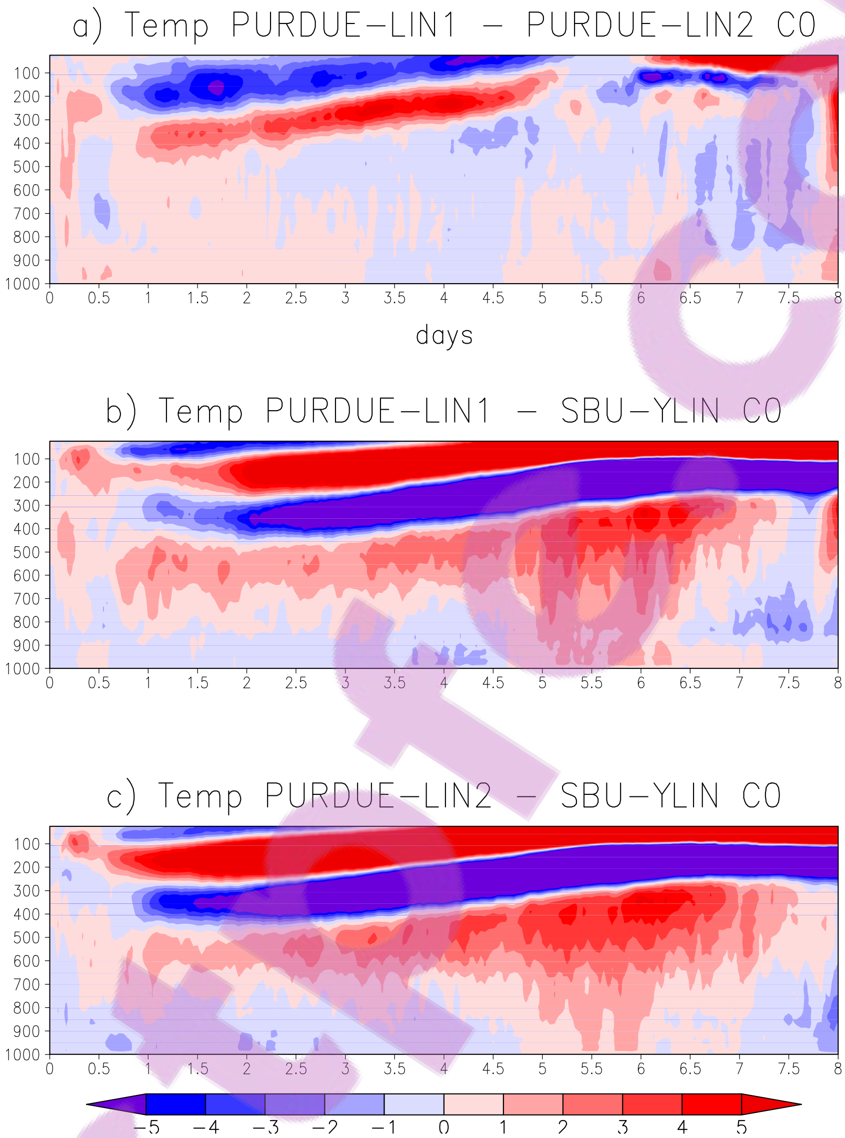

Figure 5.4.12: The simulated temperature difference between a) PURDUE-LIN1 and PURDUE-LIN2, b) PURDUE-LIN1 and SBU-YLIN and c) PURDUE-LIN2 and SBU-YLIN in the C0 experiment. The x-axis shows time in days and y-axis shows height in hPa.

than PURDUE-LIN1 and simulates smaller maximum updrafts than PURDUE-LIN1. The simulated hydrometeors increase towards the end of the active period in all three simulations.

5.4.4.3 C0 experiment

The simulated maximum updrafts are stronger in the PURDUE-LIN simulations. SBU-YLIN simulates the smallest values of the maximum updrafts and is at the same time the coldest in the troposphere. These results are unexpected because throughout the simulations the warmest atmosphere was found to simulate the smallest updrafts. Although the updrafts are smaller, SBU-YLIN simulates the highest values of total ice.

5.5 Summary and Conclusions

Simulations were made for three periods that started with deep convection to spin up the model, suppressed conditions followed, the transition period then followed and then deep convection was observed. Two of the periods are 12-days long (A0 and B0), while the other is eight-days (C0) long. The deep convection, transition and suppressed periods are of different lengths. The simulations are made with the PURDUE-LIN and SBU-YLIN microphysics schemes. The PURDUE-LIN scheme was run both with graupel (PURDUE-LIN1) and without graupel (PURDUE-LIN2).

The NSM simulations are found to be much colder and drier compared to observations for all the experiments and using all three microphysics schemes. The model is however able to capture general differences in the different experiments. Experiment A0 was generally warmer throughout the troposphere but cooler in a layer between 900 hPa and 600 hPa level. The model captured a much cooler region in the same layer but the simulated layer is thicker. A cooler region across almost the entire troposphere is simulated by all the three microphysics schemes in the B0 experiment, however, the region is not observed. The C0 experiment was the coolest of all the experiments compared to the initial conditions, and the NSM was able to capture that.

SBU-YLIN is found to be generally warmer compared to the PURDUE-LIN simulations especially in the lower troposphere. This is generally because of the effect of the downdrafts which are stronger in the PURDUE-LIN simulations. During the active periods, SBU-YLIN seems to respond best to the large scale forcing, while the cold pool seems to have a stronger effect on the PURDUE-LIN1 simulations. SBU-YLIN is found to be generally closer to the observations because it is mostly warmer than PURDUE-LIN simulations in the lower troposphere. The simulations suggest that PURDUE-LIN1 removes more moisture from the atmosphere, while forming stronger cold pools that trigger more storms than the SBU-YLIN scheme during active periods.

The NSM was able to capture the differences in the supressed, transition and active convection periods. The highest values of the maximum updrafts were generally simulated during the active periods. The suppressed periods were associated with smaller maximum updrafts and less simulated ice. The simulated updrafts in the transition period were found to be bigger than during the suppressed periods. A general recovery in the amount of the specific humidity is simulated during the transition periods. More ice was simulated during the active periods, which is in line with stronger updrafts during active periods.

The simulations compare relatively well with the GCSS intercomparison results shown by Woolnough et al. (2010). A lack of a sophisticated radiation scheme may have contributed to a bigger cold and dry bias in the simulations. A realistic representation of the atmopshere will include greenhouse gases that will trap some of the heat in the atmosphere and hence may correct the bias. Work has already started which is not part of the PhD to introduce a sophisticated radiation scheme and preliminary results show a small correction in the bias.

Another possible cause of a dry bias is that our model is two-dimensional while the real atmosphere is three-dimensional. As soon as the radiation scheme is fully introduced in the model, the NSM will be written in three-dimensions to allow for real atmospheric simulations to be made. The model will also be written in parallel to take advantage of the available high performance computing facilities. Further tests will be made to compare the PURDUE-LIN1 and SBU-YLIN scheme simulations. Our study shows that SBU-YLIN reduces precipitation efficiency, which is a result found with newer double-moment schemes when compared to single-moment schemes.

Chapter 6

Conclusions

The development of nonhydrostatic atmospheric models that can explicitly simulate the dynamics of atmospheric convection has been ongoing since the 1960s. These models have been utilised largely for research purposes, as their application to operational weather forecasting and climate simulation was hindered by computational restrictions. However, with the advent of faster computers, the operational numerical integration of weather prediction models at spatial resolutions beyond the hydrostatic limit has become a reality. This has led to a renewed and worldwide effort to develop nonhydrostatic models. A nonhydrostatic σ-coordinate model has been developed by Engelbrecht (2006) and Engelbrecht et al. (2007) for purposes of simulating weather at spatial resolutions where the hydrostatic approximation is not valid.

Geometric height can be used as the vertical coordinate in atmospheric models. However, the use of pressure-based coordinates is more popular. The use of pressure as a vertical coordinate is prompted by the availability of observational data at pressure levels and the relative simple form that the governing equations assume on this coordinate system. Miller (1974) developed one of the first nonhydrostatic models in pressure coordinates and Miller and Pearce (1974) used that model to simulate cumulonimbus clouds. This model assumes that departures from a reference state occur because of convective processes, and can therefore not be applied globally. White (1989) developed a pressure coordinate model that did not make use of the reference profile, and therefore has the potential to be applied globally. However, coordinates that do not follow the terrain are difficult to deal with when the surface is not flat. Engelbrecht et al. (2007) developed a nonhydrostatic model equivalent to that of White (1989), but based on a terrain-following σ coordinate - the Nonhydrostatic σ-coordinate Model (NSM). The σ-coordinate in the NSM is based on the full pressure field. In this study the NSM was extended through the improvement of its diffusion scheme and introduction of two microphysics schemes. These schemes were subsequently applied to study the interaction between the microphysics processes occurring within thunderstorms, and the related thunderstorm dynamics.

6.1 Diffusion Scheme Improvement

Turbulence is a natural consequence of instabilities in a flow, as it acts to reduce the instability (Stull, 2006). Clouds are turbulent because of cloud-top radiative cooling and cloud-base radiative warming, and also because of latent heat release and absorption. The rate of entrainment in clouds is partly determined by turbulent processes (Randall et al., 2003; Houze, 1993). In numerical atmospheric models, the degree of mixing due to turbulence can be quantified by means of turbulent flux terms (Jacobson, 2005) in the mean flow's basic equations of motion. To solve the mean equations, closure assumptions need to be made to approximate the unknown fluxes in terms of the known mean state variables. The traditional approach is to assume that turbulent eddies act in a manner that the flux of a given field is proportional to the local gradient of the mean (Holton, 2004). This closure scheme is often referred to as K-theory, and is of the first order. Engelbrecht et al. (2007) used this approach with constant coefficients. In this study diffusion coefficients that change based on the gradient Richardson number were introduced to the nonhydrostatic σ-coordinate equations, in order to make the diffusion scheme physically more realistic (Louis, 1979).

The NSM was first converted from Fortran 77 to modules and subroutines in Fortran 90. A warm bubble simulation by Engelbrecht et al. (2007) was repeated in this study, to show that reorganisation of the code was successful. The elliptic equation used in the model was also derived to be consistent with the diffusion terms applied in the governing equations (the effects of the diffusion terms through the elliptic equation were neglected by Engelbrecht et al. (2007)).

Simulations were made with the extended diffusion scheme that calculates the eddy diffusivity coefficients based on the Richardson number. The coefficients vary depending on height above the surface, the amount of buoyancy and shear in the atmosphere. The advantange of this scheme is that it is physically more realistic and the value of the coefficients do not have to be assumed for different simulations, because they are inter-actively calculated by the model as a function of the characteristics of the flow. The bubble simulated with the improved diffusion scheme is slightly less diffused compared to the simulation that uses constant coefficients in the vertical. Simulations were also made with single and double precision. If diffusion is not applied, the bubble simulated using single precision is not symmetrical. However, when diffusion is applied to both single and double precision runs, the results are almost indistinguishable. These results indicate that single precission can still be of value in numerical atmospheric modelling. The result is relevant in particular to the use of Graphical Processing Units (GPUs), which are thought to function best with single precision (Farber, 2012). Double precision is preferred though, for the simulations described here, because it is more accurate and it saves computer power - the elliptic solver converges more quickly for the case of double precission compared to single precission.

6.2 Bulk Microphysics Parameterisation schemes

Cloud resolving models employ microphysics parameterisations, grouped into bin and bulk approaches, to simulate clouds explicitly (Rutledge and Hobbs, 1983; Stensrud, 2007). A bin approach divides the particle into a number of finite sizes and categories. However, the division of particle distribution into numerous bins requires much larger memory and computational capabilities, and poor knowledge of ice phase physics hampers the accurate representation of evolving ice particle concentrations (Stensrud, 2007).

Bulk Microphysics Parameterisation (BMP) approaches use a specified functional form for the particle size distributions and predict the particle mixing ratio. The particle size distribution is usually approximated by the inverse exponential distribution. The distribution equation has two free parameters, when one is fixed or diagnosed as a single function of the other, the scheme is called single-moment. By predicting more than one moment of the size distribution, a multi-moment scheme can be formulated (Dawson II et al., 2010). The advantage of using multi-moment schemes over single-moment schemes is that multi-moment schemes should be applicable across a wider range of environments. This is because multi-moment schemes require less tuning of parameters that are related to particle number concentrations (Stensrud, 2007). Multi-moment schemes are only starting to become available in numerical models, however, since the increased computational cost due to the prediction of a second moment (number concentration in most cases) deters from their use in real-time numerical weather prediction (Thompson et al., 2008).

Two BMP schemes were obtained from the NCAR WRF model and included in the NSM code as sub-routines. The first scheme is that of Chen and Sun, and is called the PURDUE-LIN scheme - of which two configurations are used in this study (the scheme is applied with and without graupel). It is based on conventional schemes of Lin et al. (1983) and Rutledge and Hobbs (1983). The scheme assumes that precipitating particles follow a gamma distribution and predicts the mixing ratios of the six water species. Cloud water and ice are assumed to be monodispersed and to have a negligible terminal speed. The second scheme, SBU-YLIN, was developed using the PURDUE-LIN scheme as a starting point. In this scheme, snow and graupel share the same category and the number of microphysics schemes was reduced from 40 to less than 20. Cloud water follows a generalized gamma distribution and cloud ice is allowed to fall. The SBU-YLIN scheme uses general formulations that consider the influence of riming intensity and temperature on the prediction of precipitating ice.

6.3 Thunderstorm simulations

Thunderstorm simulations based on the thermodynamic profile of Weisman and Klemp (1982), initiated with a positive temperature perturbation, were performed, for an integration time of two hours, at a horizontal resolution of $500m$. The PURDUE-LIN microphysics scheme was used with graupel (called PURDUE-LIN1) and without graupel (called PURDUE-LIN2). The biggest ice particle is therefore graupel in the PURDUE-LIN1 simulation and snow in the PURDUE-LIN2 simulation. At the beginning of the simulation only water vapour was provided to the model, and hydrometeors formed through the simulated microphysics. The PURDUE-LIN1 simulation produced more rainfall than the PURDUE-LIN2 run. These findings are in agreement with those of Hong and Lim (2006). More water vapour was lost in the simulation that produced the most rainfall, and warming due to latent heating was larger. Two clouds were simulated, a bigger one at the beginning of the simulation and a second smaller cloud towards the end of the simulation. The first cloud is triggered by the temperature perturbation while the second cloud is triggered by the cold pool. The cold pool is stronger in the PURDUE-LIN1 simulation, in line with the amount of the simulated rainfall. The updrafts in the second cloud are smaller in the PURDUE-LIN1 simulation because of hydrometeor loading, which reduces the strength of the updraft. The simulations are indicative of the complex interaction between microphysics and thunderstorm dynamics, and of the great sensitivity of simulated rainfall amounts to the choice of microphysics scheme.

Another simulation was made with the SBU-YLIN microphysics scheme, which was developed from the PURDUE-LIN scheme. In this scheme, snow and graupel share a category and processes. The precipitating ice simulated by the NSM with the SBU-YLIN scheme follows more closely the behaviour of snow in the PURDUE-LIN2 scheme, than graupel in the PURDUE-LIN1 scheme. This suggests that the precipitating particles that are simulated by the SBU-YLIN scheme are smaller. For all three simulations, the largest precipitating ice species was the dominating (that is, the most abundant) hydrometeor. Graupel dominated in the PURDUE-LIN1 scheme, snow dominated in the PURDUE-LIN2 scheme while precipitating ice (snow and graupel together) dominated in the SBU-YLIN scheme simulations.

Graupel was found to be the most variable hydrometeor, it reached maximum concentration relatively fast (compared to other hydrometeors) and as soon as the updraft reduced in strength, it started falling. As it falls, it gets converted into rain water and water vapour, whilst cooling the atmosphere at the same time because of latent heat absorption. Snow (in the PURDUE-LIN2 simulation) and precipitating ice (in the SBU-YLIN simulation) reach maximum concentrations at the same time - somewhat later compared to graupel. When the updrafts get weaker, both these hydrometeors start to decrease in concentration. However, snow reduces faster than precipitating ice, again confirming that precipitating ice particles simulated by the SBU-YLIN scheme are smaller compared to snow and graupel simulated by the PURDUE-LIN scheme. The second smaller cloud that developed towards the end of the simulation in the PURDUE-LIN simulations is not found in the SBU-YLIN simulations. This finding is due to a weaker cold pool simulated by the SBU-YLIN scheme that is not able to trigger a second cloud.

The effect of horizontal resolution on thunderstorm simulations was also tested. It is found that the lower the resolution, the smaller are the updraft and downdraft maxima. This result is to be expected, because winds can be better resoved at high resolution. The different intensities of updrafts, for various choices of model resolution, also influenced the hydrometeors. A good example is that of graupel, which has two maxima in time in the 500 m and 1 km resolution simulations, however the size of the maxima is reduced in the 1 km resolution simulations. In the 2 km resolution simulations, the second maximum disappears because the updraft towards the end of the simulation is not strong enough to transport moisture to higher altitudes, where temperatures are much lower, and the formation of ice is enabled. When the updraft is smaller, and in the lower atmosphere, more cloud and rain water form. When the updraft is much stronger, more cloud and precipitating ice form.

PURDUE-LIN1 and PURDUE-LIN2 simulations produce two clouds even with the lower $1km$ and $2km$ horizontal resolutions, however the updrafts are weaker (as mentioned above). The SBU-YLIN scheme did not simulate the second cloud that is triggered by the cold pool in the 500 m and 1 km resolution simulations. It however simulated the second cloud with much stronger updrafts compared to the PURDUE-LIN schemes in the 2 km resolution simulations. Bryan and Morrison (2012) made simulations with horizontal resolutions of 4 km, 1 km and 0.25 km resolution, and found that the high resolution simulations rained less because of increased condensation and evaporation rate of cloud water as a result of increased mixing. SBU-YLIN seems to behave similar to the schemes used by Bryan and Morrison (2012), converting more water vapour to hydrometeors in the low resolution simulations. The low resolution simulation therefore simulates a stronger cold pool that is able to trigger a second cloud. The updrafts in the second cloud are stronger compared to the PURDUE-LIN updrafts because of increased water loading in the PURDUE-LIN simulations - hydrometeor particles simulated by PURDUE-LIN schemes are bigger compared to those simulated by the SBU-YLIN scheme.

Weisman and Klemp (1982) found that without shear, there was no redevelopment, however in the NSM simulations redevelopment is simulated as noted above. The redevelopment varied depending on the microphysics scheme and resolution used. Weisman and Klemp (1982) used the Kessler scheme which does not have ice, whilst ice was included in the simulations performed in this research. This suggests that the redevelopment taking places in the simulations in this study is because of a stronger downdraft that forms in the simulations with ice. The cold pool acts as a trigger for the formation of a second smaller cloud. Although there is no shear in the atmosphere to support the redevelopment, the subsiding cold air and resulting cold pool is strong enough to act as a trigger for a second, smaller thunderstorm.

The three microphysics schemes/settings were also applied to simulate thunderstorms in an environment with moderate shear. As expected, stronger redevelopment of storms occurred in the simulations with shear. This finding is because of the vorticity caused by the cold outflow from the initial storm and the environmental vorticity, that combine to produce stronger secondary storms (Weisman and Klemp, 1982). The maximum updrafts and downdrafts are however smaller in the simulations with shear, because shear induces mixing that increases entrainment, thereby diluting the cloud microphysics and dynamics.

6.4 TOGA COARE simulations

Simulations were made for three periods of the TOGA COARE experiment. These included deep convection to spin up the model, followed by a period of suppressed convection, a transition period and finally a period of observed deep convection. Two of the periods (A0 and B0) are 12 days long, whilst the third is eight days in length (Woolnough et al., 2010). The deep convection, transition and suppressed periods are of different lengths within each of these periods. The simulations are made with the PURDUE-LIN with graupel (PURDUE-LIN1), without graupel (PURDUE-LIN2) and SBU-YLIN microphysics schemes with a horizontal resolution of 2 km.

The NSM was found to be capable of capturing the general differences in the different experiments. Experiment A0 was generally warmer compared to the initial conditions throughout the troposphere, but cooler in a layer between 900 hPa and 600 hPa level. The NSM was able to capture the cooler region found in the observations, it was however thicker than observed. The B0 experiment is generally cooler than initial conditions in the upper troposphere throughout the twelve day period. The first half of the period is also cooler compared to the second half of the period. The NSM was able to capture that the first half of the simulation period is cooler, and this was best captured by the SBU-YLIN scheme. The model however simulated a cooler region throughout the troposphere between days five and eight with all the microphysics schemes, that is not observed. The C0 experiment was the coolest of all the experiments compared to the initial conditions, and the NSM was able to capture that. In all the simulations, the NSM is found to be generally cooler in the lower and middle troposphere and warmer in the upper troposphere compared to the initial conditions and observations.

SBU-YLIN is found to be generally warmer compared to the PURDUE-LIN simulations especially, in the lower troposphere. This is largely because of the effects of downdrafts, which are stronger in the PURDUE-LIN simulations. During active periods, SBU-YLIN seems to respond best to the large scale forcing, while the cold pool seems to have a stronger effect on the PURDUE-LIN1 simulations. Too much warming by processes relating to the formation or growth of hydrometeor tends to limit the magnitude of the updrafts in the subsequent periods. SBU-YLIN is found to be generally closer to the observations because it is mostly warmer than PURDUE-LIN simulations in the lower troposphere. The simulations suggest that PURDUE-LIN1 removes more moisture from the atmosphere, while forming stronger cold pools that trigger more storms that the SBU-YLIN scheme during active periods.

The NSM was able to capture the differences in the supressed, transition and active convection periods. The highest values of the maximum updrafts were generally simulated during the active periods. The suppressed periods were associated with smaller maximum updrafts and less simulated ice. The simulated updrafts in the transition period were found to be bigger than during the suppressed periods. A general recovery in the amount of the specific humidity is simulated during the transition period. More ice was simulated during the active periods, which is in line with stronger updrafts during active periods.

6.5 Recommendations

While the equations in this study were presented in three dimensions, the experiments performed were made with a two-dimensional model. The experiments have shown that the NSM with newly added microphysics can be used to study idealised and real thunderstorms. The NSM was found to be generally colder and drier compared to the observations, a feature that may be associated with the fact that the simulations were made without a radiation scheme. The experiments presented in this study are to be extended to three-dimensions in the future. The NSM will be written in parallel, which will make feasible the introduction of an interactive radiation scheme. The development of the model is to continue beyond this study, until it is a fully developed cloud model that can be used to simulate thunderstorms even over complex topography. The development of a new but similar model is also planned at the CSIR, which will be based on the flux form of the governing equations. This approach offers improved conservation properties for the simulated microphysics.

Appendix A

Derivation of the Elliptic equation with moisture and radiation in σ-coordinate with diffusion

The bar and primes will only appear on diffusion terms.

$$s = \left(\sigma + \tfrac{p_T}{p_s}\right)\left(\tfrac{g}{R_d T}\right) = \left(\tfrac{p-p_T}{p_s} + \tfrac{p_T}{p_s}\right)\left(\tfrac{g}{R_d T}\right) = \tfrac{p}{p_s}\tfrac{g}{R_d T}$$

Multiply vertical momentum by s

$$\tfrac{s}{g}\tfrac{D}{Dt}\left(\tfrac{R_d \omega T}{p}\right) + sg + s^2\tfrac{\partial\phi}{\partial\sigma} - s\left[\tfrac{\partial\overline{u'w'}}{\partial x} + \tfrac{\partial\overline{v'w'}}{\partial y} + \tfrac{\partial\overline{w'\dot{\sigma}'}}{\partial\sigma}\right] = 0 \text{ (A.1)}$$

Taking $\frac{\partial}{\partial x}$ of the x-horizontal momentum equation, $\frac{\partial}{\partial y}$ of the y-horizontal momentum equation and $\frac{\partial}{\partial\sigma}$of (A.1) and adding the three terms gives

$$\tfrac{\partial^2\phi}{\partial x^2} + \tfrac{\partial^2\phi}{\partial y^2} + \tfrac{\partial}{\partial\sigma}\left[s^2\tfrac{\partial\phi}{\partial\sigma}\right] + \tfrac{\partial}{\partial x}\left[-\sigma\tfrac{\partial\phi}{\partial\sigma}\tfrac{\partial\ln p_s}{\partial x}\right] + \tfrac{\partial}{\partial y}\left[-\sigma\tfrac{\partial\phi}{\partial\sigma}\tfrac{\partial\ln p_s}{\partial y}\right]$$

$$= -\tfrac{\partial}{\partial x}\left(\tfrac{Du}{Dt}\right) - \tfrac{\partial}{\partial y}\left(\tfrac{Dv}{Dt}\right) - \tfrac{\partial}{\partial\sigma}\left[\tfrac{s}{g}\tfrac{D}{Dt}\left(\tfrac{R_d\omega T}{p}\right)\right] - \tfrac{\partial}{\partial\sigma}(sg) + f\left(\tfrac{\partial v}{\partial x} - \tfrac{\partial u}{\partial y}\right) - u\tfrac{\partial f}{\partial y}$$

$$+\tfrac{\partial}{\partial\sigma}\left\{s\left[\tfrac{\partial\overline{u'w'}}{\partial x} + \tfrac{\partial\overline{v'w'}}{\partial y} + \tfrac{\partial\overline{w'\dot{\sigma}'}}{\partial\sigma}\right]\right\} - \tfrac{\partial}{\partial y}\left[\tfrac{\partial\overline{u'v'}}{\partial x} + \tfrac{\partial\overline{v'v'}}{\partial y} + \tfrac{\partial\overline{v'\dot{\sigma}'}}{\partial\sigma}\right]$$

$$-\tfrac{\partial}{\partial x}\left[\tfrac{\partial\overline{u'u'}}{\partial x} + \tfrac{\partial\overline{v'u'}}{\partial y} + \tfrac{\partial\overline{u'\dot{\sigma}'}}{\partial\sigma}\right]$$

but

$$\tfrac{\partial}{\partial x}\left[-\sigma\tfrac{\partial\phi}{\partial\sigma}\tfrac{\partial\ln p_s}{\partial x}\right] = -\sigma\tfrac{\partial\phi}{\partial\sigma}\tfrac{\partial^2\ln p_s}{\partial x^2} - \sigma\tfrac{\partial\ln p_s}{\partial x}\tfrac{\partial^2\phi}{\partial x\partial\sigma} \text{ and}$$

$$\tfrac{\partial}{\partial y}\left[-\sigma\tfrac{\partial\phi}{\partial\sigma}\tfrac{\partial\ln p_s}{\partial y}\right] = -\sigma\tfrac{\partial\phi}{\partial\sigma}\tfrac{\partial^2\ln p_s}{\partial y^2} - \sigma\tfrac{\partial\ln p_s}{\partial y}\tfrac{\partial^2\phi}{\partial y\partial\sigma}.$$

Therefore

$$\tfrac{\partial^2\phi}{\partial x^2} + \tfrac{\partial^2\phi}{\partial y^2} + \tfrac{\partial}{\partial\sigma}\left[s^2\tfrac{\partial\phi}{\partial\sigma}\right] - \sigma\tfrac{\partial\phi}{\partial\sigma}\left(\tfrac{\partial^2\ln p_s}{\partial x^2} + \tfrac{\partial^2\ln p_s}{\partial y^2}\right)$$

$$-\sigma\left[\frac{\partial\ln p_s}{\partial x}\left(\frac{\partial^2\phi}{\partial x\partial\sigma}\right)+\frac{\partial\ln p_s}{\partial y}\left(\frac{\partial^2\phi}{\partial y\partial\sigma}\right)\right]=-\frac{\partial}{\partial x}\left(\frac{Du}{Dt}\right)-\frac{\partial}{\partial y}\left(\frac{Dv}{Dt}\right)-\frac{\partial}{\partial\sigma}\left[\frac{p}{p_sR_dT}\frac{D}{Dt}\left(\frac{R_d\omega T}{p}\right)\right]-$$

$$\frac{\partial}{\partial\sigma}\left(sg\right)$$

$$+f\left(\frac{\partial v}{\partial x}-\frac{\partial u}{\partial y}\right)-u\frac{\partial f}{\partial y}$$

$$+\frac{\partial}{\partial\sigma}\left\{s\left[\frac{\partial\overline{u'w'}}{\partial x}+\frac{\partial\overline{v'w'}}{\partial y}+\frac{\partial\overline{w'\dot{\sigma}'}}{\partial\sigma}\right]\right\}-\frac{\partial}{\partial y}\left[\frac{\partial\overline{u'v'}}{\partial x}+\frac{\partial\overline{v'v'}}{\partial y}+\frac{\partial\overline{v'\dot{\sigma}'}}{\partial\sigma}\right]$$

$$-\frac{\partial}{\partial x}\left[\frac{\partial\overline{u'u'}}{\partial x}+\frac{\partial\overline{v'u'}}{\partial y}+\frac{\partial\overline{u'\dot{\sigma}'}}{\partial\sigma}\right]$$

But

$$\frac{\partial}{\partial x}\left(\frac{Du}{Dt}\right)=\frac{\partial}{\partial x}\left[\frac{\partial u}{\partial t}+u\frac{\partial u}{\partial x}+v\frac{\partial u}{\partial y}+\dot{\sigma}\frac{\partial u}{\partial\sigma}\right]$$

$$=\frac{\partial^2u}{\partial x\partial t}+\frac{\partial u}{\partial x}\frac{\partial u}{\partial x}+u\frac{\partial^2u}{\partial x^2}+\frac{\partial v}{\partial x}\frac{\partial u}{\partial y}+v\frac{\partial^2u}{\partial x\partial y}+\frac{\partial\dot{\sigma}}{\partial x}\frac{\partial u}{\partial\sigma}+\dot{\sigma}\frac{\partial^2u}{\partial x\partial\sigma}$$

$$=\frac{D}{Dt}\left(\frac{\partial u}{\partial x}\right)+\left(\frac{\partial u}{\partial x}\frac{\partial u}{\partial x}+\frac{\partial v}{\partial x}\frac{\partial u}{\partial y}+\frac{\partial\dot{\sigma}}{\partial x}\frac{\partial u}{\partial\sigma}\right)\text{ and similarly}$$

$$\frac{\partial}{\partial y}\left(\frac{Dv}{Dt}\right)=\frac{D}{Dt}\left(\frac{\partial v}{\partial y}\right)+\left(\frac{\partial u}{\partial y}\frac{\partial v}{\partial x}+\frac{\partial v}{\partial y}\frac{\partial v}{\partial y}+\frac{\partial\dot{\sigma}}{\partial y}\frac{\partial v}{\partial\sigma}\right)$$

To simplify the term that is derived from the vertical momentum equation it is noted that

$$\sigma=\frac{p-p_T}{p_s}\Longrightarrow p=\sigma p_s+p_T$$

$$\frac{\omega}{p}=\frac{1}{p}\frac{Dp}{Dt}=\frac{1}{p_a}\frac{D}{Dt}\left(\sigma p_s+p_T\right)$$

$$=\frac{1}{p}\left[\sigma\frac{Dp_s}{Dt}+p_s\frac{D\sigma}{Dt}\right]$$

$$=\frac{p_s}{p}\left[\frac{\sigma}{p_s}\frac{Dp_s}{Dt}+\frac{D\sigma}{Dt}\right]$$

$$=\frac{p_s}{p}\left[\sigma\frac{D\ln p_s}{Dt}+\dot{\sigma}\right]$$

$$=\frac{p_s}{P}\left[\sigma\frac{D\ln p_s}{Dt}+\dot{\sigma}\right]$$

Therefore

$$\left[\frac{p}{p_sR_dT}\frac{D}{Dt}\left(\frac{R_d\omega T}{p}\right)\right]=\frac{p}{p_sR_dT}\frac{D}{Dt}\left[\frac{R_dTp_s}{p}\left(\sigma\frac{D\ln p_s}{Dt}+\dot{\sigma}\right)\right]$$

$$=\frac{p}{p_sR_dT}\left[\frac{D}{Dt}\left(\frac{R_dTp_s\sigma}{p}\frac{D\ln p_s}{Dt}\right)+\frac{D}{Dt}\left(\frac{R_dTp_s}{p}\dot{\sigma}\right)\right]$$

$$=\sigma\frac{D^2\ln p_s}{Dt^2}+\frac{p}{p_sR_dT}\frac{D\ln p_s}{Dt}\frac{D}{Dt}\left(\frac{R_dTp_s\sigma}{p}\right)+\frac{p}{p_sR_dT}\frac{D}{Dt}\left(\frac{R_dTp_s}{p}\dot{\sigma}\right)$$

The first term will be referred to as A the second one as B while the third one will be C. Noting that

$$B=\left[\dot{\sigma}+\frac{\sigma p}{R_dp_sT}\frac{D}{Dt}\left(\frac{R_dTp_s}{p}\right)\right]\frac{D\ln p_s}{Dt}\quad\text{A.6}$$

and $C = \frac{D\dot{\sigma}}{Dt} + \dot{\sigma}\left(\frac{p}{R_d p_s T}\right)\frac{D}{Dt}\left(\frac{R_d T p_s}{p}\right)$ A.7

it follows that

$\frac{\partial A}{\partial \sigma} = \frac{D^2 \ln p_s}{Dt^2}\frac{\partial \sigma}{\partial \sigma} + \sigma\frac{\partial}{\partial \sigma}\left(\frac{D^2 \ln p_s}{Dt^2}\right)$ A.8

$\frac{\partial B}{\partial \sigma} = \frac{\partial}{\partial \sigma}\left\{\left[\dot{\sigma} + \frac{\sigma p}{R_d p_s T}\frac{D}{Dt}\left(\frac{R_d T p_s}{p}\right)\right]\frac{D \ln p_s}{Dt}\right\}$ A.9

and

$\frac{\partial C}{\partial \sigma} = \frac{D}{Dt}\left(\frac{\partial \dot{\sigma}}{\partial \sigma}\right) + \left[\frac{\partial u}{\partial \sigma}\frac{\partial \dot{\sigma}}{\partial x} + \frac{\partial v}{\partial \sigma}\frac{\partial \dot{\sigma}}{\partial y} + \frac{\partial \dot{\sigma}}{\partial \sigma}\frac{\partial \dot{\sigma}}{\partial \sigma}\right] + \frac{\partial}{\partial \sigma}\left[\dot{\sigma}\left(\frac{p}{R_d p_s T}\right)\frac{D}{Dt}\left(\frac{R_d T p_s}{p}\right)\right]$ A.10

From combining A.8 t

$$-\frac{D}{Dt}\left(\frac{D \ln p_s}{Dt}\right) + \sigma\frac{\partial}{\partial \sigma}\left(\frac{D^2 \ln p_s}{Dt^2}\right) + \frac{\partial}{\partial \sigma}\left\{\left[\dot{\sigma} + \frac{\sigma p}{R_d p_s T}\frac{D}{Dt}\left(\frac{R_d T p_s}{p}\right)\right]\frac{D \ln p_s}{Dt}\right\}$$

Combining everything gives

$$\frac{\partial^2 \phi}{\partial x^2} + \frac{\partial^2 \phi}{\partial y} + \frac{\partial}{\partial \sigma}\left[s^2\frac{\partial \phi}{\partial \sigma}\right] - \sigma\frac{\partial \phi}{\partial \sigma}\left(\frac{\partial^2 \ln p_s}{\partial x^2} + \frac{\partial^2 \ln p_s}{\partial y^2}\right) - \sigma\left[\frac{\partial \ln p_s}{\partial x}\left(\frac{\partial^2 \phi}{\partial x \partial \sigma}\right) + \frac{\partial \ln p_s}{\partial y}\left(\frac{\partial^2 \phi}{\partial y \partial \sigma}\right)\right] =$$

$$\left(-\frac{\partial u}{\partial x}\frac{\partial u}{\partial x} - \frac{\partial v}{\partial x}\frac{\partial u}{\partial y} - \frac{\partial \dot{\sigma}}{\partial x}\frac{\partial u}{\partial \sigma}\right) + \left(-\frac{\partial u}{\partial y}\frac{\partial v}{\partial x} - \frac{\partial v}{\partial y}\frac{\partial v}{\partial y} - \frac{\partial \dot{\sigma}}{\partial y}\frac{\partial v}{\partial \sigma}\right) + \left(-\frac{\partial u}{\partial \sigma}\frac{\partial \dot{\sigma}}{\partial x} - \frac{\partial v}{\partial \sigma}\frac{\partial \dot{\sigma}}{\partial y} - \frac{\partial \dot{\sigma}}{\partial \sigma}\frac{\partial \dot{\sigma}}{\partial \sigma}\right)$$

$$-\frac{\partial}{\partial \sigma}\left[\dot{\sigma}\left(\frac{p}{R_d p_s T}\right)\frac{D}{Dt}\left(\frac{R_d T p_s}{p}\right)\right] - \sigma\frac{\partial}{\partial \sigma}\left(\frac{D^2 \ln p_s}{Dt}\right) - \frac{\partial}{\partial \sigma}\left\{\left[\dot{\sigma} + \frac{\sigma p}{R_d p_s T}\frac{D}{Dt}\left(\frac{R_d T p_s}{p}\right)\right]\frac{D \ln p_s}{Dt}\right\}$$

$$-\frac{\partial}{\partial \sigma}(sg) - \frac{D}{Dt}\left(\frac{D \ln p_s}{Dt}\right) - \frac{D}{Dt}\left(\frac{\partial u}{\partial x}\right) - \frac{D}{Dt}\left(\frac{\partial v}{\partial y}\right) - \frac{D}{Dt}\left(\frac{\partial \dot{\sigma}}{\partial \sigma}\right) + f\left(\frac{\partial v}{\partial x} - \frac{\partial u}{\partial y}\right) - u\frac{\partial f}{\partial y}$$

$$+\frac{\partial}{\partial \sigma}\left\{s\left[\frac{\partial \overline{u'w'}}{\partial x} + \frac{\partial \overline{v'w'}}{\partial y} + \frac{\partial \overline{w'\dot{\sigma}'}}{\partial \sigma}\right]\right\} - \frac{\partial}{\partial y}\left[\frac{\partial \overline{u'v'}}{\partial x} + \frac{\partial \overline{v'v'}}{\partial y} + \frac{\partial \overline{v'\dot{\sigma}'}}{\partial \sigma}\right]$$

$$-\frac{\partial}{\partial x}\left[\frac{\partial \overline{u'u'}}{\partial x} + \frac{\partial \overline{v'u'}}{\partial y} + \frac{\partial \overline{u'\dot{\sigma}'}}{\partial \sigma}\right]$$

The last four terms of the last equation give the continuity equation and therefore disappear. But

$-\sigma\frac{\partial}{\partial \sigma}\left(\frac{D^2 \ln p_s}{Dt^2}\right) = -\sigma\frac{\partial}{\partial \sigma}\left[\frac{D}{Dt}\left(\frac{\partial \ln p_s}{\partial t} + u\frac{\partial \ln p_s}{\partial x} + v\frac{\partial \ln ps}{\partial y} + \dot{\sigma}\frac{\partial \ln p_s}{\partial \sigma}\right)\right]$however $\frac{\partial \ln p_s}{\partial \sigma} = 0$ because surface pressure doesn't change with σ.

$$= -\sigma\frac{\partial}{\partial \sigma}\left[\frac{D}{Dt}\left(\frac{\partial \ln p_s}{\partial t}\right) + \frac{\partial \ln p_s}{\partial x}\frac{Du}{Dt} + \frac{\partial \ln p_s}{\partial y}\frac{Dv}{Dt} + u\frac{D}{Dt}\left(\frac{\partial \ln p_s}{\partial t}\right) + v\frac{D}{Dt}\left(\frac{\partial \ln p_s}{\partial y}\right)\right]$$

$$= -\sigma\frac{\partial}{\partial \sigma}\frac{D}{Dt}\left(\frac{\partial \ln p_s}{\partial t}\right) - \sigma\frac{\partial \ln p_s}{\partial x}\frac{\partial}{\partial \sigma}\left(\frac{Du}{Dt}\right) - \sigma\frac{\partial \ln p_s}{\partial y}\frac{\partial}{\partial \sigma}\left(\frac{Dv}{Dt}\right) - \sigma\frac{Du}{Dt}\frac{\partial}{\partial \sigma}\left(\frac{\partial \ln p_s}{\partial x}\right) -$$
$$\sigma\frac{Dv}{Dt}\frac{\partial}{\partial \sigma}\left(\frac{\partial \ln p_s}{\partial y}\right)$$

$$-\sigma\frac{\partial u}{\partial \sigma}\frac{D}{Dt}\left(\frac{\partial \ln p_s}{\partial x}\right) - \sigma\frac{\partial v}{\partial \sigma}\frac{D}{Dt}\left(\frac{\partial \ln p_s}{\partial y}\right) - \sigma u\frac{\partial}{\partial \sigma}\left[\frac{D}{Dt}\left(\frac{\partial \ln p_s}{\partial x}\right)\right] - \sigma v\frac{\partial}{\partial \sigma}\left[\frac{D}{Dt}\left(\frac{\partial \ln p_s}{\partial y}\right)\right]$$

Term 4 and 5 equal zero if the order to differentiating $\ln p_s$ is reversed.

$$-\sigma\frac{\partial}{\partial \sigma}\left(\frac{D^2 \ln p_s}{Dt^2}\right) = -\sigma\left[\frac{\partial \ln p_s}{\partial x}\frac{\partial}{\partial \sigma}\left(\frac{Du}{Dt}\right) + \frac{\partial \ln p_s}{\partial y}\frac{\partial}{\partial \sigma}\left(\frac{Dv}{Dt}\right)\right]$$

$$-\sigma\left[\frac{\partial u}{\partial \sigma}\frac{D}{Dt}\left(\frac{\partial \ln p_s}{\partial x}\right) + \frac{\partial v}{\partial \sigma}\frac{D}{Dt}\left(\frac{\partial \ln p_s}{\partial y}\right)\right]\text{-}\sigma\frac{\partial}{\partial \sigma}\frac{D}{Dt}\left(\frac{\partial \ln p_s}{\partial t}\right)$$

$$-\sigma u\frac{\partial}{\partial\sigma}\left[\frac{D}{Dt}\left(\frac{\partial\ln p_s}{\partial x}\right)\right]-\sigma v\frac{\partial}{\partial\sigma}\left[\frac{D}{Dt}\left(\frac{\partial\ln p_s}{\partial y}\right)\right]$$

But

$$-\sigma\frac{\partial}{\partial\sigma}\frac{D}{Dt}\left(\frac{\partial\ln p_s}{\partial t}\right)=-\sigma\frac{\partial}{\partial\sigma}\left[\frac{\partial^2\ln p_s}{\partial t^2}+u\frac{\partial}{\partial x}\left(\frac{\partial\ln p_s}{\partial t}\right)+v\frac{\partial}{\partial y}\left(\frac{\partial\ln p_s}{\partial t}\right)\right]$$

$=-\sigma\left[\frac{\partial u}{\partial\sigma}\frac{\partial}{\partial x}\left(\frac{\partial\ln p_s}{\partial t}\right)+\frac{\partial v}{\partial\sigma}\frac{\partial}{\partial y}\frac{\partial\ln p_s}{\partial t}\right]$ with a number of terms disappearing because of $\frac{\partial\ln p_s}{\partial\sigma}=0$

$$=-\sigma\left[\frac{\partial u}{\partial\sigma}\frac{\partial}{\partial t}\left(\frac{\partial\ln p_s}{\partial x}\right)+\frac{\partial v}{\partial\sigma}\frac{\partial}{\partial t}\left(\frac{\partial\ln p_s}{\partial y}\right)\right]$$

$$-\sigma u\frac{\partial}{\partial\sigma}\left[\frac{D}{Dt}\left(\frac{\partial\ln p_s}{\partial x}\right)\right]=-\sigma u\frac{\partial}{\partial\sigma}\left[\frac{\partial}{\partial t}\left(\frac{\partial\ln p_s}{\partial x}\right)+u\frac{\partial}{\partial x}\left(\frac{\partial\ln p_s}{\partial x}\right)+v\frac{\partial}{\partial y}\left(\frac{\partial\ln p_s}{\partial x}\right)\right]$$

$$=-\sigma u\left[\frac{\partial u}{\partial\sigma}\frac{\partial}{\partial x}\left(\frac{\partial\ln p_s}{\partial x}\right)+\frac{\partial v}{\partial\sigma}\frac{\partial}{\partial y}\left(\frac{\partial\ln p_s}{\partial x}\right)\right]$$

$$=-\sigma\left[\frac{\partial u}{\partial\sigma}u\frac{\partial}{\partial x}\left(\frac{\partial\ln p_s}{\partial x}\right)+\frac{\partial v}{\partial\sigma}u\frac{\partial}{\partial y}\left(\frac{\partial\ln p_s}{\partial x}\right)\right]$$

$=-\sigma\left[\frac{\partial u}{\partial\sigma}u\frac{\partial}{\partial x}\left(\frac{\partial\ln p_s}{\partial x}\right)+\frac{\partial v}{\partial\sigma}u\frac{\partial}{\partial x}\left(\frac{\partial\ln p_s}{\partial y}\right)\right]$ and similarly

$-\sigma v\frac{\partial}{\partial\sigma}\left[\frac{D}{Dt}\left(\frac{\partial\ln p_s}{\partial y}\right)\right]=-\sigma v\frac{\partial}{\partial\sigma}\left[\frac{\partial}{\partial t}\left(\frac{\partial\ln p_s}{\partial y}\right)+u\frac{\partial}{\partial x}\left(\frac{\partial\ln p_s}{\partial y}\right)+v\frac{\partial}{\partial y}\left(\frac{\partial\ln p_s}{\partial y}\right)\right]$ simplifies to

$$=-\sigma\left[\frac{\partial u}{\partial\sigma}v\frac{\partial}{\partial y}\left(\frac{\partial\ln p_s}{\partial x}\right)+\frac{\partial v}{\partial\sigma}v\frac{\partial}{\partial y}\left(\frac{\partial\ln p_s}{\partial y}\right)\right]$$

Putting together the baove equations gives

$$-\sigma\left[\frac{\partial u}{\partial\sigma}\frac{D}{Dt}\left(\frac{\partial\ln p_s}{\partial x}\right)+\frac{\partial v}{\partial\sigma}\frac{D}{Dt}\left(\frac{\partial\ln p_s}{\partial y}\right)\right]$$

We therefore get

$$-\sigma\frac{\partial}{\partial\sigma}\left(\frac{D^2\ln p_s}{Dt^2}\right)=-\sigma\left[\frac{\partial\ln p_s}{\partial x}\frac{\partial}{\partial\sigma}\left(\frac{Du}{Dt}\right)+\frac{\partial\ln p_s}{\partial y}\frac{\partial}{\partial\sigma}\left(\frac{Dv}{Dt}\right)\right]$$

$$-2\sigma\left[\frac{\partial u}{\partial\sigma}\frac{D}{Dt}\left(\frac{\partial\ln p_s}{\partial x}\right)+\frac{\partial v}{\partial\sigma}\frac{D}{Dt}\left(\frac{\partial\ln p_s}{\partial y}\right)\right]$$

By expanding $\frac{Du}{Dt}$ and $\frac{Dv}{Dt}$ according to the horizontal momentum equation.

$$-\sigma\frac{\partial}{\partial\sigma}\left(\frac{D^2\ln p_s}{Dt^2}\right)=$$

$$-\sigma\left[\frac{\partial\ln p_s}{\partial x}\frac{\partial}{\partial\sigma}\left(-\frac{\partial\phi}{\partial x}+\sigma\frac{\partial\phi}{\partial\sigma}\frac{\partial\ln p_s}{\partial x}+fv\right)+\frac{\partial\ln p_s}{\partial y}\frac{\partial}{\partial\sigma}\left(-\frac{\partial\phi}{\partial y}+\sigma\frac{\partial\phi}{\partial\sigma}\frac{\partial\ln p_s}{\partial y}-fu\right)\right]$$

$$-2\sigma\left[\frac{\partial u}{\partial\sigma}\frac{D}{Dt}\left(\frac{\partial\ln p_s}{\partial x}\right)+\frac{\partial v}{\partial\sigma}\frac{D}{Dt}\left(\frac{\partial\ln p_s}{\partial y}\right)\right]$$

$$=-\sigma\left[\frac{\partial\ln p_s}{\partial x}\left(-\frac{\partial^2\phi}{\partial x\partial\sigma}+\frac{\partial}{\partial\sigma}\left(\sigma\frac{\partial\phi}{\partial\sigma}\frac{\partial\ln p_s}{\partial x}\right)\right)\right]$$

$$-\sigma\left[\frac{\partial\ln p_s}{\partial y}\left(-\frac{\partial^2\phi}{\partial y\partial\sigma}+\frac{\partial}{\partial\sigma}\left(\sigma\frac{\partial\phi}{\partial\sigma}\frac{\partial\ln p_s}{\partial y}\right)\right)\right]$$

$$-2\sigma\left[\frac{\partial u}{\partial\sigma}\frac{D}{Dt}\left(\frac{\partial\ln p_s}{\partial x}\right)+\frac{\partial v}{\partial\sigma}\frac{D}{Dt}\left(\frac{\partial\ln p_s}{\partial y}\right)\right]+\sigma f\left[\frac{\partial\ln p_s}{\partial y}\frac{\partial u}{\partial\sigma}-\frac{\partial\ln p_s}{\partial x}\frac{\partial v}{\partial\sigma}\right]$$

$$= \sigma\left(\frac{\partial^2\phi}{\partial x\partial\sigma}\frac{\partial \ln p_s}{\partial x} + \frac{\partial^2\phi}{\partial y\partial\sigma}\frac{\partial \ln p_s}{\partial y}\right) - \sigma\frac{\partial}{\partial\sigma}\left(\sigma\frac{\partial\phi}{\partial\sigma}\right)\left[\left(\frac{\partial \ln p_s}{\partial x}\right)^2 + \left(\frac{\partial \ln p_s}{\partial y}\right)^2\right]$$

$$-2\sigma\left[\frac{\partial u}{\partial\sigma}\frac{D}{Dt}\left(\frac{\partial \ln p_s}{\partial x}\right) + \frac{\partial v}{\partial\sigma}\frac{D}{Dt}\left(\frac{\partial \ln p_s}{\partial y}\right)\right] + \sigma f\left[\frac{\partial \ln p_s}{\partial y}\frac{\partial u}{\partial\sigma} - \frac{\partial \ln p_s}{\partial x}\frac{\partial v}{\partial\sigma}\right]$$

Also note that using the continuity equation the following can be obtained

$$-\frac{\partial u}{\partial x}\frac{\partial u}{\partial x} - \frac{\partial v}{\partial y}\frac{\partial v}{\partial y}$$

$$= \frac{\partial u}{\partial x}\left(\frac{\partial v}{\partial y} + \frac{\partial\dot\sigma}{\partial\sigma} + \frac{D\ln p_s}{Dt}\right) + \frac{\partial v}{\partial y}\left(\frac{\partial u}{\partial x} + \frac{\partial\dot\sigma}{\partial\sigma} + \frac{D\ln p_s}{Dt}\right)$$

$$= \frac{\partial u}{\partial x}\frac{\partial v}{\partial y} + \frac{\partial u}{\partial x}\frac{\partial\dot\sigma}{\partial\sigma} + \frac{\partial u}{\partial x}\frac{D\ln p_s}{Dt} + \frac{\partial v}{\partial y}\frac{\partial u}{\partial x} + \frac{\partial v}{\partial y}\frac{\partial\dot\sigma}{\partial\sigma} + \frac{\partial v}{\partial y}\frac{D\ln p_s}{Dt}$$

$$= 2\frac{\partial u}{\partial x}\frac{\partial v}{\partial y} + \left(\frac{\partial u}{\partial x} + \frac{\partial v}{\partial y}\right)\left(\frac{D\ln p_s}{Dt} + \frac{\partial\dot\sigma}{\partial\sigma}\right)$$

Also note that from the definition $\Omega = \frac{p_s}{p}\left(\sigma\frac{D\ln p_s}{Dt} + \dot\sigma\right)$, $\dot\sigma = \frac{p}{p_s}\Omega - \sigma\frac{D\ln p_s}{Dt}$ and therefore

$$\frac{\partial\dot\sigma}{\partial\sigma} = \frac{\partial}{\partial\sigma}\left(\frac{p}{p_s}\Omega\right) - \frac{\partial\sigma}{\partial\sigma}\frac{D\ln p_s}{Dt} - \sigma\frac{\partial}{\partial\sigma}\left(\frac{D\ln p_s}{Dt}\right)$$

$$= \frac{\partial}{\partial\sigma}\left(\frac{p}{p_s}\Omega\right) - \frac{D\ln p_s}{Dt} - \sigma\frac{\partial}{\partial\sigma}\left(\frac{\partial\ln p_s}{\partial t} + u\frac{\partial\ln p_s}{\partial x} + v\frac{\partial\ln p_s}{\partial y}\right)$$

$$= \frac{\partial}{\partial\sigma}\left(\frac{p}{p_s}\Omega\right) - \frac{D\ln p_s}{Dt} - \sigma\left(\frac{\partial u}{\partial\sigma}\frac{\partial\ln p_s}{\partial x} + \frac{\partial v}{\partial\sigma}\frac{\partial\ln p_s}{\partial y}\right)$$

Also note that from applying the continuity equation

$$-\frac{\partial\dot\sigma}{\partial\sigma}\frac{\partial\dot\sigma}{\partial\sigma} = \frac{\partial\dot\sigma}{\partial\sigma}\left(\frac{\partial u}{\partial x} + \frac{\partial v}{\partial y} + \frac{D\ln p_s}{Dt}\right)$$

$$= \left(\frac{\partial u}{\partial x} + \frac{\partial v}{\partial y}\right)\frac{\partial\dot\sigma}{\partial\sigma} + \frac{D\ln p_s}{Dt}\frac{\partial\dot\sigma}{\partial\sigma}$$

Also

$$-\frac{\partial\dot\sigma}{\partial x}\frac{\partial u}{\partial\sigma} - \frac{\partial\dot\sigma}{\partial y}\frac{\partial v}{\partial\sigma} - \frac{\partial u}{\partial\sigma}\frac{\partial\dot\sigma}{\partial x} - \frac{\partial v}{\partial\sigma}\frac{\partial\dot\sigma}{\partial y}$$

$$= -2\left(\frac{\partial u}{\partial\sigma}\frac{\partial\dot\sigma}{\partial x} + \frac{\partial v}{\partial\sigma}\frac{\partial\dot\sigma}{\partial y}\right)$$

$$= -2\left(\frac{\partial u}{\partial\sigma}\frac{\partial}{\partial x}\left(\frac{p}{p_s}\Omega - \sigma\frac{D\ln p_s}{Dt}\right) + \frac{\partial v}{\partial\sigma}\frac{\partial}{\partial y}\left(\frac{p}{p_s}\Omega - \sigma\frac{D\ln p_s}{Dt}\right)\right)$$

$$= -2\left[\frac{\partial u}{\partial\sigma}\frac{\partial}{\partial x}\left(\frac{p}{p_s}\Omega\right) + \frac{\partial v}{\partial\sigma}\frac{\partial}{\partial y}\left(\frac{p}{p_s}\Omega\right)\right] + 2\left[\frac{\partial u}{\partial\sigma}\frac{\partial}{\partial x}\left(\sigma\frac{D\ln p_s}{Dt}\right) + \frac{\partial v}{\partial\sigma}\frac{\partial}{\partial y}\left(\sigma\frac{D\ln p_s}{Dt}\right)\right]$$

$$= -2\left[\frac{\partial u}{\partial\sigma}\frac{\partial}{\partial x}\left(\frac{p}{p_s}\Omega\right) + \frac{\partial v}{\partial\sigma}\frac{\partial}{\partial y}\left(\frac{p}{p_s}\Omega\right)\right] + 2\left[\frac{\partial u}{\partial\sigma}\frac{\partial\sigma}{\partial x}\frac{D\ln p_s}{Dt} + \frac{\partial v}{\partial\sigma}\frac{\partial\sigma}{\partial y}\frac{D\ln p_s}{Dt}\right]$$

$$+2\sigma\left[\frac{\partial u}{\partial\sigma}\frac{\partial}{\partial x}\left(\frac{D\ln p_s}{Dt}\right) + \frac{\partial v}{\partial\sigma}\frac{\partial}{\partial y}\left(\frac{D\ln p_s}{Dt}\right)\right]$$

Noting the σ is constant along the x and y axis and expanding the $\frac{D\ln p_s}{Dt}$ the following can be obtained

$$-\frac{\partial\dot\sigma}{\partial x}\frac{\partial u}{\partial\sigma} - \frac{\partial\dot\sigma}{\partial y}\frac{\partial v}{\partial\sigma} - \frac{\partial u}{\partial\sigma}\frac{\partial\dot\sigma}{\partial x} - \frac{\partial v}{\partial\sigma}\frac{\partial\dot\sigma}{\partial y}$$

$$= -2\left[\frac{\partial u}{\partial \sigma}\frac{\partial}{\partial x}\left(\frac{p}{p_s}\Omega\right) + \frac{\partial v}{\partial \sigma}\frac{\partial}{\partial y}\left(\frac{p}{p_s}\Omega\right)\right]$$

$$+2\sigma\left[\frac{\partial u}{\partial \sigma}\frac{\partial}{\partial x}\left(\frac{\partial \ln p_s}{\partial t} + u\frac{\partial \ln p_s}{\partial x} + v\frac{\partial \ln p_s}{\partial y}\right) + \frac{\partial v}{\partial \sigma}\frac{\partial}{\partial y}\left(\frac{\partial \ln p_s}{\partial t} + u\frac{\partial \ln p_s}{\partial x} + v\frac{\partial \ln p_s}{\partial y}\right)\right]$$

$$= -2\left[\frac{\partial u}{\partial \sigma}\frac{\partial}{\partial x}\left(\frac{p}{p_s}\Omega\right) + \frac{\partial v}{\partial \sigma}\frac{\partial}{\partial y}\left(\frac{p}{p_s}\Omega\right)\right]$$

$$+2\sigma\left[\frac{\partial u}{\partial \sigma}\left(\frac{\partial}{\partial t}\frac{\partial \ln p_s}{\partial x} + u\frac{\partial}{\partial x}\frac{\partial \ln p_s}{\partial x} + \frac{\partial u}{\partial x}\frac{\partial \ln p_s}{\partial x} + v\frac{\partial}{\partial y}\frac{\partial \ln p_s}{\partial x} + \frac{\partial v}{\partial x}\frac{\partial \ln p_s}{\partial y}\right)\right]$$

$$+2\sigma\left[\frac{\partial v}{\partial \sigma}\left(\frac{\partial}{\partial t}\frac{\partial \ln p_s}{\partial y} + u\frac{\partial}{\partial x}\frac{\partial \ln p_s}{\partial y} + \frac{\partial u}{\partial y}\frac{\partial \ln p_s}{\partial x} + v\frac{\partial}{\partial y}\frac{\partial \ln p_s}{\partial y} + \frac{\partial v}{\partial y}\frac{\partial \ln p_s}{\partial y}\right)\right]$$

$$= -2\left[\frac{\partial u}{\partial \sigma}\frac{\partial}{\partial x}\left(\frac{p}{p_s}\Omega\right) + \frac{\partial v}{\partial \sigma}\frac{\partial}{\partial y}\left(\frac{p}{p_s}\Omega\right)\right]$$

$$+2\sigma\left[\frac{\partial u}{\partial \sigma}\frac{D}{Dt}\left(\frac{\partial \ln p_s}{\partial x}\right) + \frac{\partial v}{\partial \sigma}\frac{D}{Dt}\left(\frac{\partial \ln p_s}{\partial y}\right)\right]$$

$$+2\sigma\frac{\partial u}{\partial \sigma}\left(\frac{\partial u}{\partial x}\frac{\partial \ln p_s}{\partial x} + \frac{\partial v}{\partial x}\frac{\partial \ln p_s}{\partial y}\right) + 2\sigma\frac{\partial v}{\partial \sigma}\left(\frac{\partial u}{\partial y}\frac{\partial \ln p_s}{\partial x} + \frac{\partial v}{\partial y}\frac{\partial \ln p_s}{\partial y}\right)$$

Putting all the simplifications back into the elliptic equation gives:

$$\frac{\partial^2 \phi}{\partial x^2} + \frac{\partial^2 \phi}{\partial y} + \frac{\partial}{\partial \sigma}\left[s^2\frac{\partial \phi}{\partial \sigma}\right]$$

$$-\sigma\frac{\partial \phi}{\partial \sigma}\left(\frac{\partial^2 \ln p_s}{\partial x^2} + \frac{\partial^2 \ln p_s}{\partial y^2}\right) - \sigma\left[\frac{\partial \ln p_s}{\partial x}\left(\frac{\partial^2 \phi}{\partial x \partial \sigma}\right) + \frac{\partial \ln p_s}{\partial y}\left(\frac{\partial^2 \phi}{\partial y \partial \sigma}\right)\right] =$$

$$\left(-\frac{\partial v}{\partial x}\frac{\partial u}{\partial y}\right) + \left(-\frac{\partial u}{\partial y}\frac{\partial v}{\partial x}\right)$$

$$+\left(\frac{\partial u}{\partial x} + \frac{\partial v}{\partial y}\right)\frac{\partial \dot{\sigma}}{\partial \sigma} + \frac{D\ln p_s}{Dt}\frac{\partial \dot{\sigma}}{\partial \sigma}$$

$$+2\frac{\partial u}{\partial x}\frac{\partial v}{\partial y} + \left(\frac{\partial u}{\partial x} + \frac{\partial v}{\partial y}\right)\left(\frac{D\ln p_s}{Dt} + \frac{\partial \dot{\sigma}}{\partial \sigma}\right)$$

$$-\frac{\partial}{\partial \sigma}\left[\dot{\sigma}\left(\frac{p}{R_d p_s T}\right)\frac{D}{Dt}\left(\frac{R_d T p_s}{p}\right)\right]$$

$$-2\left[\frac{\partial u}{\partial \sigma}\frac{\partial}{\partial x}\left(\frac{p}{p_s}\Omega\right) + \frac{\partial v}{\partial \sigma}\frac{\partial}{\partial y}\left(\frac{p}{p_s}\Omega\right)\right]$$

$$+2\sigma\left[\frac{\partial u}{\partial \sigma}\frac{D}{Dt}\left(\frac{\partial \ln p_s}{\partial x}\right) + \frac{\partial v}{\partial \sigma}\frac{D}{Dt}\left(\frac{\partial \ln p_s}{\partial y}\right)\right]$$

$$+2\sigma\frac{\partial u}{\partial \sigma}\left(\frac{\partial u}{\partial x}\frac{\partial \ln p_s}{\partial x} + \frac{\partial v}{\partial x}\frac{\partial \ln p_s}{\partial y}\right) + 2\sigma\frac{\partial v}{\partial \sigma}\left(\frac{\partial u}{\partial y}\frac{\partial \ln p_s}{\partial x} + \frac{\partial v}{\partial y}\frac{\partial \ln p_s}{\partial y}\right)$$

$$+\sigma\left(\frac{\partial^2 \phi}{\partial x \partial \sigma}\frac{\partial \ln p_s}{\partial x} + \frac{\partial^2 \phi}{\partial y \partial \sigma}\frac{\partial \ln p_s}{\partial y}\right) - \sigma\frac{\partial}{\partial \sigma}\left(\sigma\frac{\partial \phi}{\partial \sigma}\right)\left[\left(\frac{\partial \ln p_s}{\partial x}\right)^2 + \left(\frac{\partial \ln p_s}{\partial y}\right)^2\right]$$

$$-2\sigma\left[\frac{\partial u}{\partial \sigma}\frac{D}{Dt}\left(\frac{\partial \ln p_s}{\partial x}\right) + \frac{\partial v}{\partial \sigma}\frac{D}{Dt}\left(\frac{\partial \ln p_s}{\partial y}\right)\right]$$

$$-\frac{\partial}{\partial \sigma}\left\{\left[\dot{\sigma} + \frac{\sigma p}{R_d p_s T}\frac{D}{Dt}\left(\frac{R_d T p_s}{p}\right)\right]\frac{D\ln p_s}{Dt}\right\}$$

$$-\frac{\partial}{\partial \sigma}(sg)$$

$$+\sigma f\left[\frac{\partial \ln p_s}{\partial y}\frac{\partial u}{\partial \sigma} - \frac{\partial \ln p_s}{\partial x}\frac{\partial v}{\partial \sigma}\right] + f\left(\frac{\partial v}{\partial x} - \frac{\partial u}{\partial y}\right) - u\frac{\partial f}{\partial y}$$

$$+\frac{\partial}{\partial\sigma}\left\{s\left[\frac{\partial\overline{u'w'}}{\partial x}+\frac{\partial\overline{v'w'}}{\partial y}+\frac{\partial\overline{w'\dot{\sigma}'}}{\partial\sigma}\right]\right\}-\frac{\partial}{\partial y}\left[\frac{\partial\overline{u'v'}}{\partial x}+\frac{\partial\overline{v'v'}}{\partial y}+\frac{\partial\overline{v'\dot{\sigma}'}}{\partial\sigma}\right]$$

$$-\frac{\partial}{\partial x}\left[\frac{\partial\overline{u'u'}}{\partial x}+\frac{\partial\overline{v'u'}}{\partial y}+\frac{\partial\overline{u'\dot{\sigma}'}}{\partial\sigma}\right]$$

Which becomes

$$\frac{\partial^2\phi}{\partial x^2}+\frac{\partial^2\phi}{\partial y}+\frac{\partial}{\partial\sigma}\left[s^2\frac{\partial\phi}{\partial\sigma}\right]-\sigma\frac{\partial\phi}{\partial\sigma}\left(\frac{\partial^2\ln p_s}{\partial x^2}+\frac{\partial^2\ln p_s}{\partial y^2}\right)$$

$$+\sigma\frac{\partial}{\partial\sigma}\left(\sigma\frac{\partial\phi}{\partial\sigma}\right)\left[\left(\frac{\partial\ln p_s}{\partial x}\right)^2+\left(\frac{\partial\ln p_s}{\partial y}\right)^2\right]$$

$$-2\sigma\left[\frac{\partial\ln p_s}{\partial x}\left(\frac{\partial^2\phi}{\partial x\partial\sigma}\right)+\frac{\partial\ln p_s}{\partial y}\left(\frac{\partial^2\phi}{\partial y\partial\sigma}\right)\right]=$$

$$2\left(\frac{\partial u}{\partial x}\frac{\partial v}{\partial y}-\frac{\partial v}{\partial x}\frac{\partial u}{\partial y}\right)+2\left(\frac{\partial u}{\partial x}+\frac{\partial v}{\partial y}\right)\frac{\partial\dot{\sigma}}{\partial\sigma}+\frac{D\ln p_s}{Dt}\frac{\partial\dot{\sigma}}{\partial\sigma}+\left(\frac{\partial u}{\partial x}+\frac{\partial v}{\partial y}\right)\left(\frac{D\ln p_s}{Dt}\right)$$

$$-2\left[\frac{\partial u}{\partial\sigma}\frac{\partial}{\partial x}\left(\frac{p}{p_s}\Omega\right)+\frac{\partial v}{\partial\sigma}\frac{\partial}{\partial y}\left(\frac{p}{p_s}\Omega\right)\right]$$

$$+2\sigma\frac{\partial u}{\partial\sigma}\left(\frac{\partial u}{\partial x}\frac{\partial\ln p_s}{\partial x}+\frac{\partial v}{\partial x}\frac{\partial\ln p_s}{\partial y}\right)+2\sigma\frac{\partial v}{\partial\sigma}\left(\frac{\partial u}{\partial y}\frac{\partial\ln p_s}{\partial x}+\frac{\partial v}{\partial y}\frac{\partial\ln p_s}{\partial y}\right)$$

$$-\frac{\partial}{\partial\sigma}(sg)-\frac{\partial}{\partial\sigma}\left[\dot{\sigma}\left(\frac{p}{R_dp_sT}\right)\frac{D}{Dt}\left(\frac{R_dTp_s}{p}\right)\right]-\frac{\partial}{\partial\sigma}\left\{\left[\dot{\sigma}+\frac{\sigma p}{R_dp_sT}\frac{D}{Dt}\left(\frac{R_dTp_s}{p}\right)\right]\frac{D\ln p_s}{Dt}\right\}$$

$$+\sigma f\left[\frac{\partial\ln p_s}{\partial y}\frac{\partial u}{\partial\sigma}-\frac{\partial\ln p_s}{\partial x}\frac{\partial v}{\partial\sigma}\right]+f\left(\frac{\partial v}{\partial x}-\frac{\partial u}{\partial y}\right)-u\frac{\partial f}{\partial y}$$

$$+\frac{\partial}{\partial\sigma}\left\{s\left[\frac{\partial\overline{u'w'}}{\partial x}+\frac{\partial\overline{v'w'}}{\partial y}+\frac{\partial\overline{w'\dot{\sigma}'}}{\partial\sigma}\right]\right\}-\frac{\partial}{\partial y}\left[\frac{\partial\overline{u'v'}}{\partial x}+\frac{\partial\overline{v'v'}}{\partial y}+\frac{\partial\overline{v'\dot{\sigma}'}}{\partial\sigma}\right]$$

$$-\frac{\partial}{\partial x}\left[\frac{\partial\overline{u'u'}}{\partial x}+\frac{\partial\overline{v'u'}}{\partial y}+\frac{\partial\overline{u'\dot{\sigma}'}}{\partial\sigma}\right]$$

But

$$-2\left[\frac{\partial u}{\partial\sigma}\frac{\partial}{\partial x}\left(\frac{p}{p_s}\Omega\right)+\frac{\partial v}{\partial\sigma}\frac{\partial}{\partial y}\left(\frac{p}{p_s}\Omega\right)\right]$$

$$=-\frac{2}{p_s}\left[\frac{\partial u}{\partial\sigma}\frac{\partial}{\partial x}(p\Omega)+\frac{\partial v}{\partial\sigma}\frac{\partial}{\partial y}(p\Omega)\right]-2p\Omega\left[\frac{\partial u}{\partial\sigma}(-1)\frac{1}{p_s^2}\frac{\partial p_s}{\partial x}+\frac{\partial v}{\partial\sigma}(-1)\frac{1}{p_s^2}\frac{\partial p_s}{\partial y}\right]$$

$$=-\frac{2}{p_s}\left[\frac{\partial u}{\partial\sigma}\frac{\partial}{\partial x}(p\Omega)+\frac{\partial v}{\partial\sigma}\frac{\partial}{\partial y}(p\Omega)\right]+\frac{2}{p_s}(p\Omega)\left[\frac{\partial u}{\partial\sigma}\frac{\partial\ln p_s}{\partial x}+\frac{\partial v}{\partial\sigma}\frac{\partial\ln p_s}{\partial y}\right]$$

and

$$2\left(\frac{\partial u}{\partial x}+\frac{\partial v}{\partial y}\right)\frac{\partial\dot{\sigma}}{\partial\sigma}+\frac{D\ln p_s}{Dt}\frac{\partial\dot{\sigma}}{\partial\sigma}+\left(\frac{\partial u}{\partial x}+\frac{\partial v}{\partial y}\right)\left(\frac{D\ln p_s}{Dt}\right)$$

$=2\left(\frac{\partial u}{\partial x}+\frac{\partial v}{\partial y}\right)\frac{\partial\dot{\sigma}}{\partial\sigma}+\frac{D\ln p_s}{Dt}\frac{\partial\dot{\sigma}}{\partial\sigma}+\left(-\frac{\partial\dot{\sigma}}{\partial\sigma}-\frac{D\ln p_s}{Dt}\right)\left(\frac{D\ln p_s}{Dt}\right)$ from continuity equation

$$=2\left(\frac{\partial u}{\partial x}+\frac{\partial v}{\partial y}\right)\frac{\partial\dot{\sigma}}{\partial\sigma}-\left(\frac{D\ln p_s}{Dt}\right)^2$$

$$=2\left(\frac{\partial u}{\partial x}+\frac{\partial v}{\partial y}\right)\frac{\partial}{\partial\sigma}\left(\frac{\Omega p}{p_s}-\sigma\frac{D\ln p_s}{Dt}\right)-\left(\frac{D\ln p_s}{Dt}\right)^2$$

$$= 2\left(\frac{\partial u}{\partial x}+\frac{\partial v}{\partial y}\right)\frac{\partial}{\partial\sigma}\left(\frac{\Omega p}{p_s}\right)-2\left(\frac{\partial u}{\partial x}+\frac{\partial v}{\partial y}\right)\frac{D\ln p_s}{Dt}-2\sigma\left(\frac{\partial u}{\partial x}+\frac{\partial v}{\partial y}\right)\frac{\partial}{\partial\sigma}\left(\frac{D\ln p_s}{Dt}\right)-\left(\frac{D\ln p_s}{Dt}\right)^2$$

$$=2\left(\frac{\partial u}{\partial x}+\frac{\partial v}{\partial y}\right)\frac{\partial}{\partial\sigma}\left(\frac{\Omega p}{p_s}\right)-2\left(-\frac{\partial\dot{\sigma}}{\partial\sigma}-\frac{D\ln p_s}{Dt}\right)\frac{D\ln p_s}{Dt}-2\sigma\left(\frac{\partial u}{\partial x}+\frac{\partial v}{\partial y}\right)\frac{\partial}{\partial\sigma}\left(\frac{D\ln p_s}{Dt}\right)-\left(\frac{D\ln p_s}{Dt}\right)^2$$

$$=2\left(\frac{\partial u}{\partial x}+\frac{\partial v}{\partial y}\right)\frac{\partial}{\partial\sigma}\left(\frac{\Omega p}{p_s}\right)-2\left(-\frac{\partial\dot{\sigma}}{\partial\sigma}-\frac{D\ln p_s}{Dt}\right)\frac{D\ln p_s}{Dt}$$

$$-2\sigma\left(\frac{\partial u}{\partial x}+\frac{\partial v}{\partial y}\right)\left(\frac{\partial u}{\partial\sigma}\frac{\partial\ln p_s}{\partial x}+\frac{\partial v}{\partial\sigma}\frac{\partial\ln p_s}{\partial y}\right)-\left(\frac{D\ln p_s}{Dt}\right)^2$$

and

$$-\frac{\partial}{\partial\sigma}\left[\dot{\sigma}\left(\frac{p}{R_d p_s T}\right)\frac{D}{Dt}\left(\frac{R_d T p_s}{p}\right)\right]-\frac{\partial}{\partial\sigma}\left\{\left[\dot{\sigma}+\frac{\sigma p}{R_d p_s T}\frac{D}{Dt}\left(\frac{R_d T p_s}{p}\right)\right]\frac{D\ln p_s}{Dt}\right\}$$

$$=-\frac{\partial}{\partial\sigma}\left(\dot{\sigma}\frac{D\ln p_s}{Dt}\right)-\frac{\partial}{\partial\sigma}\left[\dot{\sigma}\left(\frac{p}{R_d p_s T}\right)\frac{D}{Dt}\left(\frac{R_d T p_s}{p}\right)\right]-\frac{\partial}{\partial\sigma}\left\{\left[\frac{\sigma p}{R_d p_s T}\frac{D}{Dt}\left(\frac{R_d T p_s}{p}\right)\right]\frac{D\ln p_s}{Dt}\right\}$$

$$=-\frac{\partial}{\partial\sigma}\left(\dot{\sigma}\frac{D\ln p_s}{Dt}\right)-\frac{\partial}{\partial\sigma}\left\{\left[\dot{\sigma}\left(\frac{p}{R_d p_s T}\right)\frac{D}{Dt}\left(\frac{R_d T p_s}{p}\right)\right]+\left[\frac{\sigma p}{R_d p_s T}\frac{D}{Dt}\left(\frac{R_d T p_s}{p}\right)\right]\frac{D\ln p_s}{Dt}\right\}$$

$$=-\frac{\partial}{\partial\sigma}\left(\dot{\sigma}\frac{D\ln p_s}{Dt}\right)-\frac{\partial}{\partial\sigma}\left[\left(\frac{p}{R_d p_s T}\right)\frac{D}{Dt}\left(\frac{R_d T p_s}{p}\right)\left(\dot{\sigma}+\sigma\frac{D\ln p_s}{Dt}\right)\right]$$

$$=-\frac{\partial}{\partial\sigma}\left(\dot{\sigma}\frac{D\ln p_s}{Dt}\right)-\frac{\partial}{\partial\sigma}\left[\left(\frac{p}{R_d p_s T}\right)\frac{D}{Dt}\left(\frac{R_d T p_s}{p}\right)\frac{p}{p_s}\Omega\right]$$

$$=-\frac{\partial}{\partial\sigma}\left(\dot{\sigma}\frac{D\ln p_s}{Dt}\right)-\frac{\partial}{\partial\sigma}\left[\left(\frac{p^2}{R_d p_s^2 T}\Omega\right)\frac{D}{Dt}\left(\frac{R_d T p_s}{p}\right)\right]$$

$$=-\frac{\partial}{\partial\sigma}\left(\dot{\sigma}\frac{D\ln p_s}{Dt}\right)-\frac{\partial}{\partial\sigma}\left[\left(\frac{p^2}{R_d p_s^2 T}\Omega\right)\left[\frac{R_d p_s}{p}\frac{DT}{Dt}+\frac{R_d T}{p}\frac{Dp_s}{Dt}+R_d T p_s\frac{D}{Dt}\left(\frac{1}{p}\right)+\frac{T p_s}{p}\frac{DR_m}{Dt}\right]\right]$$

$$=-\frac{\partial}{\partial\sigma}\left(\dot{\sigma}\frac{D\ln p_s}{Dt}\right)-\frac{\partial}{\partial\sigma}\left[\frac{p\Omega}{p_s T}\frac{DT}{Dt}+\frac{P\Omega}{p_s^2}\frac{Dp_s}{Dt}+\frac{p^{2}\Omega}{p_s}\frac{D}{Dt}\left(\frac{1}{p}\right)\right]$$

$$=-\frac{\partial}{\partial\sigma}\left(\dot{\sigma}\frac{D\ln p_s}{Dt}\right)-\frac{\partial}{\partial\sigma}\left[\frac{p\Omega}{p_s T}\frac{DT}{Dt}+\frac{P\Omega}{p_s}\frac{D\ln p_s}{Dt}+\frac{(-1)p^{-2}p^2\Omega}{p_s}\frac{Dp}{Dt}\right]$$

$$=-\frac{\partial}{\partial\sigma}\left(\dot{\sigma}\frac{D\ln p_s}{Dt}\right)-\frac{\partial}{\partial\sigma}\left[\frac{p\Omega}{p_s T}\frac{DT}{Dt}-\frac{\Omega}{p_s}\frac{Dp}{Dt}\right]$$

$$-\frac{p\Omega}{p_s}\frac{\partial}{\partial\sigma}\left(\frac{D\ln p_s}{Dt}\right)-\frac{\partial}{\partial\sigma}(p\Omega)\frac{1}{p_s}\frac{D\ln p_s}{Dt}$$

$=-\frac{\partial}{\partial\sigma}\left(\dot{\sigma}\frac{D\ln p_s}{Dt}\right)-\frac{\partial}{\partial\sigma}\left[\frac{p\Omega}{p_s T}\left(\frac{R_d\omega T}{c_p p}+\frac{S_h}{c_p}+rad+\left(\frac{p}{\hat{p}}\right)^{R_d/c_p}\left[\frac{\partial\overline{u'\theta'}}{\partial x}+\frac{\partial\overline{v'\theta'}}{\partial y}+\frac{\partial\overline{\dot{\sigma}'\theta'}}{\partial\sigma}\right]\right)-\frac{\Omega\omega}{p_s}\right]$ using thermodynamic equation and definition of ω.

$$-\frac{p\Omega}{p_s}\frac{\partial}{\partial\sigma}\left(\frac{D\ln p_s}{Dt}\right)-\frac{\partial}{\partial\sigma}(p\Omega)\frac{1}{p_s}\frac{D\ln p_s}{Dt}$$

$$=-\frac{\partial}{\partial\sigma}\left(\dot{\sigma}\frac{D\ln p_s}{Dt}\right)-\frac{\partial}{\partial\sigma}\left[\frac{p\Omega}{p_s T}\left(\frac{R_d\omega T}{c_p p}\right)-\frac{\Omega\omega}{p_s}\right]-\frac{\partial}{\partial\sigma}\left(\frac{S_h p\Omega}{p_s T c_p}\right)$$

$$-\frac{p\Omega}{p_s}\frac{\partial}{\partial\sigma}\left(\frac{D\ln p_s}{Dt}\right)-\frac{\partial}{\partial\sigma}(p\Omega)\frac{1}{p_s}\frac{D\ln p_s}{Dt}$$

$$-\frac{\partial}{\partial\sigma}\left(\frac{p\Omega rad}{p_sT}\right)-\frac{\partial}{\partial\sigma}\left\{\frac{p\Omega}{p_sT}\left(\frac{p}{\hat{p}}\right)^{R_d/c_p}\left[\frac{\partial\overline{u'\theta'}}{\partial x}+\frac{\partial\overline{v'\theta'}}{\partial y}+\frac{\partial\overline{\dot{\sigma}'\theta'}}{\partial\sigma}\right]\right\}$$

$$=-\frac{\partial}{\partial\sigma}\left(\dot{\sigma}\frac{D\ln p_s}{Dt}\right)-\frac{\partial}{\partial\sigma}\left[\frac{\Omega\omega(\kappa-1)}{p_s}\right]-\frac{\partial}{\partial\sigma}\left(\frac{S_hp\Omega}{p_sTc_p}\right)$$

$$-\frac{p\Omega}{p_s}\frac{\partial}{\partial\sigma}\left(\frac{D\ln p_s}{Dt}\right)-\frac{\partial}{\partial\sigma}\left(p\Omega\right)\frac{1}{p_s}\frac{D\ln p_s}{Dt}-\frac{\partial}{\partial\sigma}\left(\frac{p\Omega rad}{p_sT}\right)$$

$$-\frac{\partial}{\partial\sigma}\left\{\frac{p\Omega}{p_sT}\left(\frac{p}{\hat{p}}\right)^{R_d/c_p}\left[\frac{\partial\overline{u'\theta'}}{\partial x}+\frac{\partial\overline{v'\theta'}}{\partial y}+\frac{\partial\overline{\dot{\sigma}'\theta'}}{\partial\sigma}\right]\right\}$$

But

$$-\frac{\partial}{\partial\sigma}\left[\frac{\Omega\omega(\kappa-1)}{p_s}\right]=\left(1-\kappa\right)\frac{\partial}{\partial\sigma}\left(\frac{\omega\Omega}{p_s}\right)$$

$$=\left(1-\frac{R_d}{c_p}\right)\frac{\partial}{\partial\sigma}\left(\frac{\omega\Omega}{p_s}\right)$$

$$=\left(\frac{c_p-R_d}{c_p}\right)\frac{\partial}{\partial\sigma}\left(\frac{\omega\Omega}{p_s}\right)$$

$$=\left(\frac{c_v}{c_p}\right)\frac{\partial}{\partial\sigma}\left(\frac{\omega\Omega}{p_s}\right)$$

$$=\frac{1}{\gamma}\frac{\partial}{\partial\sigma}\left(\frac{p\Omega^2}{p_s}\right)$$

Therefore

$$-\frac{\partial}{\partial\sigma}\left[\dot{\sigma}\left(\frac{p}{R_mp_sT}\right)\frac{D}{Dt}\left(\frac{R_mTp_s}{p}\right)\right]-\frac{\partial}{\partial\sigma}\left\{\left[\dot{\sigma}+\frac{\sigma p}{R_mp_sT}\frac{D}{Dt}\left(\frac{R_mTp_s}{p}\right)\right]\frac{D\ln p_s}{Dt}\right\}$$

$$=-\frac{\partial}{\partial\sigma}\left(\dot{\sigma}\frac{D\ln p_s}{Dt}\right)+\frac{1}{\gamma}\frac{\partial}{\partial\sigma}\left(\frac{p\Omega^2}{p_s}\right)-\frac{\partial}{\partial\sigma}\left(\frac{S_hp\Omega}{p_sTc_p}\right)$$

$$-\frac{p\Omega}{p_s}\frac{\partial}{\partial\sigma}\left(\frac{D\ln p_s}{Dt}\right)-\frac{\partial}{\partial\sigma}\left(p\Omega\right)\frac{1}{p_s}\frac{D\ln p_s}{Dt}-\frac{\partial}{\partial\sigma}\left(\frac{p\Omega rad}{p_sT}\right)$$

$$-\frac{\partial}{\partial\sigma}\left\{\frac{p\Omega}{p_sT}\left(\frac{p}{\hat{p}}\right)^{R_d/c_p}\left[\frac{\partial\overline{u'\theta'}}{\partial x}+\frac{\partial\overline{v'\theta'}}{\partial y}+\frac{\partial\overline{\dot{\sigma}'\theta'}}{\partial\sigma}\right]\right\}$$

$$=-\frac{\partial\dot{\sigma}}{\partial\sigma}\frac{D\ln p_s}{Dt}-\dot{\sigma}\frac{\partial}{\partial\sigma}\left(\frac{\partial\ln p_s}{\partial t}+u\frac{\partial\ln p_s}{\partial x}+v\frac{\partial\ln p_s}{\partial y}\right)$$

$$-\frac{p\Omega}{p_s}\frac{\partial}{\partial\sigma}\left(\frac{\partial\ln p_s}{\partial t}+u\frac{\partial\ln p_s}{\partial x}+v\frac{\partial\ln p_s}{\partial y}\right)-\frac{\partial}{\partial\sigma}\left(\omega\right)\frac{1}{p_s}\frac{D\ln p_s}{Dt}$$

$$+\frac{1}{\gamma}\frac{\partial}{\partial\sigma}\left(\frac{p\Omega^2}{p_s}\right)-\frac{\partial}{\partial\sigma}\left(\frac{S_hp\Omega}{p_sTc_p}\right)-\frac{\partial}{\partial\sigma}\left(\frac{p\Omega rad}{p_sT}\right)-\frac{\partial}{\partial\sigma}\left\{\frac{p\Omega}{p_sT}\left(\frac{p}{\hat{p}}\right)^{R_d/c_p}\left[\frac{\partial\overline{u'\theta'}}{\partial x}+\frac{\partial\overline{v'\theta'}}{\partial y}+\frac{\partial\overline{\dot{\sigma}'\theta'}}{\partial\sigma}\right]\right\}$$

$$=-\frac{\partial\dot{\sigma}}{\partial\sigma}\frac{D\ln p_s}{Dt}-\frac{p\Omega}{p_s}\left(\frac{\partial u}{\partial\sigma}\frac{\partial\ln p_s}{\partial x}+\frac{\partial v}{\partial\sigma}\frac{\partial\ln p_s}{\partial y}\right)$$

$$-\frac{\partial}{\partial\sigma}\left[p_s\left(\sigma\frac{D\ln p_s}{Dt}+\dot{\sigma}\right)\right]\frac{1}{p_s}\frac{D\ln p_s}{Dt}-\dot{\sigma}\frac{\partial u}{\partial\sigma}\frac{\partial\ln p_s}{\partial x}-\dot{\sigma}\frac{\partial v}{\partial\sigma}\frac{\partial\ln p_s}{\partial y}$$

$$+\frac{1}{\gamma}\frac{\partial}{\partial\sigma}\left(\frac{p\Omega^2}{p_s}\right)-\frac{\partial}{\partial\sigma}\left(\frac{S_hp\Omega}{p_sTc_p}\right)-\frac{\partial}{\partial\sigma}\left(\frac{p\Omega rad}{p_sT}\right)-\frac{\partial}{\partial\sigma}\left\{\frac{p\Omega}{p_sT}\left(\frac{p}{\hat{p}}\right)^{R_d/c_p}\left[\frac{\partial\overline{u'\theta'}}{\partial x}+\frac{\partial\overline{v'\theta'}}{\partial y}+\frac{\partial\overline{\dot{\sigma}'\theta'}}{\partial\sigma}\right]\right\}$$

$$=-\frac{\partial\dot{\sigma}}{\partial\sigma}\frac{D\ln p_s}{Dt}-\frac{p\Omega}{p_s}\left(\frac{\partial u}{\partial\sigma}\frac{\partial\ln p_s}{\partial x}+\frac{\partial v}{\partial\sigma}\frac{\partial\ln p_s}{\partial y}\right)$$

$$-\frac{\partial\dot{\sigma}}{\partial\sigma}\frac{D\ln p_s}{Dt}-\frac{\partial\sigma}{\partial\sigma}\left(\frac{D\ln p_s}{Dt}\right)\frac{D\ln p_s}{Dt}-\sigma\frac{\partial}{\partial\sigma}\left(\frac{D\ln p_s}{Dt}\right)\frac{D\ln p_s}{Dt}-\dot{\sigma}\left(\frac{\partial u}{\partial\sigma}\frac{\partial\ln p_s}{\partial x}+\frac{\partial v}{\partial\sigma}\frac{\partial\ln p_s}{\partial y}\right)$$

$$+\frac{1}{\gamma}\frac{\partial}{\partial\sigma}\left(\frac{p\Omega^2}{p_s}\right)-\frac{\partial}{\partial\sigma}\left(\frac{S_hp\Omega}{p_sTc_p}\right)-\frac{\partial}{\partial\sigma}\left(\frac{p\Omega rad}{p_sT}\right)-\frac{\partial}{\partial\sigma}\left\{\frac{p\Omega}{p_sT}\left(\frac{p}{\hat{p}}\right)^{R_d/c_p}\left[\frac{\partial\overline{u'\theta'}}{\partial x}+\frac{\partial\overline{v'\theta'}}{\partial y}+\frac{\partial\overline{\dot{\sigma}'\theta'}}{\partial\sigma}\right]\right\}$$

$$=-2\frac{\partial\dot{\sigma}}{\partial\sigma}\frac{D\ln p_s}{Dt}-\frac{p\Omega}{p_s}\left(\frac{\partial u}{\partial\sigma}\frac{\partial\ln p_s}{\partial x}+\frac{\partial v}{\partial\sigma}\frac{\partial\ln p_s}{\partial y}\right)-\left(\frac{D\ln p_s}{Dt}\right)^2$$

$$-\sigma\left[\frac{\partial u}{\partial\sigma}\frac{\partial\ln p_s}{\partial x}+\frac{\partial v}{\partial\sigma}\frac{\partial\ln p_s}{\partial y}\right]\frac{D\ln p_s}{Dt}-\dot{\sigma}\left(\frac{\partial u}{\partial\sigma}\frac{\partial\ln p_s}{\partial x}+\frac{\partial v}{\partial\sigma}\frac{\partial\ln p_s}{\partial y}\right)$$

$$+\frac{1}{\gamma}\frac{\partial}{\partial\sigma}\left(\frac{p\Omega^2}{p_s}\right)-\frac{\partial}{\partial\sigma}\left(\frac{S_hp\Omega}{p_sTc_p}\right)-\frac{\partial}{\partial\sigma}\left(\frac{p\Omega rad}{p_sT}\right)-\frac{\partial}{\partial\sigma}\left\{\frac{p\Omega}{p_sT}\left(\frac{p}{\hat{p}}\right)^{R_d/c_p}\left[\frac{\partial\overline{u'\theta'}}{\partial x}+\frac{\partial\overline{v'\theta'}}{\partial y}+\frac{\partial\overline{\dot{\sigma}'\theta'}}{\partial\sigma}\right]\right\}$$

$$=-2\frac{\partial\dot{\sigma}}{\partial\sigma}\frac{D\ln p_s}{Dt}-\frac{p\Omega}{p_s}\left(\frac{\partial u}{\partial\sigma}\frac{\partial\ln p_s}{\partial x}+\frac{\partial v}{\partial\sigma}\frac{\partial\ln p_s}{\partial y}\right)-\left(\frac{D\ln p_s}{Dt}\right)^2$$

$$-\left(\sigma\frac{D\ln p_s}{Dt}+\dot{\sigma}\right)\left(\frac{\partial u}{\partial\sigma}\frac{\partial\ln p_s}{\partial x}+\frac{\partial v}{\partial\sigma}\frac{\partial\ln p_s}{\partial y}\right)$$

$$+\frac{1}{\gamma}\frac{\partial}{\partial\sigma}\left(\frac{p\Omega^2}{p_s}\right)-\frac{\partial}{\partial\sigma}\left(\frac{S_hp\Omega}{p_sTc_p}\right)-\frac{\partial}{\partial\sigma}\left(\frac{p\Omega rad}{p_sT}\right)-\frac{\partial}{\partial\sigma}\left\{\frac{p\Omega}{p_sT}\left(\frac{p}{\hat{p}}\right)^{R_d/c_p}\left[\frac{\partial\overline{u'\theta'}}{\partial x}+\frac{\partial\overline{v'\theta'}}{\partial y}+\frac{\partial\overline{\dot{\sigma}'\theta'}}{\partial\sigma}\right]\right\}$$

$$=-2\frac{\partial\dot{\sigma}}{\partial\sigma}\frac{D\ln p_s}{Dt}-2\frac{p\Omega}{p_s}\left(\frac{\partial u}{\partial\sigma}\frac{\partial\ln p_s}{\partial x}+\frac{\partial v}{\partial\sigma}\frac{\partial\ln p_s}{\partial y}\right)-\left(\frac{D\ln p_s}{Dt}\right)^2$$

$$+\frac{1}{\gamma}\frac{\partial}{\partial\sigma}\left(\frac{p\Omega^2}{p_s}\right)-\frac{\partial}{\partial\sigma}\left(\frac{S_hp\Omega}{p_sTc_p}\right)-\frac{\partial}{\partial\sigma}\left(\frac{p\Omega rad}{p_sT}\right)-\frac{\partial}{\partial\sigma}\left\{\frac{p\Omega}{p_sT}\left(\frac{p}{\hat{p}}\right)^{R_d/c_p}\left[\frac{\partial\overline{u'\theta'}}{\partial x}+\frac{\partial\overline{v'\theta'}}{\partial y}+\frac{\partial\overline{\dot{\sigma}'\theta'}}{\partial\sigma}\right]\right\}$$

Putting everything together to the elliptic equation the following is obtained

$$\frac{\partial^2\phi}{\partial x^2}+\frac{\partial^2\phi}{\partial y}+\frac{\partial}{\partial\sigma}\left[s^2\frac{\partial\phi}{\partial\sigma}\right]-\sigma\frac{\partial\phi}{\partial\sigma}\left(\frac{\partial^2\ln p_s}{\partial x^2}+\frac{\partial^2\ln p_s}{\partial y^2}\right)$$

$$+\sigma\frac{\partial}{\partial\sigma}\left(\sigma\frac{\partial\phi}{\partial\sigma}\right)\left[\left(\frac{\partial\ln p_s}{\partial x}\right)^2+\left(\frac{\partial\ln p_s}{\partial y}\right)^2\right]$$

$$-2\sigma\left[\frac{\partial\ln p_s}{\partial x}\left(\frac{\partial^2\phi}{\partial x\partial\sigma}\right)+\frac{\partial\ln p_s}{\partial y}\left(\frac{\partial^2\phi}{\partial y\partial\sigma}\right)\right]=$$

$$2\left(\frac{\partial u}{\partial x}\frac{\partial v}{\partial y}-\frac{\partial v}{\partial x}\frac{\partial u}{\partial y}\right)$$

$$+2\sigma\frac{\partial u}{\partial\sigma}\left(\frac{\partial u}{\partial x}\frac{\partial\ln p_s}{\partial x}+\frac{\partial v}{\partial x}\frac{\partial\ln p_s}{\partial y}\right)+2\sigma\frac{\partial v}{\partial\sigma}\left(\frac{\partial u}{\partial y}\frac{\partial\ln p_s}{\partial x}+\frac{\partial v}{\partial y}\frac{\partial\ln p_s}{\partial y}\right)$$

$$-\frac{2}{p_s}\left[\frac{\partial u}{\partial\sigma}\frac{\partial}{\partial x}(p\Omega)+\frac{\partial v}{\partial\sigma}\frac{\partial}{\partial y}(p\Omega)\right]+\frac{2}{p_s}(p\Omega)\left[\frac{\partial u}{\partial\sigma}\frac{\partial\ln p_s}{\partial x}+\frac{\partial v}{\partial\sigma}\frac{\partial\ln p_s}{\partial y}\right]$$

$$-\frac{\partial}{\partial\sigma}(sg)$$

$$+2\left(\frac{\partial u}{\partial x}+\frac{\partial v}{\partial y}\right)\frac{\partial}{\partial\sigma}\left(\frac{\Omega p}{p_s}\right)-2\left(-\frac{\partial\dot{\sigma}}{\partial\sigma}-\frac{D\ln p_s}{Dt}\right)\frac{D\ln p_s}{Dt}$$

$$-2\sigma\left(\frac{\partial u}{\partial x}+\frac{\partial v}{\partial y}\right)\left(\frac{\partial u}{\partial\sigma}\frac{\partial\ln p_s}{\partial x}+\frac{\partial v}{\partial\sigma}\frac{\partial\ln p_s}{\partial y}\right)-\left(\frac{D\ln p_s}{Dt}\right)^2$$

$$-2\frac{\partial\dot{\sigma}}{\partial\sigma}\frac{D\ln p_s}{Dt}-2\frac{p\Omega}{p_s}\left(\frac{\partial u}{\partial\sigma}\frac{\partial\ln p_s}{\partial x}+\frac{\partial v}{\partial\sigma}\frac{\partial\ln p_s}{\partial y}\right)-\left(\frac{D\ln p_s}{Dt}\right)^2$$

$$+\frac{1}{\gamma}\frac{\partial}{\partial\sigma}\left(\frac{p\Omega^2}{p_s}\right)-\frac{\partial}{\partial\sigma}\left(\frac{S_hp\Omega}{p_sTc_p}\right)-\frac{\partial}{\partial\sigma}\left(\frac{p\Omega rad}{p_sT}\right)$$

$$+\sigma f\left[\frac{\partial \ln p_s}{\partial y}\frac{\partial u}{\partial \sigma}-\frac{\partial \ln p_s}{\partial x}\frac{\partial v}{\partial \sigma}\right]+f\left(\frac{\partial v}{\partial x}-\frac{\partial u}{\partial y}\right)-u\frac{\partial f}{\partial y}$$

$$+\frac{\partial}{\partial \sigma}\left\{s\left[\frac{\partial \overline{u'w'}}{\partial x}+\frac{\partial \overline{v'w'}}{\partial y}+\frac{\partial \overline{w'\dot{\sigma}'}}{\partial \sigma}\right]\right\}-\frac{\partial}{\partial y}\left[\frac{\partial \overline{u'v'}}{\partial x}+\frac{\partial \overline{v'v'}}{\partial y}+\frac{\partial \overline{v'\dot{\sigma}'}}{\partial \sigma}\right]$$

$$-\frac{\partial}{\partial x}\left[\frac{\partial \overline{u'u'}}{\partial x}+\frac{\partial \overline{v'u'}}{\partial y}+\frac{\partial \overline{u'\dot{\sigma}'}}{\partial \sigma}\right]-\frac{\partial}{\partial \sigma}\left\{\frac{p\Omega}{p_sT}\left(\frac{p}{\hat{p}}\right)^{R_d/c_p}\left[\frac{\partial \overline{u'\theta'}}{\partial x}+\frac{\partial \overline{v'\theta'}}{\partial y}+\frac{\partial \overline{\dot{\sigma}'\theta'}}{\partial \sigma}\right]\right\}$$

After reorganizing everything the following is obtained

$$\frac{\partial^2 \phi}{\partial x^2}+\frac{\partial^2 \phi}{\partial y}+\frac{\partial}{\partial \sigma}\left[s^2\frac{\partial \phi}{\partial \sigma}\right]$$

$$-2\sigma\left[\frac{\partial \ln p_s}{\partial x}\left(\frac{\partial^2 \phi}{\partial x\partial \sigma}\right)+\frac{\partial \ln p_s}{\partial y}\left(\frac{\partial^2 \phi}{\partial y\partial \sigma}\right)\right]$$

$$+\sigma\frac{\partial}{\partial \sigma}\left(\sigma\frac{\partial \phi}{\partial \sigma}\right)\left[\left(\frac{\partial \ln p_s}{\partial x}\right)^2+\left(\frac{\partial \ln p_s}{\partial y}\right)^2\right]-\sigma\frac{\partial \phi}{\partial \sigma}\left(\frac{\partial^2 \ln p_s}{\partial x^2}+\frac{\partial^2 \ln p_s}{\partial y^2}\right)=$$

$$+2\left(\frac{\partial u}{\partial x}+\frac{\partial v}{\partial y}\right)\frac{\partial}{\partial \sigma}\left(\frac{\Omega p}{p_s}\right)$$

$$-\frac{2}{p_s}\left[\frac{\partial u}{\partial \sigma}\frac{\partial}{\partial x}(p\Omega)+\frac{\partial v}{\partial \sigma}\frac{\partial}{\partial y}(p\Omega)\right]+2\left(\frac{\partial u}{\partial x}\frac{\partial v}{\partial y}-\frac{\partial v}{\partial x}\frac{\partial u}{\partial y}\right)$$

$$+2\sigma\left[\frac{\partial \ln p_s}{\partial x}\left(\frac{\partial u}{\partial y}\frac{\partial v}{\partial \sigma}-\frac{\partial v}{\partial y}\frac{\partial u}{\partial \sigma}\right)+\frac{\partial \ln p_s}{\partial y}\left(\frac{\partial v}{\partial x}\frac{\partial u}{\partial \sigma}-\frac{\partial u}{\partial x}\frac{\partial v}{\partial \sigma}\right)\right]$$

$$-\frac{\partial}{\partial \sigma}\left(sg-\frac{p}{p_s}\Omega^2\frac{1}{\gamma}\right)-\frac{\partial}{\partial \sigma}\left(\frac{S_hp\Omega}{p_sTc_p}\right)-\frac{\partial}{\partial \sigma}\left(\frac{p\Omega rad}{p_sT}\right)$$

$$+\sigma f\left[\frac{\partial \ln p_s}{\partial y}\frac{\partial u}{\partial \sigma}-\frac{\partial \ln p_s}{\partial x}\frac{\partial v}{\partial \sigma}\right]+f\left(\frac{\partial v}{\partial x}-\frac{\partial u}{\partial y}\right)-u\frac{\partial f}{\partial y}$$

$$+\frac{\partial}{\partial \sigma}\left\{s\left[\frac{\partial \overline{u'w'}}{\partial x}+\frac{\partial \overline{v'w'}}{\partial y}+\frac{\partial \overline{w'\dot{\sigma}'}}{\partial \sigma}\right]\right\}-\frac{\partial}{\partial y}\left[\frac{\partial \overline{u'v'}}{\partial x}+\frac{\partial \overline{v'v'}}{\partial y}+\frac{\partial \overline{v'\dot{\sigma}'}}{\partial \sigma}\right]$$

$$-\frac{\partial}{\partial x}\left[\frac{\partial \overline{u'u'}}{\partial x}+\frac{\partial \overline{v'u'}}{\partial y}+\frac{\partial \overline{u'\dot{\sigma}'}}{\partial \sigma}\right]-\frac{\partial}{\partial \sigma}\left\{\frac{p\Omega}{p_sT}\left(\frac{p}{\hat{p}}\right)^{R_d/c_p}\left[\frac{\partial \overline{u'\theta'}}{\partial x}+\frac{\partial \overline{v'\theta'}}{\partial y}+\frac{\partial \overline{\dot{\sigma}'\theta'}}{\partial \sigma}\right]\right\}$$

But

$$\sigma\frac{\partial}{\partial \sigma}\left(\sigma\frac{\partial \phi}{\partial \sigma}\right)\left[\left(\frac{\partial \ln p_s}{\partial x}\right)^2+\left(\frac{\partial \ln p_s}{\partial y}\right)^2\right]-\sigma\frac{\partial \phi}{\partial \sigma}\left(\frac{\partial^2 \ln p_s}{\partial x^2}+\frac{\partial^2 \ln p_s}{\partial y^2}\right)=$$

$$=\sigma\frac{\partial}{\partial \sigma}\left(\sigma\frac{\partial \phi}{\partial \sigma}\right)\left[\left(\frac{\partial \ln p_s}{\partial x}\right)^2+\left(\frac{\partial \ln p_s}{\partial y}\right)^2\right]-\sigma\frac{\partial \phi}{\partial \sigma}\left[\frac{\partial}{\partial x}\left(\frac{\partial \ln p_s}{\partial x}\right)+\frac{\partial}{\partial y}\left(\frac{\partial \ln p_s}{\partial y}\right)\right]$$

$$=\sigma\frac{\partial}{\partial \sigma}\left(\sigma\frac{\partial \phi}{\partial \sigma}\right)\left[\left(\frac{\partial \ln p_s}{\partial x}\right)^2+\left(\frac{\partial \ln p_s}{\partial y}\right)^2\right]-\sigma\frac{\partial \phi}{\partial \sigma}\left[\frac{\partial}{\partial x}\frac{1}{p_s}\left(\frac{\partial p_s}{\partial x}\right)+\frac{\partial}{\partial y}\frac{1}{p_s}\left(\frac{\partial p_s}{\partial y}\right)\right]$$

$$=\sigma\frac{\partial}{\partial \sigma}\left(\sigma\frac{\partial \phi}{\partial \sigma}\right)\left[\left(\frac{\partial \ln p_s}{\partial x}\right)^2+\left(\frac{\partial \ln p_s}{\partial y}\right)^2\right]-\sigma\frac{\partial \phi}{\partial \sigma}\left[-\frac{1}{p_s^2}\left(\frac{\partial p_s}{\partial x}\right)^2+\frac{1}{p_s}\left(\frac{\partial^2 p_s}{\partial x^2}\right)-\frac{1}{p_s^2}\left(\frac{\partial p_s}{\partial y}\right)^2+\frac{1}{p_s}\left(\frac{\partial^2 p}{\partial y^2}\right)\right]$$

$$=\sigma\frac{\partial}{\partial \sigma}\left(\sigma\frac{\partial \phi}{\partial \sigma}\right)\left[\left(\frac{\partial \ln p_s}{\partial x}\right)^2+\left(\frac{\partial \ln p_s}{\partial y}\right)^2\right]+\sigma\frac{\partial \phi}{\partial \sigma}\left[\left(\frac{1}{p_s^2}\frac{\partial p_s}{\partial x}\right)^2+\left(\frac{1}{p_s}\frac{\partial p_s}{\partial y}\right)^2\right]-\frac{\sigma}{p_s}\frac{\partial \phi}{\partial \sigma}\left[\left(\frac{\partial^2 p_s}{\partial x^2}\right)+\left(\frac{\partial^2 p}{\partial y^2}\right)\right]$$

$$=\frac{\partial}{\partial \sigma}\left(\sigma^2\frac{\partial \phi}{\partial \sigma}\right)\left[\left(\frac{\partial \ln p_s}{\partial x}\right)^2+\left(\frac{\partial \ln p_s}{\partial y}\right)^2\right]-\frac{\sigma}{p_s}\frac{\partial \phi}{\partial \sigma}\left[\left(\frac{\partial^2 p_s}{\partial x^2}\right)+\left(\frac{\partial^2 p}{\partial y^2}\right)\right]$$

The elliptic equation the becomes:

$$\frac{\partial^2\phi}{\partial x^2} + \frac{\partial^2\phi}{\partial y} + \frac{\partial}{\partial\sigma}\left[s^2\frac{\partial\phi}{\partial\sigma}\right]$$

$$-2\sigma\left[\frac{\partial\ln p_s}{\partial x}\left(\frac{\partial^2\phi}{\partial x\partial\sigma}\right) + \frac{\partial\ln p_s}{\partial y}\left(\frac{\partial^2\phi}{\partial y\partial\sigma}\right)\right]$$

$$+\frac{\partial}{\partial\sigma}\left(\sigma^2\frac{\partial\phi}{\partial\sigma}\right)\left[\left(\frac{\partial\ln p_s}{\partial x}\right)^2 + \left(\frac{\partial\ln p_s}{\partial y}\right)^2\right] - \frac{\sigma}{p_s}\frac{\partial\phi}{\partial\sigma}\left[\left(\frac{\partial^2 p_s}{\partial x^2}\right) + \left(\frac{\partial^2 p}{\partial y^2}\right)\right] =$$

$$2\left(\frac{\partial u}{\partial x} + \frac{\partial v}{\partial y}\right)\frac{\partial}{\partial\sigma}\left(\frac{\Omega p}{p_s}\right)$$

$$-\frac{2}{p_s}\left[\frac{\partial u}{\partial\sigma}\frac{\partial}{\partial x}(p\Omega) + \frac{\partial v}{\partial\sigma}\frac{\partial}{\partial y}(p\Omega)\right] + 2\left(\frac{\partial u}{\partial x}\frac{\partial v}{\partial y} - \frac{\partial v}{\partial x}\frac{\partial u}{\partial y}\right)$$

$$+2\sigma\left[\frac{\partial\ln p_s}{\partial x}\left(\frac{\partial u}{\partial y}\frac{\partial v}{\partial\sigma} - \frac{\partial v}{\partial y}\frac{\partial u}{\partial\sigma}\right) + \frac{\partial\ln p_s}{\partial y}\left(\frac{\partial v}{\partial x}\frac{\partial u}{\partial\sigma} - \frac{\partial u}{\partial x}\frac{\partial v}{\partial\sigma}\right)\right]$$

$$-\frac{\partial}{\partial\sigma}\left(sg - \frac{p}{p_s}\Omega^2\frac{1}{\gamma}\right) - \frac{\partial}{\partial\sigma}\left(\frac{S_h p\Omega}{p_s T c_p}\right) - \frac{\partial}{\partial\sigma}\left(\frac{p\Omega rad}{p_s T}\right)$$

$$+\sigma f\left[\frac{\partial\ln p_s}{\partial y}\frac{\partial u}{\partial\sigma} - \frac{\partial\ln p_s}{\partial x}\frac{\partial v}{\partial\sigma}\right] + f\left(\frac{\partial v}{\partial x} - \frac{\partial u}{\partial y}\right) - u\frac{\partial f}{\partial y}$$

$$+\frac{\partial}{\partial\sigma}\left\{s\left[\frac{\partial\overline{u'w'}}{\partial x} + \frac{\partial\overline{v'w'}}{\partial y} + \frac{\partial\overline{w'\dot{\sigma}'}}{\partial\sigma}\right]\right\} - \frac{\partial}{\partial y}\left[\frac{\partial\overline{u'v'}}{\partial x} + \frac{\partial\overline{v'v'}}{\partial y} + \frac{\partial\overline{v'\dot{\sigma}'}}{\partial\sigma}\right]$$

$$-\frac{\partial}{\partial x}\left[\frac{\partial\overline{u'u'}}{\partial x} + \frac{\partial\overline{v'u'}}{\partial y} + \frac{\partial\overline{u'\dot{\sigma}'}}{\partial\sigma}\right] - \frac{\partial}{\partial\sigma}\left\{\frac{p\Omega}{p_s T}\left(\frac{p}{\hat{p}}\right)^{R_d/c_p}\left[\frac{\partial\overline{u'\theta'}}{\partial x} + \frac{\partial\overline{v'\theta'}}{\partial y} + \frac{\partial\overline{\dot{\sigma}'\theta'}}{\partial\sigma}\right]\right\}$$

where

$$\frac{Dq_v}{Dt} = S_v = -PCOND - PREVP - PSDEP - PMLTEV - PDEPI - PINT$$

$$S_h = L_v\left(PCOND + PREVP + PMLTEV\right) + L_s\left(PINT + PDEPI + PSDEP\right) + L_f\left(PSMLT - PSMLTI + PSACW\right)$$

Appendix B

Microphysics Processes of the PURDUE-LIN Scheme

Autoconversion of cloud ice to snow (PSAUT)

The aggregation of ice crystals to form snow is

$PSAUT = \max\left[0, \alpha_1 \left(q_i - q_{i0}\right)\right]$

where $\alpha_1 = 10^{-3} exp\left[0.025\left(T_C\right)\right]$. $q_{i0}$is the threshold of ice that when reached, ice will then be regarded as snow. T_C is the temperature in ^oC.

Autoconversion of snow to graupel or hail (PGAUT)

The autoconversion of snow to graupel or hail was defined in a similar way as:

$PGAUT = \max\left[0, \alpha_2 \left(q_s - q_{s0}\right)\right]$

The rate coefficient α_2 is assumed to be temperature dependent and is given by $\alpha_2 = 10^{-3} exp\left[0.09\left(T - T_0\right)\right]$. q_{s0} is a mass threshold of snow.

Autoconversion of cloud water to rainwater (PRAUT)

Autoconversion of cloud water is the process where small cloud droplets collide and coalesce with each other and eventually form rain drops (Houze, 1993) and is given by

$PRAUT = \max\left[0, \alpha \left(q_c - q_{c0}\right)\right]$

where α is a conversion rate given by 0.001 and $q_{c0}$is a threshold value for q_c below which autoconversion does not occur.

Collection of cloud ice by snow (PSACI)

The collection of cloud ice by snow (PSACI) parameterisaton is based on the geometric sweep-out concept intergrated over all snow sizes for the assumed snow size distribution. It is given by

$$PSACI = \frac{\pi N_{0S} E_{SI} q_i c \Gamma(3+d)}{4\lambda_S^{3+d}} \left(\frac{\rho_0}{\rho}\right)^{0.5}$$

where E_{SI} is the collection efficiency of the snow for cloud ice which is defined as $E_{SI} = exp\left[0.025\left(T_C\right)\right]$.

Collection of cloud water by snow (PSACW)

The accretion of cloud water by snow is given by:

$$PSACW = \frac{\pi N_{0S} E_{SW} q_c c \Gamma(3+d)}{4\lambda_S^{3+d}} \left(\frac{\rho_0}{\rho}\right)^{0.5}$$

where E_{SW} is the collection efficiency of snow for cloud water and is assumed to be 1. PSACW is a source for snow and a sink for cloud water, the cloud water freezes when the temperature is less than 0 celsius. When the temperature is greater than 0 ^0C , PSACW will contribute to the rain with the assumption that unfrozen water will be shed from the snow particles.

Collection of cloud ice by rain water (PRACI)

When temperature is less than 0 ^0C, supercooled water drops will freeze due to contact with solid particles. Raindrops accreting cloud ice will freeze and the result in solid particle contributing to the solid precipitation (snow or graupel). Collection of cloud ice by rain is a sink for the cloud ice content and a source for snow or graupel depending on the mass threshold criterion. Applying the geometric sweepout concept distribution and intergrating over all rain sizes for the assumed distribution it is given by

$$PRACI = \frac{\pi N_{0R} E_{RI} q_i a \Gamma(3+b)}{4\lambda_R^{3+d}} \left(\frac{\rho_0}{\rho}\right)^{0.5}$$

where E_{RI} is the collection efficiency of rain for cloud ice and is assumed to be 1.

Collection of rain by cloud ice (PIACR)

Raindrops freeze when they collide with cloud ice particles and this process is a sink term for rain and a source term for snow and rain. The cloud ice is monodispersed and has the same mass, $M_i = 4.19x10^{-13}$kg. The accretion rate of rain by cloud ice particles is

$$PIACR = \frac{\pi^2 N_{0R} E_{RI} q_i a \Gamma(6+b)}{24 M_i \lambda_R^{6+b}} \left(\frac{\rho_0}{\rho}\right)^{0.5}.$$

Collection of snow by rain (PRACS)

The definition of the collection of snow by rain requires that all raindrops and snow particles fall at their appropriate mass-weighted mean terminal velocities. The accretion of rain for snow is

$$PRACS = \pi^2 N_{0R} N_{0S} E_{SR} |U_R - U_S| \left(\frac{\rho_S}{\rho}\right)$$

$$x \left(\frac{5}{\lambda_S^6 \lambda_R} + \frac{2}{\lambda_S^5 \lambda_R^2} + \frac{0.5}{\lambda_S^4 \lambda_R^3}\right)$$

where the collection efficiency of snow(rain) for rain(snow), E_{SR}, is assumed to be 1.

Collection of rain by snow (PSACR)

The accretion of snow by rain is given by

$$PSACR = \pi^2 N_{0S} N_{0R} E_{SR} |U_S - U_R| \left(\frac{\rho_W}{\rho}\right)$$

$$x \left(\frac{5}{\lambda_R^6 \lambda_S} + \frac{2}{\lambda_R^5 \lambda_S^2} + \frac{0.5}{\lambda_R^4 \lambda_S^3}\right)$$

If temperature is less than 0 ^0C and q_r is greater than $10^{-4} g/g^{-1}$ or q_s is greater than$10^{-4} g/g^{-1}$ both PSACR and PRACS contribute to the formation of hail. If the mass threshold is not met, snow grows at the expense of rain and only PSACR needs to be calculated, i.e. PRACS is not calculated. If temperature is greater than 0 ^0C PSACR will not be active.

Collection of snow by graupel (PGACS)

The accretion of snow by hail, PGACS, always contributes to hail content whether or not the temperature is below 0 ^0C.

$PGACS = \pi^2 N_{0S} N_{0G} E_{GS} |U_S - U_R| \left(\frac{\rho_S}{\rho}\right)$

$x \left(\frac{5}{\lambda_S^6 \lambda_G} + \frac{2}{\lambda_S^5 \lambda_G^2} + \frac{0.5}{\lambda_S^4 \lambda_G^3}\right)$

where E_{GS} is the collection effciency of hail particles for snow particles and is assumed to be a function of temperature given by $E_{GS} = exp\left[0.09\left(T_C\right)\right]$ when $T_C < 0^o$ and $E_{GS} = 1.0$ when $T_C \geq 0^o C$. The collection efficiency of hail for snow is considerably less than that of snow for ice crystals.

Collection of cloud water by graupel (PGACW)

The collection of cloud water by graupel is given by

$PGACW = \frac{\pi N_{0G} E_{GW} q_i \Gamma(3.5)}{4\lambda_G^{3.5}} \left(\frac{4 g \rho \rho_G}{3 C_D \rho}\right)^{0.5}$

where $E_{GW} = 1$.

Collection of cloud ice by graupel (PGACI)

Lin et al. (1983) defined it as

$PGACI = \frac{\pi N_{0G} E_{GI} q_i \Gamma(3.5)}{4\lambda_G^{3.5}} \left(\frac{4 g \rho \rho_G}{3 C_D \rho}\right)^{0.5}$

where $E_{GI} = 1$

Collection of cloud water by rain water (PRACW)

Once rain drops are formed they continue to grow by accretion of cloud water. which is defined as

$PRACW = \frac{\pi a N_{0R} E_{rc} q_c \Gamma(3+b)}{4\lambda_r^{3+b}} \left(\frac{\rho_0}{\rho}\right)^{0.5}$

where $E_{RW} = 1$.

Collection of rain drops by graupel (PGACR)

Lin et al. (1983) is defined as

$PGACR = \pi^2 N_{0G} N_{0R} E_{GR} |U_G - U_R| \left(\frac{\rho_W}{\rho}\right)$

$x \left(\frac{5}{\lambda_R^6 \lambda_G} + \frac{2}{\lambda_R^5 \lambda_G^2} + \frac{0.5}{\lambda_R^4 \lambda_G^3}\right)$

where $E_{GR} = 1$.

Melting of graupel (PGMLT)

The melting of hail is given by

$$PGMLT = -\frac{2\pi}{\rho L_f}\left(K_a T_c - L_v \psi \rho \triangle q_{vs}\right) N_{OG}$$

$$\left[0.78\lambda_G^{-2} + 0.31 S_c^{1/3}\Gamma\left(2.75\right)\left(\frac{4g\rho G}{3C_D}\right)^{1/4} v^{-1/2}\lambda_G^{-2.75}\right]$$

$$\frac{C_W T_C}{L_f}\left(P_{gacw} + P_{gacr}\right)$$

Evaporation of rain water (PREVP)

Evaporation of rain water only occurs where there are cloud droplets , that is when the air is not saturated with vapor (Kessler, 1969).The evaporation of rainwater is calculated if the air is subsaturated with respect to water and the evaporation of cloud water is insufficient to remove subsaturation. It is defined as

$$PREVP = 2\pi\left(S - 1\right) N_{OS}$$

$$\left[0.78\lambda_s^{-2} + 0.31 S_c^{1/3}\Gamma\left(\frac{d+5}{2}\right) a^{1/2}\left(\frac{\rho_0}{\rho}\right)^{1/4} v^{-1/2}\lambda_S^{-(b+5)/2}\right]$$

$$x\left(\frac{1}{\rho}\right)\left(\frac{L_v^2}{K_a R_w T^2} + \frac{1}{\rho q_{sv}\psi}\right)$$

S is the saturation ratio.

Raindrop freezing (PGFR)

The formation of hail from raindrops through freezing is defined as

$$PGFR = 20\pi^2 B' N_{OR}\left(\frac{\rho_W}{\rho}\right)$$

$$x\left\{exp\left[A'\left(T_0 - T\right)\right] - 1\right\}\lambda_R^{-7}$$

where $A' = 0.66K^{-1}$ and $B' = 100\text{m}^{-3}\text{s}^{-1}$.

Melting of snow (PSMLT)

All snow upon melting is assumed to contribute to rain. Lin et al. (1983) expressed the melting of snow to form rain as

$$PSMLT = -\frac{2\pi}{\rho L_f}\left(K_a T_c - L_v \psi \rho \triangle r_s\right) N_{OS}$$

$$\left[0.78\lambda_s^{-2} + 0.31 S_c^{1/3} \Gamma\left(\frac{d+5}{2}\right) c^{1/2} \left(\frac{\rho_0}{\rho}\right)^{1/4} \upsilon^{-1/2} \lambda_S^{-(d+5)/2}\right]$$

$$-\frac{C_w T_c}{L_f}\left(PSACW + PSACR\right)$$

Evaporation of melting snow (PSMLTEV)

The evaporation of melting snow is given by

$$PSMLTEVP = \frac{2\pi N_{0S}(S-1)}{\rho(C" + D")}\left[\frac{0.78}{\lambda_s^2} + \frac{0.31 S_C^{1/3} c^{1/2} \Gamma\left(\frac{d+5}{2}\right)}{\upsilon^{1/2} \lambda_s^{(d+5)/2}} \left(\frac{\rho_0}{\rho}\right)^{0.25}\right]$$

where $C" = \frac{L_v}{K_a T}\left(\frac{L_v M_w}{R{*}T} - 1\right)$ and $D" = \frac{R{*}T}{\psi M_w e_{sw}}$

Evaporation of melting graupel (PGMLTEV)

Evaporation of melting graupel is

$$PGMLTEVP = \frac{2\pi N_{0G}(S-1)}{(C" + D")}\left[\frac{0.78}{\lambda_G^2} + 0.31\left(\frac{\bar{a}\rho}{\upsilon}\right)^{0.5}\left(\frac{p_{00}^{0.2}}{p}\right)\frac{\Gamma\left(\bar{b}/2 + 5/2\right)}{\lambda_G^{\bar{b}/2+5/2}}\right]$$

Depositional or sublimation growth of snow (PSDEP OR PSSUB)

When the air is supersaturated with respect to ice, the growth rate of snow by deposition of vapour is as defined below over all sizes of snow particles.

$$PSDEP\left(/PSSUB\right) = \frac{2\pi(S_i - 1)N_{OS}}{\rho(A" + B")}$$

$$\left[0.78\lambda_s^{-2} + 0.31 S_c^{1/3} \Gamma\left(\frac{d+5}{2}\right) c^{1/2} \left(\frac{\rho_0}{\rho}\right)^{1/4} \upsilon^{-1/2} \lambda_S^{-(d+5)/2}\right]$$

where

$$A" = \frac{L_s^2}{K_a R_w T^2},\ B" = \frac{1}{\rho q_{si} \psi}$$

Sublimation occurs when the air is subsaturated with respect to ice. Deposition only takes place inside a cloud when the temperature is lower than 0 ^0C.

Sublimation of graupel (PGSUB)

When the air is supersaturated with respect to ice, the growth rate of snow by deposition of vapour is as defined below over all sizes of snow particles. The sublimation of graupel is given by

$$PGSUB\,(/PGDEP) = -\frac{2\pi(S_i-1)}{\rho(A"+B")}N_{OG}$$

$$\left[0.78\lambda_G^{-2}+0.31S_c^{1/3}\Gamma\left(2.75\right)\left(\frac{4g\rho G}{3C_D}\right)^{1/4}\upsilon^{-1/2}\lambda_G^{-2.75}\right]$$

Transfer of cloud water to snow (PSFW)

The rate at which cloud water transforms to snow by deposition based on the growth of a 50 μm radius ice crystals.

$$PSFW = N_{150}\left(a_1 m_{150}^{a_2}+\pi E_{IW}\rho q_c R_{150}^2 U_{150}\right)$$

where $a_1$and $a_2$are the temperature-dependent parameters in the Bergeron process and R_{150}, m_{150} and U_{150} are the radius, mass and terminal velocity of a 50μm size ice crystal. E_{IW} is the collection efficiency of cloud ice for cloud water which is assumed to be 1 in Lin et al 1983's model.

Transfer of cloud ice to snow (PSFI)

The rate at which cloud ice transforms to snow by riming is expressed as:

$$PSFI = q_i/\triangle t_1$$

where $\triangle t_1$is the temperature-dependent time scale.

$$\Delta t_1 = \frac{1}{a_1(1-a_2)}\left[m_{I50}^{(1-a_2)}-m_{I40}^{(1-a_2)}\right]$$

Wet growth of graupel (PGWET)

$$PGWET = \frac{2\pi N_{0G}(\rho L_v\psi\triangle q_{vs}-K_aT_C)}{\rho(L_f+C_WT_C)}$$

$$\left[0.78\lambda_G^{-2}+0.31S_c^{1/3}\Gamma\left(2.75\right)\left(\frac{4g\rho G}{3C_D}\right)^{1/4}\upsilon^{-1/2}\lambda_G^{-2.75}\right]$$

$$+\left(PGACI'+PGACS\right)\left(1-\frac{C_iT_C}{L_f+C_WT_C}\right)$$

Melting of cloud ice (PIMLT)

Melted cloud ice is a source for cloud water. Rutledge and Hobbs (1983) assumed that the process happens instantaneously for $T \geq 0^0 C$ is given by

$PIMLT = \frac{q_i}{\triangle t}$

Appendix C

Deposition and Autoconversion parameterisations of the SBU-YLIN Scheme

Depositional or sublimation growth of precepitating ice (PSDEP OR PSSUB)

Precipitating ice deposition and sublimation with the consideration of latent heat release due to concurrent riming growth assuming exponential distribution with intercept (N_{0S}) and slope λ.

$$PSDEP\,(/PSSUB) = \tfrac{4\pi C S_i N_{OS}}{g(t,p)}$$

$$\left[\tfrac{0.65}{\lambda^2} + 0.44 S_c \left(\tfrac{a_v}{v}\right)^{0.5} \left(\tfrac{\rho_0}{\rho}\right)^{0.25} \tfrac{\Gamma(2.5+0.5b_v)}{\lambda^{2.5+0.5b_v}}\right]$$

$$-\tfrac{L_s L_f a_a a_v E_{sc} N_{0S} q_c}{K R_w T^2 g(t,p)} \left(\tfrac{\rho_0}{\rho}\right)^{0.5} \left(\tfrac{\Gamma(1+b_a+b_v)}{\lambda^{1+b_a+b_v}}\right)$$

Autoconversion of cloud water to rainwater (PRAUT)

A new parameterization of autoconversion of cloud water to rain is given by

$$PRAUT = \left(\tfrac{3\rho}{4\pi\rho_w}\right)^2 \kappa_2 \beta_6^6 N^{-1} q_c^3 H\left(R_6 - R_{6c}\right)$$

where

$$\beta_6^6 = \tfrac{\left(1+3\varepsilon^2\right)\left(1+4\varepsilon^2\right)\left(1+5\varepsilon^2\right)}{\left(1+\varepsilon^2\right)\left(1+2\varepsilon^2\right)},$$

$$R_{6c} = \beta_6 R_{3c},\ R_6 = \beta_6 R_3$$

Bibliography

[1] Abiodun BJ, JM Prusa and WJ Gutowski Jr, 2008a: Implementation of a nonhydrostatic, adaptation, adaptive-grid dynamics core in CAM3. Part I: Comparison of dynamics cores in aquaplanet simulations. *Climate Dynamics*. **31**,795-810.

[2] Abiodun BJ, WJ Gutowski Jr and JM Prusa and 2008b: Implementation of a nonhydrostatic, adaptation, adaptive-grid dynamics core in CAM3. Part II: Dynamical Influences on ITCZ behaviour and tropical precipitation. *Climate Dynamics*. **31**, 811-822.

[3] Arakawa A and WH Schubert, 1974: Interaction of cumulus cloud ensemble with the largescale environment, Part I. *Journal of Atmospheric Science*, **31**, 674-70.

[4] Arakawa A, 2004: Review article: The Cumulus parameterisation Problem: Past, Present and Future. *Journal of Climate*, **17**, 2493-252.

[5] Bates JR and A McDonald, 1982: Multiply-Upstream, semi-lagrangian advective scheme: Analysis and application to a multi-level primitive equation model. *Monthly Weather Review*, **110**, 1831-1842.

[6] Bates JR, 1984: An efficient semi-lagrangian and alternating direction Implicit method for integrating the shallow water equations. *Monthly Weather Review*, **112**, 2033-2047.

[7] Betts AK and MJ Miller, 1986: A new convective adjustment scheme. Part II: Single column tests using GATE wave, BOMEX,

ATEX and Arctic air-mass datasets. *Quarterly Journal of Royal of Meteorological Society*, **112**, 693-702

[8] Bougeault P, 1985: A simple parameterisation of the Large-scale Effects of Cumulus Convection. *Monthly Weather Review*, **113**, 2108-2121.

[9] Bryan GH and JM Fritsch, 2002: A Benchmark Simulation for Moist Nonhydrostatic Numerical Models. *Monthly Weather Review*, **130**, 2917-2928.

[10] Bryan GH, JC Wyngaard, and JM Fritsh, 2003: Resolution Requirements for the Simulation of Deep Moist Convection. *Monthly Weather Review*, **131**, 2394-2416.

[11] Bryan, GH, H Morrison, 2012: Sensitivity of a Simulated Squall Line to Horizontal Resolution and Parameterization of Microphysics. *Monthly Weather Review*, **140**, 202–225.

[12] Chen M and JR Bates, 1996: A comparison of climate simulations from a semi-lagrangian and an eulerian GCM. *Journal of Climate*, **9**, 1126-1149.

[13] Chen S and W Sun, 2002: A One-dimensional Time Dependent Cloud Model. *Journal of the Meteorological Society of Japan*, **80**, 99-118.

[14] Ciesielski PE, RH Johnson, PT Haertel and J Wang, 2003: Corrected TOGA COARE sounding Humidity Data: Impact on Diagnosed Properties of Convection and Climate over the Warm Pool. *Journal of Climate*, **16**,2370-2384.

[15] Cotton WR and RA Anthes, 1989: Storm and Cloud Dynamics. Academic Press Inc. 883pp

[16] Daniel M, 2011: Two tornadoes strike South Africa. http://earthsky.org/earth/two-tornadoes-strike-south-africa.

[17] Davies T, A Staniforth, N Wood and J Thuburn, 2003: Validity of anelastic and other equation sets inferred from normal-mode analysis. *Quarterly Journal of Royal Meteorological Society*, **129**, 2761-2775.

[18] Davies T, MJP Cullen, AJ Malcolm, MH Mawson, A Staniforth, AA White and N Wood, 2005: A new dynamical core for the Met Office's global and regional modelling of the atmosphere. *Quaterly Journal of Royal Meteorological Society*, **131**, 1759-1782.

[19] Dawson II DT, M Xue, JA Milbrandt and MK Yau, 2010: Comparison of Evaporation and Cold Pool Development between Single-Moment and Multimoment Bulk Microphysics Schemes in Idealized Simulations of Tornadic Thunderstorms. *Monthly Weather Review*, **138**, 1152-1171.

[20] de Coning E, G S Forbes and E Poolman, 1998: Heavy Precipitation and Flooding on 12-14 February 1996 over the summer rainfall regions of South Africa: Synoptic and Isentropic analysis. *National Weather Digest*, **22**, 25-36.

[21] de Coning E and BF Adam, 2000: The tornadic thunderstorm events during the 1998-1999 South African summer. *Water SA*, **26**, 361-376.

[22] de Coning E, BF Adam and L Banitz, 2000: A severe weather event on 29 December 1997: Synoptic and mesoscale perspectives. *Water SA*, **26**, 137-146.

[23] de Coning E, 2011: Applications of Meteorological Satellite Products for Short Term Forecasting of Convection Over Southern Africa. Doctoral Thesis. University of South Africa. 129pp.

[24] de Coning E, M Koenig and Jana Olivier, 2011: The Combined Instability Index: a new very short range Convection forecasting technique for Souther Africa. *Meteorological Applications*, **18**, 421-439.

[25] de Coning and E Poolman, 2011: South African Weather Service operational satellite based precipitation estimation technique: Applications and Improvements. *Hydroplogy and Earth System Sciences*, **15**, 1131-1145.

[26] Du Plessis L, 2002: A review of effective flood forecasting, warning and response system for application in South Africa. *Water SA*, **28**, 129-138.

[27] Durran DR, 1999: Numerical Methods for Wave Equations in Geophisical Fluid Dynamics. Springer. 465pp.

[28] Dyson LL, 2009: Heavy daily-rainfall characteristics over the Gauteng Province, *Water SA*, **35**, 627-638.

[29] Eliassen A, 1949: The quasi-static equations of motion with pressure as independent variable. *Geof. Publ.*, **17**, 5-44.

[30] Emanuel KA, 1991: A Scheme for Representing Cumulus Convection in Large-Scale Models. *Journal of the Atmospheric Science*, **48**, 2313-2335.

[31] Emanuel KA, 1994: Atmospheric Convection. Oxford University Press, 580pp.

[32] Engelbrecht FA, 2006: Theory and application of quasi-elastic equations in terrain – following coordinates based on the full pressure field. Doctoral thesis. University of Pretoria. Published online. 208 pp.

[33] Engelbrecht FA, JL McGregor and CJdeW Rautenbach, 2007: On the development of a new nonhydrostatic atmospheric model in South Africa. *South African Journal of Science*, **103**, 127-134.

[34] Engelbrecht FA, 2010: The Scientific Basis for Climate Change Over Southern Africa. In Climate Change and Trade: The Challenges for Southern Africa. Ed: Peter Draper and Ivan Mbirimi. Fanele. 127-144.

[35] Engelbrecht FA, WA Landman, CJ Engelbrecht, S Landman, MM Bopape, B Roux, JL McGregor, and M Thatcher, 2011: Multiscale Climate Modelling over Southern Africa using a variable-resolution global model. *Water SA*, **37**, 647-658.

[36] Engelbrecht FA, M Tsugawa and JL McGregor, 2012: Development of a new coupled climate model in South Africa. Recent developments and future plans. SASAS 2012: Bridging the

Gap. Protea Breakwater Lodge, Water Front, Cape Town, South Africa. 26-27 September. ISBM: 978-0-620-53375-1.

[37] Farber R, 2012: Numerical Precision: How much is Enough? http://www.scientificcomputing.com/article-hpc-Numerical-Precision-How-Much-is-Enough-063009.aspx

[38] Franklin CN, PA Vaillancourt, MK Yau and P Bartello, 2005: Collision rates of Cloud Droplets in Turbulent Flow. *Journal of the Atmospheric Sciences*, **62**, 2451-2466.

[39] Gadd AJ, 1978: A split explicit integration scheme for numerical weather prediction. *Quarterly Journal of Royal Meteorological Society*, **104**, 569-582.

[40] Gao S, L Ran and X Li, 2006: Impacts of Ice Microphysics on Rainfall and Thermodynamic Processes in the Tropical Deep Convective Regime: A 2D Cloud-Resolving Model Study. *Monthly Weather Review*, **134**, 3015-3024.

[41] Gill T, 2008: Initial Steps in the Development of a Comprehensive Lightning Climatology of South Africa. Masters Thesis, 108 pp.

[42] Grabowski WW, X Wu and MW Moncrieff, 1996: Cloud-Resolving Modeling of Tropical Cloud Systems during Phase III of GATE. Part I: Two-Dimensional Experiments. *Journal of the Atmospheric Sciences*, **53**, 3684-3708.

[43] Grabowski WW, 1998: Toward Cloud resolving Modeling of Large-scale Tropical Circulations: A Simple Cloud Microphysics Parameterisation. *Journal of the Atmospheric Sciences*, **55**,3283-3298.

[44] Grabowski W, X Wu, MW Moncrieff and WD Hall, 1998: Cloud Resolving Modeling of Cloud Systems during the Phase III od GATE. Part II: Effects of Resolution and the third Spatial Dimension. *Journal of the Atmospheric Sciences*, **55**, 3262-3282.

[45] Grabowski, W. W., and P. K. Smolarkiewicz, 1999: CRCP: A Cloud Resolving Convection Parameterization for Modeling

the Tropical Convecting Atmosphere. *Physica D*, **133**, 171–178. (Special Issue: Predictability: Quantifying Uncertainty in Models of Complex Phenomena, 18th Annual Conference of the Center for Nonlinear Studies, Los Alamos, NM, USA, 11-15 May 1998).

[46] Grabowski WW, 2000: Cloud Microphysics and the Tropical Climate: Cloud-Resolving Model Perspective. *Journal of Climate*, **13**, 2306-2322.

[47] Grabowski WW, 2001: Coupling Cloud Processes with the Large-Scale Dynamics Using the Cloud-Resolving Convection parameterisation (CRCP). *Journal of the Atmospheric Sciences*, **58**, 978-997.

[48] Grabowski WW, P Bachtold, A Cheng, R Forbes, C Halliweli, M Khairoutdinov, S Lang, T Nasuno, J Petch, W-K Tao, R Wong, X Wu and K-M Xu, 2006: Daytime convective development over land: A model intercomparison based on LBA observations. *Quarterly Journal of Royal Meteorological Society*, **132**, 317-344.

[49] Gilmore MS, JM Straka and EN Rasmussen, 2004: Precipitation Uncertainty Due to Variations in Precipitation Particle Parameters within a Simple Microphysics Scheme. *Monthly Weather Review*, **132**, 2610-2627.

[50] Grell, G. A., 1993: Prognostic evaluation of assumptions used by cumulus parameterisations. *Monthly Weather Review*, **121**, 764–787.

[51] Grollman T and Simon S, 2002: Flood disasters-harbingers of climate change? General CologneRe.

[52] Guichard F, JC Petch, J-L Redelsperger, P Bechtold, J-P Chaboureau, S Cheinet, W Grabowski, H Grenier, CG Jones, M Kohler, J-M Piriou, R Tailleux and M Tomasini, 2004: Modelling the diurnal cycle of deep precipitating convection over land with Cloud-Resolcing models and single-column models. *Quarterly Journal of Royal Meteorological Society*, **130**, 3139-3172.

[53] Haltiner GJ and RT Williams, 1980: Numerical prediction and dynamic meteorology second edition. John Wiley and sons, 477pp.

[54] Harper K, LW Uccellini, E Kalnay, K Carey and L Morone, 2007: 50th Anniversary of Operational Numerical Weather Prediction. *Bulletin of American Society*, **88**, 639-650.

[55] Harrison MSJ, 1984: A generalized classification of South African summer rain-bearing synoptic systems. *International Journal of Climatology*, **4**, 547–560.

[56] Hart NCG, CJC Reason, and N Fauchereau, 2010: Tropical-Extratropical Interactions over Southern Africa: Three Cases of Heavy Summer Season Rainfall. *Monthly Weather Review*, **128**, 2608-2623.

[57] Holton JR, 1992: An Introduction to Dynamic Meteorology, Third Edition. Academic Press. 511pp.

[58] Holton JR, 2004: An Introduction to Dynamic Meteorology, Fourth Edition. Academic, 535 pp.

[59] Holtslag AAM and BA Boville, 1993: Local Versus Nonlocal Boundary-Layer Diffusion in a Global Climate Model. *Journal of Climate*, **6**, 1825-1842.

[60] Hong S and JJ Lim, 2006: The WRF Single-Moment 6-Class Microphysics Scheme (WSM6). *Journal of the Korean Meteorological Society*, **42**, 129-151.

[61] Houze Jr RA, 1993: Cloud Dynamics.Academic Press, 573pp.

[62] Jacobson MZ, 2005: Fundamentals of Atmopsheric Modelling Second Edition. Cambridge University Press. 813pp.

[63] Jakob C, 2010: Accelerating Progress in Global Atmospheric Model Development Through Improved parameterisations. American Meteorological Society. DOI:10.1175/2009BAMS2898.

[64] Janjic ZI, JP Gerrity Jr. and S Nickovic, 2001: An alternative approach to nonhydrostatic modeling. *Monthly Weather Review*, **129**, 1164–1178.

[65] Johnson DE, W-K Tao and C-K Sui, 2002: A study of the Response of Deep Tropical Clouds to Large-Scale Thermodynamic Forcings. Part I: Modeling Strategies and Simulation of TOGA COARE Convective Systems. *Journal of the Atmospheric Sciences*, **59**, 3492-3518.

[66] Kessler E, 1969: On the Distribution and Continuity of Water Substance in Atmospheric Circulations. Meteorological Monographs, American Meteorological Society, 84 pp.

[67] Khairoutdinov MF and DA Randall, 2001: A Cloud Resolving Model as a Cloud Parameterisation in the NCAR Community Climate System Model. Preliminary Results. *Geophysical Research Letters*, **28**, 3617-3620.

[68] Khairoutdinov MF and DA Randall, 2003: Cloud Resolving Modelling of the ARM Summer 1997 IOP: Model Formulation, Results, Uncertanties, and Sensitivities. *Journal of the Atmospheric Sciences*, **60**, 607-625

[69] Khairoutdinov M, C DeMott and D Randall, 2008: Evaluation of the Simulated Interannual and Subseasonal Variability in an AMIP-style Simulation Using the CSU Modeling Framework. *Journal of Climate*, **21**, 413-431.

[70] Kirkpatrick C, EW McCaul Jr, and C Cohen, 2009: Variability of Updraft and Downdraft and Characteristics in a Large Parameter Space Study of Convective Storms. *Monthly Weather Review*, **137**, 1550-1561.

[71] Kuo HL, 1974: Further studies of the parameterisation of the Influence of Cumulus Convection on large-scale flow. *Journal of the Atmospheric Sciences*, **3**, 1232-1240.

[72] Kuo H and RT Williams, 1990: Semi-lagrangian solutions to the inviscid Burgers Equation. *Monthly Weather Review*, **118**, 1278-1288.

[73] Landman WA, FA Engelbrecht, R Park, MM Bopape, and D Lotter, 2010: Atmospheric modelling and prediction at time scales

from days to seasons. The 3rd CSIR Biennial Conference, 30 August-01 September 2010.

[74] Li X, C-H Sui and KM Lau, 2002: Dominant Cloud Microphysical Processes in a Tropical Oceanic Convective System: A 2D Cloud Resolving Modeling Study. *Monthly Weather Review*, **130**, 2481-2491.

[75] Lin Y, RD Farley and HD Orville, 1983: Bulk Parametrization of the Snow Field in a Cloud Model. *Journal of Climate and Applied Meteorology*, **22**, 1065-1090

[76] Liu JY and HD Orville, 1969: Numerical Modelling of Precipitation and Cloud Shadow Effects on Mountain-Induced Cumuli. *Journal of the Atmospheric Sciences*, **26**, 1283-1298.

[77] Liu Y and PH Daum, 2004: Parameterization of the Autoconversion Process. Part I: Analytical Formulation of the Kessler-Type Parameterizations. *Journal of the Atmospheric Sciences*, **61**, 1539-1548.

[78] Liu C and MW Moncrief, 2007: Sensitivity of Cloud-Resolving Simulations of Warm-Season Convection to Cloud Microphysics parameterisations. *Monthly Weather Review*, **135**, 2854-2868.

[79] Lin Y and BA Colle, 2011: A New Bulk Microphysical Scheme That Includes Riming Intensity and Temperature-Dependent Ice Characteristics. *Monthly Weather Review*, **139**, 1013-1035.

[80] Louis J-F, 1979: A Parametric Model of Vertical Eddy Fluxes in the Atmosphere. *Boundary Layer Meteorology*, **17**, 187-202.

[81] Lucas C and EJ Zipser, 2000: Environmental Variability during TOGA COARE. *Journal of the Atmopsheric Sciences*, **57**, 2333-2350.

[82] Malherbe J, FA Engelbrecht, WA Landman and CJ Engelbrecht, 2012: Tropical Systems from the southwest Indian Ocean making landfall over the Limpopo River Basin, southern Africa: a historical perspective. *International Journal of Climatology*, **32**, 1018-1032.

[83] Mathes C, 2011: Tropical storm Dando kills five. http://www.eyewitnessnews.co.za/Story.aspx?Id=81095

[84] McDonald A., 1984: Accuracy of Multiply-Upstream, Semi-Lagrangian Advective Schemes. *Monthly Weather Review*, **112**, 1267-1275.

[85] McGregor JL, 1993: Economical Determination of Departure Points for semi-lagrangian models. *Monthly Weather Review*, **121**, 221-230.

[86] Mesinger, F., and A. Arakawa, 1976: Numerical methods used in atmospheric models. GARP Publication Series, Vol. 1, No. 17, WMO-ICSU, 64 pp.

[87] Milbrant JA and MK Yau, 2006a: A multimoment bulk microphysics parameterisation. Part III: Control Simulation of a Hailstorm. *Journal of the Atmospheric Sciences*, **63**, 3114-3136.

[88] Milbrant JA and MK Yau, 2006b: A multimoment bulk microphysics parameterisation. Part IV: Sensitivity Experiment. *Journal of the Atmospheric Sciences*, **63**, 3137-3159.

[89] Milbrandt JA, MK Yau, J Mailhot and S belair, 2008: Simulation of an Orographic Precipitation Event IMPROVE-2. PART I: Evaluation of the Control Run Using a Triple-Moment Bulk Microphysics Scheme. *Monthly Weather Review*, **136**, 3873-3893.

[90] Milbrandt JA, MK Yau, J Mailhot, S Belair and R McTagar-Cowan, 2010: Simulation of an Orographic Prediction Event during IMPROVE-2. Part II: Sensitivity to the Number of Moments in the Bulk Microphysics scheme. *Monthly Weather Review*, **138**, 625-642.

[91] Miller MJ, 1974: On the use of pressure as vertical co-ordinate in modelling convection. *Quarterly Journal of Royal Meteorological Society*, **100**, 155-162.

[92] Miller MJ and RP Pearce, 1974: A three dimensional primitive equation model of cumulonimbus convection. *Quarterly Journal of the Royal Meteorological Society*, **100**, 133-154.

[93] Miller MJ and AA White, 1984: On the nonhydrostatic equation in pressure and sigma coordinates. *Quartely Journal of the Royal Meteorological Society*, **110**, 515-533.

[94] Morrison H and WW Grabowski, 2007: Comparison of Bulk and Bin Warm-Rain Microphysics Models Using a Kinematic Framework. *Journal of the Atmospheric Sciences*, **64**, 2839-2861.

[95] Morrison H, G Thompson, and V Tatarskii, 2009: Impact of cloud microphysics on the development of trailing stratiform precipitation in a simulated squall line: Comparison of one- and two-moment schemes. *Monthly Weather Review*, **137**, 991–1007.

[96] Morrison H and J Milbrandt, 2011: Comparison of Two-Moment Bulk Microphysics Schemes in Idealised Supercell Thunderstorm Simulations. *Monthly Weather Review*, **139**, 1103-1130.

[97] Ogura Y and T Takahashi, 1971: Numerical Simulation of the Life Cycle of a Thunderstorm Cell. *Monthly Weather Review*, **99**, 895-911

[98] Petch JC, AR Brown and MEB Gray, 2002: The impact of horizontal resolution on the simulations od convective development over land. *Quarterly Journal of the Royal Meteorological Society*, **128**, 2031-2044.

[99] Petch JC, M Willet, RY Wong and SJ Woolnough, 2007: modelling suppressed and active convection. Comparing a numerical weather prediction, cloud-resolving and single-column model. *Quarterly Journal of the Royal Meteorological Society*, **133**,1087-1100.

[100] Phillips NA, 1957: A coordinate system having some special advantages for numerical forecasting. *Journal of Meteorology*, **14**, 184-185.

[101] Preston-Whyte RA and PD Tyson, 1988: The atmosphere and weather of southern Africa. Oxford University Press. 374pp.

[102] Preston B, 2005: Global Warming and Extreme Weather Events. Catastrophic Risk management. 22-23

[103] Pyle DM, 2006: Severe Convective Storm Risk in the Eastern Cape Province of South Africa. Doctoral Thesis. Rhodes University, 219 pp.

[104] Randall DA, 1996: A University Perspective on Global Climate Modeling. *Bullettin American Meteorological Society*, **77**, 2685-2690.

[105] Randall DA, K Xu, RJC Sommerville and S Iacobellis, 1996: Single-Column Models and Cloud Ensemble Models as Links between Observations and Climate Models. *Journal of Climate*, **9**, 1683-1697.

[106] Randall D, M Khairoutdinov, A Arakawa and W Grabowski, 2003a: Breaking the Cloud Parameterisation Deadlock. *Bulletin of the American Meteorological Society*, **84**, 1547-1564.

[107] Randall D and coauthors, 2003b: Confronting Models With Data: The GEWEX Cloud Systems Study. *Bulletin of the American Meteorological Society*, **84**, 455-469.

[108] Randall D, 2004: An introduction to Atmospheric Modeling. Colorado State University. 350 pp. http://kiwi.atmos.colostate.edu/group/dave/at604.html

[109] Reason CJC and A Keibel 2004: Tropical cyclone Eline and Its Unusual and Impacts over southern African mainland. *Weather and Forecasting*, **19**, 789-805.

[110] Reason, CJC., F Engelbrecht, WA Landman, JRE Lutjeharms, S Piketh, H Rautenbach, and BC Hewitson, 2006: A review of South African research in atmospheric science and physical oceanography during 2000-2005. *South African Journal of Science*, **102**, 35-45.

[111] Rickenbach TM and SA Rutledge, 1998: Convection in TOGA COARE: Horizontal Scale, Morphology and Rain Production. *Journal of the Atmospheric Sciences*, **55**, 2715-2729.

[112] Robert A, JL Yee and H Ritchie, 1985: A Semi-Lagrangian and Semi-Implicit Numerical Integration scheme for Multilevel Atmospheric Models. *Monthly Weather Review*, **113**, 388-394.

[113] Roberts N, 2003a: Numerical Weather Prediction: results from high resolution modelling of convective events. Forecasting Research Technical Report No. 402. Joint Centre for Mesoscale Meteorology Report No 140. 47 pp.

[114] Roberts N, 2003b: The Impact of a Change to the Use of the Convection scheme in high-resolution simulations of convective events. Joint Centre for Mesoscale Meteorology Internal Report No 142, Forecasting Research Technical Report 407. 30pp

[115] Room R, PMA Miranda and AJ Thorpe, 2001: Filtered nonhydrostatic models in pressure-related coordinates. *Quarterly Journal of Royal Meteorological Society*, **127**, 1277-1292.

[116] Rotunno R, JB Klemp and ML Weisman, 1988: A theory for strong, long-lived Squall Lines. *Journal of the Atmospheric Sciences*, **45**, 463-485.

[117] Rutledge SA and PV Hobbs, 1983: The Mesoscale and Microscale Structure and Organization of Clouds and Precipitation in Midlatitude Cyclones. VII: A Model for the “seeder-feeder” process in warm-frontal rainbands. *Journal of the Atmospheric Sciences*, **40**, 1185-1206

[118] Rutledge and Hobbs, 1984: The mesoscale and microscale structure and organization of clouds and precipitation in midlatitude cyclones. XII: A diagnostic modeling study of precipitation development in narrow cold-frontal rainbands. *Journal Atmospheric Science*, **41**, 2949-2972.

[119] Sapa, 2011: Gauteng Sizzles in Heat Wave. http://www.news24.com/SouthAfrica/News/Gauteng-sizzles-in-heat-wave-20111024.

[120] Sapa, 2012: Deadly Storm Hits KwaZulu-Natal. http://www.news24.com/SouthAfrica/News/Deadly-storm-hits-KwaZulu-Natal-20120101.

[121] Satoh M, H Tomita, H Miura, S Iga and T Nasuno, 2005: Development of a global cloud resolving model – a multi-scale structure of tropical convection. *Journal of Earth Simulator*, **3**, 11-19.

[122] Singleton AT and CJC Reason, 2007: Variability in the characteristics of cut-off lows pressure systems over subtropical southern Africa. *International Journal of Climatology*, **27**, 295-310.

[123] Skamarock, W. C., J. B. Klemp, J. Dudhia, D. O. Gill, D. M. Barker, W. Wang, and J. G. Powers, 2005: A description of the Advanced Research WRF Version 2. NCAR Tech Notes-468+S.

[124] Skamarock WC, JB Klemp, J Dudhia, DO Gill, DM Barker, MG Duda, X-Y Huang, W Wang and JG Powers, 2008: A description of the Advanced Research WRF Version 3. NCAR Technical Note. NCAR/TN-475+STR.

[125] Smagorinsky J, S Manabe and JL Holloway Jr, 1965: Numerical Results from a nine-level General Circulation Model of the atmosphere. *Monthly Weather Review*, **93**, 727-768.

[126] Soong S and Y Ogura, 1973: A Comparison Between Axisymmetric and Slab-Symmetric Cumulus Models. *Journal of the Atmospheric Sciences*, **30**, 879-893.

[127] Staniforth A and J Cote, 1991: Semi-Lagrangian Integration Schemes for Atmospheric Models – A review, *Monthly Weather Review*. **119**, 2206-2223.

[128] Stensrud, D. J., 2007: parameterisation Schemes: Keys to Understanding Numerical Weather Prediction Models. Cambridge University Press, 488 pp.

[129] Straka JM and ER Mansell, 2005: A Bulk Microphysics parameterisation with Multiple Ice Precipitation Categories. *Journal of Applied Meteorology*, **44**, 445-466.

[130] Stull R, The Atmospheric Boundary Layer in Wallace and Hobbs, 2006, Atmospheric science: an introductory survey. Acqdemic Press483pp. 375-417.

[131] Tadross, M.A., Jack C., and Hewitson B.C., 2005: On RCM-based projections of change in southern African summer climate. *Geophysical Research Letters*, **32**, L23713, doi 10.1029/2005GL024460.

[132] Tao W-K, J Simpson and M McCumber, 1989: Notes and Correspondence, An Ice-Water Saturation Adjustment. *Monthly Weather Review*, **117**, 231-235.

[133] Tao W-K and J Simpson, 1993: The Goddard Cumulus Ensemble Model. Part I: Model description. Terrestrial, *Atmospheric and Oceanic Sciences*, **4**, 19-54.

[134] Thompson G, PR Field, RM Rasmussen, and WD Hall, 2008: Explicit Forecasts of Winter Precipitation Using an Improved Bulk Microphysics Scheme. Part II: Implementation of a New Snow parameterisation. *Monthly Weather Review*, **136**, 5095-5115.

[135] Troen IB and L Mahrt, 1986: A simple model of the Atmospheric Boundary layer; sensitivity to surface evaporation. *Boundary-layer Meteorology*, **37**, 129-148.

[136] Tyson PD and RA Preston-Whyte, 2000: The Weather and Climate of Southern Africa. Oxford University Press.396pp

[137] Van den Heever S and WR Cotton, 2004: The Impact of the Hail Size on Simulated Supercell Storms. *Journal of the Atmospheric Sciences*, **61**, 1596-1609.

[138] Van Weverberg K, NPM Van Lipzig and L Delobbe, 2011: The Impact of Size Distribution Assumptions in a Bulk One-moment Microphysics Scheme on Simulated Surface Precipitation and Storm Dynamics during a Low-Topped Supercell Case in Belgium. *Monthly Weather Review*, **139**, 1131-1147

[139] Washington R and A Preston, 2006: Extreme wet years over southern Africa: Role of Indian Ocean sea surface temperatures, *Journal of Geophysical Research*, **111**, D15104, doi:10.1029/2005JD006724.

[140] Webster PJ and R Lukas, 1992: TOGA COARE - The Coupled Ocean - Atmosphere response Experiment. *Bulletin American Meteorological Society*, **73**, 1377-1416.

[141] Weisman ML and JB Klemp, 1982: The Dependence of Numerically Simulated Convective Storms on Vertical Wind Shear and Buoyancy. *Monthly Weather Review*, **110**, 504-520

[142] Weisman ML, WC Skamarock and JB Klemp, 1997: The resolution dependence of explicitly modelled convective systems. *Monthly Weather Review*, **125**, 527-548.

[143] Weissbluth MJ and WR Cotton, 1993: The representation of convection in mesoscale models. Part I: Scheme Fabrication and Calibration. *Journal of the Atmospheric Sciences*, **50**, 3852-3872.

[144] White AA, 1989: An extended version of a nonhydrostatic, pressure coordinate model. *Quarterly Journal of Royal Meteorological Society*, **115**, 1243-1251.

[145] Wilhemson RB and JB Klemp, 1978: A Numerical Study of Storm Splitting that Leads to Long-Lived Storms. *Journal of the Atmopsheric Sciences*, **35**, 1974-1986.

[146] Willet MR, P Bechtold. DL Williamson, JC Petch, SF Milton and SJ Woolnough, 2008: Modelling suppressed and active convection; Comparisons between three global atmospheric models. *Quarterly Journal of the Royal Meteorological Society*, **134**, 1881-1896.

[147] Woolnough SJ and PN Blossey, K-M Xu, P Bechtold, J-P Chaboureau, J Hosom, Sf Iacobellis, Y Luo, JC Petch, RY Wong and S Xie, 2008: Modelling Convective processes during the suppressed phase of the single-column models with cloud-resolving models. *Quarterly Journal of the Royal Meteorological Society*, **136**, 333-353.

[148] Wu X, WW Grabowski and MW Moncrieff, 1998: Long-term behavior of Cloud Systems in TOGA COARE and Their Interactions with Radiative and Surface Processes. Part I: Two-dimensional Modelling Study. *Journal of the Atmospheric Sciences*, **55**, 2693-2714.

[149] Wu L and GW Petty, 2010: Intercomparison of Bulk Microphysics Schemes in Model Simulations of Polar Lows. *Monthly Weather Review*, **138**, 2211–2228.

[150] Xie M and AJ Thorpe, 1991: A Mesoscale numerical model using the nonhydrostatic pressure-based sigma-coordinate equations: Model experiment with dry mountain flows. *Monthly Weather Review*, **119**, 1168-1185.

[151] Xu L, S Raman and RV Madala, 1991: A review of non-hydrostatic numerical models for the atmosphere. *Mathematics Subject Classification*, **86A10**, 3595-3609.

[152] Xu K and DA Randall, 1996: Explicit Simulation of Cumulus Ensembles with the GATE Phase III Data: Comparison with Observations. *Journal of the Atmospheric Sciences*, **53**, 3710-3736.

[153] Xu K and coauthors, 2000: Cloud-Resolving Model Intercomparison with ARM Summer IOP Data, 2000, Tenth RM Science Team Meeting Processes, San Antonio, March 13-17 2000.

[154] Xu K and DA Randall, 2000: Explicit Simulation of Midlatitude Cumulus Ensembles: Comparison with ARM Data. *Journal of the Atmospheric Science*, **57**, 2839-2858.

[155] Xu K and DA Randall, 2001: Updraft and Downdraft Statistics of Simulated Tropical and Midlatitude Cumulus Convection. *Journal of the Atmospheric Sciences*, **58**, 1630-1649.

[156] Yau MK and PM Austin, 1979: A Model for Hydrometeor Growth and Evolution of Raindrop Size Spectra in Cumulus Cells. *Journal of the Atmospheric Sciences*, **36**, 655-668.